

DIPLOMARBEIT

Numerische Simulation von
instationären dreidimensionalen viskoelastischen
Oldroyd-B- und Phan-Thien Tanner-Strömungen

Angefertigt am
Institut für Numerische Simulation

Vorgelegt der
Mathematisch-Naturwissenschaftlichen Fakultät der
Rheinischen Friedrich-Wilhelms-Universität Bonn

Juli 2008

Von
Susanne Claus
Aus
Saarbrücken

DIPLOMA THESIS

Numerical Simulation of Unsteady Three-Dimensional
Viscoelastic Oldroyd-B and Phan-Thien Tanner Flows

Developed at
the Institute for Numerical Simulation

Presented to
the Faculty of Mathematics and Natural Sciences of the
Rheinische Friedrich-Wilhelms-University Bonn, Germany

July 2008

By
Susanne Claus
From
Saarbrücken

Acknowledgements

I would like to thank Prof. Michael Griebel for his support and ideas and for giving me the opportunity to work on the great topic of my thesis. I am greatly indebted to my supervisors Roberto Croce, Margrit Klitz and Martin Engel, who have given me ideas, advice and inspiration along the way and who always assisted me with great expertise and patience. I would have been lost without them. Special thanks to Bram Metsch, Dr. Marc Alexander Schweitzer and Markus Bürger for their suggestions and assistance. I would also like to thank Prof. Tim Phillips for hosting me during a very inspiring and most interesting week in his research group at Cardiff University and for his numerous helpful ideas. I also want to thank Giancarlo Russo for our numerous enriching discussions and Ursula Claus, Jürgen Zimmer, Roland Wessels, Steven Lind and Paul Wakeley for reviewing this thesis.

Contents

Einleitung	i
1 Introduction	1
1.1 Non-Newtonian Fluids	1
1.2 Phenomena in Viscoelastic Flows	2
1.3 About this Thesis	3
1.4 Outline	7
2 Review of Continuum Mechanics	9
2.1 Kinematics	9
2.1.1 Velocity and Acceleration	9
2.1.2 Deformation and Vorticity	10
2.1.3 Strain	13
2.2 Stress and Body Forces	14
2.3 Conservation Laws	16
2.3.1 Conservation of Mass	16
2.3.2 Conservation of Linear Momentum	17
3 Constitutive Equations	19
3.1 Simple Flows, Viscosities and Stress Differences	19
3.1.1 Steady Shear Flow and Viscometric Functions	19
3.1.2 Steady Uniaxial Extensional Flow and Elongational Viscosity	21
3.2 The Newtonian Fluid	22
3.3 The Generalized Newtonian Fluid	23
3.4 Linear Viscoelasticity	24
3.4.1 Maxwell Model	24
3.4.2 Jeffreys Model	27
3.5 Nonlinear Models	28
3.5.1 Differential Models	28
3.5.2 Integral Models	31
3.6 Molecular Theories	33
3.6.1 Dilute Polymer Solutions	34
3.6.2 Polymer Melts and Concentrated Solutions	43
3.7 Summary of Behaviour in Simple Flows	53
4 Mathematical Model	55
4.1 Governing Equations	55
4.2 Non-Dimensionalization	56
4.3 Boundary and Initial Conditions	57

4.3.1	Initial Conditions	57
4.3.2	Solid Boundaries	57
4.3.3	Inflow and Outflow Boundaries	57
4.4	The High Weissenberg Number Problem	59
5	Numerical Method	63
5.1	Temporal Discretization	63
5.1.1	Explicit Projection Method	63
5.1.2	Time-Step Control	65
5.1.3	Semi-Implicit Projection Method	66
5.2	Spatial Discretization	67
5.2.1	Staggered Grid	67
5.2.2	Discretized Equations	69
5.2.3	Discrete Boundary Values	72
5.3	Algorithm	76
6	Parallelization	77
6.1	Domain Decomposition and Communication	77
6.2	Measuring Performance	79
7	Numerical Results	81
7.1	Unsteady Poiseuille Flow of an Oldroyd-B Fluid	83
7.1.1	Analytical Solution	83
7.1.2	Numerical Approximation	86
7.2	Flow through a Rectangular Channel	95
7.3	Convergence Study on a Flow through an Infinite Channel	99
7.4	Flow over a Hole	105
7.5	Kármán Vortex Street	114
8	Conclusion	125
A	Components of the Governing Equations	127
B	Analytical Solution of the Poiseuille Flow of an Oldroyd-B Fluid	131
	Bibliography	137

Einleitung

Viele Fluide, die in der Natur oder in industriellen Verfahren vorkommen, zeigen interessante und überraschende Fließmuster, die außerhalb des Bereiches der Newtonschen Fluide liegen. Für ein Newtonsches Fluid nehmen wir an, dass

1. die Spannung unabhängig von der Deformationsgeschichte ist, d.h. sie hängt nur vom Deformationszustand des gegenwärtigen Zeitpunktes ab (**Momentanreaktion**)
2. die Spannung nur von der Deformationsgeschwindigkeit am lokalen Ort abhängt (**lokale Wirkung**)
3. die Spannung linear von der Deformationsgeschwindigkeit abhängt (**Linearität**)
4. das Material isotropisch ist, dies bedeutet die physikalischen Eigenschaften sind richtungsunabhängig (**Isotropie**)

Alle Fluide, die Fließmuster aufweisen, die unter diesen Annahmen nicht vorhersagbar sind, werden **nicht-Newtonsche** Fluide genannt. Die Entwicklung mathematischer Modelle zur Beschreibung des Spannungszustandes und die experimentelle Untersuchung von nicht-Newtonschen Fluiden wird als **Rheologie** bezeichnet. Diese Arbeit beschäftigt sich mit **viskoelastischen** Fluiden, die eine wichtige Gruppe **nicht-Newtonscher** Fluide bilden. Ihr Verhalten wird durch viskose und elastische Kräfte beeinflusst. Beispiele umfassen flüssige Kunststoffe, Maschinenöle, Farben, Salben, Gele und viele biologische Fluide wie Eiweiß und Blut. Daher spielen sie in vielen industriellen Bereichen eine wichtige Rolle, wie z.B. in der chemischen, pharmazeutischen, Nahrungsmittel- und Ölindustrie. Deshalb ist die numerische Simulation dieser Fluide sehr erstrebenswert. Eine Vielzahl numerischer Verfahren wurde bereits dazu benutzt, um viskoelastische Strömungsprobleme zu lösen, aber die Berechnungen sind normalerweise auf zweidimensionale stationäre Kriechströmungen beschränkt. Um jedoch dreidimensionale und normalerweise instationäre industrielle Strömungsprozesse zu simulieren, ist es wichtig numerische Verfahren zu entwickeln, die dreidimensionale instationäre Strömungsprobleme lösen können. In dieser Arbeit entwickeln wir eine numerische Methode, um instationäre viskoelastische Probleme in drei Raumdimensionen zu lösen. Um viskoelastische Strömungsprobleme simulieren zu können, müssen wir uns zunächst für ein mathematisches Modell zur Beschreibung der Viskoelastizität entscheiden.

Mathematische Modellierung von Viskoelastizität

Jedes viskoelastische Fluid ist gekennzeichnet durch lange Molekülketten, deren Deformation zu ungewöhnlichem Fließverhalten wie dem Weissenberg-Effekt oder der Strangaufweitung führt. Diese Molekülketten und deren Wechselwirkungen mit umgebenen Fluidpartikeln müssen in jedem mathematischen Modell zur Beschreibung von Viskoelastizität berücksichtigt werden. Da die molekulare Struktur eines Fluids sehr komplex sein kann und von Material

zu Material sehr unterschiedlich ist, ist es unmöglich ein generelles Modell zur Beschreibung aller viskoelastischen Materialien zu entwickeln. Deshalb findet sich in der Literatur eine immense Vielzahl an unterschiedlichen Modellen. Dies zwingt uns, eine Entscheidung bezüglich des mathematischen Modells zu fällen und uns für bestimmte Klassen von viskoelastischen Fluiden zu entscheiden. In dieser Arbeit geben wir einen Überblick über die bekanntesten viskoelastischen Stoffmodelle. Da die mathematische Beschreibung der Viskoelastizität eine schwierige Aufgabe ist, geben wir eine detaillierte Einführung in die mathematische Modellierung. Wir beginnen mit den grundlegenden Definitionen von Scherviskosität, Normalspannungsdifferenzen und Dehnviskosität. Diese Größen sind wichtige Materialparameter und ermöglichen die Klassifizierung von Materialien. Für Newtonsche Fluide zum Beispiel sind die Scher- und Dehnviskosität konstant und die Normalspannungsdifferenzen sind Null. Aber für viskoelastische Fluide sind die Viskositäten Funktionen der Deformationsgeschwindigkeit und es treten Normalspannungsdifferenzen auf.

Wir nutzen diese Viskositätsfunktionen und Normalspannungsdifferenzen, um unsere vorgestellten Modelle zu kategorisieren, die Fluidklassen zu bestimmen, die sie beschreiben und um ihre Vor- und Nachteile aufzuzeigen. Dazu lösen wir die Stoffgleichungen für zwei einfache Strömungen (die stationäre Scherströmung und die homogene Dehnströmung) mit dem Newton-Verfahren und plotten die Viskositätsfunktionen und die Normalspannungsdifferenzen.

Wir beginnen unseren Modellüberblick mit linearen viskoelastischen Modellen und deren Verallgemeinerung in eine 3D-Tensorformulierung. Danach stellen wir die grundlegenden Ideen zur Modellierung von Viskoelastizität mittels molekularer Theorien vor. Dabei fokussieren wir uns auf die Herleitung des Oldroyd-B Modells zur Modellierung dünner Polymerlösungen und des Phan-Thien Tanner (PTT) Modells zur Modellierung von konzentrierten Polymerlösungen. Wir leiten das Oldroyd-B Modell von der Vorstellung elastischer Hanteln, bestehend aus zwei identischen Kugeln und einer elastischen Verbindungsfeder, die in einem Newtonschen Fluid schwimmen, ab. Um die Gleichung für den Spannungstensor zu erhalten, leiten wir die Bewegungsgleichung für die Hantel her und erhalten eine Fokker-Planck Gleichung für die Wahrscheinlichkeitsverteilung des Verbindungsvektors zwischen den Hantelkugeln. Die Gleichung für den Spannungstensor kann dann mit Hilfe der von der Hantel auf das Fluid durchschnittlich übertragenen Kraft ermittelt werden. Das Phan-Thien Tanner Modell wird hergeleitet aus einem Netzwerk von Molekülketten, die an temporären Knotenpunkten verbunden sind. Dabei benutzen wir die nicht affine Bewegungsgleichung des Netzwerks und die Liouville Gleichung für die Zerstörungs- und Erzeugungsrate der Knotenpunkte, um die Gleichung für den Spannungstensor herzuleiten. Nachdem wir die beiden Modelle in zwei einfachen Strömungen untersucht haben, stellen wir abschließend in einer Tabelle die Modelleigenschaften aller vorgestellten Modelle bezüglich der Viskositätsfunktionen und Normalspannungsdifferenzen dar.

Wir entscheiden uns für das Oldroyd-B und das lineare sowie das exponentielle Phan-Thien Tanner Modell mit nicht affiner Bewegungsvorhersage und einem Newtonschen Anteil an dem Spannungstensor, um die Viskoelastizität zu modellieren. Dies ermöglicht uns ein weites Spektrum an viskoelastischen Fluiden zu simulieren. Außerdem gehören beide Modelle zu den am weitesten entwickelten Modellen.

Numerische Methode

Nachdem wir uns für die viskoelastischen Stoffmodelle entschieden haben, können wir nun mit der Diskussion über ihre numerische Lösung beginnen. Um die Strömung eines viskoelastischen Fluids zu simulieren, benötigen wir die Kontinuitätsgleichung, die Bewegungsgleichung und die viskoelastischen Stoffgleichungen. Wir nehmen an, dass unsere Fluide inkompressibel sind und dass thermische Effekte vernachlässigt werden können. Da sowohl das Oldroyd-B als auch das PTT Modell einen Newtonschen Anteil an dem Spannungstensor besitzen, ergibt das Einsetzen der Stoffgleichungen in die Bewegungsgleichung die folgende Gleichung

$$\rho \frac{D\mathbf{u}}{Dt} = -\nabla p + \eta_0 \beta \Delta \mathbf{u} + \operatorname{div} \boldsymbol{\tau}, \quad (0.1)$$

wobei ρ die Dichte des Fluids ist, η_0 die Gesamtviskosität (= Newtonsche Viskosität + polymerische Viskosität), β das Verhältnis von Newtonscher zur Gesamtviskosität, \mathbf{u} die Geschwindigkeit, p der Druck und $\boldsymbol{\tau}$ der elastische Spannungstensor, der durch die Oldroyd-B bzw. Phan-Thien Tanner Gleichungen gegeben ist. Die Bewegungsgleichung (0.1) ist eine Erweiterung der Navier-Stokes Gleichungen. Der diffusive Term wird durch β skaliert und die Divergenz des elastischen Spannungstensors wird addiert. Deshalb können wir einen Navier-Stokes Löser als Basis für unsere numerische Lösung nutzen. Wir nutzen das CFD-Paket NaSt3DGP [1], das einen komplett parallelisierten, dreidimensionalen Navier-Stokes Löser enthält und am Institut für Numerische Simulation der Universität Bonn in der Arbeitsgruppe von Prof. Michael Griebel entwickelt wird, als Basis für unsere Modifikationen. Zusammengefasst implementieren wir die folgenden Erweiterungen und Modifikationen, um das Oldroyd-B Modell und das PTT Modell in den Strömungscode zu integrieren:

- Wir wählen passende Diskretisierungspunkte für die Komponenten des elastischen Spannungstensors.
- Wir lösen die Oldroyd-B und Phan-Thien Tanner Gleichungen und implementieren passende Rand- und Anfangswerte für sechs Komponenten des Spannungstensors.
- Wir erweitern die Navier-Stokes Gleichungen, um die Bewegungsgleichung (0.1) zu erhalten.
- Wir erweitern das Zeitdiskretisierungsschema, um das gekoppelte Gleichungssystem inklusive der viskoelastischen Stoffgleichungen zu lösen.
- Wir parallelisieren alle Modifikationen, um unsere Berechnungen zu beschleunigen.
- Wir suchen nach passenden Visualisierungsmöglichkeiten für den Spannungstensor.

Bevor wir anfangen unsere Gleichungen zu implementieren und zu erweitern, müssen wir passende Diskretisierungspunkte für die Komponenten des Spannungstensors bestimmen. In NaSt3DGP sind die Geschwindigkeiten und der Druck auf einem versetzten Gitter diskretisiert, wobei der Druck in den Zellmittelpunkten und die Geschwindigkeiten an den Zellseitenflächen diskretisiert sind. Nun müssen wir uns entscheiden, an welchem Punkt wir unsere Spannungstensor-Komponenten in diesem Gitter positionieren wollen. In der Literatur sind hauptsächlich zwei Ansätze vertreten: der eine diskretisiert die Normalspannungskomponenten im Zellmittelpunkt und die Scherspannungskomponenten an den Zellkanten und der andere diskretisiert alle Spannungskomponenten im Zellmittelpunkt. Wir diskretisieren alle Spannungskomponenten im Zellmittelpunkt, da dies vermeidet, dass Unbekannte an einem

singulären Hindernispunkt liegen.

Wir diskretisieren die Ortsableitungen der Geschwindigkeiten in den Oldroyd-B und Phan-Thien Tanner Gleichungen mittels zentraler Differenzen mit Ausnahme der konvektiven Terme, die wir mittels Verfahren höherer Ordnung diskretisieren. NaSt3DGP bietet mehrere Verfahren höherer Ordnung inklusive des VONOS- und WENO-Schemas. Darüber hinaus implementieren wir Dirichlet- und homogene Neumannrandwerte für Ein- und Ausströmränder sowie Haftbedingungen für die festen Wände für die Spannungstensorcomponenten. Außerdem erweitern wir die Navier-Stokes Gleichungen um den Parameter β und diskretisieren die Divergenz des Spannungstensors mittels zentraler Differenzen.

Natürlich müssen wir auch das Zeitdiskretisierungsschema modifizieren, um die viskoelastischen Stoffmodelle in das Schema zu integrieren. NaSt3DGP nutzt eine Chorinsche Projektionsmethode und eine semi-implizite Projektionsmethode mit impliziter Behandlung der diffusiven Terme zur Lösung der Gleichungen. Wir erweitern beide Projektionsmethoden, indem wir im ersten Schritt der Methode die Oldroyd-B und Phan-Thien Tanner Gleichungen explizit in der Zeit diskretisieren. Die so ermittelten Spannungstensorcomponenten werden dann in der Berechnung des Schätzgeschwindigkeitsfeldes genutzt. Des Weiteren müssen wir eine zusätzliche Zeitschrittweitenbeschränkung berücksichtigen, die aus der expliziten Behandlung der viskoelastischen Stoffgleichungen resultiert.

Da wir Gleichungen für zehn Unbekannte in jedem Zeitschritt lösen müssen, ist die Berechnung von dreidimensionalen instationären viskoelastischen Strömungen sehr kostenintensiv, insbesondere für komplexe Strömungen. Dies ist einer der Gründe, warum die meisten der bisher entwickelten numerischen Methoden nur in 2D implementiert sind. Durch Parallelisierung können wir unsere Berechnungen beschleunigen und die Rechenzeit reduzieren. Deshalb parallelisieren wir unsere Erweiterungen und testen die Beschleunigung an Hand eines Effizienz- und Speedup-Tests. Dieser Test zeigt hervorragende Werte sogar für große Prozessoranzahlen, die kleine Gebiete bearbeiten.

Wir visualisieren den Spannungstensor mit Hilfe einer strömungsrichtungsabhängigen Zerlegung des Spannungstensors in eine Scher- und eine Normalspannung, damit wir eine physikalisch sinnvolle Messgröße für komplexe Strömungen erhalten. Mit diesen Messgrößen ist es möglich, eine Gesamtspannung zu berechnen, die dann zusammen mit der Scher- und Normalspannung visualisiert werden kann.

Validierung and Resultate

Wir validieren unsere Implementierung, indem wir

- die numerische Approximation der analytischen Lösung für die instationäre Poiseuille-Strömung eines Oldroyd-B Fluides untersuchen und
- die Konvergenzordnung des numerischen Verfahrens anhand einer dreidimensionalen Strömung durch einen unendlichen Kanal, der mit Hilfe der Gravitation angetrieben wird, bestimmen.

Dazu implementieren und parallelisieren wir die analytische Lösung der instationären Poiseuille-Strömung für das Geschwindigkeitsfeld und die Spannungstensorcomponenten in NaSt3DGP, um unsere numerischen Resultate mit der instationären analytischen Lösung zu

vergleichen. Wir finden eine ausgezeichnete Übereinstimmung der numerischen mit der analytischen Lösung und erhalten quadratische Konvergenzraten für die Geschwindigkeit und die Spannungstensoranteile mit zunehmender Gitterverfeinerung. Um den Code in drei Raumdimensionen zu validieren, führen wir eine Konvergenzanalyse für die Oldroyd-B und die Phan-Thien Tanner Gleichungen bei einer per Gravitation betriebenen Strömung durch einen dreidimensionalen unendlichen Kanal durch und finden quadratische Konvergenzraten für alle Komponenten.

Des Weiteren untersuchen wir

- eine Strömung durch einen dreidimensionalen rechteckigen Kanal,
- eine Nischenströmung und
- eine Kármánsche Wirbelstraße

und vergleichen die Resultate für die verschiedenen Modelle. Für die Strömung durch einen dreidimensionalen rechteckigen Kanal plotten und vergleichen wir die Geschwindigkeits- und Spannungsprofile der verschiedenen Modelle. Danach untersuchen wir eine Nischenströmung und beobachten eine asymmetrische Wirbelstruktur für das Oldroyd-B und die PTT Fluide, die auch in Experimenten zu beobachten ist. Danach analysieren wir das Verhalten der Spannungstensoranteile an den singulären Punkten der Geometrie und finden sehr hohe Spannungsgradienten, die insbesondere problematisch im Falle des Oldroyd-B Modells sind. Abschließend betrachten wir eine Kármánsche Wirbelstraße für die verschiedenen Modelle und beobachten Unterschiede im Wirbeldehnungsverhalten und eine Unterdrückung von Geschwindigkeitsfluktuationen, die auch in Laborexperimenten zu beobachten sind. Unseres Wissens ist die Kármánsche Wirbelstraße für viskoelastische Fluide noch nicht numerisch untersucht worden.

Überblick

Diese Arbeit ist wie folgt aufgebaut:

Kapitel 2 enthält einen kurzen Überblick über die kontinuumsmechanischen Grundlagen, die zur Beschreibung von Strömungen notwendig sind.

Kapitel 3 beinhaltet die bekanntesten viskoelastischen Stoffmodelle. Wir beginnen mit der Definition der Scher- und Dehnviskosität sowie der Normalspannungsdifferenzen. Danach präsentieren wir linear viskoelastische Stoffmodelle und erläutern die Begriffe Relaxationszeit und schwindendes Gedächtnis. Außerdem diskutieren wir ihre Verallgemeinerung in eine 3D-Tensorformulierung. Dann stellen wir die grundlegenden Ideen zur Modellierung von Viskoelastizität mittels molekularer Theorien vor. Dabei fokussieren wir uns auf die Herleitung des Oldroyd-B Modells und des Phan-Thien Tanner (PTT) Modells. Wir untersuchen das Verhalten des Oldroyd-B und Phan-Thien Tanner Modells an Hand von einfachen Strömungen und diskutieren ihre Vor- und Nachteile. Abschließend, geben wir einen Überblick über alle vorgestellten Modelle.

Kapitel 4 gibt das vollständige Gleichungssystem zur Beschreibung viskoelastischer Strömungen an. Wir diskutieren die Entdimensionalisierung der Gleichungen und besprechen die Randwerte die notwendig zur Lösung des Gleichungssystem sind. Die Entdimensionalisierung führt zur dimensionslosen Weissenbergzahl, die mit dem sogenannten "High Weissenberg number problem" (HWNP) in Zusammenhang steht. Das HWNP beschreibt den Zusammenbruch

numerischer Verfahren über einem kritischen Wert der Weissenbergzahl. Wir diskutieren einige wichtige Aspekte, die zu diesem Problem führen.

Kapitel 5 beschäftigt sich mit der numerischen Lösung der Gleichungen. Dazu stellen wir zunächst die Chorinsche Projektionsmethode vor und diskutieren die Zeitschrittweitenbeschränkungen, die durch die explizite Behandlung der Gleichungen entstehen. Da die Zeitschrittweiteinschränkung zu sehr kleinen Zeitschrittweiten im Falle der Simulation von Strömungen mit niedrigen Reynoldszahlen führt, stellen wir zudem eine semi-implizite Projektionsmethode vor. Danach diskutieren wir die räumliche Diskretisierung auf einem versetzten Gitter und die diskreten Randwerte.

Kapitel 6 erläutert eine Parallelisierungsstrategie per Gebietszerlegung, um unsere Berechnungen zu beschleunigen. Wir messen die Beschleunigung mit Hilfe der Effizienz und des Speedups und erhalten hervorragende Werte.

Kapitel 7 enthält die numerischen Resultate. Wir validieren unseren Code, indem wir die numerische Approximation der analytischen Lösung für die instationäre Poiseuille-Strömung eines Oldroyd-B Fluides untersuchen und die Konvergenzordnung des numerischen Verfahrens anhand einer dreidimensionalen Strömung durch einen unendlichen Kanal, der mit Hilfe der Gravitation angetrieben wird, bestimmen. Des Weiteren untersuchen wir eine Strömung durch einen dreidimensionalen rechteckigen Kanal, eine Nischenströmung und eine Kármán-sche Wirbelstraße und vergleichen die Resultate für die verschiedenen Modelle.

Kapitel 8 rundet diese Arbeit durch eine Zusammenfassung und einen Ausblick ab.

Im **Anhang** befinden sich alle Gleichungen in Komponentenschreibweise und die Herleitung der analytischen Lösung der Spannungstensor-Komponenten für die instationäre Poiseuille-Strömung eines Oldroyd-B Fluides.

Chapter 1

Introduction

1.1 Non-Newtonian Fluids

Many fluids appearing in nature and in industrial processes show interesting and unexpected flow patterns, which fall outside the scope of Newtonian fluid mechanics. For a **Newtonian fluid**, we assume that

1. the stress is independent of any previous history of distortion, i.e. it depends only on the deformation state at the present time (**present time**),
2. the stress depends only on the local kinematic state of the immediate neighbourhood (**local action**),
3. the stress depends linearly on the rate of deformation (**linearity**),
4. the material is considered to be isotropic, that means its physical properties are independent of direction (**isotropy**).

All fluids with flow patterns that cannot be predicted under these assumptions are called **non-Newtonian fluids**. The development of mathematical models for the stress and the experimental investigation of non-Newtonian fluids is called **rheology**.

This thesis is concerned with **viscoelastic fluids**, which form an important group among non-Newtonian fluids. Their behaviour is influenced by viscous and elastic forces. Examples include molten plastics, engine oils, paints, ointments, gels, and many biological fluids such as egg white and blood. They appear in many industrial processes, e.g. in the chemical, pharmaceutical, food, and oil industries. Thus, the numerical simulation of these fluids is highly desirable. A variety of numerical techniques has been used to solve viscoelastic flow problems, but usually the calculations are restricted to two-dimensional stationary creeping flows. However, industrial flow processes are usually transient and have to be modelled in three dimensions. In this thesis, we develop a numerical method for solving transient viscoelastic flow problems in three space dimensions. Let us start with a look at some of the most famous and spectacular viscoelastic fluid phenomena and their qualitative explanation.

1.2 Phenomena in Viscoelastic Flows



(a) Weissenberg effect (G. McKinley [48]). (b) Die swell in Newtonian and polymeric liquids (YouTube, Psidot [56]).

Figure 1.1: Normal stress effects.

The basic feature of viscoelastic fluids is the presence of long chain molecules within the fluid. These have to be taken into account in order to describe viscoelastic flow behaviour. The molecular chains affect the surrounding fluid particles, whereas the surrounding particles deform the chain molecules. This interplay of differently shaped and sized particles gives rise to typical macroscopic viscoelastic fluid phenomena. Polymeric liquids, which are characterized by very long molecular chains, show viscoelastic effects in a distinctive manner. Thus, they are used in all experiments introduced in this section.

We start with one of the most striking viscoelastic phenomena: the rod-climbing or Weissenberg effect. Experimentally, a rotating rod is inserted into a beaker filled with liquid. In a Newtonian fluid, the rotating motion generates a centrifugal force which pushes the liquid outward and the free surface dips near the rod. In contrast, in viscoelastic fluids, the free surface rises and the fluid climbs up the rod (see Figure 1.1(a)). The rod-climbing is caused by tension along the concentric streamlines, which leads to a force pushing the fluid inward. This tension force arises from the deformation of the molecular chains. The molecular chains are aligned and stretched out with the flow direction by the drag forces exerted on them by the surrounding fluid. Their natural tendency to retract from this stretched configuration generates the tension, which tries to reduce the length of the streamlines, hence pulling the liquid towards the rod. This tension is usually referred to as a “normal stress”.

Another effect linked to the normal stress is die swell. When a fluid is forced out of the orifice of a syringe, the jet of extrudate swells, i.e. it expands radially to a diameter greater than that of the orifice. Newtonian fluids exert this effect as well, but the increase in diameter is considerably greater for polymeric fluids. This is again due to the tension along the streamlines, which is generated by the shearing motion, which stretches the molecular chains inside the orifice. When the fluid exits the orifice, the tension is relieved, causing the jet to shrink in the longitudinal direction and expand in the transverse direction. See Figure 1.1(b) for a contrast between a Newtonian and a polymeric die swell.

The normal stress can become very large and can even enable a fluid to flow against gravity as observed in the tubeless syphon experiment, illustrated in Figure 1.2. In the experiment, a nozzle is dipped into a dish of a polymeric liquid and is sucked into the syringe. Then, the

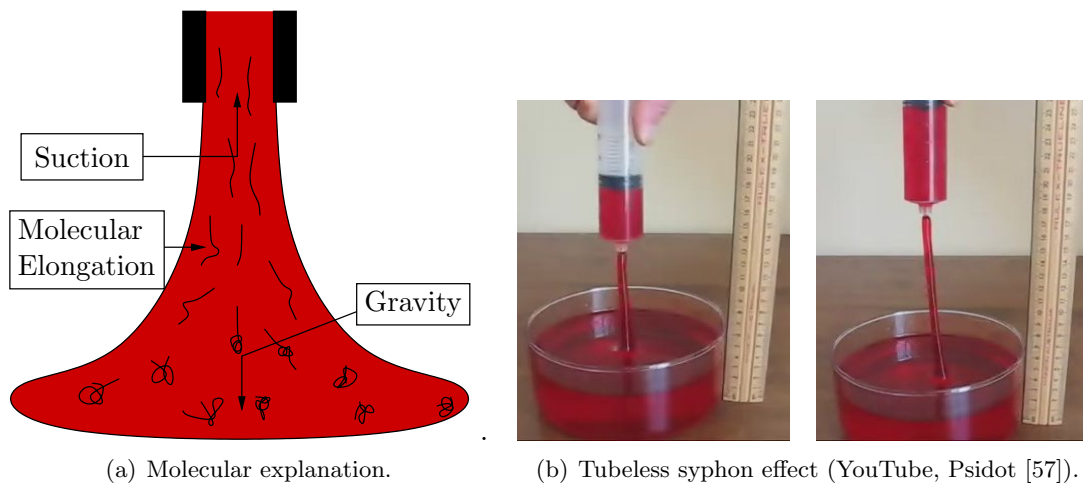


Figure 1.2: Tubeless syphon.

syringe is raised above the free surface under continuous pulling. In contrast to Newtonian fluids, where the jet of fluid would immediately break, the polymeric fluid continues to flow into the syringe against gravity. The strong and fast stretching of the fluid causes the molecular chains to stretch very rapidly generating a huge normal stress strong enough to pull the liquid out of the dish. A schematic sketch of the stretching of the molecular chains is presented in Figure 1.2(a).

1.3 About this Thesis

The main aim of this thesis is to develop a numerical method for solving transient viscoelastic flow problems in three space dimensions. The first step toward the numerical simulation of viscoelastic flows is to make a choice on the mathematical model to describe viscoelasticity.

Mathematical Modelling of Viscoelastic Fluids

As observed in the previous section, any mathematical model of viscoelasticity has to take the molecular chains and their interaction with the flow into account. Since the molecular structure of a fluid can be very complex and differs enormously from one material to another, it is impossible to find a general model suitable for the description of all classes of viscoelastic materials. Therefore, there exists a huge amount of different models in literature. This forces us to make a choice on the mathematical model and therewith on the kinds of fluids, we wish to describe. In this thesis, we give an overview over the most famous models in viscoelasticity. Since the mathematical description of viscoelasticity is a difficult task, we give a detailed introduction to the mathematical modelling starting with the basic definitions of shear-rate dependent viscosity, normal stress differences and elongational viscosity. These terms describe important material properties and offer a way to categorize materials. For example, for Newtonian fluids both the shear-rate dependent viscosity and the elongational

viscosity are constant and there are no normal stress differences, but for viscoelastic fluids the viscosities are functions of the deformation rate and normal stress differences occur.

In a next step, we investigate the viscosity functions and normal stress differences in order to categorize the introduced models according to the classes of fluids they describe, as well as to show their respective advantages and disadvantages. Therefore, we solve the model equations for two simple flows (the steady shear flow and the uniaxial extension) by Newton's method and plot the viscosity functions and normal stress differences.

Our general overview commences with linear viscoelasticity models and their generalization into a 3D tensor formulation. Then, we present the basic ideas for models derived from molecular theories. Among these models, we focus on the derivation of the Oldroyd-B equations to model dilute polymer solutions and the derivation of the Phan-Thien Tanner equations to model polymer melts and concentrated solutions. We derive the Oldroyd-B model from the notion of elastic dumbbells consisting of two beads connected by a spring, which swim in a Newtonian fluid. To obtain the expression for the stress tensor, we deduce the equation of motion for the dumbbell and obtain a Fokker-Planck equation for the distribution of the end-to-end vector of such an elastic dumbbell. Then, we acquire the equation for the stress tensor through averaging of the forces transmitted from the dumbbells to the fluid. Afterwards, we derive the Phan-Thien Tanner equations from a network of molecular chains that are linked at temporary junctions. Here, we use the equation for the non-affine motion of the network and the Liouville equation for the loss and creation rates of the junctions to obtain the equation for the stress tensor. After investigating these models in two simple flows, we conclude the overview by a table describing the properties of all introduced models in terms of viscosities and normal stress differences as described above.

We choose the Oldroyd-B equations and both the exponential form and the linear form of the Phan-Thien Tanner equations including the prediction of non-affine motion and a Newtonian contribution to the stress tensor to model viscoelasticity. This enables us to simulate a wide variety of viscoelastic fluids including dilute polymer solutions, polymer melts and concentrated solutions. Furthermore, both the Oldroyd-B and the Phan-Thien Tanner models are sophisticated models describing viscoelastic flow behaviour quite accurately.

Numerical Method

After choosing the viscoelastic models, we can proceed to discuss their numerical solution. In order to simulate the flow of a viscoelastic fluid, we need the continuity equation, the momentum equation and the viscoelastic model equation. We assume that the fluids are incompressible and that thermal effects can be neglected. Both the Oldroyd-B and the Phan-Thien Tanner equations have a Newtonian contribution to the stress tensor so that their insertion into the momentum equation results in

$$\rho \frac{D\mathbf{u}}{Dt} = -\nabla p + \eta_0 \beta \Delta \mathbf{u} + \operatorname{div} \boldsymbol{\tau}, \quad (1.1)$$

where ρ is the density of the fluid, η_0 is the total viscosity (= Newtonian viscosity + polymeric viscosity), β is the ratio of the Newtonian viscosity to the total viscosity, \mathbf{u} is the velocity, p is the pressure and $\boldsymbol{\tau}$ is the elastic stress tensor described by the Oldroyd-B or Phan-Thien Tanner equations. The momentum equation (1.1) is an extension of the Navier-Stokes equations: the diffusive terms are scaled through the parameter β and the divergence of the

elastic stress tensor is added. Therefore, we can use a Navier-Stokes solver as the basis for our numerical solution. We use the CFD package NaSt3DGP [1], which contains a fully parallelized, three-dimensional Navier-Stokes solver developed at the Institute for Numerical Simulation in the research group of Prof. Michael Griebel. In summary, we implement the following modifications and extensions into NaSt3DGP in order to include the Oldroyd-B and PTT equations:

- We choose a proper spatial discretization point for the elastic stress tensor components.
- We solve the Oldroyd-B and Phan-Thien Tanner equations and implement appropriate boundary and initial conditions for the six elastic stress tensor components (the elastic stress tensor is symmetric, therefore we have to calculate only six components).
- We extend the Navier-Stokes equations to the momentum equation (1.1).
- We extend the temporal discretization scheme to solve the coupled system of equations including the viscoelastic stress equations.
- We parallelize all modifications to accelerate the computation.
- We find appropriate ways to visualize the stress tensor.

Before, we implement any equations, we have to choose the discretization points of the stress tensor components. NaSt3DGP uses a staggered grid approach, where the pressure is discretized at the centre of the cells, while the velocities are discretized at the cell sides. However, it remains to locate the stress tensor components on this grid. There are mainly two approaches in literature: one, which discretizes the normal stress tensor components in the middle of the cells and the shear stress components at the vertices of the cells and the other, which discretizes all stress components in the middle of the cells. We decided to discretize all stress tensor components in the middle of the cells, which avoids having an unknown located at a cell vertex, that may happen to be at a geometric singularity.

Then, we discretize the spatial derivatives in the Oldroyd-B and Phan-Thien Tanner equations by central differences except for the convective terms, which we discretize by higher order methods. Here, NaSt3DGP offers several higher order methods including the VONOS scheme and the WENO scheme. To our knowledge, the WENO scheme has not yet been used in the simulation of viscoelastic fluids. In most published work the first order upwind method or the QUICK scheme are used. However, these schemes have some severe disadvantages. The first order upwind method introduces a lot of numerical diffusion polluting the results and the QUICK scheme produces unphysical oscillations. Therefore, the usage of more sophisticated higher order methods such as the WENO scheme can produce better results. Moreover, we implement Dirichlet, homogeneous Neumann and no-slip boundary conditions for the stress tensor components. In a next step, we extend the Navier-Stokes equations by the parameter β and discretize the divergence of the elastic stress tensor by central differences.

Of course, also the temporal discretization scheme has to be modified in order to include the viscoelastic model equations. For the temporal discretization NaSt3DGP employs a Chorin-type projection method and a semi-implicit projection method with implicit treatment of the diffusive terms developed by Klitz [42]. We extend both projection methods. Therefore, we advance the Oldroyd-B and Phan-Thien Tanner equations explicitly in time by the Euler method to obtain the stress components at the new time-step. These stress tensor components are then used in the calculation of the intermediate velocity field. Furthermore, we have to include a time-step restriction arising from the explicit treatment of the viscoelastic model

equations.

Since we need to solve the governing equations for ten unknowns: three velocity components, the pressure and six stress tensor components at each time-step, the computation of three-dimensional transient viscoelastic flows is a huge computational task, especially for complex flow situations. This is one reason why most of the numerical methods currently available are only implemented for 2D cases. Therefore, we have to accelerate our computations. We can reduce the total computing time by parallelization, which divides the work between several processors. We parallelized all our extensions and we tested the parallelization by efficiency and speed-up computations. The tests show excellent results even for large processor numbers treating very small domains.

To visualize the stress tensor, we compute a flow directed decomposition of the stress tensor into shear and normal stress to obtain a physically meaningful stress measure in complex flows [10]. These values can be used to calculate a principal stress. We implement different file writing routines for the stress tensor components and the computed shear, normal and principal stress to visualize the data with Matlab and ParaView [32].

Validation and Results

To validate our implementation, we investigate

- the numerical approximation of the analytical solution for transient plane Poiseuille flow of an Oldroyd-B fluid,
- the order of convergence for a three-dimensional gravity driven flow through an infinite rectangular channel.

We implement and parallelize the analytical solution for the plane Poiseuille flow of an Oldroyd-B fluid for both the velocity and stress tensor components into NaSt3DGP in order to compare our numerical results with the transient analytical solution. We find a very good agreement between the transient analytical solution and the numerical solution for the velocities and stress tensor components. Further, we find that the numerical solution converges quadratically to the steady state analytical solution with mesh refinement. To validate the code in three space dimensions for both the Oldroyd-B and the Phan-Thien Tanner equations, we carry out a convergence study for the three-dimensional gravity driven flow through an infinite rectangular channel. We find the fantastic result of quadratic convergence for all components.

Furthermore, we examine

- the flow through a three-dimensional rectangular channel,
- the flow over a hole,
- the Kármán vortex street behind an inclined plate

and compare the results for the different models. For the flow through a three-dimensional rectangular channel, we plot and compare the velocity and stress tensor components for the different models. Then, we examine the flow over a hole and observe an asymmetric vortex structure for the Oldroyd-B fluid and the PTT fluids, as seen in experiments with viscoelastic fluids. Subsequently, we analyze the stress behaviour on the corner singularities of the flow for the different models and find very steep stress gradients for the Oldroyd-B model, while

the stress gradients for the Phan-Thien Tanner models are much less problematic. Finally, we investigate the Kármán vortex street behind an inclined plate for the different models. We are able to observe different vortex stretching behaviour and suppression of velocity fluctuations as seen in laboratory experiments. To our knowledge, the Kármán vortex street behind an inclined plate, has not yet been numerically investigated for viscoelastic flows.

1.4 Outline

This thesis is organized as follows:

Chapter 2 gives a short overview over the basic principles of continuum mechanics needed for the mathematical description of fluid flows.

Chapter 3 introduces the most famous models describing viscoelasticity. We start with the definition of the shear-rate dependent viscosity, normal stress differences and elongational viscosity. Then, we present the linear viscoelasticity models, explain the terms relaxation time and fading memory and discuss their generalization into a 3D tensor formulation. In a next step, we introduce the basic ideas for models derived from molecular theories and discuss in detail the derivation of the Oldroyd-B equations and of the Phan-Thien Tanner equations. Afterwards, we investigate the behaviour of the Oldroyd-B model and the Phan-Thien Tanner model in simple flows, discuss their advantages and disadvantages, and consider the fluids they describe. Finally, we present an overview over all the models introduced.

Chapter 4 gives the full set of equations necessary to describe viscoelastic flows. We discuss their non-dimensionalization and the boundary conditions needed in order to solve them. The non-dimensionalization introduces the Weissenberg number, which is associated with a problem called the high Weissenberg number problem (HWNP) describing the numerical breakdown beyond some critical value of the Weissenberg number. We will discuss some of the important aspects causing this problem.

Chapter 5 deals with the numerical solution of the governing equations. First, we present a Chorin-type explicit project method. Then, we discuss the time-step restrictions resulting from the explicit treatment of the equations. Since the time-step restriction for the diffusive terms leads to very small time-steps for low Reynolds number flows, we also introduce a semi-implicit projection method. Afterwards, we discuss the spatial discretization on a staggered grid and the discrete boundary values.

Chapter 6 discusses a parallelization strategy by domain decomposition, which enables us to accelerate our computations. We measure the acceleration in terms of speed-up and efficiency and obtain very good results.

Chapter 7 contains our numerical results. We validate our code by the investigation of the numerical approximation of the analytical solution for transient plane Poiseuille flow of an Oldroyd-B fluid and by a convergence study on a three-dimensional gravity driven flow through an infinite rectangular channel. Furthermore, we examine the flow through a three-dimensional rectangular channel, the flow over a hole and the Kármán vortex street behind an inclined plate for different models and compare their results.

Chapter 8 concludes this thesis by a summary of its main results and a presentation of various possibilities for future research.

The **Appendix** gives the components of the set of equations and the derivation of the analytical solution of the plane Poiseuille flow of an Oldroyd-B fluid for the stress components.

Chapter 2

Review of Continuum Mechanics

In this chapter, we give a short overview over the basic principles of continuum mechanics needed for the mathematical description of fluid flows. The presentation is based on Phillips and Owens [50], Chorin and Marsden [16], Böhme [12], Phan-Thien [54] and Tanner [67].

2.1 Kinematics

2.1.1 Velocity and Acceleration

Let $V \subset \mathbb{R}^3$ be a region filled with a fluid consisting of particles. Consider a fixed Cartesian frame of reference with orthonormal base vectors \mathbf{e}_1 , \mathbf{e}_2 and \mathbf{e}_3 . The position of a particle is then given by the position vector

$$\mathbf{x}(t) = (x(t), y(t), z(t)) \equiv x(t)\mathbf{e}_1 + y(t)\mathbf{e}_2 + z(t)\mathbf{e}_3 \quad (2.1)$$

at some time t . Then we define the velocity of the particle as

$$\mathbf{u}(\mathbf{x}(t), t) = \frac{d\mathbf{x}(t)}{dt}. \quad (2.2)$$

The acceleration of the fluid particle is given by

$$\mathbf{a}(\mathbf{x}(t), t) = \frac{d^2}{dt^2}\mathbf{x}(t) = \frac{d}{dt}\mathbf{u}(\mathbf{x}(t), t). \quad (2.3)$$

By the chain rule, this becomes

$$\mathbf{a}(\mathbf{x}(t), t) = \frac{\partial \mathbf{u}}{\partial t} + \frac{\partial \mathbf{u}}{\partial x} \frac{dx}{dt} + \frac{\partial \mathbf{u}}{\partial y} \frac{dy}{dt} + \frac{\partial \mathbf{u}}{\partial z} \frac{dz}{dt} = \frac{\partial}{\partial t} \mathbf{u} + (\mathbf{u} \cdot \nabla) \mathbf{u}. \quad (2.4)$$

Definition 2.1 [MATERIAL DERIVATIVE]

We define the **material derivative** to be the operator

$$\frac{D}{Dt} := \frac{\partial}{\partial t} + \mathbf{u} \cdot \nabla. \quad (2.5)$$

The material derivative differs from the local time derivative $\frac{\partial}{\partial t}$ in the part $\mathbf{u} \cdot \nabla$, which originates from the motion of the particle. Thus, we see that the material derivative includes the motion of the particle.

As seen above, the acceleration of a fluid particle is given by the sum of the local time derivative and the convective term $\mathbf{u} \cdot \nabla \mathbf{u}$.

Definition 2.2 [VELOCITY GRADIENT TENSOR]

The expression $\nabla \mathbf{u}$ is a second-order tensor containing the velocity field derivatives. Therefore, we call it the **velocity gradient tensor**. It is given by

$$\nabla \mathbf{u} = \begin{pmatrix} \frac{\partial u}{\partial x} & \frac{\partial u}{\partial y} & \frac{\partial u}{\partial z} \\ \frac{\partial v}{\partial x} & \frac{\partial v}{\partial y} & \frac{\partial v}{\partial z} \\ \frac{\partial w}{\partial x} & \frac{\partial w}{\partial y} & \frac{\partial w}{\partial z} \end{pmatrix}. \quad (2.6)$$

2.1.2 Deformation and Vorticity

We can decompose the velocity gradient tensor into a **symmetric part** \mathbf{D} (i.e. $\mathbf{D}^T = \mathbf{D}$) and an **anti-symmetric part** \mathbf{W} (i.e. $\mathbf{W}^T = -\mathbf{W}$), as

$$\nabla \mathbf{u} = \mathbf{D} + \mathbf{W}.$$

Definition 2.3 [RATE OF DEFORMATION TENSOR]

The symmetric part is called the **rate of deformation tensor** and it is given by

$$\mathbf{D} := \frac{1}{2}(\nabla \mathbf{u} + \nabla \mathbf{u}^T) = \begin{pmatrix} \frac{\partial u}{\partial x} & \frac{1}{2}(\frac{\partial u}{\partial y} + \frac{\partial v}{\partial x}) & \frac{1}{2}(\frac{\partial u}{\partial z} + \frac{\partial w}{\partial x}) \\ \frac{1}{2}(\frac{\partial u}{\partial y} + \frac{\partial v}{\partial x}) & \frac{\partial v}{\partial y} & \frac{1}{2}(\frac{\partial v}{\partial z} + \frac{\partial w}{\partial y}) \\ \frac{1}{2}(\frac{\partial u}{\partial z} + \frac{\partial w}{\partial x}) & \frac{1}{2}(\frac{\partial v}{\partial z} + \frac{\partial w}{\partial y}) & \frac{\partial w}{\partial z} \end{pmatrix}. \quad (2.7)$$

Definition 2.4 [VORTICITY TENSOR]

The anti-symmetric part is called the **vorticity tensor** and it is given by

$$\mathbf{W} := \frac{1}{2}(\nabla \mathbf{u} - \nabla \mathbf{u}^T) = \begin{pmatrix} 0 & -\frac{1}{2}(\frac{\partial v}{\partial x} - \frac{\partial u}{\partial y}) & \frac{1}{2}(\frac{\partial u}{\partial z} - \frac{\partial w}{\partial x}) \\ \frac{1}{2}(\frac{\partial v}{\partial x} - \frac{\partial u}{\partial y}) & 0 & -\frac{1}{2}(\frac{\partial w}{\partial y} - \frac{\partial v}{\partial z}) \\ -\frac{1}{2}(\frac{\partial u}{\partial z} - \frac{\partial w}{\partial x}) & \frac{1}{2}(\frac{\partial w}{\partial y} - \frac{\partial v}{\partial z}) & 0 \end{pmatrix}. \quad (2.8)$$

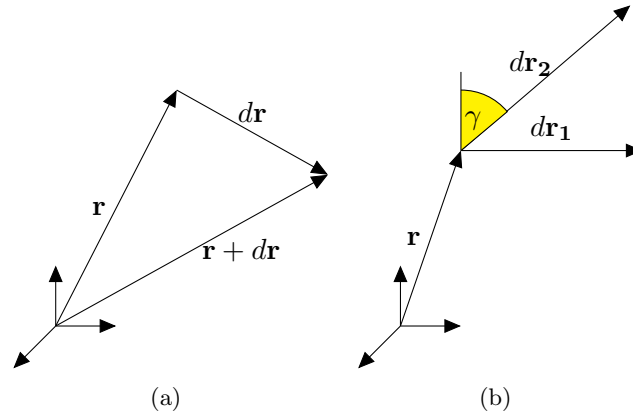
We will now discuss their physical interpretation. Let \mathbf{r} denote the position of a particle and $\mathbf{r} + d\mathbf{r}$ the position of a neighbouring particle at a small distance $d\mathbf{r}$ as illustrated in Figure 2.1(a). Then, we obtain by Taylor's theorem

$$\mathbf{u}(\mathbf{r} + d\mathbf{r}) = \mathbf{u}(\mathbf{r}) + \nabla \mathbf{u}(\mathbf{r})d\mathbf{r}.$$

With $\mathbf{u}(\mathbf{r}) = d\mathbf{r}/dt$ and $\mathbf{u}(\mathbf{r} + d\mathbf{r}) = d(\mathbf{r} + d\mathbf{r})/dt$, we get

$$\frac{d(d\mathbf{r})}{dt} = \nabla \mathbf{u}(\mathbf{r})d\mathbf{r}. \quad (2.9)$$

Therefore, we see that the velocity gradient tensor $\nabla \mathbf{u}$ transforms the filament $d\mathbf{r}$ into its time derivative. For the physical interpretation of the rate of deformation tensor \mathbf{D} , we take two filaments $d\mathbf{r}_1$ and $d\mathbf{r}_2$ (see Figure 2.1(b)). Let $(90^\circ - \gamma)$ be the angle between them. Now we examine the time derivative of the standard scalar product $\langle \cdot, \cdot \rangle$ of these two filaments.

Figure 2.1: Physical interpretation of $\nabla \mathbf{u}$ and \mathbf{D} .

On the one hand, we obtain

$$\frac{d}{dt}(\langle d\mathbf{r}_1, d\mathbf{r}_2 \rangle) = \left\langle \frac{d(d\mathbf{r}_1)}{dt}, d\mathbf{r}_2 \right\rangle + \left\langle d\mathbf{r}_1, \frac{d(d\mathbf{r}_2)}{dt} \right\rangle \quad (2.10)$$

$$\stackrel{(2.9)}{=} \langle \nabla \mathbf{u}(\mathbf{r}) d\mathbf{r}_1, d\mathbf{r}_2 \rangle + \langle d\mathbf{r}_1, \nabla \mathbf{u}(\mathbf{r}) d\mathbf{r}_2 \rangle \quad (2.11)$$

$$= \langle d\mathbf{r}_1, \nabla \mathbf{u}(\mathbf{r})^T d\mathbf{r}_2 \rangle + \langle d\mathbf{r}_1, \nabla \mathbf{u}(\mathbf{r}) d\mathbf{r}_2 \rangle \quad (2.12)$$

$$= 2 \langle d\mathbf{r}_1, \mathbf{D} d\mathbf{r}_2 \rangle. \quad (2.13)$$

On the other hand, we obtain

$$\frac{d}{dt}(\langle d\mathbf{r}_1, d\mathbf{r}_2 \rangle) = \frac{d}{dt}(\|d\mathbf{r}_1\| \|d\mathbf{r}_2\| \sin \gamma) \quad (2.14)$$

$$= \left[\frac{d(\|d\mathbf{r}_1\|)}{dt} \|d\mathbf{r}_2\| + \frac{d(\|d\mathbf{r}_2\|)}{dt} \|d\mathbf{r}_1\| \right] \sin \gamma + \|d\mathbf{r}_1\| \|d\mathbf{r}_2\| \dot{\gamma} \cos \gamma. \quad (2.15)$$

Together, we obtain

$$\left[\frac{d(\|d\mathbf{r}_1\|)}{dt} \frac{1}{\|d\mathbf{r}_1\|} + \frac{d(\|d\mathbf{r}_2\|)}{dt} \frac{1}{\|d\mathbf{r}_1\|} \right] \sin \gamma + \dot{\gamma} \cos \gamma = 2 \left\langle \frac{d\mathbf{r}_1}{\|d\mathbf{r}_1\|}, \mathbf{D} \frac{d\mathbf{r}_2}{\|d\mathbf{r}_2\|} \right\rangle. \quad (2.16)$$

Now, we choose

$$\frac{d\mathbf{r}_1}{\|d\mathbf{r}_1\|} = \frac{d\mathbf{r}_2}{\|d\mathbf{r}_2\|} = \mathbf{e}_1 \quad \text{and} \quad d\mathbf{r}_1 = d\mathbf{r}_2, \quad \text{i.e. } \gamma = 90^\circ. \quad (2.17)$$

Then, we obtain

$$\frac{d(\|d\mathbf{r}_1\|)}{dt} = D_{xx} \|d\mathbf{r}_1\|. \quad (2.18)$$

In the same manner, we can obtain the expressions for filaments oriented in the direction of \mathbf{e}_2 and \mathbf{e}_3 . The equation (2.18) shows, that the diagonal elements of \mathbf{D} describe the expansion or contraction of filaments oriented in the direction of the axes $\{\mathbf{e}_1, \mathbf{e}_2, \mathbf{e}_3\}$.

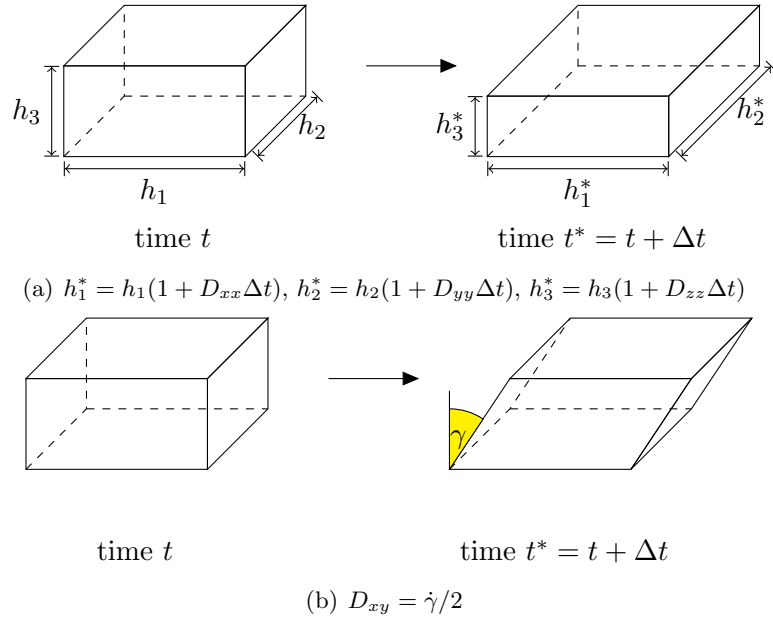


Figure 2.2: Physical interpretation of the rate of deformation tensor \mathbf{D} .

The rate of change of the volume of a box with sides of length h_1, h_2, h_3 parallel to the $\mathbf{e}_1, \mathbf{e}_2, \mathbf{e}_3$ axes is

$$\frac{d}{dt}(h_1 h_2 h_3) = \frac{dh_1}{dt} h_2 h_3 + h_1 \frac{dh_2}{dt} h_3 + h_1 h_2 \frac{dh_3}{dt} = (D_{xx} + D_{yy} + D_{zz})(h_1 h_2 h_3). \quad (2.19)$$

That means the trace of \mathbf{D} describes the rate of change of the volume $dV = h_1 h_2 h_3$ of a box (see Figure 2.2(a)), i.e.

$$\frac{d(dV)}{dt} = \text{tr } \mathbf{D} dV = \text{div } \mathbf{u} dV. \quad (2.20)$$

Now let us choose two filaments orthogonal to each other, e.g.

$$\frac{d\mathbf{r}_1}{\|d\mathbf{r}_1\|} = \mathbf{e}_1 \quad \text{and} \quad \frac{d\mathbf{r}_2}{\|d\mathbf{r}_2\|} = \mathbf{e}_2, \quad \text{i.e. } \gamma = 0^\circ. \quad (2.21)$$

So we obtain

$$\dot{\gamma} = 2D_{xy}. \quad (2.22)$$

Therefore, the non-diagonal elements of \mathbf{D} are equal to the half of the rate of change of the angle γ (see Figure 2.2(b)). That means for a box the rate of deformation tensor describes the expansion rate of the edges and the rate of change of the angle between them. For the vorticity tensor \mathbf{W} for an arbitrary vector \mathbf{r} , we can write

$$\mathbf{W} \cdot \mathbf{r} = \frac{1}{2} ((\nabla \times \mathbf{u}) \times \mathbf{r}). \quad (2.23)$$

For filaments, we can obtain from (2.9) the following relation

$$\frac{d(d\mathbf{r})}{dt} = \frac{(\nabla \times \mathbf{u})}{2} \times d\mathbf{r}. \quad (2.24)$$

That means the vorticity tensor \mathbf{W} describes the rotation of a filament $d\mathbf{r}$ with angular velocity $(\nabla \times \mathbf{u})/2$.

2.1.3 Strain

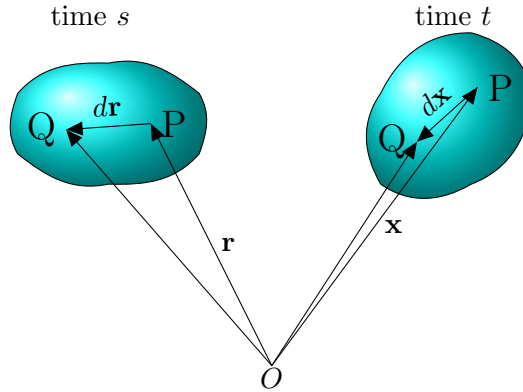


Figure 2.3: Motion of a body from time t to time s .

The quantities \mathbf{D} and \mathbf{W} are sufficient for Newtonian fluid mechanics, but additional quantities are required to describe solid materials or materials with memory. Looking at Figure 2.3, if P and Q are neighbouring points separated by a small distance $d\mathbf{x}$ at time t and by a distance $d\mathbf{r}$ at time s . Let $\mathbf{r}(\mathbf{x}, t, s)$ denote the position at time s of the fluid particle P , which occupies position \mathbf{x} at time t . By definition, we have

$$\mathbf{r}(x, t, t) = \mathbf{x}. \quad (2.25)$$

As we move to the neighbouring particle Q the mapping $\mathbf{r}(\mathbf{x}, t, s)$ means that the relation between $d\mathbf{r}$ and $d\mathbf{x}$ is:

$$dr_i = \frac{\partial r_i}{\partial x_1} dx_1 + \frac{\partial r_i}{\partial x_2} dx_2 + \frac{\partial r_i}{\partial x_3} dx_3 \quad \text{with} \quad r_i = r_i(x_i, t, t'), \quad i = 1, 2, 3. \quad (2.26)$$

This gives us the possibility to define the following strain tensor.

Definition 2.5 [DEFORMATION GRADIENT TENSOR]

We define the **deformation gradient tensor** \mathbf{F} relating $d\mathbf{r}$ and $d\mathbf{x}$ as

$$d\mathbf{r} = \mathbf{F}(\mathbf{x}, t, s)d\mathbf{x}, \quad (2.27)$$

i.e.

$$F_{ij} = \frac{\partial r_i}{\partial x_j}. \quad (2.28)$$

Unfortunately, the deformation gradient tensor is not suitable for the description of strain, because it violates the principle of frame indifference. This principle states that a physical process is invariant under changes of observers. The deformation gradient tensor is $\mathbf{F} = \mathbf{I}$ for uniform translations, but $\mathbf{F} \neq \mathbf{I}$ for rigid rotations. That is why we choose to investigate the magnitudes of $d\mathbf{r}$ and $d\mathbf{x}$. We can form $\|d\mathbf{r}\|^2$ and find

$$\|d\mathbf{r}\|^2 = dr_1^2 + dr_2^2 + dr_3^2 = d\mathbf{r}^T d\mathbf{r} = (\mathbf{F}d\mathbf{x})^T \mathbf{F}d\mathbf{x} = d\mathbf{x}^T (\mathbf{F}^T \mathbf{F}) d\mathbf{x}. \quad (2.29)$$

Definition 2.6 [CAUCHY-GREEN STRAIN TENSOR]

The quantity $\mathbf{F}^T \mathbf{F}$ is called the *Cauchy-Green strain tensor*.

$$\mathbf{C}(\mathbf{x}, t, s) := \mathbf{F}^T(\mathbf{x}, t, s) \mathbf{F}(\mathbf{x}, t, s) \text{ with } s \in (-\infty, t]. \quad (2.30)$$

The Cauchy-Green strain tensor represents the strain history of filaments of the material. Note that $\mathbf{C}(\mathbf{x}, t, t) = \mathbf{I}$.

2.2 Stress and Body Forces

We recognize two types of forces acting on an infinitesimal fluid element, which occupies a volume V at some time (see Figure 2.4). One, due to the action-at-a-distance type of forces such as gravitation and electromagnetic forces, can be expressed as force per unit mass, and is called **body force**; the other, due to the direct action across the boundary surface S , is called the **surface force**. To describe the body force, we assume that the fluid element has

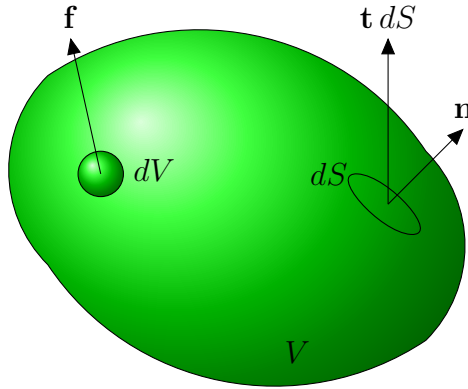


Figure 2.4: Stress and body force definition.

a well-defined **mass density** ρ . The mass of the fluid element with volume V is then given by

$$m = \int_V \rho dV. \quad (2.31)$$

So that the total body force acting on the volume V is given by

$$\mathbf{F}_b = \int_V \rho \mathbf{b} dV, \quad (2.32)$$

where \mathbf{b} is the body force per unit mass.

To describe the surface force, let us consider a small surface element of area dS with an outward pointing unit normal vector \mathbf{n} . Then the total surface force acting on S is given by

$$\mathbf{F}_t = \int_S \mathbf{t} dS, \quad (2.33)$$

where \mathbf{t} is the force per unit area acting on the surface and is called the **stress vector**. The clear isolation of surface forces in a continuum is usually attributed to Cauchy.

Then the total force experienced by the fluid occupying V will now be

$$\text{total force} = \int_V \rho \mathbf{b} dV + \int_S \mathbf{t} dS. \quad (2.34)$$

Theorem 2.7 [EXISTENCE AND SYMMETRY OF THE STRESS TENSOR]

Let $V \subset \mathbb{R}^3$ be some bounded region and let \mathbf{t} be the stress vector defined above. Then there exists a second-order stress tensor $\boldsymbol{\sigma}$ such that throughout V

$$(i) \quad \mathbf{t} = \boldsymbol{\sigma} \cdot \mathbf{n}, \quad (2.35)$$

i.e. the stress tensor $\boldsymbol{\sigma}$ can be seen as a linear mapping of the unit normal vector \mathbf{n} into the stress vector \mathbf{t} .

$$(ii) \quad \boldsymbol{\sigma} \text{ is symmetric.} \quad (2.36)$$

$\boldsymbol{\sigma}$ is called the **Cauchy stress tensor**.

Proof. See e.g. Phillips and Owens [50], p. 361ff.

□

Notation: The components of the stress tensor are usually denoted as seen in Figure 2.5 by

$$\boldsymbol{\sigma} = \begin{bmatrix} \sigma_{xx} & \sigma_{xy} & \sigma_{xz} \\ \sigma_{yx} & \sigma_{yy} & \sigma_{yz} \\ \sigma_{zx} & \sigma_{zy} & \sigma_{zz} \end{bmatrix}, \quad (2.37)$$

where the $\sigma_{xx}, \sigma_{yy}, \sigma_{zz}$ components are called **normal stresses** and $\sigma_{xy} = \sigma_{yx}, \sigma_{xz} = \sigma_{zx}, \sigma_{yz} = \sigma_{zy}$ are called **shear stresses**.

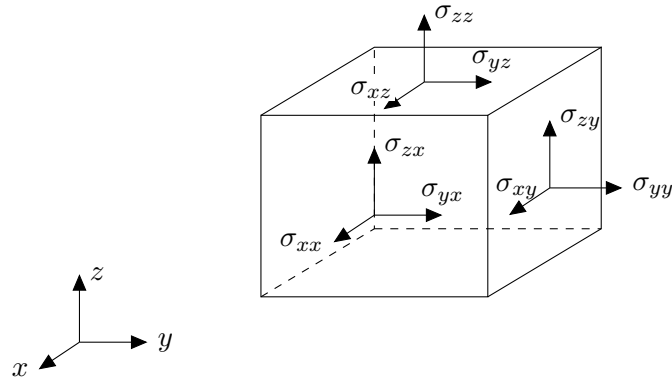


Figure 2.5: Notation used for the stress tensor.

Definition 2.8 [DEVIATORIC STRESS/EXTRA-STRESS TENSOR]

For fluids, we decompose the Cauchy stress tensor into one from the rate of deformation independent spherical-symmetrical pressure part and the **deviatoric stress** or more generally **extra-stress tensor** part \mathbf{T} .

$$\boldsymbol{\sigma} = -p\mathbf{I} + \mathbf{T}. \quad (2.38)$$

2.3 Conservation Laws

The motion of every fluid is governed by the conservation of mass and momentum, and if thermal effects are important, the balance of energy. In this thesis, we will be only concerned with purely mechanical problems, where we assume a constant temperature. We will also assume that the fluids are **incompressible**, i.e. $\frac{D\rho}{Dt} = 0$. In order to proceed, we first need the Reynolds transport theorem, which enables us to compute the rate of change of certain volume integrals.

Theorem 2.9 [REYNOLDS TRANSPORT THEOREM]

Let $V(t)$ a region filled with a fluid and let $f(\mathbf{x}, t)$ be a scalar or vector function defined over $V(t)$. Then

$$\frac{d}{dt} \int_{V(t)} f dV = \int_{V(t)} \left(\frac{Df}{Dt} + f \operatorname{div} \mathbf{u} \right) dV. \quad (2.39)$$

Proof. See e.g. Phan-Thien [54], p.49 □

2.3.1 Conservation of Mass

The mass in the volume $V(t)$ is conserved at all time, i.e.

$$\frac{d}{dt} \int_{V(t)} \rho dV = 0, \quad (2.40)$$

where $\rho(\mathbf{x}, t)$ is the density field at time t . By Reynolds transport theorem (2.39), we get

$$\int_{V(t)} \left(\frac{D\rho}{Dt} + \rho \operatorname{div} \mathbf{u} \right) dV = 0. \quad (2.41)$$

Since the volume $V(t)$ is arbitrary, we deduce that

$$\frac{D\rho}{Dt} + \rho \cdot \operatorname{div} \mathbf{u} = 0. \quad (2.42)$$

For incompressible fluids (i.e. $\frac{D\rho}{Dt} = 0$), we get

$$\operatorname{div} \mathbf{u} = 0. \quad (2.43)$$

2.3.2 Conservation of Linear Momentum

By (2.33) the total force acting on a volume element is given by

$$\text{total force} = \int_V \rho \mathbf{b} dV + \int_S \mathbf{t} dS. \quad (2.44)$$

By Newton's second law (force = mass · acceleration), (2.35) and the divergence theorem (DT), we are led to

$$\int_V \rho \frac{D\mathbf{u}}{Dt} dV = \int_V \rho \mathbf{b} dV + \int_S \boldsymbol{\sigma} \cdot \mathbf{n} dS \stackrel{\text{DT}}{=} \int_V \rho \mathbf{b} dV + \int_V \operatorname{div} \boldsymbol{\sigma} dV. \quad (2.45)$$

With equation (2.38), we obtain

$$\int_V \rho \frac{D\mathbf{u}}{Dt} dV = \int_V \rho \mathbf{b} dV - \int_V \nabla p dV + \int_V \operatorname{div} \mathbf{T} dV. \quad (2.46)$$

Since the integrand is continuous on an arbitrary V , the conservation of linear momentum becomes

$$\rho \frac{D\mathbf{u}}{Dt} = -\nabla p + \operatorname{div} \mathbf{T} + \rho \mathbf{b}. \quad (2.47)$$

Chapter 3

Constitutive Equations

To complete the mathematical formulation, we need to relate the extra-stress tensor \mathbf{T} to the motion. These supplementary relations, which are called the **constitutive equations** or the **rheological equations of state**, differentiate one material from another. The first step in evaluating constitutive models is to consider their predictions in a number of simple flows. We will look at two simple types of flows: steady shear flow and uniaxial extensional flow. This will lead us to the definition of shear-dependent viscosity, normal stress differences and elongational viscosity. This chapter is based on the books of Tanner [67], Böhme [12], Bird [6, 7], Renardy [61] and Owens [50].

3.1 Simple Flows, Viscosities and Stress Differences

3.1.1 Steady Shear Flow and Viscometric Functions

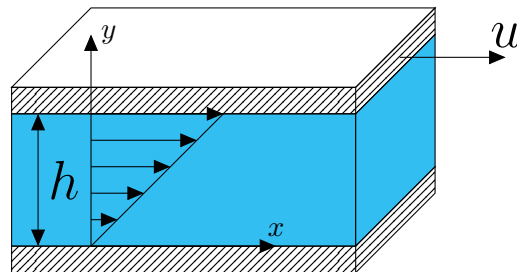


Figure 3.1: Steady shearing.

Consider a fluid between two infinite parallel plates separated by a distance h as shown in Figure 3.1. Now, suppose that the top plate moves with a constant velocity u in the x -direction. This flow is called **steady shear flow** or **viscometric flow**. The velocity field is given by

$$\mathbf{u} = (u(y), 0, 0).$$

Consequently, the velocity gradient and the rate of deformation tensor are

$$\nabla \mathbf{u} = \begin{pmatrix} 0 & \frac{\partial u(y)}{\partial y} & 0 \\ 0 & 0 & 0 \\ 0 & 0 & 0 \end{pmatrix}; \quad 2\mathbf{D} = \begin{pmatrix} 0 & \frac{\partial u(y)}{\partial y} & 0 \\ \frac{\partial u(y)}{\partial y} & 0 & 0 \\ 0 & 0 & 0 \end{pmatrix}. \quad (3.1)$$

The quantity

$$\dot{\gamma} := \frac{\partial u(y)}{\partial y}, \quad (3.2)$$

is known as the **shear rate**. If we consider an isotropic material, the zx - and zy -components of stress must be zero. This can be seen in the following way. Consider two observers; one in our standard Cartesian frame and one in a coordinate frame rotated 180° about the z -axis as shown in Figure 3.2. Because both observers see the same flow, the stresses investigated by

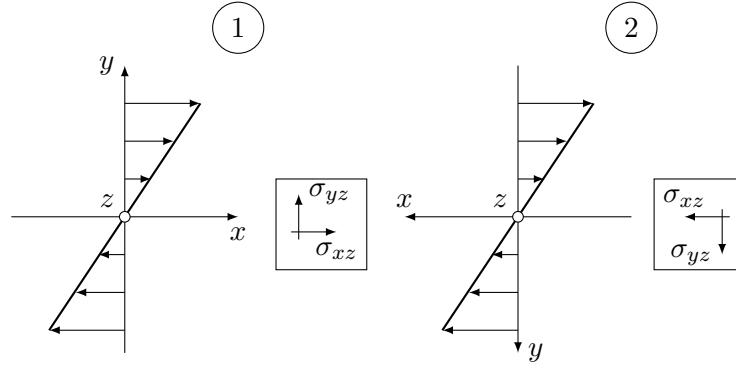


Figure 3.2: Two observers.

them must be the same in an isotropic material. Therefore, we must have $\sigma_{xz} = \sigma_{yz} = 0$ and the stress tensor has the form

$$\boldsymbol{\sigma} = \begin{bmatrix} \sigma_{xx} & \sigma_{xy} & 0 \\ \sigma_{xy} & \sigma_{yy} & 0 \\ 0 & 0 & \sigma_{zz} \end{bmatrix}. \quad (3.3)$$

When a viscoelastic liquid is brought from rest into a state of steady shearing motion, a time-dependent shear stress is built up. However, if the shearing motion continues at a constant rate, the shear stress approaches a steady-state value that depends only on the shear rate.

Definition 3.1 [VISCOMETRIC FUNCTIONS]

The ratio of the shear stress σ_{xy} to the shear rate is a function

$$\eta(\dot{\gamma}) = \frac{\sigma_{xy}}{\dot{\gamma}} \quad (3.4)$$

called the (**shear-rate dependent**) **viscosity**. The shear viscosity η is typically a monotonically decreasing function of shear rate that tends to some limit η_∞ for very high-shear rates. Such fluids are termed **shear-thinning**. At low shear rates, the viscosity approaches a constant value

$$\eta_0 = \lim_{\dot{\gamma} \rightarrow 0} \eta(\dot{\gamma}),$$

which is called **zero-shear-rate-viscosity**.

The two independent differences

$$N_1(\dot{\gamma}) := \sigma_{xx} - \sigma_{yy}, \quad (3.5)$$

$$N_2(\dot{\gamma}) := \sigma_{yy} - \sigma_{zz} \quad (3.6)$$

are called the **first and second normal stress differences** respectively. Polymeric fluids usually have non-zero normal stress differences, where the first normal stress difference is positive, the second normal stress difference is negative and its absolute value is much smaller than that of N_1 .

3.1.2 Steady Uniaxial Extensional Flow and Elongational Viscosity

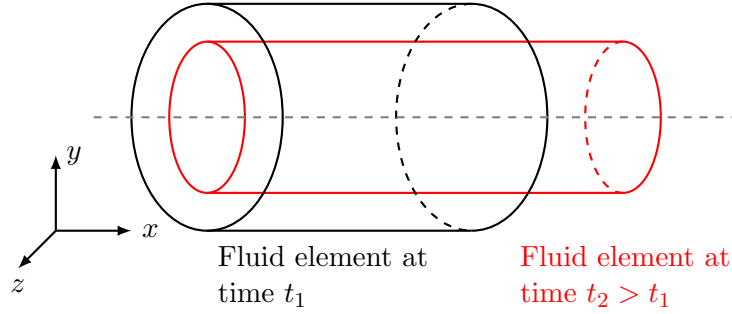


Figure 3.3: Steady uniaxial extensional flow.

Suppose that a rod of material is being extended homogeneously along its x -axis, so that each part of the rod is stressed uniformly as shown in Figure 3.3. We suppose that the constant rate of elongation $\partial u/\partial x (\equiv \dot{\epsilon})$ is independent of x . For an incompressible fluid, mass conservation and axial symmetry then demand that $\partial v/\partial y = \partial w/\partial z = -\dot{\epsilon}/2$. Thus, the velocity in a steady elongational flow is given by

$$\mathbf{u} = (\dot{\epsilon}x, -\frac{\dot{\epsilon}}{2}y, -\frac{\dot{\epsilon}}{2}z). \quad (3.7)$$

Consequently, the velocity gradient tensor and the rate of deformation tensor are equal and

$$\nabla \mathbf{u} = \mathbf{D} = \begin{pmatrix} \dot{\epsilon} & 0 & 0 \\ 0 & -\frac{\dot{\epsilon}}{2} & 0 \\ 0 & 0 & -\frac{\dot{\epsilon}}{2} \end{pmatrix}. \quad (3.8)$$

All shear stress components are zero and $\sigma_{yy} = \sigma_{zz}$ by symmetry. Shear stresses would lead to an angle change in volume elements. Therefore, the stress tensor becomes

$$\boldsymbol{\sigma} = \begin{bmatrix} \sigma_{xx} & 0 & 0 \\ 0 & \sigma_{yy} & 0 \\ 0 & 0 & \sigma_{yy} \end{bmatrix}. \quad (3.9)$$

The stress response is then completely defined by the dependence of $\sigma_{xx} - \sigma_{yy}$ on the constant rate of extension $\dot{\epsilon}$.

Definition 3.2 [ELONGATIONAL VISCOSITY]

The ratio of the stress difference $\sigma_{xx} - \sigma_{yy}$ to the elongation rate $\dot{\epsilon}$

$$\eta_E(\dot{\epsilon}) = \frac{\sigma_{xx} - \sigma_{yy}}{\dot{\epsilon}}, \quad (3.10)$$

is called **elongational** or **extensional viscosity**. For polymeric fluids, the elongational viscosity is usually seen to increase as the elongation rate is increased. This behaviour is termed **extensional-thickening**. The ratio between the extensional viscosity and the shear viscosity is called **Trouton ratio**

$$\text{Trouton ratio} = \frac{\eta_E(\dot{\epsilon})}{\eta(\dot{\gamma})}. \quad (3.11)$$

3.2 The Newtonian Fluid

The constitutive law for a **Newtonian fluid** is given by

$$\mathbf{T} = 2\eta_0\mathbf{D}. \quad (3.12)$$

This constitutive relation reflects the four assumptions introduced in Section 1.1. As seen in Section 2.1.2 the rate of deformation tensor \mathbf{D} contains information about the deformation rate at the present time at a local point. It is symmetric, which means it is suitable for the description of isotropic materials. In the relation, we assume that the extra stress \mathbf{T} depends linearly on the rate of deformation \mathbf{D} . The proportionality coefficient η_0 is called the **viscosity**. This law shows that the viscosity, i.e. the friction of particles at the molecular level, is uniquely responsible for the existence of extra stresses.

Substituting equation (3.12) into the momentum equation (2.47) leads in the case of incompressible flow to the **Navier-Stokes equations**

$$\rho \frac{D\mathbf{u}}{Dt} = -\nabla p + \eta_0 \Delta \mathbf{u} + \rho \mathbf{b}. \quad (3.13)$$

For steady simple shear flow (see Section 3.1.1), the stress tensor of a Newtonian fluid becomes

$$\boldsymbol{\sigma} = \begin{bmatrix} -p & \eta_0 \dot{\gamma} & 0 \\ \eta_0 \dot{\gamma} & -p & 0 \\ 0 & 0 & -p \end{bmatrix}. \quad (3.14)$$

Therefore, a Newtonian fluid has a constant shear viscosity η_0 , i.e. it is not shear-thinning and it has zero first and second normal stress differences. For steady uniaxial elongation (see Section 3.1.2), we obtain

$$\boldsymbol{\sigma} = \begin{bmatrix} -p + 2\eta\dot{\epsilon} & 0 & 0 \\ 0 & -p - \eta\dot{\epsilon} & 0 \\ 0 & 0 & -p - \eta\dot{\epsilon} \end{bmatrix}. \quad (3.15)$$

Therefore, the elongational viscosity

$$\eta_E(\dot{\epsilon}) = 3\eta_0, \quad (3.16)$$

is three times larger than the shear viscosity, i.e. the Trouton ratio is $\eta_E(\dot{\epsilon})/\eta_0 = 3$.

3.3 The Generalized Newtonian Fluid

As a first step towards deriving constitutive relations for non-Newtonian fluids, we take the shear-thinning effect into account. Therefore, we abandon the assumption that the extra stress tensor depends linearly on the rate of deformation tensor. To derive a model, which is independent of the coordinate system, we write the viscosity η as a function of the invariants of \mathbf{D} . We use the symmetry of the rate of deformation tensor by noticing that every symmetric second order tensor can be diagonalized and its eigenvalues are guaranteed to be real, i.e.

$$\mathbf{D} = \begin{pmatrix} \lambda_1 & 0 & 0 \\ 0 & \lambda_2 & 0 \\ 0 & 0 & \lambda_3 \end{pmatrix}, \quad (3.17)$$

$$\det(\mathbf{D} - \lambda\mathbf{I}) = -\lambda^3 + I_D\lambda^2 - II_D\lambda + III_D = 0, \quad (3.18)$$

where

$$I_D = D_{xx} + D_{yy} + D_{zz} = \text{tr } \mathbf{D}, \quad (3.19)$$

$$II_D = D_{xx}D_{yy} + D_{yy}D_{zz} + D_{zz}D_{xx} - D_{xy}^2 - D_{xz}^2 - D_{yz}^2 = \frac{1}{2}[(\text{tr } \mathbf{D})^2 - \text{tr } \mathbf{D}^2], \quad (3.20)$$

$$III_D = \det \mathbf{D} \quad (3.21)$$

are called the **principal invariants** of \mathbf{D} and they are independent of the coordinate system. Hence, we obtain the following relation between the extra stress tensor and the rate of deformation tensor

$$\mathbf{T} = 2\eta_0(I_D, II_D, III_D)\mathbf{D}. \quad (3.22)$$

Note that (see Böhme [12])

- $I_D = 0$ for incompressible fluids. Then $II_D \leq 0$, $|III_D| \leq \frac{2}{3\sqrt{3}}(-II_D)^{\frac{3}{2}}$.
- $III_D = 0$ for simple shear flow.

This model is only suitable for the description of flows, where elastic effects are negligible and the shear-thinning effect has a strong influence on the flow behaviour. Its principal usefulness is for calculating flow rates and shearing forces in steady-state simple shear flow such as tube flow. The most widely used form of the general viscous constitutive relation is the **power law model**

$$\mathbf{T} = 2K|II_D|^{\frac{(n-1)}{2}}\mathbf{D}, \quad (3.23)$$

where K and n are positive material parameters. Details on models of this kind can be found in Macosko [47], Bird [6], Böhme [12] and Owens [50]. As well as the Newtonian fluid, the generalized Newtonian fluid has zero first and second normal stress differences, but it shows shear-thinning for $n < 1$ or shear thickening for $n > 1$.

3.4 Linear Viscoelasticity

In viscoelastic fluids, the stress depends on the history of the motion and not only on the current motion of the fluid.

3.4.1 Maxwell Model

As a first attempt to obtain a viscoelastic constitutive equation, we consider a spring with spring constant G and a purely viscous dashpot with viscosity η_0 in series as seen in Figure 3.4. Such an element is called **Maxwell element**. The dashpot represents viscous behaviour and the spring represents elastic behaviour.

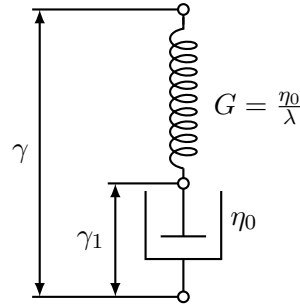


Figure 3.4: Maxwell model.

The stress T_1 in the spring is given by Hooke's law

$$T_1 = G \cdot (\gamma - \gamma_1),$$

where $(\gamma - \gamma_1)$ is the displacement of the spring. The stress T_2 in the dashpot is

$$T_2 = \eta_0 \dot{\gamma}_1,$$

where $\dot{\gamma}_1 = \frac{\partial \gamma_1}{\partial t}$ is the velocity, the rate of change of γ_1 . Because they are in series, i.e. $T_1 = T_2 = T$, after eliminating γ_1 , we obtain the **Maxwell model**

$$T(t) + \frac{\eta}{G} \frac{\partial T(t)}{\partial t} = \eta_0 \dot{\gamma}(t). \quad (3.24)$$

We call

$$\lambda = \frac{\eta_0}{G} \quad (3.25)$$

relaxation time. The general solution to Maxwell's model is given by

$$T(t) = K e^{-\frac{t}{\lambda}} + \int_{-\infty}^t \frac{\eta_0}{\lambda} e^{-\frac{(t-t')}{\lambda}} \dot{\gamma}(t') dt', \quad (3.26)$$

where K is the integration constant. If we prescribe that the stress is finite at $t' = -\infty$, we must choose K to be zero. Therefore, we obtain the following solution for the stress

$$T(t) = \int_{-\infty}^t \left[\frac{\eta_0}{\lambda} e^{-\frac{(t-t')}{\lambda}} \right] \dot{\gamma}(t') dt'. \quad (3.27)$$

This equation shows that the stress is determined by the history of the rate of deformation of γ . The quantity

$$G(t-t') = \frac{\eta_0}{\lambda} \cdot e^{-\frac{t-t'}{\lambda}} \quad (3.28)$$

is called **relaxation modulus**. It is more naturally to express the deformation $\gamma(t)$ as the deformation at a past time relative to the configuration of the fluid at the present time t . Therefore, we define

$$\gamma(t, t') := \int_{t'}^t \dot{\gamma}(t'') dt''. \quad (3.29)$$

Then integration by parts of (3.27) yields

$$T(t) = - \int_{-\infty}^t \left[\frac{\eta_0}{\lambda^2} e^{-\frac{(t-t')}{\lambda}} \right] \gamma(t, t') dt', \quad (3.30)$$

where

$$M(t-t') := -\frac{\eta_0}{\lambda^2} e^{-\frac{(t-t')}{\lambda}} = \frac{dG(t-t')}{dt} \quad (3.31)$$

is called **memory function**.

Example 3.1: [Stress relaxation after a sudden shearing displacement] To understand the meaning of the relaxation modulus $G(t-t')$ and the relaxation time λ , we examine the following experiment. Consider a Maxwell fluid at rest between two parallel plates for all times $t < 0$. At time $t = 0$, the upper plate is moved slightly in the x -direction (see Figure 3.5) with displacement angle $\gamma_0 \ll 1$. Then, we keep γ_0 constant for all $t > 0$. Since

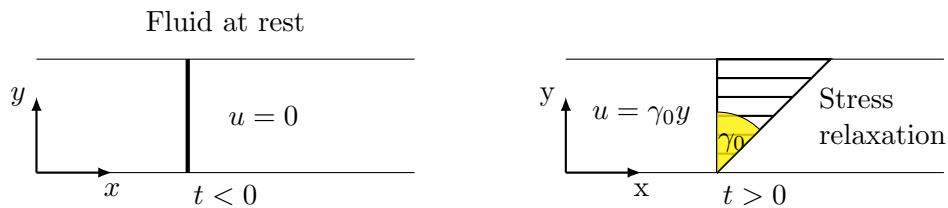


Figure 3.5: Sudden shearing displacement.

the rate of deformation $\dot{\gamma}$ is zero except during the time interval $[-\epsilon, \epsilon]$, we obtain from (3.27) after taking the limit $\epsilon \rightarrow 0$ using L'Hôpital's rule

$$T(t) = \gamma_0 G(t) = \gamma_0 \frac{\eta_0}{\lambda} e^{-\frac{t}{\lambda}}. \quad (3.32)$$

Thus, we see that the stress $T(t)$ decreases exponentially with the relaxation modulus

$G(t) = \frac{\eta_0}{\lambda} e^{-\frac{t}{\lambda}}$ (see Figure 3.6) and finally reaches zero, i.e. the fluid relaxes again and it forgets that a change of motion state had taken place. We thus speak of the "fading memory" of a fluid. The relaxation time is a measure for this fading memory. It describes how long it takes the fluid to relax and how long the fluid remembers the flow history. It is a material parameter. Even Newtonian fluids show memory effects, but their relaxation time is very short.

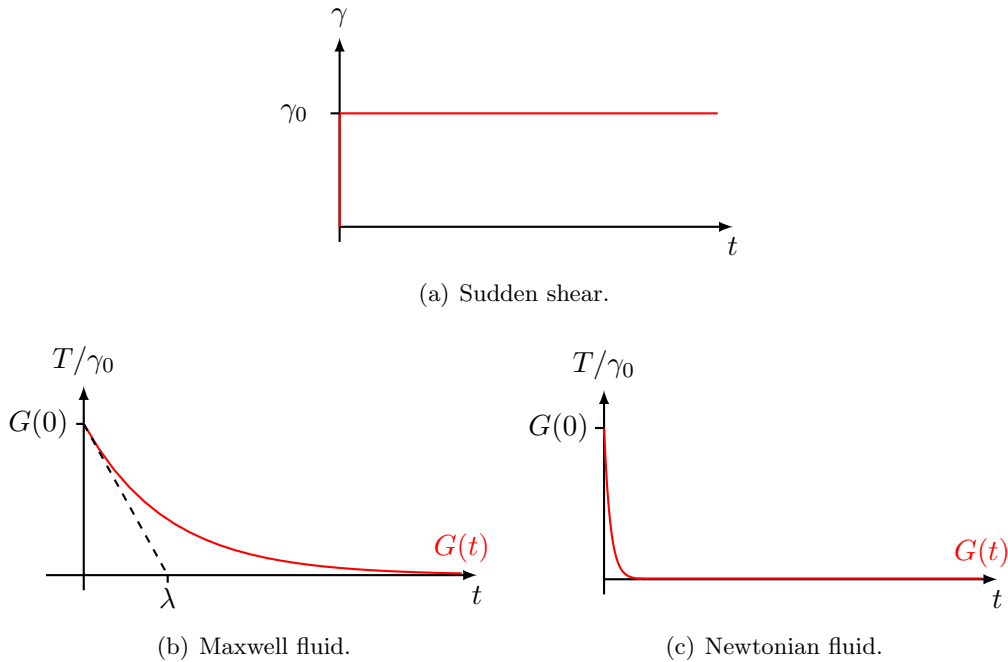


Figure 3.6: Relaxation modulus and relaxation time.

The behaviour of a viscoelastic fluid depends crucially on how the relaxation time relates to other time scales relevant to the flow, e.g. the observation time scale of an experiment. If the observation time scale is large compared to the memory of the fluid, then memory is unimportant, and the material responds like a Newtonian fluid. If the observation time scale is small, memory effects are crucial and the material behaves like an elastic solid. The ratio of the relaxation time to a time scale of the flow is an important dimensionless measure of the importance of elasticity

$$\text{De} = \frac{\text{relaxation time}}{\text{characteristic time scale}}. \quad (3.33)$$

It is called **Deborah number**. It is named after the prophetess Deborah in the Old Testament, who said, "the mountains flowed before the Lord."

3.4.2 Jeffreys Model

One can easily extend Maxwell's model to get relations for the stress with other rheological properties. The so-called Jeffreys model is a dashpot and a Maxwell element in parallel. Now,

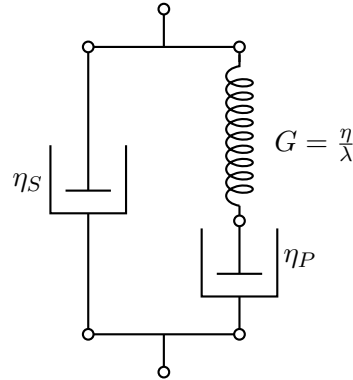


Figure 3.7: Jeffreys model.

the stress consists of the stress at the viscous dashpot $\eta_S \dot{\gamma}$ and of the stress at the Maxwell element τ . The two elements are in parallel so the stresses are additive

$$T(t) = \eta_S \dot{\gamma} + \tau, \quad (3.34)$$

$$\tau + \lambda \dot{\tau} = \eta_P \dot{\gamma}. \quad (3.35)$$

After eliminating variable τ , we obtain the **Jeffreys model**

$$T(t) + \lambda \dot{T}(t) = \eta_0 [\dot{\gamma}(t) + \lambda_r \ddot{\gamma}(t)], \quad (3.36)$$

where $\ddot{\gamma}(t) = \frac{\partial^2 \gamma}{\partial t^2}$, $\eta_0 = \eta_S + \eta_P$ is the **total viscosity** and $\lambda_r = \frac{\eta_S}{\eta_0} \lambda$ is the **retardation time**.

3.5 Nonlinear Models

3.5.1 Differential Models

In this section, we will generalize the one-dimensional Maxwell and Jeffreys Model into a 3D tensor formulation. However, we cannot just use the partial time or material time derivative, because they violate the principle of frame indifference (i.e. the material response must be independent of the observer) for our tensor formulations. We need an objective time derivative formulated in a coordinate system, which is embedded in a flowing fluid and deforms with it, so that the coordinates associated with a particular material point do not change in time. Such a coordinate system is called convected coordinate system. Following this approach, we can define the objective time derivatives

Definition 3.3 [OBJECTIVE TIME DERIVATIVES]

Let \mathbf{A} be an arbitrary 3D tensor. Then, we define

- *Upper convected derivative*

$$\overset{\nabla}{\mathbf{A}} := \frac{D\mathbf{A}}{Dt} - \nabla\mathbf{u} \cdot \mathbf{A} - \mathbf{A} \cdot \nabla\mathbf{u}^T \quad (3.37)$$

is a time derivative in a coordinate system, which stretches and rotates with material lines.

- *Lower convected derivative*

$$\overset{\Delta}{\mathbf{A}} := \frac{D\mathbf{A}}{Dt} + \nabla\mathbf{u}^T \cdot \mathbf{A} + \mathbf{A} \cdot \nabla\mathbf{u} \quad (3.38)$$

is a time derivative in a coordinate system, which deforms and rotates with surface elements (i.e. with area and direction).

- *Corotational derivative*

$$\overset{\circ}{\mathbf{A}} := \frac{D\mathbf{A}}{Dt} - \mathbf{W} \cdot \mathbf{A} + \mathbf{A} \cdot \mathbf{W} \quad (3.39)$$

is a time derivative in a coordinate system, which rotates with material lines, but it does not stretch with them.

Rigorous derivations of these derivatives can be found in Joseph [34] or Bird [6]. These three derivatives may be combined in one formula given by

$$\frac{\delta_a \mathbf{A}}{\delta t} := \frac{D\mathbf{A}}{Dt} - \mathbf{W} \cdot \mathbf{A} + \mathbf{A} \cdot \mathbf{W} - a(\mathbf{D} \cdot \mathbf{A} + \mathbf{A} \cdot \mathbf{D}), \quad -1 \leq a \leq +1. \quad (3.40)$$

It contains as special cases the upper convected derivative, if $a = 1$, the lower convected derivative, if $a = -1$, and the corotational derivative, if $a = 0$, but other values of a lead to frame indifferent time derivatives as well. By using these objective time derivatives and Maxwell's one-dimensional Model (3.24), we get the following relation between the extra stress

tensor \mathbf{T} and the rate of deformation tensor \mathbf{D}

$$\mathbf{T} + \lambda \frac{\delta_a \mathbf{T}}{\delta t} = 2\eta_0 \mathbf{D}, \quad (3.41)$$

where η is the viscosity of the fluid. Of particular importance is the upper convected version of the model. The upper convected derivative occurs naturally in the derivation of models from molecular theories as seen in Section 3.6. The **Upper Convected Maxwell (UCM) model** is given by

$$\mathbf{T} + \lambda \overset{\nabla}{\mathbf{T}} = 2\eta_0 \mathbf{D}. \quad (3.42)$$

It can be written in the integral form (see e.g. Joseph [34])

$$\mathbf{T}(\mathbf{r}, t) = - \int_{-\infty}^t \frac{\eta_0}{\lambda^2} e^{-\frac{(t-t')}{\lambda}} (\mathbf{C}^{-1}(\mathbf{r}, t, t') - \mathbf{I}) dt', \quad (3.43)$$

where \mathbf{C}^{-1} is the inverse of the Cauchy-Green strain tensor introduced in Definition 2.6. For steady simple shear flow, i.e. $\frac{D\mathbf{T}}{Dt} = 0$, the UCM equations become

$$\begin{aligned} \begin{pmatrix} T_{xx} & T_{xy} & 0 \\ T_{xy} & T_{yy} & 0 \\ 0 & 0 & T_{zz} \end{pmatrix} - \lambda \left\{ \begin{pmatrix} 0 & \dot{\gamma} & 0 \\ 0 & 0 & 0 \\ 0 & 0 & 0 \end{pmatrix} \begin{pmatrix} T_{xx} & T_{xy} & 0 \\ T_{xy} & T_{yy} & 0 \\ 0 & 0 & T_{zz} \end{pmatrix} + \begin{pmatrix} T_{xx} & T_{xy} & 0 \\ T_{xy} & T_{yy} & 0 \\ 0 & 0 & T_{zz} \end{pmatrix} \begin{pmatrix} 0 & 0 & 0 \\ \dot{\gamma} & 0 & 0 \\ 0 & 0 & 0 \end{pmatrix} \right\} \\ = \eta_0 \begin{pmatrix} 0 & \dot{\gamma} & 0 \\ \dot{\gamma} & 0 & 0 \\ 0 & 0 & 0 \end{pmatrix}, \end{aligned}$$

so that solving this system yields

$$T_{xy} = \eta_0 \dot{\gamma}, \quad T_{xx} = 2\eta_0 \lambda \dot{\gamma}^2, \quad T_{yy} = T_{zz} = 0. \quad (3.44)$$

Therefore, the viscometric functions are given by

$$\eta(\dot{\gamma}) = \frac{\sigma_{xy}}{\dot{\gamma}} = \eta_0, \quad N_1(\dot{\gamma}) = \sigma_{xx} - \sigma_{yy} = 2\lambda\eta_0 \dot{\gamma}^2, \quad N_2(\dot{\gamma}) = \sigma_{yy} - \sigma_{zz} = 0. \quad (3.45)$$

Hence, we see that the UCM model predicts a constant shear-rate viscosity, a quadratic first normal stress difference and a zero second normal stress difference. For steady elongational flow, the equations

$$\begin{aligned} \begin{pmatrix} T_{xx} & 0 & 0 \\ 0 & T_{yy} & 0 \\ 0 & 0 & T_{zz} \end{pmatrix} - \lambda \left\{ \begin{pmatrix} \dot{\epsilon} & 0 & 0 \\ 0 & -\frac{\dot{\epsilon}}{2} & 0 \\ 0 & 0 & -\frac{\dot{\epsilon}}{2} \end{pmatrix} \begin{pmatrix} T_{xx} & 0 & 0 \\ 0 & T_{yy} & 0 \\ 0 & 0 & T_{zz} \end{pmatrix} + \begin{pmatrix} T_{xx} & 0 & 0 \\ 0 & T_{yy} & 0 \\ 0 & 0 & T_{zz} \end{pmatrix} \begin{pmatrix} \dot{\epsilon} & 0 & 0 \\ 0 & -\frac{\dot{\epsilon}}{2} & 0 \\ 0 & 0 & -\frac{\dot{\epsilon}}{2} \end{pmatrix} \right\} \\ = \eta_0 \begin{pmatrix} \dot{\epsilon} & 0 & 0 \\ 0 & -\frac{\dot{\epsilon}}{2} & 0 \\ 0 & 0 & -\frac{\dot{\epsilon}}{2} \end{pmatrix} \end{aligned}$$

yield

$$T_{xx} = \frac{2\eta_0\dot{\epsilon}}{1 - 2\lambda\dot{\epsilon}}, \quad T_{yy} = T_{zz} = -\frac{\eta_0\dot{\epsilon}}{1 + \lambda\dot{\epsilon}}. \quad (3.46)$$

That means, the elongational viscosity is given by

$$\eta_E(\dot{\epsilon}) = \frac{3\eta_0}{(1 - 2\lambda\dot{\epsilon})(1 + \lambda\dot{\epsilon})}. \quad (3.47)$$

As shown in Figure 3.5.1 the elongational viscosity becomes infinitely large at the finite

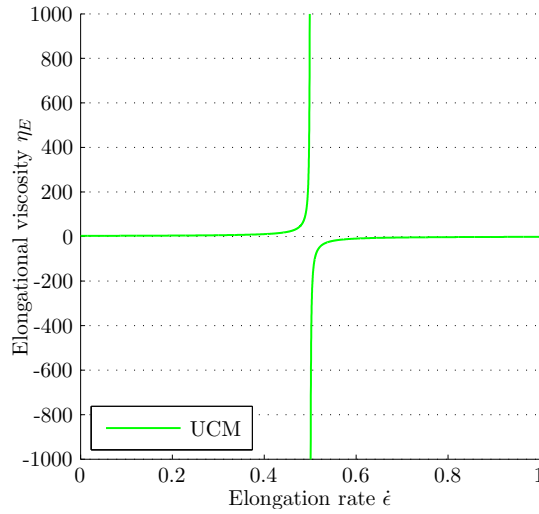


Figure 3.8: Elongational behaviour UCM model.

elongation rate $\dot{\epsilon} = \frac{1}{2\lambda}$. Of course, this behaviour is totally unrealistic.

The generalization of Jeffreys model (3.36) yields

$$\mathbf{T} + \lambda \frac{\delta_a \mathbf{T}}{\delta t} = 2\eta_0 \left[\mathbf{D} + \lambda_r \frac{\delta_a \mathbf{D}}{\delta t} \right]. \quad (3.48)$$

This generalization can also be written down like equation (3.34) in a split form with a Newtonian and an elastic Maxwell part

$$\mathbf{T} = 2\eta_S \mathbf{D} + \boldsymbol{\tau}, \quad (3.49)$$

$$\boldsymbol{\tau} + \lambda \frac{\delta_a \boldsymbol{\tau}}{\delta t} = 2\eta_P \mathbf{D}. \quad (3.50)$$

In Table 3.1, a few names of famous models are summarized. The Oldroyd-B, UCM and the Johnson-Segalman model can also be motivated by molecular theories. The behaviour in simple flows of the Oldroyd-B and the Johnson-Segalman model will be discussed in Section 3.6.1 and Section 3.6.2 respectively.

Model name	a	λ_r
Lower Convected Maxwell	-1	0
Upper Convected Maxwell	1	0
Corotational Maxwell	0	0
Johnson-Segalman	$\in [-1, 1]$	0
Oldroyd-A	-1	> 0
Oldroyd-B	1	> 0

Table 3.1: Famous differential models.

3.5.2 Integral Models

In an integral model, the stress is given in the form of integrals of the deformation history. The most and widely used incompressible integral models are the Rivlin-Sawyers equations [62] and the K-BKZ equation [37, 5]. These are

K-BKZ equation

$$\mathbf{T}(t) = - \int_{-\infty}^t \left[\frac{\partial V(t-t', I_1, I_2)}{\partial I_1} (\mathbf{C}^{-1}(\mathbf{x}, t, t') - \mathbf{I}) + \frac{\partial V(t-t', I_1, I_2)}{\partial I_2} (\mathbf{C}(\mathbf{x}, t, t') - \mathbf{I}) \right], \quad (3.51)$$

Rivlin-Sawyers equation

$$\mathbf{T}(t) = - \int_{-\infty}^t [\psi_1(t-t', I_1, I_2)(\mathbf{C}^{-1}(\mathbf{x}, t, t') - \mathbf{I}) + \psi_2(t-t', I_1, I_2)(\mathbf{C}(\mathbf{x}, t, t') - \mathbf{I})], \quad (3.52)$$

where V , ψ_1 and ψ_2 are scalar functions and I_1, I_2 are given by

$$I_1 = \text{tr } \mathbf{C}^{-1}(\mathbf{x}, t, t'), \quad I_2 = \text{tr } \mathbf{C}(\mathbf{x}, t, t'). \quad (3.53)$$

It has been customary to introduce the additional assumption that the scalar functions V and ψ_i may be written as a product of time-dependent and strain-dependent factors as follows:

$$V(t-t', I_1, I_2) = M(t-t')W(I_1, I_2), \quad (3.54)$$

$$\psi_i(t-t', I_1, I_2) = M(t-t')\phi_i(I_1, I_2). \quad (3.55)$$

Setting $\phi_1 = 1$ and $\phi_2 = 0$ and using the memory function $M(t-t') = \frac{\eta_0}{\lambda^2} e^{-\frac{(t-t')}{\lambda}}$, we recover the integral form of the Maxwell model (3.43). These models are based on the idea that every prior configuration of the material can be viewed as a temporary equilibrium configuration, and the stress is found by superposition of the elastic stresses resulting from all deformations relative to these temporary equilibrium states. Throughout experimental tests, one finds that real fluids violate such a hypothesis. Despite its shortcomings, these models are widely used,

and it is a reasonable first step in the investigation of integral models. They predict a shear-dependent viscosity, a non-zero first normal stress difference and a non-zero second normal stress difference, if $\phi_2 \neq 0$, as well as a finite elongational viscosity at all elongation rates.

3.6 Molecular Theories

As mentioned in the beginning all viscoelastic effects are caused by the deformation of molecular chains. Therefore, by taking account of the microstructure of substances, we expect to gain more insight into the type of constitutive equation needed to describe their mechanical behaviour. At the extremes, we can deal either with dilute polymer solutions or with concentrated solutions.

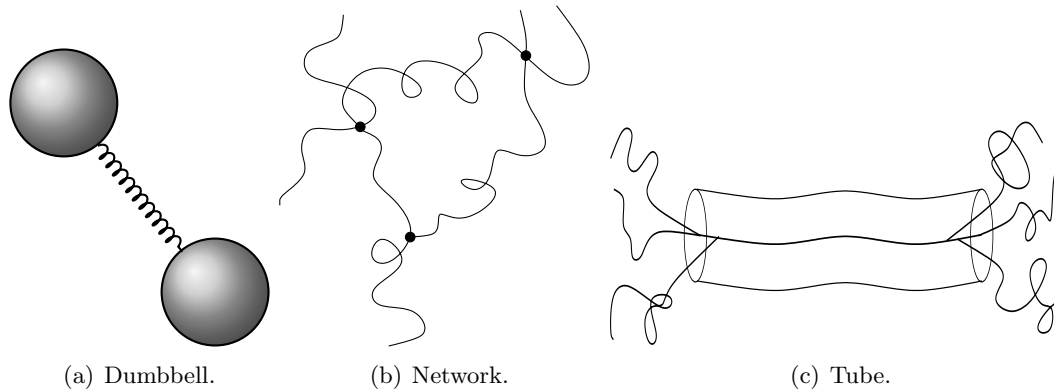


Figure 3.9: Molecular approaches.

1. Dilute Polymer Solutions

We treat polymer molecules individually. Each molecule interacts only with the solvent and not with other molecules. A molecule is modelled as a chain of beads and springs or beads and rods. In the simplest case, it is modelled as a dumbbell (see Figure 3.9(a)). Models derived from the notion of elastic dumbbells, i.e. two beads connected by a spring, swimming in a Newtonian fluid, include the upper convected Maxwell, Oldroyd-B, finitely extensible non-linear elastic spring (FENE) and Giesekus model [26, 27].

2. Polymer Melts and Concentrated Solutions

The molecule-molecule interactions are important and molecular entanglements may form. There are two basic approaches toward this theory.

a) Network theories

We treat the polymer as a network of molecular chains that are linked at junction points (see Figure 3.9(b)). The junctions are temporary, i.e. they are formed and destroyed. The interaction between the polymer molecule and the flow results from the motion of the junctions. Models derived using this approach include the Phan-Thien Tanner [55, 53] and Johnson-Segalman [33] models.

b) Reptation theories

The motion of a polymer chain is constrained by a tube, which represents the other molecules (see Figure 3.9(c)). The essential idea is that the transverse motions of each chain are strongly reduced by the surrounding polymers, while each chain is free to diffuse along its own length by random snakelike motions called reptations. For linear polymers, we can find the Doi-Edwards [18, 19, 20] model, and for branched polymers, the Pom-Pom [49] and eXtended Pom-Pom [70] model.

In this thesis, the Oldroyd-B model and the Phan-Thien Tanner model are used for the computation of viscoelastic fluids. In Section 3.6.1, the Oldroyd-B equations are derived and investigated in simple flows. Afterwards, in Section 3.6.2, the Phan-Thien Tanner model is derived and investigated.

3.6.1 Dilute Polymer Solutions

Derivation of the Oldroyd-B Model

We will derive the Oldroyd-B model from a molecular model consisting of a suspension of Hookean dumbbells in a Newtonian solvent. We start with considering an elastic dumbbell, which is thought of as two identical beads connected by a Hookean spring, as shown in Figure 3.10, immersed in a Newtonian solvent, which is treated as a continuum. Each of the two beads has mass m and has position vectors \mathbf{r}_1 and \mathbf{r}_2 relative to some fixed coordinate frame. Let $\mathbf{Q} = \mathbf{r}_2 - \mathbf{r}_1$ denote the end-to-end vector of the dumbbell.

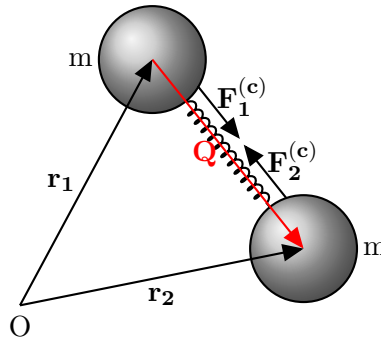


Figure 3.10: Elastic dumbbell.

a. The Equations of Motion for the Beads of the Dumbbell

We can write an equation of motion for each bead of the dumbbell indicating that the mass of the bead times its acceleration is equal to the sum of all forces acting on the bead. Inertial forces at the molecular level can be safely neglected. A detailed discussion of the effects of bead inertia by Schieber and Öttinger [63] shows that bead inertia in polymer models may be neglected. Additionally, we neglect external forces such as gravity on a bead. Hence, we get the following “force balance” for each bead:

$$\mathbf{F}_i^{(f)} + \mathbf{F}_i^{(c)} + \mathbf{F}_i^{(b)} = 0, \quad i=1,2 \quad (3.56)$$

consisting of a friction force $\mathbf{F}_i^{(f)}$, a connecting spring force $\mathbf{F}_i^{(c)}$ and a Brownian force $\mathbf{F}_i^{(b)}$. They will now be described in the foregoing section.

1. Friction force $\mathbf{F}_i^{(f)}$

This is the force of resistance experienced by a bead as it moves through the solution. This friction force is for spherical beads assumed to be given by Stoke's Law:

$$\mathbf{F}_i^{(f)} = 6\pi\eta_S a \left(\frac{d\mathbf{r}_i}{dt} - u(\mathbf{r}_i) \right) = \zeta \left(\frac{d\mathbf{r}_i}{dt} - u(\mathbf{r}_i) \right). \quad (3.57)$$

Here, η_S is the solvent viscosity, a is the radius of the bead and $u(\mathbf{r}_i)$ is the velocity of the surrounding fluid at the point with position vector \mathbf{r}_i . Hence, $\left(\frac{d\mathbf{r}_i}{dt} - u(\mathbf{r}_i) \right)$ is the velocity of the i -th bead relative to the surrounding fluid. We shall write ζ for $6\pi\eta_S a$. This constant ζ is the so-called **friction coefficient**.

Note that we have neglected any effect which one bead may have on the velocity of the solvent in the neighbourhood of the other bead. Therefore, our model is restricted to extremely dilute polymer solutions so that the polymer molecules do not see each other and interact only with the solvent.

2. Spring force $\mathbf{F}_i^{(c)}$

The spring connecting the beads exerts a spring force $\mathbf{F}_i^{(c)}$ on the i -th bead. We assume this spring force to be given by Hooke's law:

$$\mathbf{F}_1^{(c)} = -H(\mathbf{r}_1 - \mathbf{r}_2) = H\mathbf{Q}, \quad (3.58)$$

$$\mathbf{F}_2^{(c)} = -H(\mathbf{r}_2 - \mathbf{r}_1) = -H\mathbf{Q}, \quad (3.59)$$

where H is the spring constant.

3. Brownian forces $\mathbf{F}_i^{(b)}$

Brownian forces are the cumulative effect of the exceedingly frequent collisions between a large particle, called a Brownian particle, and the many surrounding much smaller fluid particles, which are in incessant thermal motion. The mathematical model to describe these random movements is the so called Wiener process $\mathbf{W}_i = \mathbf{W}_i(t)$ ($i=1,2$), which is a Gaussian stochastic process and is therefore completely characterized by the mean and autocorrelation of its components $W_{i,j}$:

$$\langle W_{i,j}(t) \rangle = 0, \quad \langle W_{i,j}(t)W_{i,j}(t') \rangle = \min(t', t). \quad (3.60)$$

We assume that a bead is large compared to the solvent molecules. This assumption justifies the continuum description of the solvent. With the Wiener process we may write the Brownian force $\mathbf{F}_i^{(b)}$ acting on the i -th bead in the form

$$\mathbf{F}_i^{(b)} dt = \sqrt{2kT\zeta} d\mathbf{W}_i, \quad (3.61)$$

where k is the Boltzmann constant, T is the absolute Temperature and ζ is the friction coefficient. The coefficient $\sqrt{2kT\zeta}$ may be derived from the principle of equipartition of energy from kinetic gas theory, which states that in equilibrium

$$E_{kin} = \frac{1}{2} \langle \mathbf{V}(t)^2 \rangle = \frac{kT}{2}, \quad (3.62)$$

where $\mathbf{V}(t)$ is the velocity of the Brownian particle, which is the solution of the stochastic differential equation describing the motion of a Brownian particle

$$m \frac{d\mathbf{V}(t)}{dt} = -\zeta \mathbf{V}(t) + \mathbf{F}_i^{(b)}. \quad (\text{Langevin equation}) \quad (3.63)$$

A detailed derivation may be found in Phan-Thien [54] or Öttinger [78].

Therefore, we obtain the following force balance laws for each bead

$$-\zeta \left(\frac{d\mathbf{r}_1}{dt} - \mathbf{u}(\mathbf{r}_1, t) \right) + H\mathbf{Q} + \sqrt{2kT\zeta} \frac{d\mathbf{W}_1}{dt} = 0, \quad (3.64)$$

$$-\zeta \left(\frac{d\mathbf{r}_2}{dt} - \mathbf{u}(\mathbf{r}_2, t) \right) - H\mathbf{Q} + \sqrt{2kT\zeta} \frac{d\mathbf{W}_2}{dt} = 0. \quad (3.65)$$

We subtract the two equations from each other. Moreover, we assume that the solvent flow field is homogeneous so that we may write

$$\mathbf{u}(\mathbf{r}_2, t) = \mathbf{u}(\mathbf{r}_1, t) + (\nabla \mathbf{u})(\mathbf{r}_2 - \mathbf{r}_1). \quad (3.66)$$

If we set $\mathbf{W}(t) := (\mathbf{W}_2(t) - \mathbf{W}_1(t))/\sqrt{2}$, we obtain the following equation of change for the end-to-end vector of the dumbbell

$$\frac{d\mathbf{Q}}{dt} = \nabla \mathbf{u} \cdot \mathbf{Q} - \frac{2H}{\zeta} \mathbf{Q} - \sqrt{\frac{4kT}{\zeta}} d\mathbf{W}(t). \quad (3.67)$$

b. The Fokker-Planck Equation of the dumbbell

The equation (3.67) is a stochastic differential equation and $\mathbf{Q}(t)$ is a stochastic process. Methods of stochastic differential equations can be used to convert the stochastic differential equation (3.67) to the corresponding **Fokker-Planck** or **diffusion equation**

$$\frac{\partial}{\partial t} p(\mathbf{Q}, t) = -\frac{\partial}{\partial \mathbf{Q}} \cdot \left[\left(\nabla \mathbf{u} \cdot \mathbf{Q} - \frac{2H}{\zeta} \mathbf{Q} \right) p(\mathbf{Q}, t) - \frac{2kT}{\zeta} \frac{\partial}{\partial \mathbf{Q}} p(\mathbf{Q}, t) \right], \quad (3.68)$$

where $p(\mathbf{Q}, t)$ is the probability density function, which characterizes the continuous distribution of $\mathbf{Q}(t)$. That means that the probability that a dumbbell has an orientation in the range \mathbf{Q} to $\mathbf{Q} + d\mathbf{Q}$ is given by $p(\mathbf{Q}, t)d\mathbf{Q}$. Moreover, if g is a function of the connector vector \mathbf{Q} , the expectation of g can be defined as

$$\langle g(\mathbf{Q}) \rangle = \int g(\mathbf{Q}) p(\mathbf{Q}, t) d\mathbf{Q}. \quad (3.69)$$

If we multiply the Fokker-Planck equation (3.68) by $\langle g(\mathbf{Q}) \rangle$, integrate over \mathbb{R}^3 , use the divergence theorem and the fact that p approaches zero rapidly enough as \mathbf{Q} goes to infinity so that surface integrals can be disregarded, we obtain **the equation of change** for $\langle g(\mathbf{Q}) \rangle$

as

$$\frac{d}{dt} \langle g(\mathbf{Q}) \rangle = \left\langle (\nabla \mathbf{u} \cdot \mathbf{Q}) \frac{\partial}{\partial \mathbf{Q}} g(\mathbf{Q}) \right\rangle + \frac{2kT}{\zeta} \left\langle \frac{\partial}{\partial \mathbf{Q}} \cdot \frac{\partial}{\partial \mathbf{Q}} g(\mathbf{Q}) \right\rangle - \frac{2H}{\zeta} \left\langle \mathbf{Q} \cdot \frac{\partial}{\partial \mathbf{Q}} g(\mathbf{Q}) \right\rangle. \quad (3.70)$$

A similar relation holds for a tensor function $\mathbf{g}(\mathbf{Q})$ of any order. We shall be particularly interested in the case where $\mathbf{g}(\mathbf{Q})$ is the second-order tensor $\mathbf{Q}\mathbf{Q}$:

$$\frac{\partial}{\partial t} \langle \mathbf{Q}\mathbf{Q} \rangle - \nabla \mathbf{u} \langle \mathbf{Q}\mathbf{Q} \rangle - \langle \mathbf{Q}\mathbf{Q} \rangle \nabla \mathbf{u}^T = \frac{4kT}{\zeta} \mathbf{I} - \frac{4H}{\zeta} \langle \mathbf{Q}\mathbf{Q} \rangle. \quad (3.71)$$

The left hand side of (3.71) is called upper-convected derivative of $\langle \mathbf{Q}\mathbf{Q} \rangle$ denoted by $\overset{\nabla}{\langle \mathbf{Q}\mathbf{Q} \rangle}$

$$\overset{\nabla}{\langle \mathbf{Q}\mathbf{Q} \rangle} := \frac{\partial}{\partial t} \langle \mathbf{Q}\mathbf{Q} \rangle - \nabla \mathbf{u} \langle \mathbf{Q}\mathbf{Q} \rangle - \langle \mathbf{Q}\mathbf{Q} \rangle \nabla \mathbf{u}^T. \quad (3.72)$$

Finally we note that, in a system at equilibrium (that is, $\nabla \mathbf{u} = 0$, $\frac{d}{dt} \langle \mathbf{Q}\mathbf{Q} \rangle = 0$), Eq. (3.71) gives

$$\langle \mathbf{Q}\mathbf{Q} \rangle_{eq} = \frac{kT}{H} \mathbf{I}. \quad (3.73)$$

We need these equations to establish expressions for the stress tensor.

c. The Stress Tensor

We follow Bird [7] in this section in deriving the expression for the stress tensor. The total stress $\boldsymbol{\sigma}$ (as defined in (2.35)) in a polymer solution is presumed to be the sum of a contribution from the solvent $\boldsymbol{\sigma}_S$ and another $\boldsymbol{\sigma}_P$, resulting from the presence of the polymer molecules

$$\boldsymbol{\sigma} = \boldsymbol{\sigma}_S + \boldsymbol{\sigma}_P \quad (3.74)$$

$$= (-p_S \mathbf{I} + \mathbf{T}_S) + (-p_P + \boldsymbol{\tau}) \quad (3.75)$$

$$= -p \mathbf{I} + \mathbf{T}, \quad (3.76)$$

where $p = p_S + p_P$ and $\mathbf{T} = \mathbf{T}_S + \boldsymbol{\tau} = 2\eta_S \mathbf{D} + \boldsymbol{\tau}$; here η_S is the solvent viscosity, $\mathbf{D} = \frac{1}{2}(\nabla \mathbf{u} + \nabla \mathbf{u}^T)$ is the rate-of-deformation tensor. The stress tensor \mathbf{T} is zero at equilibrium. In order to obtain a kinetic theory expression for $\boldsymbol{\sigma}_P$, we follow the elementary physical derivation provided by Kramers [43]. The dumbbell will contribute to the stress in the suspension for two principal reasons:

1. Contribution from the Spring Force

An arbitrary plane of area S in the suspension moving with the local solution velocity v may at any moment be straddled by the two beads of the dumbbell, and there will be a force of tension or compression transmitted through the connector $\boldsymbol{\sigma}_P^{(c)}$. The orientation of the plane is given by the unit vector \mathbf{n} .

We want to obtain the average force exerted by all springs of all dumbbells from the left of the oriented plane (“the negative side”) on the right of that plane (“the positive side”). For every dumbbell straddling the plane, this force is given by $\mathbf{F}_1^{(c)}$ if bead “1” is on the left

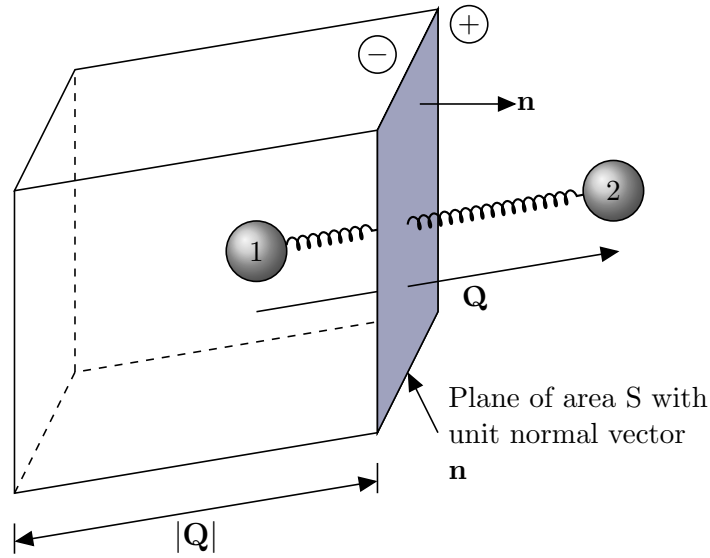


Figure 3.11: Spring force.

of the plane (i.e. $\mathbf{n} \cdot \mathbf{Q} > 0$), or $\mathbf{F}_2^{(c)}$ if bead “2” is on the left of the plane (i.e. $\mathbf{n} \cdot \mathbf{Q} < 0$). If we set $\mathbf{F}^{(c)} = \mathbf{F}_1^{(c)} = -\mathbf{F}_2^{(c)}$, we obtain the average force exerted by all dumbbells of all orientations for which the connector vector \mathbf{Q} intersects the plane in the direction of \mathbf{n} as

$$\langle \text{sgn}(\mathbf{n} \cdot \mathbf{Q}) \mathbf{F}^{(c)} \rangle = \int_{\text{over all } \mathbf{Q}} \text{sgn}(\mathbf{n} \cdot \mathbf{Q}) \mathbf{F}^{(c)} p(\mathbf{Q}, t) d\mathbf{Q}. \quad (3.77)$$

Now suppose, we have N_P elastic dumbbells in the system. The connector vector \mathbf{Q} of a dumbbell intersects the plane S if and only if either \mathbf{r}_1 or \mathbf{r}_2 is contained in the box of volume $S|\mathbf{n} \cdot \mathbf{Q}|$ as shown in Figure 3.11. The probability of finding \mathbf{r}_i ($i=1,2$) in this box is given by the volume of the box divided by the volume of the system V

$$\frac{S|\mathbf{n} \cdot \mathbf{Q}|}{V}.$$

Since, for the assumed homogeneous system $\mathbf{Q}(t)$ and $\mathbf{r}_i(t)$ are independent random variables, we can first integrate over \mathbf{r}_i and obtain the average force exerted by all springs through the given plane

$$\mathbf{n} \cdot \mathbf{F} = \left[\mathbf{n} \cdot nS \int \mathbf{Q} \mathbf{F}^{(c)} p(\mathbf{Q}, t) d\mathbf{Q} \right], \quad (3.78)$$

where $n = N_P/V$ is the number of dumbbells per unit volume and \mathbf{F} is the total averaged force. This average is to be identified with $\mathbf{n} \cdot \boldsymbol{\sigma}_P^{(c)} = \mathbf{n} \cdot \frac{\mathbf{F}}{S}$. Hence, the contribution of the dumbbell spring connectors to the stress in the solution is

$$\boldsymbol{\sigma}_P^{(c)} = n \int \mathbf{Q} \mathbf{F} p(\mathbf{Q}, t) d\mathbf{Q} = n \langle \mathbf{Q} \mathbf{F}^{(c)} \rangle = nH \langle \mathbf{Q} \mathbf{Q} \rangle. \quad (3.79)$$

2. Contribution from the Bead Motion

The beads themselves may cross an arbitrary plane and bring with them a certain amount of

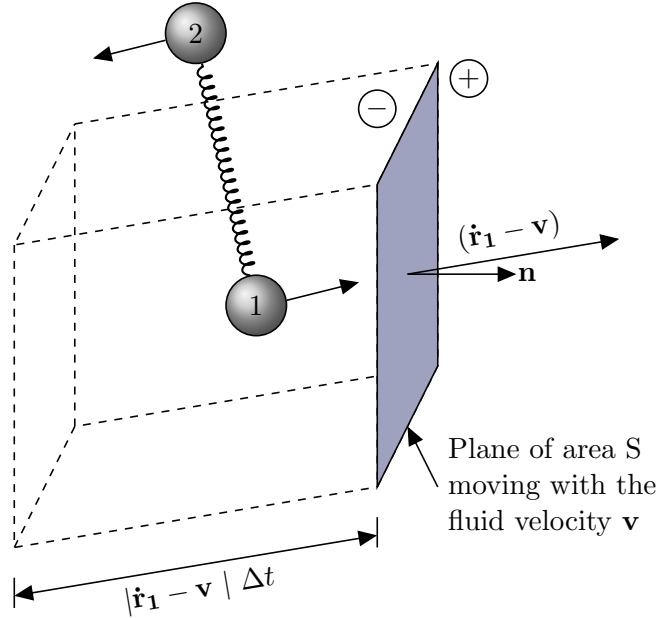


Figure 3.12: Spring force.

momentum. Now, how many “1” beads with velocity $\frac{d\mathbf{r}_1}{dt}$ will cross the arbitrary surface S in time δt ? All beads within the volume $(\frac{d\mathbf{r}_1}{dt} - \mathbf{v}) \cdot \delta t \cdot S$ will cross S in time δt . The probability that \mathbf{r}_1 is in this box is given by

$$\frac{(\frac{d\mathbf{r}_1}{dt} - \mathbf{v}) \cdot \delta t \cdot S}{V}. \quad (3.80)$$

Every bead transports the momentum $\mathbf{p} = m \cdot (\frac{d\mathbf{r}_1}{dt} - \mathbf{v})$. The amount of momentum transported across the plane in the normal direction \mathbf{n} is then given by

$$n((\frac{d\mathbf{r}_1}{dt} - \mathbf{v}) \cdot S \cdot \mathbf{n})m(\frac{d\mathbf{r}_1}{dt} - \mathbf{v})\delta t, \quad (3.81)$$

where n is the number of dumbbells per unit volume and m is the mass of the bead. If we assume that the velocity distribution in a flow system (here consisting of the dumbbells swimming in the Newtonian solvent) is the same as that in a solution at equilibrium, we can use the Maxwell-Boltzmann distribution from kinetic gas theory to describe the velocity distribution of the beads. The Maxwell-Boltzmann distribution is a Gaussian distribution given by

$$\langle \mathbf{X} \rangle = 0, \quad (3.82)$$

$$\langle \mathbf{X}^2 \rangle = \frac{kT}{m} \mathbf{I}, \quad (3.83)$$

where \mathbf{X} is a random variable. Therefore, we get

$$\left\langle nS \cdot \mathbf{n} m \left(\frac{d\mathbf{r}_1}{dt} - \mathbf{v} \right)^2 \delta t \right\rangle = nS \cdot \mathbf{n} m \left\langle \left(\frac{d\mathbf{r}_1}{dt} - \mathbf{v} \right)^2 \right\rangle \delta t = \mathbf{n} \cdot nS \delta t kT\mathbf{I}. \quad (3.84)$$

Hence, the average value of the momentum flux (momentum per unit time per unit area) resulting from beads “1” of all possible velocities and dumbbells of all possible configurations is given by

$$\mathbf{n} \cdot n \int kT\mathbf{I} p(\mathbf{Q}, t) d\mathbf{Q} = \mathbf{n} \cdot nkT\mathbf{I} \int p(\mathbf{Q}, t) d\mathbf{Q} = \mathbf{n} \cdot nkT\mathbf{I}. \quad (3.85)$$

We obtain the same result for bead “2”. Since the resulting average value $\mathbf{n} \cdot 2nkT\mathbf{I}$ must be identified with $\mathbf{n} \cdot \boldsymbol{\sigma}_P^{(b)}$, we get

$$\boldsymbol{\sigma}_P^{(b)} = 2nkT\mathbf{I}. \quad (3.86)$$

Therefore, the total polymeric stress is given by

$$\boldsymbol{\sigma}_P = -p_P\mathbf{I} + \boldsymbol{\tau} = nH \langle \mathbf{Q}\mathbf{Q} \rangle + 2nkT\mathbf{I}. \quad (3.87)$$

The corresponding equation at equilibrium (i.e. $\boldsymbol{\tau} = 0$) gives us the polymeric contribution to the pressure

$$p_P\mathbf{I} = -nH \langle \mathbf{Q}\mathbf{Q} \rangle_{eq} - 2nkT\mathbf{I} \stackrel{(3.73)}{=} -3nkT\mathbf{I}. \quad (3.88)$$

Finally, we get the **Kramers expression** for the extra stress tensor

$$\mathbf{T} = \mathbf{T}_S + \boldsymbol{\tau} = 2\eta_S\mathbf{D} + nH \langle \mathbf{Q}\mathbf{Q} \rangle - nkT\mathbf{I}. \quad (3.89)$$

If we use the equation (3.71) in the derivation of the expression for the extra stress tensor, we obtain the **Giesekus expression**

$$\mathbf{T} = 2\eta_S\mathbf{D} - \frac{n\zeta}{4} \langle \overset{\nabla}{\mathbf{Q}\mathbf{Q}} \rangle. \quad (3.90)$$

We can now eliminate $\langle \mathbf{Q}\mathbf{Q} \rangle$ between (3.89) and (3.90) by taking the upper-convected derivative of (3.89) and observing that

$$\overset{\nabla}{\mathbf{I}} = -\nabla\mathbf{u} - (\nabla\mathbf{u})^T = -2\mathbf{D}, \quad (3.91)$$

so that

$$\mathbf{T} - 2\eta_S\mathbf{D} = -\frac{\zeta}{4H} \left[\overset{\nabla}{\mathbf{T}} - nkT2\mathbf{D} - 2\eta_S\overset{\nabla}{\mathbf{D}} \right]. \quad (3.92)$$

We define the relaxation time λ (time constant for the Hookean elastic dumbbells) and the polymeric viscosity η_P in terms of the parameters appearing in (3.92) by

$$\lambda = \frac{\zeta}{4H} \quad \text{and} \quad \eta_P = \frac{nkT\zeta}{4H} = nkT\lambda. \quad (3.93)$$

With the total viscosity $\eta_0 = \eta_S + \eta_P$, we define the characteristic retardation time for the fluid by

$$\lambda_r = \frac{\eta_S}{\eta_0} \lambda. \quad (3.94)$$

Then, equation (3.92) can be written in the form

$$\mathbf{T} + \lambda \overset{\nabla}{\mathbf{T}} = 2\eta_0(\mathbf{D} + \lambda_2 \overset{\nabla}{\mathbf{D}}), \quad (3.95)$$

called **Oldroyd-B model**. By separating out the solvent and polymeric contributions to the stress and substituting the result into (3.95), we obtain the **split form of the Oldroyd-B model**

$$\begin{cases} \mathbf{T} = 2\eta_S \mathbf{D} + \boldsymbol{\tau}, \\ \boldsymbol{\tau} + \lambda \overset{\nabla}{\boldsymbol{\tau}} = 2\eta_P \mathbf{D}. \end{cases} \quad (3.96)$$

We call $\boldsymbol{\tau}$ the **elastic stress tensor**. Note that the equations (3.96) reduce to the UCM model for $\eta_S = 0$.

Behaviour in Simple Flows

For the steady simple shear flow, we obtain similarly to the viscometric functions of the UCM model (3.45)

$$\eta(\dot{\gamma}) = \frac{\sigma_{xy}}{\dot{\gamma}} = \eta_0, \quad N_1(\dot{\gamma}) = \sigma_{xx} - \sigma_{yy} = 2\lambda\eta_P\dot{\gamma}^2, \quad N_2(\dot{\gamma}) = \sigma_{yy} - \sigma_{zz} = 0 \quad (3.97)$$

and for the steady uniaxial elongational flow, we obtain

$$T_{xx} = -2\eta_S\dot{\epsilon} + \frac{2\eta_P\dot{\epsilon}}{1 - 2\lambda\dot{\epsilon}}, \quad T_{yy} = T_{zz} = \eta_S\dot{\epsilon} - \frac{\eta_P\dot{\epsilon}}{1 + \lambda\dot{\epsilon}}, \quad (3.98)$$

$$\Rightarrow \eta_E(\dot{\epsilon}) = \frac{\sigma_{xx} - \sigma_{yy}}{\dot{\epsilon}} = 3\eta_S + 3\frac{\eta_P}{[1 - 2\lambda\dot{\epsilon}][1 + \lambda\dot{\epsilon}]}. \quad (3.99)$$

Hence, the elongational viscosity still blows up for the Oldroyd-B equations at an elongational rate of $\frac{1}{2\lambda}$. This is caused by the fact that the dumbbells are infinitely extensible and become infinitely extended at $\dot{\epsilon} = \frac{1}{2\lambda}$. This can be seen by taking traces throughout Kramers expression (3.89), so as to obtain

$$\langle Q^2 \rangle = \frac{1}{nH} \text{tr } \mathbf{T} + \frac{3kT}{H} \quad (3.100)$$

and using the expressions for T_{xx}, T_{yy}, T_{zz} (3.98), we see that

$$\langle Q^2 \rangle = \frac{6\eta_P\lambda\dot{\epsilon}^2}{nH(1 - 2\lambda\dot{\epsilon})(1 + \lambda\dot{\epsilon})} + \frac{3kT}{H}, \quad (3.101)$$

so that $\langle Q^2 \rangle \rightarrow \infty$ as $\dot{\epsilon} \rightarrow 2\lambda$.

The Oldroyd-B model has been seen to be useful in providing qualitative predictions of the flow of Boger fluids, which have a constant viscosity over a range of shear-rates and a quadratic first normal stress difference. Unfortunately, the Oldroyd-B model is unable to adequately predict extensional flow behaviour. Nevertheless, it is a good first approach in modelling dilute polymer solutions.

Models with Finite Elongational Viscosity

To overcome the disadvantage of infinitely extensible springs, one might consider deriving models with finitely extensible springs. As an alternative to the Hookean spring, Warner [72] proposed the connector force law

$$\mathbf{F} = \frac{H\mathbf{Q}}{1 - (Q^2/Q_0^2)}, \quad (3.102)$$

for which the spring cannot be extended beyond some finite constant length Q_0 and $Q^2 = \text{tr } \mathbf{Q}\mathbf{Q}$. Based on this idea the FENE-P [8, 52] and FENE-CR [14] models were derived. Both models predict a finite elongational viscosity at all elongation rates, a non-zero first and a zero second normal stress difference. The FENE-P model shows shear-thinning, the FENE-CR a constant shear viscosity. Giesekus [26, 27] chose the approach to consider anisotropic effects in the equations of motion for the beads of the dumbbell. He allowed the friction force and the Brownian motion to be anisotropic and derived an expression for the polymeric part of the extra-stress tensor, which differs only in the addition of a term from the Oldroyd-B equations

$$\left(1 + \frac{\alpha\lambda}{\eta_P}\boldsymbol{\tau}\right)\boldsymbol{\tau} + \lambda\frac{\delta_a\boldsymbol{\tau}}{\delta t} = 2\eta_P\mathbf{D}, \quad 0 \leq \alpha \leq 1, \quad (3.103)$$

where α is a material parameter, which controls the anisotropy of the fluid. The material parameter α is obtained for a specific material through fitting of experimental data to the Giesekus model. The Giesekus model predicts shear-thinning, a non-zero first and second normal stress difference and a finite elongational viscosity at all elongation rates.

3.6.2 Polymer Melts and Concentrated Solutions

Derivation of the PTT Model

In the elastic dumbbell model used in the previous section for the description of dilute polymer solutions, polymer-polymer interactions are neglected. However, the range in which this assumption applies is limited to very small concentrations. Therefore, we take a different approach to model the interactions of the polymer molecules: the network theories of polymeric liquids as described by Green and Tobolsky [28], Lodge [45, 46] and Yamamoto [75, 76, 77]. It will allow us to describe concentrated polymer solutions and polymer melts. The presentation in this section is based on the books of Bird [7], Tanner [67] and Huilgol and Phan-Thien [30].

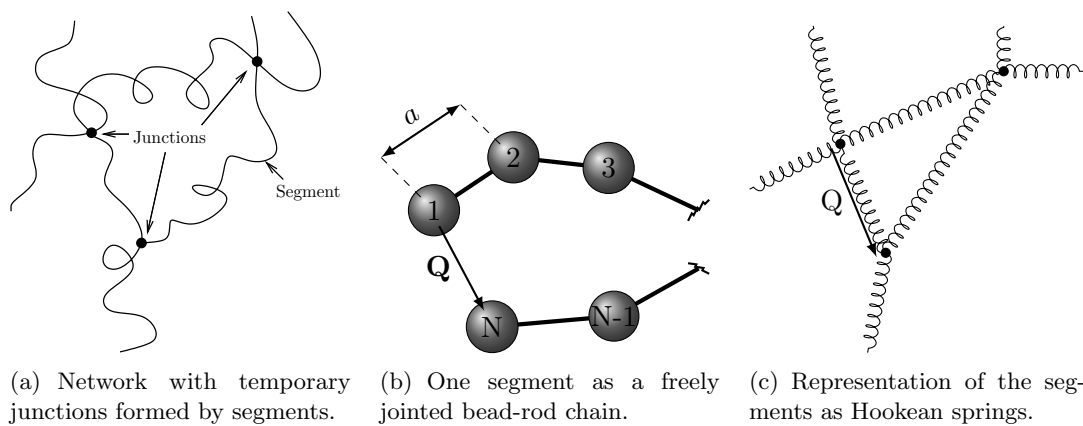


Figure 3.13: The network model.

We imagine a polymeric material as a collection of tangled polymer chains as shown in Figure 3.13. The entangled points, or **junctions**, are not permanent and are continually being created or destroyed. The chain between two junctions, or segment, is taken to be a freely jointed, bead-rod chain with end-to-end distance vector \mathbf{Q} , i.e. N beads connected by $N - 1$ rigid rods of length a . The statistical treatment of the freely jointed bead-rod chain (for details see Bird [7]) shows that the chain can be replaced by a Hookean spring with spring constant

$$H_N = \frac{3kT}{(N - 1)a^2}, \quad (3.104)$$

where k is the Boltzmann constant and T is the absolute temperature. We will suppose that N is constant for all chains. Eventually, this assumption leads to a single relaxation time.

a. The Equation of Non-Affine Motion for Network Segments

If we assume that the junction points move affinely, it follows that the segment vector \mathbf{Q} , which joints two junctions must also move affinely, i.e.

$$\frac{d\mathbf{Q}}{dt} = \nabla\mathbf{u} \cdot \mathbf{Q}. \quad (3.105)$$

Phan-Thien and Tanner [55, 53], and Johnson and Segalman [33] assumed a non-affine motion of the form

$$\frac{d\mathbf{Q}}{dt} = (\nabla\mathbf{u} - \xi\mathbf{D}) \cdot \mathbf{Q} =: \mathcal{L} \cdot \mathbf{Q}, \quad (3.106)$$

where ξ is an arbitrary “slip constant” and $\mathcal{L} := (\nabla\mathbf{u} - \xi\mathbf{D})$ is called **effective velocity gradient tensor**. The motivation leading to this special form for the effective velocity gradient tensor is based on the notion that the network slips with respect to the effective medium, and this slip velocity is an isotropic function of the rate of deformation tensor for the macroscopically imposed velocity field.

b. Liouville Equation of the Network Segments

Let $D(\mathbf{Q}, t)$ be the distribution function of segments, i.e. the number of segments per unit volume at time t that have an end-to-end vector ranging from \mathbf{Q} to $\mathbf{Q} + d\mathbf{Q}$ is given by $D(\mathbf{Q}, t)d\mathbf{Q}$. We have

$$\int D(\mathbf{Q}, t)d\mathbf{Q} = n, \quad (3.107)$$

where n is the number density of segments, i.e. the number of segments per unit volume. The probability density, which gives the probability that a segment has an end-to-end vector between \mathbf{Q} to $\mathbf{Q} + d\mathbf{Q}$, is then given by

$$p(\mathbf{Q}, t) = \frac{D(\mathbf{Q}, t)}{\int D(\mathbf{Q}, t)d\mathbf{Q}} = \frac{D(\mathbf{Q}, t)}{n}. \quad (3.108)$$

We can write a balance equation for the distribution function $D(\mathbf{Q}, t)$

$$\frac{d}{dt}D(\mathbf{Q}, t) = (\text{rate of segment creation} - \text{rate of segment destruction}). \quad (3.109)$$

We shall write the rate of segment creation as c , and the rate of segment destruction as $\beta D(\mathbf{Q}, t)$, it being natural to write the destruction rate as being proportional to the number of segments present. Thus, equation (3.109) can be written as

$$\frac{d}{dt}D(\mathbf{Q}, t) = (c - \beta D(\mathbf{Q}, t)). \quad (3.110)$$

This yields the following **Liouville equation**

$$\frac{\partial D(\mathbf{Q}, t)}{\partial t} = -\frac{\partial}{\partial \mathbf{Q}} \cdot \left[\frac{d\mathbf{Q}}{dt} D(\mathbf{Q}, t) \right] + c - \beta D(\mathbf{Q}, t). \quad (3.111)$$

We can now define the expectation of a function g of \mathbf{Q} by

$$\langle g(\mathbf{Q}) \rangle_D = \int g(\mathbf{Q}) D(\mathbf{Q}, t) d\mathbf{Q}. \quad (3.112)$$

Similar to (3.70) of section 3.6.1, we obtain the following equation of change for $\frac{d\mathbf{Q}}{dt} = \mathcal{L} \cdot \mathbf{Q}$ by multiplying (3.111) by $\mathbf{Q}\mathbf{Q}$ and integrating over all configuration space

$$\frac{d}{dt} \langle g(\mathbf{Q}) \rangle_D = - \left\langle \mathcal{L} \cdot \mathbf{Q} \frac{\partial}{\partial \mathbf{Q}} \cdot g(\mathbf{Q}) \right\rangle_D \int c g(\mathbf{Q}) d\mathbf{Q} - \langle \beta g(\mathbf{Q}) \rangle_D. \quad (3.113)$$

For $g(\mathbf{Q}) = \mathbf{Q}\mathbf{Q}$, we can deduce

$$\frac{d}{dt} \langle \mathbf{Q}\mathbf{Q} \rangle_D - \mathcal{L} \langle \mathbf{Q}\mathbf{Q} \rangle_D - \langle \mathbf{Q}\mathbf{Q} \rangle_D \mathcal{L}^T = \int (c - \beta D(\mathbf{Q}, t)) \mathbf{Q}\mathbf{Q} d\mathbf{Q}. \quad (3.114)$$

c. The Expression for the Stress Tensor

In this section, we use a simple physical argument similar to that given in Section 3.6.1 to deduce the expression for the stress tensor. Initially, let us consider the total Cauchy stress tensor given by

$$\boldsymbol{\sigma} = \boldsymbol{\sigma}_S + \boldsymbol{\sigma}_P = -p\mathbf{I} + \mathbf{T}_S + \boldsymbol{\tau} = -p\mathbf{I} + 2\eta_S \mathbf{D} + \boldsymbol{\tau}. \quad (3.115)$$

To derive the expression for the polymeric contribution to the Cauchy stress, consider an arbitrary plane of area S with outer unit normal vector \mathbf{n} as shown in Figure 3.14. Through the tension in the segments that pass through the plane, a force is transmitted. To calculate this force, we first note that the number of segments in the configuration range \mathbf{Q} to $\mathbf{Q} + d\mathbf{Q}$ that intersect the plane is given by

$$|\mathbf{n} \cdot \mathbf{Q}| S D(\mathbf{Q}, t) d\mathbf{Q}. \quad (3.116)$$

We obtain the average force exerted by all segments through the plane by

$$\mathbf{n} \cdot \mathbf{F} = \mathbf{n} S \int \mathbf{Q} \mathbf{F}_N^{(c)} D(\mathbf{Q}, t) d\mathbf{Q}, \quad (3.117)$$

where $\mathbf{F}_N^{(c)}$ is with (3.104) given by

$$\mathbf{F}_N^{(c)} = H_N \mathbf{Q}. \quad (3.118)$$

This yields

$$\boldsymbol{\sigma}_P = \left\langle \mathbf{Q} \mathbf{F}_N^{(c)} \right\rangle_D = H_N \langle \mathbf{Q}\mathbf{Q} \rangle_D. \quad (3.119)$$

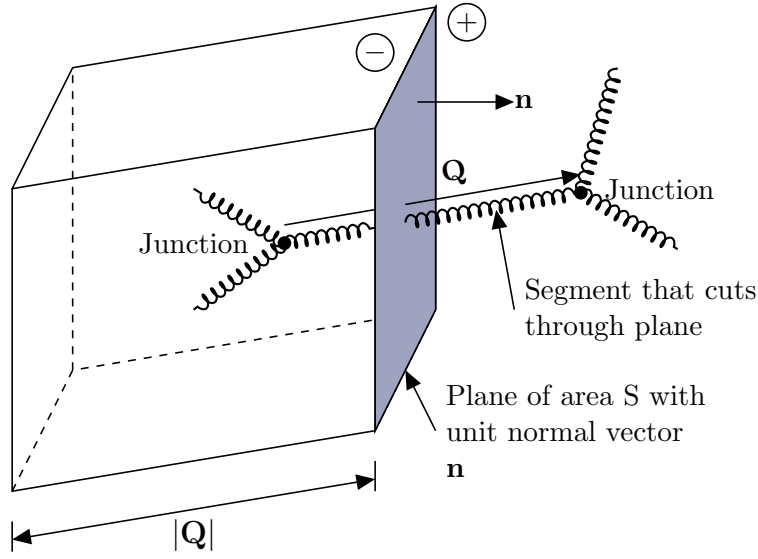


Figure 3.14: Physical argument used in calculating the stress tensor σ_P .

We find

$$\frac{d}{dt}\sigma_P = H_N \frac{d}{dt} \langle \mathbf{Q}\mathbf{Q} \rangle_D \stackrel{(3.114)}{=} \stackrel{(3.119)}{\mathcal{L}}\sigma_P + \sigma_P \mathcal{L}^T + H_N \left(\int c \mathbf{Q}\mathbf{Q} d\mathbf{Q} - \langle \beta \mathbf{Q}\mathbf{Q} \rangle_D \right). \quad (3.120)$$

To proceed further, specific forms for c and β must be nominated.

Loss and Creation Rates

First, we note that at equilibrium the creation and loss terms balance one another, so that

$$c_{eq} = \beta_{eq} D(\mathbf{Q}, t). \quad (3.121)$$

On this basis, it has been suggested that c may be considered as a function of \mathbf{Q} . We take this \mathbf{Q} -dependence of the creation rate to be the same as that for the equilibrium distribution function for a freely jointed bead-rod chain. That means, we assume that the distribution function for the network segments at the moment of creation is identical to the equilibrium distribution function for a freely jointed bead-rod chain, which is given by

$$D_c(\mathbf{Q})_{eq} = \left(\frac{H_N}{2\pi kT} \right)^{3/2} e^{-\frac{H_N}{2kT}(\mathbf{Q}\mathbf{Q})}. \quad (3.122)$$

Then, we have

$$\langle \mathbf{Q}\mathbf{Q} \rangle_{D_c} = \frac{kT}{H_N} \mathbf{I}. \quad (3.123)$$

Now, let $\overset{\circ}{c}$ denote the creation rate of all segments independent of \mathbf{Q} , then

$$c(\mathbf{Q}) = \overset{\circ}{c} \cdot D_c(\mathbf{Q})_{eq}. \quad (3.124)$$

Further, Phan-Thien and Tanner [55, 53] assumed that both the creation and loss rates depend on the mean squared segment vector length $\langle Q^2 \rangle_D$:

$$c = \overset{\circ}{c}(\langle Q^2 \rangle_D) \cdot D_c(\mathbf{Q})_{eq}, \quad (3.125)$$

$$\beta = \beta(\langle Q^2 \rangle_D). \quad (3.126)$$

To evaluate $\langle Q^2 \rangle_D$, we note that since $\boldsymbol{\sigma}_P = H_N \langle \mathbf{Q}\mathbf{Q} \rangle_D$, we must have

$$\langle Q^2 \rangle_D = \frac{1}{H_N} \text{tr} \boldsymbol{\sigma}_P = \frac{1}{H_N} (\text{tr} \boldsymbol{\tau} + 3p_P). \quad (3.127)$$

That means $\langle Q^2 \rangle_D$ is proportional to $\text{tr} \boldsymbol{\tau}$. Therefore, we can formulate the creation and loss rates in terms of $\text{tr} \boldsymbol{\tau}$. Next, we assume that the creation rate $\overset{\circ}{c}(\text{tr} \boldsymbol{\tau})$ is proportional to the loss rate $\beta(\text{tr} \boldsymbol{\tau})$ with

$$\overset{\circ}{c}(\text{tr} \boldsymbol{\tau}) = \frac{G}{kT(1-\xi)} \beta(\text{tr} \boldsymbol{\tau}), \quad (3.128)$$

where G is a constant modulus.

Derivation of the Stress Tensor

When we insert our terms for the loss and creation rates in (3.120), we get

$$\begin{aligned} \frac{d}{dt} \boldsymbol{\sigma}_P - \boldsymbol{\mathcal{L}} \boldsymbol{\sigma}_P - \boldsymbol{\sigma}_P \boldsymbol{\mathcal{L}}^T &= H_N \left(\overset{\circ}{c}(\text{tr} \boldsymbol{\tau}) \int \mathbf{Q}\mathbf{Q} D_c(\mathbf{Q})_{eq} d\mathbf{Q} - \beta(\text{tr} \boldsymbol{\tau}) \langle \mathbf{Q}\mathbf{Q} \rangle_D \right) \\ &= H_N \left(\overset{\circ}{c}(\text{tr} \boldsymbol{\tau}) \frac{kT}{H_N} \mathbf{I} \right) - \beta(\text{tr} \boldsymbol{\tau}) \boldsymbol{\sigma}_P \\ &\stackrel{(3.128)}{=} \frac{G}{(1-\xi)} \beta(\text{tr} \boldsymbol{\tau}) \mathbf{I} - \beta(\text{tr} \boldsymbol{\tau}) \boldsymbol{\sigma}_P. \end{aligned}$$

Hence, we get

$$\frac{1}{\beta(\text{tr} \boldsymbol{\tau})} \left(\frac{d}{dt} \boldsymbol{\sigma}_P - \boldsymbol{\mathcal{L}} \boldsymbol{\sigma}_P - \boldsymbol{\sigma}_P \boldsymbol{\mathcal{L}}^T \right) + \boldsymbol{\sigma}_P = \frac{G}{(1-\xi)} \mathbf{I}. \quad (3.129)$$

We can derive the expression for the polymeric contribution to the pressure p_P by evaluating the expression for the stress tensor $\boldsymbol{\sigma}_{P_{eq}} = -p_P \mathbf{I}$ at equilibrium. With (3.121), we obtain

$$\frac{d}{dt} \boldsymbol{\sigma}_P - \boldsymbol{\mathcal{L}} \boldsymbol{\sigma}_P - \boldsymbol{\sigma}_P \boldsymbol{\mathcal{L}}^T = 0. \quad (3.130)$$

Then

$$p_P \mathbf{I} = -\frac{G}{(1-\xi)} \mathbf{I}. \quad (3.131)$$

The polymeric contribution to the extra-stress tensor

$$\boldsymbol{\tau} = \boldsymbol{\sigma}_P + p\mathbf{I} \quad (3.132)$$

is then deduced from (3.129)

$$\frac{d}{dt}\boldsymbol{\tau} - \boldsymbol{\mathcal{L}}\boldsymbol{\tau} - \boldsymbol{\tau}\boldsymbol{\mathcal{L}}^T + \beta(\text{tr}\boldsymbol{\tau})\boldsymbol{\tau} = 2G\mathbf{D}. \quad (3.133)$$

Finally, we let

$$\beta(\text{tr}\boldsymbol{\tau}) = \frac{f(\text{tr}\boldsymbol{\tau})}{\lambda}, \quad (3.134)$$

where λ is a constant with unit of time and f is a dimensionless function of $\text{tr}\boldsymbol{\tau}$. The constitutive equation then becomes

$$\lambda \left(\frac{d}{dt}\boldsymbol{\tau} - \boldsymbol{\mathcal{L}}\boldsymbol{\tau} - \boldsymbol{\tau}\boldsymbol{\mathcal{L}}^T \right) + f(\text{tr}\boldsymbol{\tau})\boldsymbol{\tau} = 2\eta_P\mathbf{D}, \quad (3.135)$$

where $\eta_P = G\lambda$. To complete the model, an expression for f must be postulated. Phan-Thien and Tanner have suggested two empirical forms

$$f(\text{tr}\boldsymbol{\tau}) = \begin{cases} 1 + \frac{\lambda\varepsilon}{\eta_P}\text{tr}\boldsymbol{\tau} \\ \exp\left(\frac{\lambda\varepsilon}{\eta_P}\text{tr}\boldsymbol{\tau}\right). \end{cases} \quad (3.136)$$

The expression for the total extra-stress tensor is

$$\mathbf{T} = \mathbf{T}_S + \boldsymbol{\tau} = 2\eta_S\mathbf{D} + \boldsymbol{\tau}. \quad (3.137)$$

Therefore, in summary, the **Phan-Thien Tanner model** is given by

$$\left\{ \begin{array}{l} \mathbf{T} = 2\eta_S\mathbf{D} + \boldsymbol{\tau}, \\ \lambda \left(\frac{d}{dt}\boldsymbol{\tau} - \boldsymbol{\mathcal{L}}\boldsymbol{\tau} - \boldsymbol{\tau}\boldsymbol{\mathcal{L}}^T \right) + f(\text{tr}\boldsymbol{\tau})\boldsymbol{\tau} = 2\eta_P\mathbf{D}, \\ f(\text{tr}\boldsymbol{\tau}) = \begin{cases} 1 + \frac{\lambda\varepsilon}{\eta_P}\text{tr}\boldsymbol{\tau} \\ \exp\left(\frac{\lambda\varepsilon}{\eta_P}\text{tr}\boldsymbol{\tau}\right). \end{cases} \end{array} \right. \quad (3.138)$$

The components of the Phan-Thien Tanner model are given in Appendix A.

Models Covered by the PTT Equations

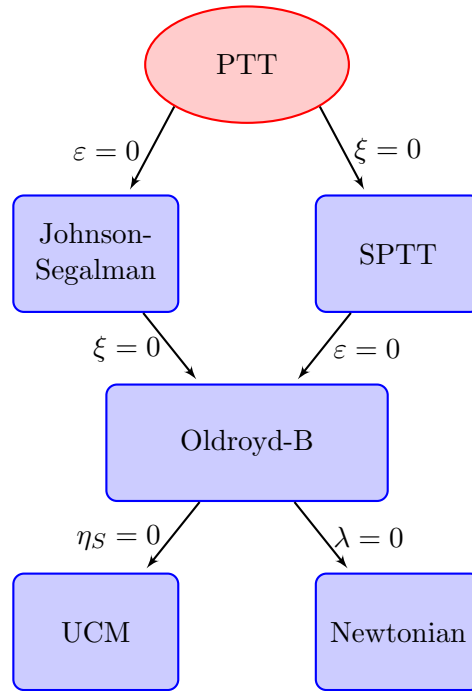


Figure 3.15: Models included in the PTT equations.

The PTT model is called **exponential PTT (EPTT)** model for the choice of

$$f(\text{tr } \boldsymbol{\tau}) = \exp\left(\frac{\lambda \varepsilon}{\eta_P} \text{tr } \boldsymbol{\tau}\right) \quad (3.139)$$

and **linear PTT (LPTT)** model for

$$f(\text{tr } \boldsymbol{\tau}) = 1 + \frac{\lambda \varepsilon}{\eta_P} \text{tr } \boldsymbol{\tau}. \quad (3.140)$$

For the choice of $\xi = 0$, it is called **simplified PTT (SPTT)** model. Further, the PTT model covers the following four kinds of constitutive models (see Figure 3.15): the Johnson-Segalman model ($\varepsilon = 0$), the Oldroyd-B model ($\varepsilon = 0, \xi = 0$), the upper-convected Maxwell model ($\varepsilon = 0, \xi = 0$ and $\eta_0 = \eta_P$) and the Newtonian fluid model ($\lambda = 0, \varepsilon = 0, \xi = 0$ and $\eta_0 = \eta_S$).

Behaviour in Simple Flows

For steady shear flow (3.135) becomes

$$\begin{aligned} f(\text{tr } \boldsymbol{\tau}) \begin{pmatrix} \tau_{xx} & \tau_{xy} & 0 \\ \tau_{xy} & \tau_{yy} & 0 \\ 0 & 0 & \tau_{zz} \end{pmatrix} - \lambda \left\{ \begin{pmatrix} 0 & \dot{\gamma} & 0 \\ 0 & 0 & 0 \\ 0 & 0 & 0 \end{pmatrix} \begin{pmatrix} \tau_{xx} & \tau_{xy} & 0 \\ \tau_{xy} & \tau_{yy} & 0 \\ 0 & 0 & \tau_{zz} \end{pmatrix} + \begin{pmatrix} \tau_{xx} & \tau_{xy} & 0 \\ \tau_{xy} & \tau_{yy} & 0 \\ 0 & 0 & \tau_{zz} \end{pmatrix} \begin{pmatrix} 0 & 0 & 0 \\ \dot{\gamma} & 0 & 0 \\ 0 & 0 & 0 \end{pmatrix} \right\} \\ + \frac{\xi\lambda}{2} \left\{ \begin{pmatrix} \tau_{xx} & \tau_{xy} & 0 \\ \tau_{xy} & \tau_{yy} & 0 \\ 0 & 0 & \tau_{zz} \end{pmatrix} \begin{pmatrix} 0 & \dot{\gamma} & 0 \\ \dot{\gamma} & 0 & 0 \\ 0 & 0 & 0 \end{pmatrix} + \begin{pmatrix} 0 & \dot{\gamma} & 0 \\ \dot{\gamma} & 0 & 0 \\ 0 & 0 & 0 \end{pmatrix} \begin{pmatrix} \tau_{xx} & \tau_{xy} & 0 \\ \tau_{xy} & \tau_{yy} & 0 \\ 0 & 0 & \tau_{zz} \end{pmatrix} \right\} = \eta_P \begin{pmatrix} 0 & \dot{\gamma} & 0 \\ \dot{\gamma} & 0 & 0 \\ 0 & 0 & 0 \end{pmatrix}. \end{aligned}$$

This leads to the following equations

$$f(\text{tr } \boldsymbol{\tau}) \tau_{xx} - 2\lambda_1 \dot{\gamma} \tau_{xy} + \lambda_1 \xi \dot{\gamma} \tau_{xy} = 0, \quad (3.141)$$

$$f(\text{tr } \boldsymbol{\tau}) \tau_{xy} - \lambda_1 \dot{\gamma} \tau_{yy} + \lambda_1 \xi \frac{\dot{\gamma}}{2} (\tau_{xx} + \tau_{yy}) = 0, \quad (3.142)$$

$$f(\text{tr } \boldsymbol{\tau}) \tau_{yy} + \lambda_1 \xi \dot{\gamma} \tau_{xy} = 0, \quad (3.143)$$

$$\tau_{zz} = 0, \quad (3.144)$$

from which we obtain the viscometric functions

$$\eta(\dot{\gamma}) = \sigma_{xy} \dot{\gamma} = \eta_S + \frac{f(\text{tr } \boldsymbol{\tau}) g}{2\lambda \dot{\gamma}^2 (1 - \xi)}, \quad (3.145)$$

$$N_1(\dot{\gamma}) = \sigma_{xx} - \sigma_{yy} = \frac{2}{2(1 - \xi)} g, \quad (3.146)$$

$$N_2(\dot{\gamma}) = \sigma_{yy} - \sigma_{zz} = -\frac{\xi}{2(1 - \xi)} g, \quad (3.147)$$

where g satisfies ($g = \tau_{xx} + \tau_{yy}$)

$$(f(\text{tr } \boldsymbol{\tau}))^2 g + (\lambda \dot{\gamma})^2 \xi (2 - \xi) g - 2\lambda \dot{\gamma}^2 (1 - \xi) \eta_P = 0. \quad (3.148)$$

In Figure 3.16, we can see that the PTT fluid and the SPTT (i.e. $\xi = 0$) fluid are both shear-thinning. The EPTT model is more shear-thinning than the LPTT model and the shear-thinning effect increases with increasing ε . We use two values of ε , 0.02 and 0.25. The former reflects low-density polyethylene (LDPE), while $\varepsilon = 0.25$ is closer to the response of high-density polyethylene melts (HDPE) (Larson [44]). In Figure 3.16(b), we see that the parameter ξ has the strongest influence on shear-thinning.

In equation (3.147), we see that for the SPTT model ($\xi = 0$), we have a zero second normal stress difference. For the Johnson-Segalman and the PTT models, the second normal stress difference is non-zero and we find the ratio of the normal stress differences to be given by

$$\frac{N_1(\dot{\gamma})}{N_2(\dot{\gamma})} = -\frac{\xi}{2}. \quad (3.149)$$

The first and second normal stress differences are plotted for different values at Figure 3.17. To obtain realistic flow behaviour, N_1 has to be larger than N_2 , so that only values of ξ between 0 and 2 need to be considered. Moreover, experimental data on LDPE and HDPE

suggest a value of ξ around 0.1 (Larson [44], Verbeeten [71]).

In the case of steady uniaxial elongation (3.135) specializes to

$$\begin{aligned}
& f(\text{tr } \boldsymbol{\tau}) \begin{pmatrix} \tau_{xx} & 0 & 0 \\ 0 & \tau_{yy} & 0 \\ 0 & 0 & \tau_{zz} \end{pmatrix} \\
& - \lambda \left\{ \begin{pmatrix} \dot{\epsilon} & 0 & 0 \\ 0 & -\frac{\dot{\epsilon}}{2} & 0 \\ 0 & 0 & -\frac{\dot{\epsilon}}{2} \end{pmatrix} \begin{pmatrix} \tau_{xx} & 0 & 0 \\ 0 & \tau_{yy} & 0 \\ 0 & 0 & \tau_{zz} \end{pmatrix} + \begin{pmatrix} \tau_{xx} & 0 & 0 \\ 0 & \tau_{yy} & 0 \\ 0 & 0 & \tau_{zz} \end{pmatrix} \begin{pmatrix} \dot{\epsilon} & 0 & 0 \\ 0 & -\frac{\dot{\epsilon}}{2} & 0 \\ 0 & 0 & -\frac{\dot{\epsilon}}{2} \end{pmatrix} \right\} \\
& + \frac{\xi\lambda}{2} \left\{ \begin{pmatrix} \tau_{xx} & 0 & 0 \\ 0 & \tau_{yy} & 0 \\ 0 & 0 & \tau_{zz} \end{pmatrix} \begin{pmatrix} \dot{\epsilon} & 0 & 0 \\ 0 & -\frac{\dot{\epsilon}}{2} & 0 \\ 0 & 0 & -\frac{\dot{\epsilon}}{2} \end{pmatrix} + \begin{pmatrix} \dot{\epsilon} & 0 & 0 \\ 0 & -\frac{\dot{\epsilon}}{2} & 0 \\ 0 & 0 & -\frac{\dot{\epsilon}}{2} \end{pmatrix} \begin{pmatrix} \tau_{xx} & 0 & 0 \\ 0 & \tau_{yy} & 0 \\ 0 & 0 & \tau_{zz} \end{pmatrix} \right\} \\
& = \eta_P \begin{pmatrix} \dot{\epsilon} & 0 & 0 \\ 0 & -\frac{\dot{\epsilon}}{2} & 0 \\ 0 & 0 & -\frac{\dot{\epsilon}}{2} \end{pmatrix},
\end{aligned}$$

which has solution

$$\tau_{xx} = \frac{2\eta_P \dot{\epsilon}}{f(\text{tr } \boldsymbol{\tau}) - 2\lambda\dot{\epsilon}(1 - \xi)}, \quad (3.150)$$

$$\tau_{yy} = \tau_{zz} = -\frac{\eta_P \dot{\epsilon}}{f(\text{tr } \boldsymbol{\tau}) + \lambda\dot{\epsilon}(1 - \xi)}. \quad (3.151)$$

Hence, the elongational viscosity is given by

$$\eta_E(\dot{\epsilon}) = \frac{\sigma_{xx} - \sigma_{yy}}{\dot{\epsilon}} = 3\eta_S + 3\frac{\eta_P f(\text{tr } \boldsymbol{\tau})}{[f(\text{tr } \boldsymbol{\tau}) - 2\lambda\dot{\epsilon}(1 - \xi)][f(\text{tr } \boldsymbol{\tau}) + \lambda\dot{\epsilon}(1 - \xi)]}. \quad (3.152)$$

For $\varepsilon = 0$, i.e. $f(\text{tr } \boldsymbol{\tau}) = 1$, we obtain the Johnson-Segalman model and as shown in Figure 3.18(a) the elongational viscosity becomes infinitely large at an elongation rate of $\frac{1}{2\lambda(1-\xi)}$. Hence, the problem of an infinitely large elongational viscosity is just a little bit shifted in comparison to the Oldroyd-B model. With $\varepsilon > 0$, this problem is solved. The difference between the exponential form of $f(\text{tr } \boldsymbol{\tau})$ and the linear form of $f(\text{tr } \boldsymbol{\tau})$ can be seen in Figure 3.18(b). With the linear form, η_E is monotonic in the elongation rate, which approaches a constant at high values of the elongation rate. For the exponential form, η_E goes through a maximum and then decreases at high elongational rates, since the rate of destruction overwhelms the rate of creation of network segments. With increasing ε the extensional-thickening effect becomes stronger.

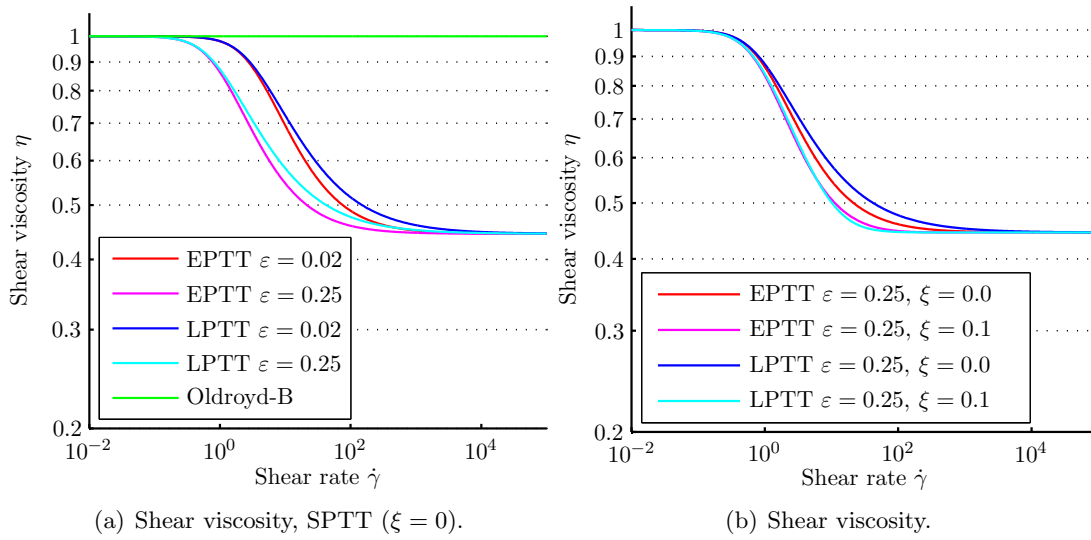


Figure 3.16: Shear-thinning.

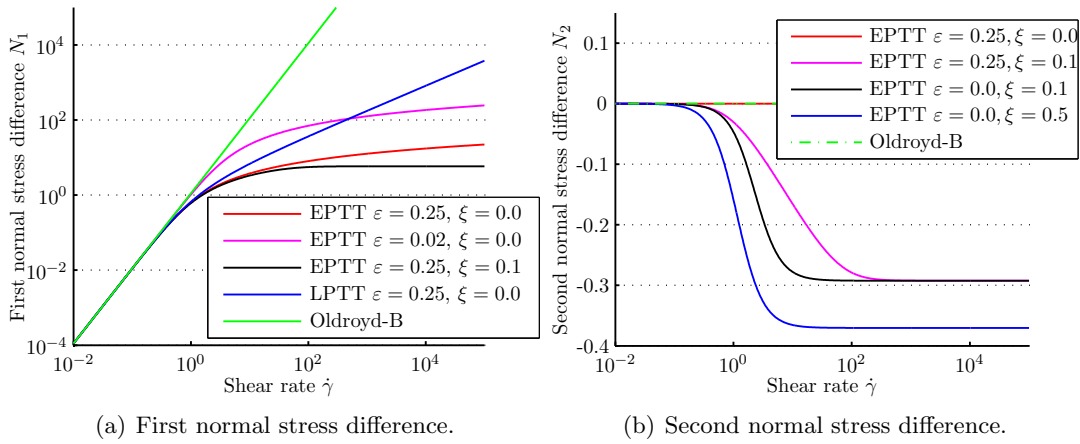


Figure 3.17: Normal stress differences.

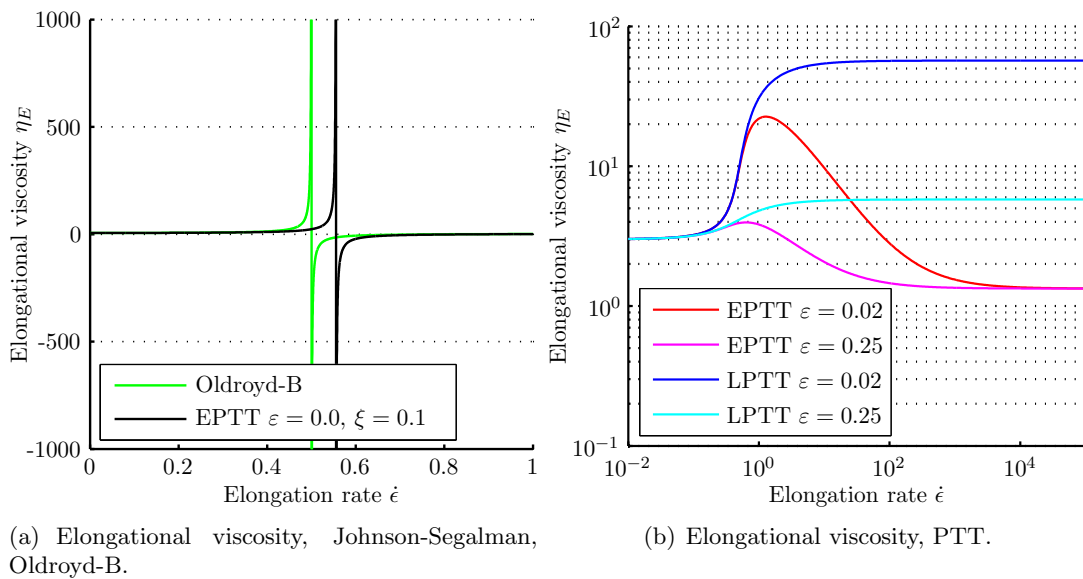




Figure 3.18: Elongational behaviour.

3.7 Summary of Behaviour in Simple Flows

To give a short overview over all introduced models in this chapter, Table 3.2 summarizes their behaviour in simple flows. The symbol  means the model predicts the property and the symbol  means the model is not able to predict the property.





























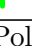
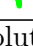
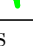






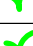















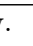


Name	shear-thinning	N_1	N_2	$\eta_E(\dot{\epsilon})$ finite
Continuum derived				
Newtonian				
Generalized Newtonian				
K-BKZ				
Dilute Polymer Solutions				
UCM				
Oldroyd-B				
FENE-P				
FENE-CR				
Giesekus				
Concentrated Polymer Solutions				
PTT				
SPTT				
Johnson-Segalman				
Doi-Edwards				
Pom-Pom				
XPP				

Table 3.2: Overview.

In this thesis, the Oldroyd-B and PTT model are used for numerical computations.

Chapter 4

Mathematical Model

In this chapter, we present the equations, which describe the motion of viscoelastic fluids and discuss their non-dimensionalization and the boundary conditions needed in order to solve them.

4.1 Governing Equations

Let $\Omega \subset \mathbb{R}^3$ be a domain with boundary $\partial\Omega$, filled by an incompressible viscoelastic fluid. Then the mathematical model describing the motion of the viscoelastic fluid consists of three coupled equations, namely the continuity equation (2.43), the momentum equation (2.47) and the constitutive equation for the extra-stress tensor given by (3.96) for an Oldroyd-B fluid and by (3.138) for a Phan-Thien Tanner fluid. Here, we will give the system of equations for a Phan-Thien Tanner fluid, because we can obtain the Oldroyd-B model by setting ξ and ε to zero. Inserting equation (3.135) into the momentum equation (2.47) yields

$$\rho \frac{D\mathbf{u}}{Dt} = \rho \mathbf{g} - \nabla p + \eta_S \Delta \mathbf{u} + \operatorname{div} \boldsymbol{\tau}, \quad (4.1)$$

where \mathbf{g} is the body force **gravity**. Further, we set

$$\beta = \frac{\eta_S}{\eta_0} \quad (4.2)$$

to obtain a non-dimensional parameter $0 \leq \beta \leq 1$ measuring the percentage of the solvent Newtonian viscosity to the total viscosity. Therefore, we have $\eta_S = \beta \eta_0$ and $\eta_P = (1 - \beta) \eta_0$. Finally, we obtain the following system of equations

$$\left\{ \begin{array}{ll} \rho \frac{D\mathbf{u}}{Dt} = \rho \mathbf{g} - \nabla p + \eta_0 \beta \Delta \mathbf{u} + \operatorname{div} \boldsymbol{\tau}, & \text{Momentum Equation} \\ \mathbf{f}(\operatorname{tr} \boldsymbol{\tau}) \boldsymbol{\tau} + \lambda \overset{\nabla}{\boldsymbol{\tau}} + \lambda \xi (\boldsymbol{\tau} \mathbf{D} + \mathbf{D} \boldsymbol{\tau}) = 2\eta_0 (1 - \beta) \mathbf{D}, & \text{PTT} \\ \mathbf{f}(\operatorname{tr} \boldsymbol{\tau}) = \begin{cases} 1 + \frac{\lambda \varepsilon}{(1 - \beta) \eta_0} \operatorname{tr} \boldsymbol{\tau} & \text{linear form} \\ \exp\left(\frac{\lambda \varepsilon}{(1 - \beta) \eta_0} \operatorname{tr} \boldsymbol{\tau}\right), & \text{exponential form} \end{cases} & (4.3) \\ \operatorname{div} \mathbf{u} = 0. & \text{Continuity Equation} \end{array} \right.$$

4.2 Non-Dimensionalization

We employ the non-dimensionalization

$$x^* = \frac{x}{L}, \mathbf{u}^* = \frac{\mathbf{u}}{U}, t^* = \frac{U}{L} t, \rho^* = \frac{\rho}{\rho_{ref}}, p^* = \frac{1}{\rho_{ref} U^2} p, \boldsymbol{\tau}^* = \frac{L}{\eta_0 U} \boldsymbol{\tau}, \mathbf{g}^* = \frac{\mathbf{g}}{\|\mathbf{g}\|},$$

where L , U , ρ_{ref} denote the characteristic length, velocity and density scales for the flow respectively. This leads to the following system of dimensionless equations

$$\begin{cases} \frac{D\mathbf{u}^*}{Dt} = -\nabla p^* + \frac{1}{Re} \beta \Delta \mathbf{u}^* + \frac{1}{Re} \operatorname{div} \boldsymbol{\tau}^* + \frac{1}{Fr^2} \mathbf{g}^*, \\ f(\operatorname{tr} \boldsymbol{\tau}^*) \boldsymbol{\tau}^* + Wi \boldsymbol{\tau}^* + Wi \xi(\boldsymbol{\tau}^* \mathbf{D}^* + \mathbf{D}^* \boldsymbol{\tau}^*) = 2(1 - \beta) \mathbf{D}^*, \\ f(\operatorname{tr} \boldsymbol{\tau}^*) = \begin{cases} 1 + \frac{Wi \varepsilon}{(1 - \beta)} \operatorname{tr} \boldsymbol{\tau}^* \\ \exp\left(\frac{Wi \varepsilon}{(1 - \beta)} \operatorname{tr} \boldsymbol{\tau}^*\right), \end{cases} \\ \operatorname{div} \mathbf{u}^* = 0. \end{cases} \quad (4.4)$$

We recall the upper convected derivative

$$\overset{\nabla}{\boldsymbol{\tau}^*} = \frac{\partial \boldsymbol{\tau}^*}{\partial t} + \mathbf{u} \cdot \nabla \boldsymbol{\tau}^* - \nabla \mathbf{u}^* \cdot \boldsymbol{\tau}^* - \boldsymbol{\tau} \cdot \nabla \mathbf{u}^{*T}. \quad (4.5)$$

The dimensionless numbers in (4.4) describe the nature of the flow and are defined as follows:

Definition 4.1 [DIMENSIONLESS NUMBERS]

$$Re = \frac{UL\rho_{ref}}{\eta_0} = \frac{\text{inertial forces}}{\text{viscous forces}} \quad (4.6)$$

is the ratio of inertial forces to viscous forces and is called the **Reynolds number**.

$$Fr = \frac{U}{\sqrt{L \|\mathbf{g}\|}} = \frac{\text{inertial forces}}{\text{gravitational forces}} \quad (4.7)$$

is the ratio of inertial forces to gravitational forces and is called the **Froude number**.

$$Wi = \lambda \frac{U}{L} = \frac{\lambda}{T} = \frac{\text{relaxation time}}{\text{characteristic time}} \quad (4.8)$$

is the ratio of the relaxation time to the characteristic time scale of the fluid process and is called the **Weissenberg number**. It can be regarded as a measure of the elasticity of the fluid in the flow. For high Weissenberg numbers, the fluid behaves like an elastic solid and for low Weissenberg numbers, it behaves like a Newtonian fluid. Another useful dimensionless number describing the importance of elasticity relative to inertial forces is the so-called **elasticity number**, which we define as

$$El = \frac{Wi}{Re}. \quad (4.9)$$

Additionally, we have the non-dimensional material parameters β giving the portion of Newtonian viscosity, ξ the "slip parameter" and ε describing the elongational behaviour of the fluid. In the following, we will drop the star notation for the sake of simplicity. The complete set of equations is given by components in 3D in Appendix A. We have to solve this system of equations in the domain Ω during the time interval $[0, T]$ under adequate boundary and initial conditions. We have ten unknown functions of $\mathbf{x} \in \Omega$ and $t \in [0, T]$, six elastic stress tensor components, the velocity field $\mathbf{u} = (u, v, w)^T$ and the scalar pressure field p . The system of partial differential equations 4.4 is of mixed type and portrays traits of elliptic, parabolic and hyperbolic character [25, 50]. The constitutive equations for the extra stress tensor contain the hyperbolic part, i.e. the components of the extra stress tensor are convected along the streamlines, while the conservation laws contain the elliptic/ parabolic part.

4.3 Boundary and Initial Conditions

A very detailed discussion on boundary and initial conditions for viscoelastic fluid flows can be found in Huilgol [30]. We just describe briefly which boundary conditions are used for the solution of the equations in our computations.

4.3.1 Initial Conditions

For time-dependent flows, a set of initial conditions at time $t = 0$ is required. We need to prescribe an initial velocity field, i.e.

$$\mathbf{u}(0) = \mathbf{u}_0. \quad (4.10)$$

For viscoelastic fluids, a set of initial values for the elastic stress components is also needed. In general, we suppose that the elastic stresses in the fluid are zero at time $t = 0$, i.e.

$$\boldsymbol{\tau}(0) = \mathbf{0}. \quad (4.11)$$

That means, we assume that the elastic stresses are completely relaxed at the beginning.

4.3.2 Solid Boundaries

At walls and obstacles $\partial\Omega$, we assume no-slip boundary conditions for the velocities, i.e.

$$u = 0, v = 0, w = 0 \quad \text{on } \partial\Omega. \quad (4.12)$$

Then, the elastic stresses result from the constitutive equation (see Section 5.2.3).

4.3.3 Inflow and Outflow Boundaries

At the inflow boundary $\partial\Omega_{in}$ of the domain, we usually know the velocity field of the flow. For viscoelastic fluids, the stresses are also required there because they represent the information

carried with the fluid from its previous deformation states. Usually, we set Dirichlet boundary conditions for the velocities at inflow

$$\mathbf{u} = \mathbf{u}_{in} \quad \text{on } \partial\Omega_{in}. \quad (4.13)$$

We have to be aware that it is not possible to simply prescribe arbitrary stress values at inflow, because they have to be consistent with the constitutive equations. Therefore, we usually assume that the elastic stresses are relaxed at inflow, i.e.

$$\boldsymbol{\tau} = \mathbf{0} \quad \text{on } \partial\Omega_{in}. \quad (4.14)$$

Renardy [58] showed that, while for the Oldroyd-B model all elastic stress components must be prescribed, for the UCM model prescribing all stress components leads to an over-determined system, which can lead to errors. Resolving this problem is quite difficult in three space dimensions. A solution to this problem may be found in Renardy [59]. However, we will not use the UCM model in this thesis.

At the outlet $\partial\Omega_{out}$, the flow is usually well developed and arranged so that a unidirectional flow results. We assume that the velocity and elastic stress tensor components do not change in the direction of the outward normal vector \mathbf{n} of the outflow boundary. That means, we assume homogeneous Neumann boundary conditions for both the velocities and elastic stresses

$$\frac{\partial u}{\partial \mathbf{n}} = \frac{\partial v}{\partial \mathbf{n}} = \frac{\partial w}{\partial \mathbf{n}} = 0 \quad \text{on } \partial\Omega_{out}, \quad (4.15)$$

$$\frac{\partial \tau_{xx}}{\partial \mathbf{n}} = \frac{\partial \tau_{yy}}{\partial \mathbf{n}} = \frac{\partial \tau_{zz}}{\partial \mathbf{n}} = \frac{\partial \tau_{xy}}{\partial \mathbf{n}} = \frac{\partial \tau_{xz}}{\partial \mathbf{n}} = \frac{\partial \tau_{yz}}{\partial \mathbf{n}} = 0 \quad \text{on } \partial\Omega_{out}. \quad (4.16)$$

4.4 The High Weissenberg Number Problem

In all published work researchers find that beyond a critical Weissenberg number numerical simulations fail. This failure is known as the high Weissenberg number problem (HWNP). Although, the critical Weissenberg number is usually frustratingly low. The nonlinearity of the governing equations, which becomes increasingly dominant with increasing Weissenberg number, has a strong impact on the performance and stability of numerical methods. Additionally, in view of the nonlinearity of the governing equations, it is not surprising that no complete mathematical theory is available on the existence and uniqueness of viscoelastic flows. That means one might attempt to compute an inexistent or non-unique solution to a problem. Nevertheless, it is often the case that critical Weissenberg numbers observed at the discrete level are numerical artefacts and not a limitation of the model [50]. An attempt to compute an inexistent or non-unique solution would be expected to manifest itself by occurring at a value Wi_{crit} to which one can demonstrate convergence with mesh refinement. However, critical values of the Weissenberg number have often been seen to be mesh dependent. Keunings [39] showed that the attainable Weissenberg number reduces with mesh refinement.

One reason why mesh refinement decreases the attainable Weissenberg number is that viscoelastic models may show loss of evolution. The loss of evolution is an instability in which short-wave disturbances sharply increase in amplitude. Joseph and Saut [36] and Joseph et al. [35] showed that viscoelastic models with zero Newtonian viscosity may show loss of evolution in time-dependent problems. In general, this instability occurs when certain stresses exceed critical values. Therefore, numerical algorithms may blow up once the Weissenberg number reaches a sufficiently large value and the problem will be exacerbated with mesh refinement [40]. This is a severe problem since it is no longer true that convergence of the discrete solution can be achieved, as the mesh is refined. Joseph and Saut [36] showed that the UCM model and models with a Newtonian component do not show this instability. For models with a Newtonian component, the elliptic term prevents the onset of the instability. The UCM model cannot show any loss of evolution either, because the positive definiteness of the tensor

$$\boldsymbol{\tau}_A = \boldsymbol{\tau} + \frac{(1 - \beta)}{Wi} \mathbf{I} \quad (4.17)$$

prevents it. The positive definiteness of the tensor $\boldsymbol{\tau}_A$ is also an important property for the Oldroyd-B model because it prevents the exponential growth of the solution for finite wave numbers [50]. One might think that by using models with a Newtonian stress component or the UCM model one might avoid any difficulties with short wave disturbances in time dependent calculations, but numerical errors can cause the loss of evolution at the discrete level [50]. For example for the UCM and the Oldroyd-B model the positive definiteness of the tensor $\boldsymbol{\tau}_A$ might be lost at the discrete level in regions of high stress gradients as observed by Dupret et al. [21]. Stabilization techniques introducing a change of variables to enhance the elliptic character of the momentum equation by making the elliptic operator as large as possible, such as elastic viscous split stress (EVSS) [51] and adaptive viscoelastic stress splitting (AVSS) [65], have been shown to improve the numerical stability for steady problems. However, they may pollute the accuracy of transient flow calculations.

Transient flow calculations have to cope with additional restrictions on the attainable Weissenberg number in comparison to steady state algorithms [25]. In a steady state algorithm

the system

$$\mathbf{Ax} = \mathbf{b} \quad (4.18)$$

can be solved if $\det \mathbf{A} \neq 0$, no matter what the eigenvalues of \mathbf{A} are. In time dependent simulations the system

$$\frac{\partial \mathbf{x}}{\partial t} + \mathbf{Ax} = \mathbf{b} \quad (4.19)$$

has a steady state solution if $\text{Re}(\sigma) < 0$, in which σ is an eigenvalue of \mathbf{A} . For eigenvalues with $\text{Re}(\sigma) \geq 0$ instabilities occur and no steady state solution can be reached. Keiller [38] showed that for the planar Couette flow of an UCM and an Oldroyd-B fluid the requirement $\text{Re}(\sigma) < 0$ depends on the grid aspect ratio $\Delta y / \Delta x$. If the wrong aspect ratio is chosen, eigenvalues with $\text{Re}(\sigma) \geq 0$ might appear. Keiller showed that this leads to the instability criterion

$$\text{Wi}_{\text{crit}} \sim \left(\frac{\Delta y}{\Delta x} \right), \quad (4.20)$$

where Δx and Δy are the resolution scales of the computational grid in the streamwise and cross-stream directions respectively. This scaling appears to hold even for complex flows. Smith et al. [66, 64] observed the same dependence of the critical Weissenberg number on the aspect ratio $\Delta y / \Delta x$ in transient calculations of a flow around a cylinder of an Oldroyd-B fluid.

Renardy [61] pointed out that the difficulty of resolving high-stress gradients, arising near solid boundaries and near corner singularities, puts severe limitations on successful numerical simulations. The cause for the steep stress gradients near solid boundaries is the existence of boundary layers. The boundary layers occur because of the no-slip condition. The velocity and all its tangential derivatives vanish at the wall, thus making the convected derivative terms disappear. However, these terms enter the dominant balance in a very short distance away from the wall. As a consequence the stress behaviour in a thin layer close to the wall substantially differs from the behaviour at a farther distance. This is a transition from viscometric behaviour near the boundary to a region where the convected derivative dominates. Renardy showed that the thickness of the boundary layers decreases with increasing Weissenberg number. For the UCM model the boundary layer thickness is of order Wi^{-1} , for the PTT model, it is of order $\text{Wi}^{-1/3}$, and for the Giesekus model, it is of order $\text{Wi}^{-1/2}$. Therefore, compared to the UCM model, the PTT and the Giesekus model have boundary layers that sharpen much less rapidly as the Weissenberg number increases. Numerical simulations with the PTT or Giesekus model are indeed seen to be successful for much higher Weissenberg numbers than simulations with the UCM model.

The numerical solution of viscoelastic flows in domains involving corner singularities is very problematic. Because of the hyperbolic nature of the constitutive equations discretization errors can be propagated along characteristics, i.e. along the streamlines [50]. Therefore, numerical errors at the corner singularity are propagated downstream. Additionally, Renardy [61] showed that the solution of an UCM fluid in the downstream region of a corner singularity develops non-integrable stress singularities. These stress singularities lead to an instability, which causes a stress growth downstream. The source of this instability is a feature of the equations themselves and has nothing to do with the choice of the numerical method. But the instability magnifies discretization errors [61]. A downstream growth of errors is also observed for the Oldroyd-B model [24]. For the PTT model, Renardy [60] did not observe a downstream growth of errors. The reason for this might be that the boundary layers in the

PTT model have a different scaling and are much wider than in the UCM model. As a result, particles enter the boundary layer and stress relaxation takes over before the downstream instability has had a chance to fully manifest itself.

Fattal and Kupferman [22, 23] identified a stability criterion on the mesh size Δx :

$$\Delta x \leq \frac{|\mathbf{u}|}{2\sqrt{-\det(\nabla\mathbf{u})} - \text{Wi}^{-1}}. \quad (4.21)$$

This stability condition is very restrictive when convection is weak and in the presence of large deformation rates. Therefore, this criterion is easily violated in regions near stagnation points and strong deformation rates (e.g. near geometric singularities). Thus, these regions are prone to such a numerical instability. Fattal and Kupferman argued that the stability criterion arises from the fact that the stress experiences a combination of deformation and convection, which gives rise to steep exponential profiles. Even for moderate Weissenberg numbers, these spatial profiles are poorly approximated by numerical schemes, which are based on polynomial interpolation. To alleviate the spatial mesh restriction, Fattal and Kupferman proposed a reformulation of the constitutive equations. Since the severe restriction on the mesh size is due to the inadequacy of polynomial interpolation to approximate exponential profiles, they proposed to make a change of variables into new variables that scale logarithmically with the stress. However, we cannot just take the logarithm of the stress tensor. In order for the logarithm of a second-rank tensor to exist, the tensor needs to be positive definite. Therefore, the stress tensor $\boldsymbol{\tau}$ needs to remain strictly positive definite, which cannot be guaranteed. A physical quantity, directly related to the stress, that preserves positive definiteness is the conformation tensor \mathbf{c} [31]. The **conformation tensor** \mathbf{c} is a dimensionless measure for the deformation, which is given by

$$\mathbf{c} = \frac{\langle \mathbf{Q}\mathbf{Q} \rangle}{\langle Q^2 \rangle_{eq}}, \quad (4.22)$$

where \mathbf{Q} is the end-to-end vector of a polymer chain and $\langle \cdot \rangle$ denotes an average over the distribution space. Hence, Fattal and Kupferman [22, 23] proposed the change of variables $\boldsymbol{\psi} = \log(\mathbf{c})$ and called the resulting equations the **log-conformation representation**. Gerritsma [25] noted that for transient viscoelastic calculations the numerical time-step required to obtain bounded solutions decreases rapidly near the limiting Weissenberg number.

Chapter 5

Numerical Method

This chapter deals with the numerical solution of the governing equations. First, we present a Chorin-type explicit project method. Then, we discuss the time-step restrictions resulting from the explicit treatment of the equations. Since the time-step restriction for the diffusive terms leads to very small time-steps for low Reynolds number flows, we also introduce a semi-implicit projection method. Afterwards, we discuss the spatial discretization on a staggered grid and the discrete boundary values.

5.1 Temporal Discretization

5.1.1 Explicit Projection Method

The solution of the equation system (4.4) is not easy to obtain because naive solution of the equations leads to a velocity field which is in general not divergence free. To avoid this problem, we solve the system of equations (4.4) by employing a Chorin-type projection method (Chorin [15], Temam [68]) consisting of the following steps:

Step 1 Solve the constitutive equations for the elastic stresses using the forward Euler method

$$\begin{aligned} \text{Wi} \left(\frac{\boldsymbol{\tau}^{n+1} - \boldsymbol{\tau}^n}{\delta t} \right) &= (1 - \beta)2\mathbf{D}^n - f(\text{tr} \boldsymbol{\tau}^n)\boldsymbol{\tau}^n - \text{Wi} (\mathbf{u} \cdot \nabla \boldsymbol{\tau}^n - \nabla \mathbf{u}^n \cdot \boldsymbol{\tau}^n - \boldsymbol{\tau}^n \cdot (\nabla \mathbf{u}^T)^n) \\ &\quad - \text{Wi} \xi(\boldsymbol{\tau}^n \cdot \mathbf{D}^n + \mathbf{D}^n \cdot \boldsymbol{\tau}^n). \end{aligned} \quad (5.1)$$

Step 2 Solve the momentum equations for an intermediate velocity field \mathbf{u}^* ignoring the incompressibility constrained

$$\text{Re} \left(\frac{\mathbf{u}^* - \mathbf{u}^n}{\delta t} \right) = \beta \Delta \mathbf{u}^n - \text{Re} \mathbf{u}^n \cdot \nabla \mathbf{u}^n + \nabla \cdot \boldsymbol{\tau}^n + \frac{1}{\text{Fr}^2} \mathbf{g}. \quad (5.2)$$

Step 3 Project the intermediate velocity field onto the incompressible velocity field \mathbf{u}^{n+1}

$$\left(\frac{\mathbf{u}^{n+1} - \mathbf{u}^*}{\delta t} \right) = -\nabla p^{n+1}, \quad (5.3)$$

$$\nabla \cdot \mathbf{u}^{n+1} = 0. \quad (5.4)$$

In Step 3, we project the velocity field \mathbf{u}^* onto a divergence free velocity field by taking the divergence of (5.3) and by enforcing $\nabla \cdot \mathbf{u}^{n+1} = 0$. This leads to a Poisson equation for the pressure

$$\Delta p^{n+1} = \left(\frac{1}{\delta t} \right) \nabla \cdot \mathbf{u}^*, \quad (5.5)$$

which we solve iteratively under adequate boundary conditions by methods like SOR, Red-Black Gauss Seidel or BiCGStab [17]. Finally, the new divergence free velocity field is given by

$$\mathbf{u}^{n+1} = \mathbf{u}^* - \delta t \nabla p^{n+1}. \quad (5.6)$$

We obtain the boundary condition for the pressure by taking the projection of (5.3) in the direction of the unit outward normal \mathbf{n} to the boundary $\partial\Omega$. This leads to a Neumann boundary condition for the pressure

$$\frac{\partial p^{n+1}}{\partial \mathbf{n}} = \nabla p^{n+1} \cdot \mathbf{n} = -\frac{1}{\delta t} (\mathbf{u}^{n+1} - \mathbf{u}^*) \cdot \mathbf{n} \text{ on } \partial\Omega. \quad (5.7)$$

The Neumann problem (5.5) - (5.7) is solvable if the compatibility condition

$$\int_{\Omega} \nabla \cdot \mathbf{u}^* dV = - \int_{\partial\Omega} (\mathbf{u}^{n+1} - \mathbf{u}^*) \cdot \mathbf{n} dS \quad (5.8)$$

is satisfied. Then this solution is unique up to an additive constant. We fix this constant by setting

$$\int_{\Omega} p^{n+1} dV = 0. \quad (5.9)$$

If the domain Ω is a bounded domain on which velocity boundary conditions are specified, the compatibility condition is satisfied, since

$$\int_{\partial\Omega} \mathbf{u}^{n+1} \cdot \mathbf{n} dS = \int_{\Omega} \nabla \cdot \mathbf{u}^{n+1} dV = 0. \quad (5.10)$$

Now, if we set on the boundary

$$\mathbf{u}^* = \mathbf{u}^{n+1} \quad \text{on } \partial\Omega, \quad (5.11)$$

we obtain homogeneous Neumann boundary conditions for the pressure

$$\frac{\partial p^{n+1}}{\partial \mathbf{n}} = -\frac{\mathbf{u}^{n+1} - \mathbf{u}^*}{\delta t} \cdot \mathbf{n} = 0 \quad \text{on } \partial\Omega. \quad (5.12)$$

This method is first-order accurate in time.

5.1.2 Time-Step Control

Since the first-order method (5.1) - (5.4) is explicit, the computational cost per time-step is relatively low. However, the explicit treatment leads to time-step restrictions for the convective and diffusive terms. These restrictions, ensuring the numerical stability of the method, can be obtained by a stability analysis of the linearized equations. Trebotich et al. [69] find the restriction of the time step for the convective terms using the Oldroyd-B model for the x -component to be

$$\delta t_x < \frac{\Delta x}{\max_{i,j,k} \left[|u| + \sqrt{2(\tau_{xx} + \frac{1-\beta}{\text{We}})/\text{Re}} \right]}, \quad (5.13)$$

where $\max_{i,j,k}[\cdot]$ denotes the discrete maximum value over all grid cells and $|\cdot|$ denotes the absolute value of the velocity component. The other components in the y and z -direction are obtained in the same manner, so that the total restriction for the convective terms is given by

$$\delta t_c = \min[\delta t_x, \delta t_y, \delta t_z]. \quad (5.14)$$

This restriction, known as Courant-Friedrich-Levy (CFL) condition, establishes that convection can take effect only on one further grid cell per time step. We use this restriction in our computations also for the PTT model, because the PTT model generally behaves stable in wider parameter regimes in numerical calculations than the Oldroyd-B model (Alves [3]). Similarly, we restrict the diffusion to act no further than one grid cell per time-step (Wesseling [74])

$$\delta t_d < \left[\frac{\beta}{\text{Re}} \left(\frac{2}{(\Delta x)^2} + \frac{2}{(\Delta y)^2} + \frac{2}{(\Delta z)^2} \right) \right]^{-1}. \quad (5.15)$$

Additionally, if gravity acts on the flow (Croce [17]), a further time-step restriction is given by

$$\delta t_{g_x} < \left[\frac{\max_{i,j,k} [|u|]}{\Delta x} + \sqrt{\left(\frac{\max_{i,j,k} [|u|]}{\Delta x} \right)^2 + \frac{4|g_x|}{\Delta x}} \right]^{-1}. \quad (5.16)$$

In the numerical simulation of viscoelastic fluids, we mainly want to investigate flow situations, which are dominated by elastic forces and not by inertial forces, i.e. we want to investigate flows with a high elasticity number $El = \frac{\text{Wi}}{\text{Re}}$. Therefore, we usually deal with low Reynolds number flows ($\text{Re} \approx 1$). In these flows, the time-step restriction for the diffusive terms forces us to use very small time-steps. To alleviate this restriction, we need to treat the diffusive terms in the momentum equation implicitly.

5.1.3 Semi-Implicit Projection Method

Details on the following projection method may be found in Klitz [42]. We use a Crank-Nicolson scheme for the discretization of the diffusive terms

$$\frac{\mathbf{u}^{n+1} - \mathbf{u}^n}{\delta t} = -\nabla p + \underbrace{\frac{\beta}{2\text{Re}} \Delta(\mathbf{u}^{n+1} + \mathbf{u}^n)}_{\text{Crank-Nicolson}} - (\mathbf{u}^n \cdot \nabla) \mathbf{u}^n + \frac{1}{\text{Re}} \nabla \cdot \boldsymbol{\tau}^n + \frac{1}{\text{Fr}^2} \mathbf{g},$$

and we include the pressure in the equations for the intermediate velocity field by a pressure correction scheme based on Bell [4]. The intermediate velocity field \mathbf{u}^* gives a better approximation of the actual velocity field \mathbf{u}^{n+1} , when the pressure term is included in Step 2 of the projection method. Then, the projection method can be divided into the following steps:

Step 1 Solve the constitutive equations for the elastic stresses using the forward Euler method

$$\begin{aligned} \boldsymbol{\tau}^{n+1} = & \left(1 - \frac{\delta t}{\text{Wi}} f(\text{tr } \boldsymbol{\tau})\right) \boldsymbol{\tau}^n + \delta t \left(\frac{2(1-\beta)}{\text{Wi}} \mathbf{D}^n - (\mathbf{u}^n \cdot \nabla) \boldsymbol{\tau}^n + \nabla \mathbf{u}^n \cdot \boldsymbol{\tau}^n + \boldsymbol{\tau}^n \cdot (\nabla \mathbf{u}^T)^n \right. \\ & \left. - \delta t \xi(\boldsymbol{\tau}^n \cdot \mathbf{D}^n + \mathbf{D}^n \cdot \boldsymbol{\tau}^n) \right). \end{aligned} \quad (5.17)$$

Step 2 Calculate the intermediate velocity field \mathbf{u}^*

$$\left(\mathbf{I} - \frac{\delta t \beta}{2\text{Re}} \Delta\right) \mathbf{u}^* = \mathbf{u}^n - \delta t \cdot \left[(\mathbf{u}^n \cdot \nabla) \mathbf{u}^n + \nabla p^{n-\frac{1}{2}} - \frac{\beta}{2\text{Re}} \Delta \mathbf{u}^n - \frac{1}{\text{Re}} \nabla \cdot \boldsymbol{\tau}^n + \frac{1}{\text{Fr}^2} \mathbf{g} \right]. \quad (5.18)$$

Step 3 Solve the Poisson equation for the pressure correction ϕ and calculate \mathbf{u}^{n+1}

$$\Delta \phi^{n+1} = \left(\frac{1}{\delta t}\right) \nabla \cdot \mathbf{u}^*, \quad (5.19)$$

$$\mathbf{u}^{n+1} = \mathbf{u}^* - \delta t \nabla \phi^{n+1}. \quad (5.20)$$

Step 4 Calculate the new pressure field following Brown [11]

$$p^{n+\frac{1}{2}} = p^{n-\frac{1}{2}} + \phi^{n+1} - \frac{\delta t \beta}{2\text{Re}} \Delta \phi^{n+1}. \quad (5.21)$$

The equation (5.21) is found by a backward substitution of \mathbf{u}^* from equation (5.20) into equation (5.18). The implicit treatment of the diffusive terms leads to three modified Helmholtz equations (5.18), which we solve by an SSOR Preconditioned Conjugate Gradient Method (Klitz [42]). In the explicit projection method, setting $\mathbf{u}^*|_{\partial\Omega} = \mathbf{u}^n|_{\partial\Omega}$ can be considered as a sufficient approximation of $\mathbf{u}^*|_{\partial\Omega} = \mathbf{u}^{n+1}|_{\partial\Omega}$. However, this approximation is not sufficient, when dealing with the Helmholtz equations $(\mathbf{I} - (\delta t \beta / 2\text{Re}) \Delta) \mathbf{u}^* = r h s$. Instead, we discretize the boundary conditions by manipulation of the appropriate entries in the matrix $(\mathbf{I} - (\delta t \beta / 2\text{Re}) \Delta)$. Therefore, we impose no-slip boundary conditions $\mathbf{u}^* = \mathbf{0}$ at walls, inflow boundary conditions $\mathbf{u}^* = \mathbf{u}_{in}$ and outflow boundary conditions $\nabla \mathbf{u}^* \cdot \mathbf{n} = \mathbf{0}$ in the matrix entries as described in detail by Klitz [42].

With this method, we can use larger time-steps for low Reynolds number flows and obtain results much faster than in the explicit case.

5.2 Spatial Discretization

5.2.1 Staggered Grid

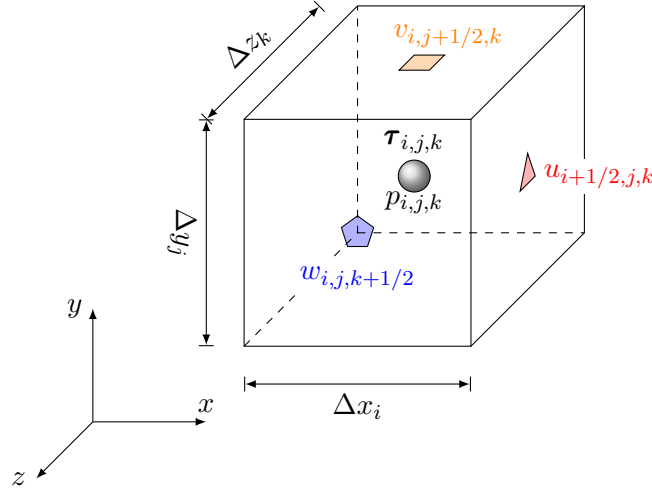


Figure 5.1: Staggered grid

We divide our domain Ω into rectangular subdomains called cells and position our variables on a staggered grid. We position the pressure $p_{i,j,k}$ at the centre of the cells, as well as all six elastic stress tensor components $\tau_{i,j,k}$, while we position the velocities $u_{i+1/2,j,k}$, $v_{i,j+1/2,k}$, $w_{i,j,k+1/2}$ at the centre of the cell faces as shown in Figure 5.1. This kind of staggering leads to a strong coupling between pressure and velocities and therefore prevents spurious modes in the computed pressure known as checkerboard type oscillations. This can be seen in the following way (Gerritsma [25]).

Example 5.1: Consider a square domain Ω in two space dimensions divided into a number of uniform cells with grid spacing Δx . The equations we want to solve are

$$\frac{\partial \mathbf{u}}{\partial t} + \nabla p = f, \quad (5.22)$$

$$\nabla \cdot \mathbf{u} = 0. \quad (5.23)$$

The elliptic equation to be solved is then given by

$$\Delta p = \nabla \cdot f. \quad (5.24)$$

Now, suppose we choose all the unknowns at the cell centres. Then, the discretization of equation (5.22) in the point \times (see Figure 5.2(a)) identified with (i, j) is given by

$$\frac{u_{i,j}^{n+1} - u_{i,j}^n}{\delta t} + \frac{p_{i+1,j} - p_{i-1,j}}{2\Delta x} = f_{i,j}^{(1)}, \quad (5.25)$$

$$\frac{v_{i,j}^{n+1} - v_{i,j}^n}{\delta t} + \frac{p_{i,j+1} - p_{i,j-1}}{2\Delta x} = f_{i,j}^{(2)}. \quad (5.26)$$

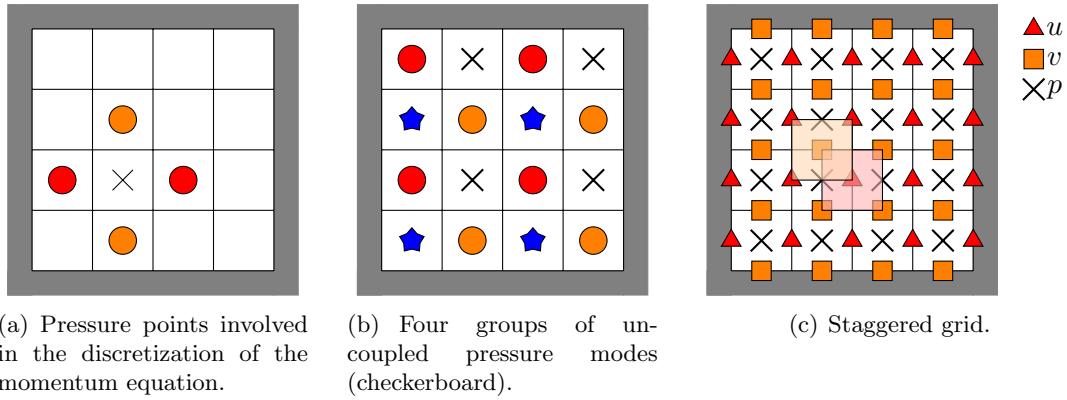


Figure 5.2: Spurious pressure modes.

It is possible to construct a function $p \neq \text{constant}$ which satisfies that the discrete approximation of ∇p , denoted by $\nabla_h p$, is zero. We can add such a solution \tilde{p} to p and this change will be invisible in the momentum equation. Then, the elliptic equation (5.24) has $\dim(\text{Null}(\Delta)) > 1$, which results in a non-uniqueness of the pressure solution. This leads to unwanted oscillations in the discrete pressure solution known as checkerboard oscillations. For example, the “checkerboard” solution $\tilde{p} = c_1$ at \times , $\tilde{p} = c_2$ at \star , $\tilde{p} = c_3$ at \bullet and $\tilde{p} = c_4$ at \blacksquare , as shown in Figure 5.2(b), satisfies $\nabla_h p = 0$. If we choose to position the variables on a staggered grid like shown in Figure 5.2(c), we have

$$\frac{u_{i+1/2,j}^{n+1} - u_{i+1/2,j}^n}{\delta t} + \frac{p_{i+1,j} - p_{i,j}}{\Delta x} = f_{i+1/2,j}^{(1)}, \quad (5.27)$$

$$\frac{v_{i,j+1/2}^{n+1} - v_{i,j+1/2}^n}{\delta t} + \frac{p_{i,j+1} - p_{i,j}}{\Delta x} = f_{i,j+1/2}^{(2)}, \quad (5.28)$$

so that

$$\nabla_h p = 0 \Leftrightarrow p = \text{constant}. \quad (5.29)$$

This leads to a discrete elliptic equation in which all pressure unknowns are connected, and the occurrence of a pressure checkerboard like in Figure 5.2(b) is avoided. Since the elliptic equation (5.24) due to incompressibility is also present in the computation of viscoelastic fluids, it seems reasonable to locate the velocity and pressure unknowns on a staggered grid.

5.2.2 Discretized Equations

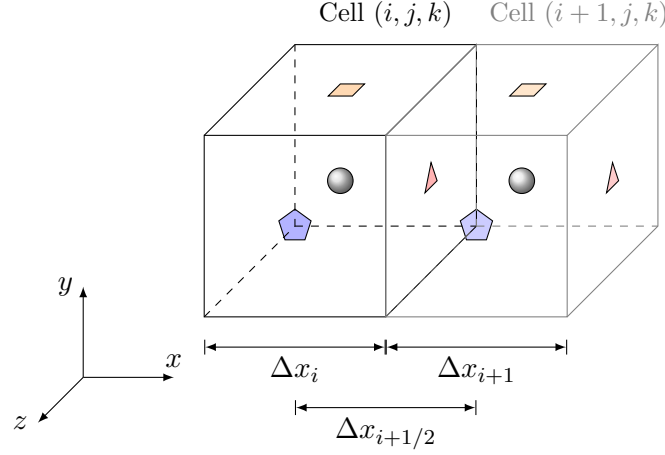


Figure 5.3: Notation of grid spacing.

We denote the discretization at the position at the cell centre by $[\cdot]_{i,j,k}$, at the centre of the left/right cell surface by $[\cdot]_{i\pm 1/2,j,k}$, at the centre of the bottom/top cell surface by $[\cdot]_{i,j,\pm 1/2,k}$, and at the centre of the front/back cell surface by $[\cdot]_{i,j,k\pm 1/2}$. Further, we use the notation

$$\Delta x_i = x_i - x_{i-1} \quad \text{and} \quad \Delta x_{i+1/2} = (\Delta x_i + \Delta x_{i+1})/2. \quad (5.30)$$

We discretize all spatial derivatives using central differences, except for the convective terms, denoted by $\mathcal{C}(\cdot)$, in the momentum equations and in the constitutive equations for the elastic stress. Here, the convective terms are approximated by high order schemes such as SMART, VONOS, ENO or WENO. Details of the implementation of these schemes can be found in Croce [17]. We will now give some discretization examples of the for the steps of the explicit projection method. The discretization formulas for the semi-implicit projection method are developed in the same manner. The xx -component τ^{xx} and the xy -component τ^{xy} of Step 1 of the projection method are approximated by

$$\begin{aligned} \tau_{i,j,k}^{xx(n+1)} = & \left(1 - \frac{\delta t}{\text{Wi}} f(\text{tr} \boldsymbol{\tau}_{i,j,k}^{(n)}) \right) \tau_{i,j,k}^{xx(n)} \\ & + \delta t \left\{ \frac{2(1-\beta)}{\text{Wi}} \left[\frac{\partial u}{\partial x} \right]_{i,j,k}^{(n)} - \mathcal{C} \left(u \frac{\partial \tau^{xx}}{\partial x} \right)_{i,j,k}^{(n)} - \mathcal{C} \left(v \frac{\partial \tau^{xx}}{\partial y} \right)_{i,j,k}^{(n)} - \mathcal{C} \left(w \frac{\partial \tau^{xx}}{\partial z} \right)_{i,j,k}^{(n)} \right\} \\ & - \delta t \left\{ 2(\xi-1) \left[\frac{\partial u}{\partial x} \right]_{i,j,k}^{(n)} \tau_{i,j,k}^{xx(n)} + \left[(\xi-2) \left[\frac{\partial u}{\partial y} \right]_{i,j,k}^{(n)} + \xi \left[\frac{\partial v}{\partial x} \right]_{i,j,k}^{(n)} \right] \tau_{i,j,k}^{xy(n)} \right\} \\ & - \delta t \left\{ \left[(\xi-2) \left[\frac{\partial u}{\partial z} \right]_{i,j,k}^{(n)} + \xi \left[\frac{\partial w}{\partial x} \right]_{i,j,k}^{(n)} \right] \tau_{i,j,k}^{xz(n)} \right\}, \end{aligned} \quad (5.31)$$

$$\begin{aligned}
\tau_{i,j,k}^{xy(n+1)} &= \left(1 - \frac{\delta t}{\text{Wi}} f(\text{tr} \boldsymbol{\tau}_{i,j,k}^{(n)})\right) \tau_{i,j,k}^{xy(n)} \\
&+ \delta t \left\{ \frac{(1-\beta)}{\text{Wi}} \left(\left[\frac{\partial u}{\partial y} \right]_{i,j,k}^{(n)} + \left[\frac{\partial v}{\partial x} \right]_{i,j,k}^{(n)} \right) - \mathcal{C} \left(u \frac{\partial \tau^{xy}}{\partial x} \right)_{i,j,k}^{(n)} - \mathcal{C} \left(v \frac{\partial \tau^{xy}}{\partial y} \right)_{i,j,k}^{(n)} - \mathcal{C} \left(w \frac{\partial \tau^{xy}}{\partial z} \right)_{i,j,k}^{(n)} \right\} \\
&+ \delta t \left\{ (\xi - 1) \left[\left[\frac{\partial u}{\partial x} \right]_{i,j,k}^{(n)} + \left[\frac{\partial v}{\partial y} \right]_{i,j,k}^{(n)} \right] \tau_{i,j,k}^{xy(n)} + \frac{1}{2} \left[(\xi - 2) \left[\frac{\partial u}{\partial y} \right]_{i,j,k}^{(n)} + \xi \left[\frac{\partial v}{\partial x} \right]_{i,j,k}^{(n)} \right] \tau_{i,j,k}^{yy(n)} \right\} \\
&+ \delta t \left\{ \frac{1}{2} \left[(\xi - 2) \left[\frac{\partial u}{\partial z} \right]_{i,j,k}^{(n)} + \xi \left[\frac{\partial w}{\partial x} \right]_{i,j,k}^{(n)} \right] \tau_{i,j,k}^{yz(n)} \right\} \\
&+ \delta t \left\{ \frac{1}{2} \left[(\xi - 2) \left[\frac{\partial v}{\partial x} \right]_{i,j,k}^{(n)} + \xi \left[\frac{\partial u}{\partial y} \right]_{i,j,k}^{(n)} \right] \tau_{i,j,k}^{xx(n)} + \frac{1}{2} \left[(\xi - 2) \left[\frac{\partial v}{\partial z} \right]_{i,j,k}^{(n)} + \xi \left[\frac{\partial w}{\partial y} \right]_{i,j,k}^{(n)} \right] \tau_{i,j,k}^{xz(n)} \right\}, \tag{5.32}
\end{aligned}$$

where e.g.

$$\left[\frac{\partial u}{\partial x} \right]_{i,j,k} = \frac{u_{i+1/2,j,k} - u_{i-1/2,j,k}}{\Delta x_i}, \tag{5.33}$$

$$\left[\frac{\partial u}{\partial y} \right]_{i,j,k} = \frac{u_{i,j+1/2,k} - u_{i,j-1/2,k}}{\Delta y_i}, \tag{5.34}$$

$$\left[\frac{\partial u}{\partial z} \right]_{i,j,k} = \frac{u_{i,j,k+1/2} - u_{i,j,k-1/2}}{\Delta z_i}. \tag{5.35}$$

The terms, which are not defined at the needed cell positions are obtained by linear interpolation that is e.g.

$$\begin{aligned}
u_{i,j+1/2,k} &= \frac{(\Delta y_j u_{i+1/2,j+1,k} + \Delta y_{j+1} u_{i+1/2,j,k}) \Delta x_{i-1/2}}{(\Delta y_j + \Delta y_{j+1})(\Delta x_{i-1/2} + \Delta x_{i+1/2})} \\
&+ \frac{(\Delta y_j u_{i-1/2,j+1,k} + \Delta y_{j+1} u_{i-1/2,j,k}) \Delta x_{i+1/2}}{(\Delta y_j + \Delta y_{j+1})(\Delta x_{i-1/2} + \Delta x_{i+1/2})}. \tag{5.36}
\end{aligned}$$

The discretization of the momentum equation for the intermediate velocity field u^* is given by

$$\begin{aligned}
u_{i+1/2,j,k}^* &= u_{i+1/2,j,k}^{(n)} + \delta t \left\{ \mathcal{C} \left(\frac{\partial(u^2)}{\partial x} \right)_{i+1/2,j,k}^{(n)} + \mathcal{C} \left(\frac{\partial(uv)}{\partial y} \right)_{i+1/2,j,k}^{(n)} + \mathcal{C} \left(\frac{\partial(uw)}{\partial z} \right)_{i+1/2,j,k}^{(n)} \right\} \\
&+ \delta t \left\{ \frac{1}{\text{Re}} \beta \left[\left[\frac{\partial^2 u}{\partial x^2} \right]_{i+1/2,j,k} + \left[\frac{\partial^2 u}{\partial y^2} \right]_{i+1/2,j,k} + \left[\frac{\partial^2 u}{\partial z^2} \right]_{i+1/2,j,k} \right] \right\} \\
&+ \delta t \left\{ \frac{1}{\text{Re}} \left[\left[\frac{\partial \tau^{xx}}{\partial x} \right]_{i+1/2,j,k}^{(n)} + \left[\frac{\partial \tau^{xy}}{\partial y} \right]_{i+1/2,j,k}^{(n)} + \left[\frac{\partial \tau^{xz}}{\partial z} \right]_{i+1/2,j,k}^{(n)} \right] \right\}. \tag{5.37}
\end{aligned}$$

Here, the diffusive terms are approximated by

$$\left[\frac{\partial^2 u}{\partial x^2} \right]_{i+1/2,j,k} = \frac{1}{\Delta x_{i+1/2}} \left(\frac{u_{i+3/2,j,k} - u_{i+1/2,j,k}}{\Delta x_{i+1}} - \frac{u_{i+1/2,j,k} - u_{i-1/2,j,k}}{\Delta x_i} \right), \quad (5.38)$$

$$\left[\frac{\partial^2 u}{\partial y^2} \right]_{i+1/2,j,k} = \frac{1}{\Delta y_j} \left(\frac{u_{i+1/2,j+1,k} - u_{i+1/2,j,k}}{\Delta y_{j+1/2}} - \frac{u_{i+1/2,j,k} - u_{i+1/2,j-1,k}}{\Delta y_{j-1/2}} \right). \quad (5.39)$$

And the terms involving the components of the elastic stress tensor are approximated by

$$\left[\frac{\partial \tau^{xx}}{\partial x} \right]_{i+1/2,j,k} = \frac{\tau_{i+1,j,k}^{xx} - \tau_{i,j,k}^{xx}}{\Delta x_{i+1/2}}, \quad (5.40)$$

$$\left[\frac{\partial \tau^{xy}}{\partial y} \right]_{i+1/2,j,k} = \frac{\tau_{i+1/2,j+1/2,k}^{xy} - \tau_{i+1/2,j-1/2,k}^{xy}}{\Delta y_i}, \quad (5.41)$$

$$\left[\frac{\partial \tau^{xz}}{\partial z} \right]_{i+1/2,j,k} = \frac{\tau_{i+1/2,j,k+1/2}^{xy} - \tau_{i+1/2,j,k-1/2}^{xy}}{\Delta z_i}, \quad (5.42)$$

where terms like $\tau_{i+1/2,j+1/2,k}^{xy}$ are obtained by linear interpolation, i.e.

$$\begin{aligned} \tau_{i+1/2,j+1/2,k}^{xy} &= \frac{(\Delta y_j \tau_{i,j+1,k}^{xy} + \Delta y_{j+1} \tau_{i,j,k}^{xy}) \Delta x_{i+1}}{(\Delta y_j + \Delta y_{j+1})(\Delta x_i + \Delta x_{i+1})} \\ &+ \frac{(\Delta y_j \tau_{i+1,j+1,k}^{xy} + \Delta y_{j+1} \tau_{i+1,j,k}^{xy}) \Delta x_i}{(\Delta y_j + \Delta y_{j+1})(\Delta x_i + \Delta x_{i+1})}. \end{aligned} \quad (5.43)$$

The Laplacian for the pressure in step 3 is discretized at cell centres

$$\begin{aligned} [\Delta p]_{i,j,k}^{(n+1)} &= \left[\frac{\partial^2 p}{\partial x^2} \right]_{i,j,k}^{(n+1)} + \left[\frac{\partial^2 p}{\partial y^2} \right]_{i,j,k}^{(n+1)} + \left[\frac{\partial^2 p}{\partial z^2} \right]_{i,j,k}^{(n+1)} \\ &= \frac{1}{\Delta x_i} \left(\frac{p_{i+1,j,k}^{(n+1)} - p_{i,j,k}^{(n+1)}}{\Delta x_{i+1/2}} - \frac{p_{i,j,k}^{(n+1)} - p_{i-1,j,k}^{(n+1)}}{\Delta x_{i-1/2}} \right) \\ &+ \frac{1}{\Delta y_i} \left(\frac{p_{i,j+1,k}^{(n+1)} - p_{i,j,k}^{(n+1)}}{\Delta y_{i+1/2}} - \frac{p_{i,j,k}^{(n+1)} - p_{i,j-1,k}^{(n+1)}}{\Delta y_{i-1/2}} \right) \\ &+ \frac{1}{\Delta z_i} \left(\frac{p_{i,j,k+1}^{(n+1)} - p_{i,j,k}^{(n+1)}}{\Delta z_{i+1/2}} - \frac{p_{i,j,k}^{(n+1)} - p_{i,j,k-1}^{(n+1)}}{\Delta z_{i-1/2}} \right). \end{aligned} \quad (5.44)$$

The right hand side of the Poisson equation is approximated by

$$\begin{aligned} \left[\frac{\nabla \cdot \mathbf{u}^*}{\delta t} \right]_{i,j,k} &= \frac{1}{\delta t} \left(\left[\frac{\partial u^*}{\partial x} \right]_{i,j,k} + \left[\frac{\partial v^*}{\partial y} \right]_{i,j,k} + \left[\frac{\partial w^*}{\partial z} \right]_{i,j,k} \right) \\ &= \frac{1}{\delta t} \left(\frac{u_{i+1/2,j,k}^* - u_{i-1/2,j,k}^*}{\Delta x_i} + \frac{v_{i,j+1/2,k}^* - v_{i,j-1/2,k}^*}{\Delta y_i} + \frac{w_{i,j,k+1/2}^* - w_{i,j,k-1/2}^*}{\Delta z_i} \right). \end{aligned} \quad (5.45)$$

For the solution of the linear equation arising from the discretization of the pressure Poisson equation, we use iterative solvers such as *SOR*, *Red-Black Gauss Seidel* or *BiCGStab* (Croce [17]). The last step is in discretized form given by

$$u_{i+1/2,j,k}^{n+1} = u_{i+1/2,j,k}^* - \delta t \left(\frac{p_{i+1,j}^{(n+1)} - p_{i,j}^{(n+1)}}{\Delta x_{i+1/2}} \right). \quad (5.46)$$

5.2.3 Discrete Boundary Values

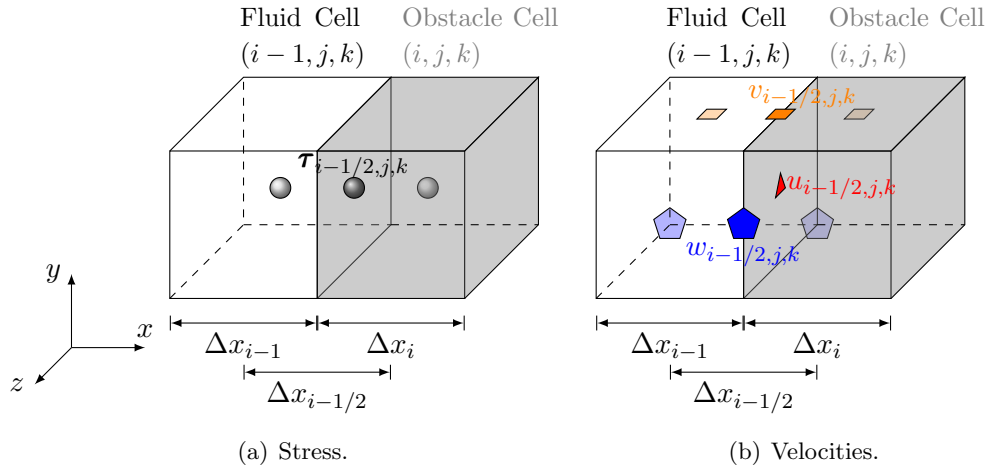


Figure 5.4: Boundary values for an obstacle cell with neighbouring fluid cell at $(i - 1, j, k)$.

In this section, we will present the boundary values for the case of an obstacle cell that has one neighbouring fluid cell at $(i - 1, j, k)$. The boundary values for other configurations can be derived analogously. For obstacle cells adjacent to more than one fluid cell, we obtain the value of the obstacle cell through averaging.

No-Slip Condition

For the no-slip boundary condition, the velocities vanish at the boundary, i.e.

$$u_b = u_{i-1/2,j,k} = 0 \quad , \quad v_b = v_{i-1/2,j,k} = 0 \quad , \quad w_b = w_{i-1/2,j,k} = 0. \quad (5.47)$$

In the case of a fluid cell at $(i - 1, j, k)$, i.e. the boundary surface is parallel to yz -plane, the no-slip condition applied to the velocity field produces

$$\frac{\partial u}{\partial y} = \frac{\partial u}{\partial z} = \frac{\partial v}{\partial y} = \frac{\partial v}{\partial z} = \frac{\partial w}{\partial y} = \frac{\partial w}{\partial z} = 0 \quad (5.48)$$

and using the continuity equation implies that

$$\frac{\partial u}{\partial x} = 0. \quad (5.49)$$

Thus, only the terms $\frac{\partial v}{\partial x}$ and $\frac{\partial w}{\partial x}$ are non-zero. Before we can calculate the elastic stresses at the boundary, we have to evaluate their values at the boundary by linear interpolation

$$\boldsymbol{\tau}_b = \boldsymbol{\tau}_{i-1/2,j,k} = \frac{\Delta x_i \boldsymbol{\tau}_{i-1,j+1,k} + \Delta x_{i-1} \boldsymbol{\tau}_{i,j,k}}{\Delta x_i + \Delta x_{i-1}}. \quad (5.50)$$

Because of the no-slip boundary condition the constitutive equations for the elastic stresses specialize to

$$\begin{aligned} \tau_{i-1/2,j,k}^{xx(n+1)} &= \left(1 - \frac{\delta t}{\text{Wi}} f(\text{tr } \boldsymbol{\tau}_{i-1/2,j,k}^{(n)})\right) \tau_{i-1/2,j,k}^{xx(n)} \\ &\quad - \delta t \left\{ \xi \left[\frac{\partial v}{\partial x} \right]_{i-1/2,j,k}^{(n)} \tau_{i-1/2,j,k}^{xy(n)} + \xi \left[\frac{\partial w}{\partial x} \right]_{i-1/2,j,k}^{(n)} \tau_{i-1/2,j,k}^{xz(n)} \right\}, \\ \tau_{i-1/2,j,k}^{yy(n+1)} &= \left(1 - \frac{\delta t}{\text{Wi}} f(\text{tr } \boldsymbol{\tau}_{i-1/2,j,k}^{(n)})\right) \tau_{i-1/2,j,k}^{yy(n)} - \delta t (\xi - 2) \left[\frac{\partial v}{\partial x} \right]_{i-1/2,j,k}^{(n)} \tau_{i-1/2,j,k}^{xy(n)}, \\ \tau_{i-1/2,j,k}^{zz(n+1)} &= \left(1 - \frac{\delta t}{\text{Wi}} f(\text{tr } \boldsymbol{\tau}_{i-1/2,j,k}^{(n)})\right) \tau_{i-1/2,j,k}^{zz(n)} - \delta t (\xi - 2) \left[\frac{\partial w}{\partial x} \right]_{i-1/2,j,k}^{(n)} \tau_{i-1/2,j,k}^{xz(n)}, \\ \tau_{i-1/2,j,k}^{xy(n+1)} &= \left(1 - \frac{\delta t}{\text{Wi}} f(\text{tr } \boldsymbol{\tau}_{i-1/2,j,k}^{(n)})\right) \tau_{i-1/2,j,k}^{xy(n)} \\ &\quad - \delta t \left\{ \frac{\xi}{2} \left[\frac{\partial v}{\partial x} \right]_{i-1/2,j,k}^{(n)} \tau_{i-1/2,j,k}^{yy(n)} + \frac{\xi}{2} \left[\frac{\partial w}{\partial x} \right]_{i-1/2,j,k}^{(n)} \tau_{i-1/2,j,k}^{yz(n)} \right\} \\ &\quad - \delta t \left\{ \frac{(\xi - 2)}{2} \left[\frac{\partial v}{\partial x} \right]_{i-1/2,j,k}^{(n)} \tau_{i-1/2,j,k}^{xx(n)} + \frac{(1 - \beta)}{\text{Wi}} \left[\frac{\partial v}{\partial x} \right]_{i-1/2,j,k}^{(n)} \right\}, \\ \tau_{i-1/2,j,k}^{xz(n+1)} &= \left(1 - \frac{\delta t}{\text{Wi}} f(\text{tr } \boldsymbol{\tau}_{i-1/2,j,k}^{(n)})\right) \tau_{i-1/2,j,k}^{xz(n)} \\ &\quad - \delta t \left\{ \frac{\xi}{2} \left[\frac{\partial v}{\partial x} \right]_{i-1/2,j,k}^{(n)} \tau_{i-1/2,j,k}^{yz(n)} + \frac{\xi}{2} \left[\frac{\partial w}{\partial x} \right]_{i-1/2,j,k}^{(n)} \tau_{i-1/2,j,k}^{zz(n)} \right\} \\ &\quad - \delta t \left\{ \frac{(\xi - 2)}{2} \left[\frac{\partial w}{\partial x} \right]_{i-1/2,j,k}^{(n)} \tau_{i-1/2,j,k}^{xx(n)} + \frac{(1 - \beta)}{\text{Wi}} \left[\frac{\partial w}{\partial x} \right]_{i-1/2,j,k}^{(n)} \right\}, \\ \tau_{i-1/2,j,k}^{yz(n+1)} &= \left(1 - \frac{\delta t}{\text{Wi}} f(\text{tr } \boldsymbol{\tau}_{i-1/2,j,k}^{(n)})\right) \tau_{i-1/2,j,k}^{yz(n)} \\ &\quad - \delta t \left\{ \frac{(\xi - 2)}{2} \left[\frac{\partial v}{\partial x} \right]_{i-1/2,j,k}^{(n)} \tau_{i-1/2,j,k}^{xz(n)} + \frac{(\xi - 2)}{2} \left[\frac{\partial w}{\partial x} \right]_{i-1/2,j,k}^{(n)} \tau_{i-1/2,j,k}^{xy(n)} \right\}, \end{aligned} \quad (5.51)$$

where

$$\left[\frac{\partial v}{\partial x} \right]_{i-1/2,j,k} = \frac{v_{i,j,k} - v_{i-1,j,k}}{\Delta x_{i-1/2}} \quad \text{and} \quad \left[\frac{\partial w}{\partial x} \right]_{i-1/2,j,k} = \frac{w_{i,j,k} - w_{i-1,j,k}}{\Delta x_{i-1/2}}, \quad (5.52)$$

with

$$v_{i,j,k} = \frac{\Delta y_{j-1/2} v_{i,j+1/2,k} + \Delta y_{j+1/2} v_{i,j-1/2,k}}{\Delta y_{j-1/2} + \Delta y_{j+1/2}}, \quad (5.53)$$

$$v_{i-1,j,k} = \frac{\Delta y_{j-1/2} v_{i-1,j+1/2,k} + \Delta y_{j+1/2} v_{i-1,j-1/2,k}}{\Delta y_{j-1/2} + \Delta y_{j+1/2}}, \quad (5.54)$$

$$w_{i,j,k} = \frac{\Delta z_{k-1/2} w_{i,j,k+1/2} + \Delta z_{k+1/2} w_{i,j,k-1/2}}{\Delta z_{k-1/2} + \Delta z_{k+1/2}}, \quad (5.55)$$

$$w_{i-1,j,k} = \frac{\Delta z_{k-1/2} w_{i-1,j,k+1/2} + \Delta z_{k+1/2} w_{i-1,j,k-1/2}}{\Delta z_{k-1/2} + \Delta z_{k+1/2}}. \quad (5.56)$$

Finally, we obtain our values $\tau_{i,j,k}^{(n+1)}$ by linear extrapolation, i.e.

$$\tau_{i,j,k}^{(n+1)} = \frac{\Delta x_i + \Delta x_{i-1}}{\Delta x_{i-1}} \tau_{i-1/2,j,k}^{(n+1)} - \frac{\Delta x_i}{\Delta x_{i-1}} \tau_{i-1,j,k}^{(n+1)}. \quad (5.57)$$

The velocity components, which are lying directly on the boundary, can be set to zero. Thus, in our example (see Figure 5.4), we have

$$u_b = u_{i-1/2,j,k} = 0. \quad (5.58)$$

For the velocity components, which have no direct value on the boundary, the zero boundary value is enforced by linear extrapolation

$$v_{i,j+1/2,k} = -\frac{\Delta x_i}{\Delta x_{i-1}} v_{i-1,j+1/2,k} \quad \text{and} \quad w_{i,j,k+1/2} = -\frac{\Delta x_i}{\Delta x_{i-1}} w_{i-1,j,k+1/2}. \quad (5.59)$$

Inflow Conditions

At inflow, we assume the elastic stresses to be zero. The boundary values for the stresses are then obtained by linear extrapolation as

$$\tau_{i-1/2,j,k} = -\frac{\Delta x_i}{\Delta x_{i-1}} \tau_{i-1,j,k}. \quad (5.60)$$

The velocities are explicitly given at the inflow boundary. Let us denote the prescribed values as $\mathbf{u}_{in} = (u_{in}, v_{in}, w_{in})$. The Dirichlet condition $\mathbf{u} = \mathbf{u}_{in}$ can be directly set for the velocity component situated at the boundary face and is obtained by linear extrapolation for the velocity values, which have no direct value on the boundary. Thus, we set

$$u_{i-1/2,j,k} = u_{in}, \quad (5.61)$$

$$v_{i,j+1/2,k} = \frac{\Delta x_i + \Delta x_{i-1}}{\Delta x_{i-1}} v_{in} - \frac{\Delta x_i}{\Delta x_{i-1}} v_{i-1,j+1/2,k}, \quad (5.62)$$

$$w_{i,j,k+1/2} = \frac{\Delta x_i + \Delta x_{i-1}}{\Delta x_{i-1}} w_{in} - \frac{\Delta x_i}{\Delta x_{i-1}} w_{i-1,j,k+1/2}. \quad (5.63)$$

Outflow Conditions

We assume homogeneous Neumann boundary conditions at the outlet for both stresses and velocities. That means, we have

$$\frac{\partial \boldsymbol{\tau}_{i-1/2,j,k}}{\partial \mathbf{n}} = (1, 0, 0)^T \cdot \nabla \boldsymbol{\tau}_{i-1/2,j,k} = \frac{\partial \boldsymbol{\tau}_{i-1/2,j,k}}{\partial x} = \frac{\boldsymbol{\tau}_{i,j,k} - \boldsymbol{\tau}_{i-1,j,k}}{\Delta x_{i-1/2}} = 0. \quad (5.64)$$

Therefore, we set

$$\boldsymbol{\tau}_{i,j,k} = \boldsymbol{\tau}_{i-1,j,k}, \quad (5.65)$$

$$u_{i-1/2,j,k} = u_{i-3/2,j,k}, \quad v_{i,j+1/2,k} = v_{i-1,j+1/2,k}, \quad w_{i,j,k+1/2} = w_{i-1,j,k+1/2}. \quad (5.66)$$

Periodic Boundary Conditions

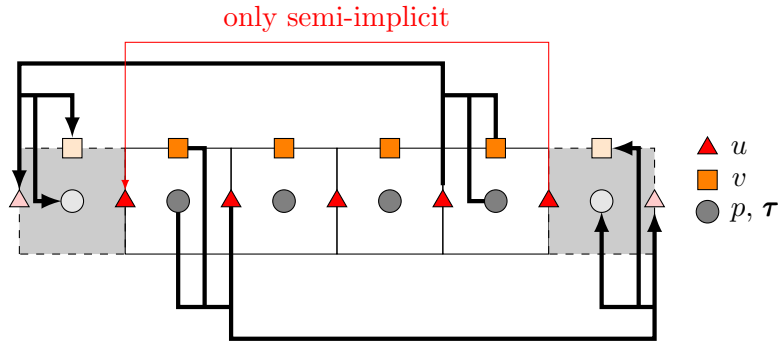


Figure 5.5: 2D periodic boundary conditions in x -direction.

Periodic boundary conditions are a set of boundary conditions used to simulate an infinitely large domain in the periodic directions. When a periodic boundary condition is set in one direction, we can use it to simulate two dimensions (e.g. x and y), while leaving the third direction (z) open and obtain pseudo 2D simulations. We glue the domain at the boundary together by exchanging the values at the boundary of the domain as shown in Figure 5.5. That means the velocity values u (\blacktriangle) and v (\blacksquare), the elastic stresses and the pressure (\bullet) are exchanged, so that the domain boundaries overlap by one cell in the periodic direction. In the semi-implicit projection method the velocity components at the boundary have to be exchanged before and after the solution of the Helmholtz system (see Figure 5.5), in addition to the exchange of the two velocity values in the explicit case (Klitz [42]).

5.3 Algorithm

Finally, we obtain the following algorithms to compute transient viscoelastic flows.

Algorithm 5.3.1: EXPLICIT COMP. OF VISCOELASTIC FLOWS($\mathbf{u}, p, \boldsymbol{\tau}$)

```

{ Set  $t = 0, n = 0$ .
{ Assign initial values to  $\mathbf{u}, p, \boldsymbol{\tau}$ .
while  $t \leq t_{\text{end}}$ 
    { Select  $\delta t$  according to (5.13)-(5.16).
    { Set boundary values for  $\mathbf{u}, p$ .
    { Set boundary values for  $\boldsymbol{\tau}$ .
    { Compute  $\boldsymbol{\tau}^{(n+1)}$  according to (5.1).
    { Update boundary values for  $\boldsymbol{\tau}$ .
do { Set boundary conditions for  $\mathbf{u}^*$ .
    { Compute  $\mathbf{u}^*$  according to (5.2).
    { Compute the right-hand side of the pressure Poisson equation (5.5).
    { Solve the pressure Poisson equation (5.5).
    { Compute  $\mathbf{u}^{(n+1)}$  according to (5.6).
    {  $t = t + \delta t, n = n + 1$ .

```

Algorithm 5.3.2: SEMI IMPLICIT COMP. OF VISCOELASTIC FLOWS($\mathbf{u}, p, \boldsymbol{\tau}$)

```

{ Set boundary values for the  $\Delta$  part of Helmholtz matrix.
{ Set  $t = 0, n = 0$ .
{ Assign initial values to  $\mathbf{u}, p, \boldsymbol{\tau}$ .
while  $t \leq t_{\text{end}}$ 
    { Select  $\delta t$ .
    { Set boundary values for  $\mathbf{u}, p$ .
    { Set boundary values for  $\boldsymbol{\tau}$ .
    { Compute  $\boldsymbol{\tau}^{(n+1)}$  according to (5.17)
    { Update boundary values for  $\boldsymbol{\tau}$ .
    { Compute the right-hand side of the Helmholtz equation (5.18).
do { Set boundary conditions for  $\mathbf{u}^*$ .
    { Solve the Helmholtz system for  $\mathbf{u}^*$  according to (5.18).
    { Compute the right-hand side of the Poisson equation (5.19).
    { Solve the Poisson equation (5.19) for the pressure difference  $\phi^{(n+1)}$ 
    { Compute  $\mathbf{u}^{(n+1)}$  according to (5.20).
    { Compute  $p^{(n+1/2)}$  according to (5.21).
    {  $t = t + \delta t, n = n + 1$ .

```

The semi-implicit approach is useful for the computation of low Reynolds number flows ($\text{Re} \approx 1$) and the explicit method is useful for the computation of flows with higher Reynolds numbers ($\text{Re} \approx 100$).

Chapter 6

Parallelization

To compute transient viscoelastic flows, we need to solve the governing equations for ten unknowns at each time-step. This is a huge computational task especially for complex flow situations. Results are only achievable within a decent time by increasing the computational efficiency. This can be done by parallelization, where the computational work and the memory requirements are divided between several processors. The processors communicate with each other and so cooperate on the solution to a problem. NaSt3DGP [1] is already fully parallelized based on a domain decomposition approach (Griebel [29]). In this chapter, we will describe this approach shortly.

6.1 Domain Decomposition and Communication

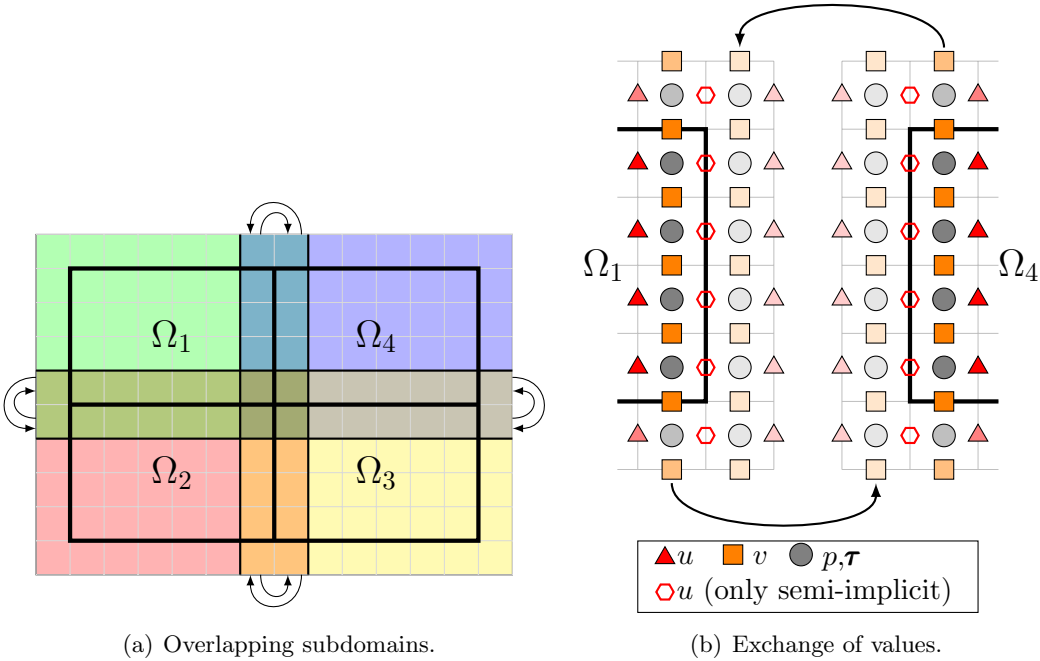


Figure 6.1: Domain decomposition and communication.

We decompose our domain Ω into subdomains $\Omega_1 \dots \Omega_N$. Each process treats one subdomain and computes the unknowns belonging to this domain. Therefore, a process does not require access to the entire data structure. Hence, the solution of iterative algorithms can be divided among the processes.

The processes interact with one another by exchanging values on an artificial boundary. This ensures the convergence of the parallelized algorithm and that the processes do not try to use uninitialized values in their computation. Depending on the discretization stencil, we need one or more cell rows wrapped around the domain (Croce [17]), e.g. we need two artificial cell rows for the VONOS scheme and three for the WENO scheme. The enlargement by this artificial boundary of the subdomains leads to an overlapping of the domains as shown in Figure 6.1(a). The velocity, pressure and stress tensor values exchanged at each time step are shown in Figure 6.1(b) for the example of two neighbouring processes in a two dimensional domain with one cell row as artificial boundary. For a process surrounded by other processes, the boundary strip values are shown in Figure 6.2. To ensure up to date corner values, we have to communicate the corner values two times in 2D and three times in 3D. In addition to the communication of the velocity, pressure and stress values at each time-step, we have to communicate the pressure values at each iteration of the Poisson solver, and if we use the semi-implicit projection method (see Section 5.1.3), the velocity values at each iteration of the Helmholtz solver. Furthermore, in the case of the semi-implicit projection method, the Helmholtz solver requires the communication of the velocity values at the boundary of the process domain denoted by \circ in Figure 6.1(b) (Klitz [42]).

We have to be aware that the computation is slowed down by the time these communications take and by the idling time, when processes are waiting to obtain necessary values. We obtain the optimal speedup if the amount of interprocessor communication is minimized and the calculated load is evenly balanced. In general, we can achieve a balanced computing load by the decomposition of the domain into subdomains of nearly equal size, so that each processor treats approximately the same number of unknowns.

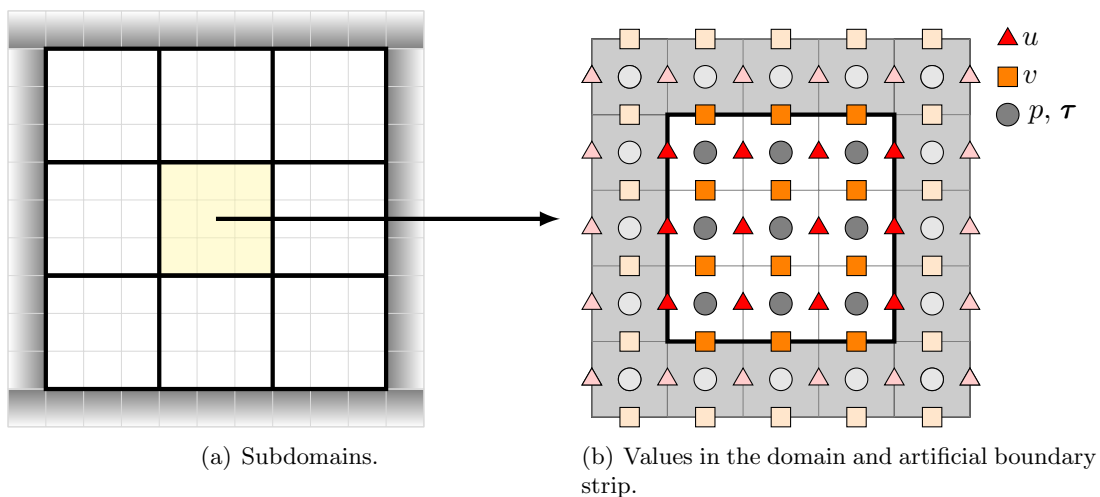


Figure 6.2: Artificial boundary strip.

6.2 Measuring Performance

For the communication between processes, we use MPICH [2], which is a freely available, portable implementation of the library specification for message-passing MPI (Message Passing Interface). MPICH consists of a set of routines callable from Fortran, C, or C++ and other programming languages. The “CH” in MPICH stands for “Chameleon,” symbol of adaptability to one’s environment and thus of portability. MPI’s portability enables it to exploit native hardware features to optimize performance and there is no need to modify your source code when you port your application to a different platform that supports the MPI standard. Additionally, MPI has a high functionality with over 115 routines.

The numerical results shown in this thesis were computed on the parallel computer Himalaya of the Institute for Numerical Simulation and the Sonderforschungsbereich 611. The High-Performance Cluster Computer Himalaya consists of 128 nodes, which are connected by a Myrinet infrastructure. This infrastructure allows fast communication between the nodes separated from the service ethernet and without the TCP/IP protocol overhead. Each node contains two Intel Xeon EM 64 T 3.2 GHz CPUs and 4-6 GB memory. Himalaya has a peak performance of 1638.4 GFlop/s.

As mentioned above, the reduction of the execution time for a parallel algorithm is limited by the cost of communications and the idling time of the processors. We want to measure the gain in computation speed for the parallel algorithm and therefore we define:

Definition 6.1 [SPEED-UP, EFFICIENCY]

Let p be the number of processors and $T(p)$ the execution time of the parallel algorithm using p processors. Then, the **speed-up** of a parallel algorithm is given by

$$S(p) = \frac{T(1)}{T(p)} = \frac{\text{execution time serial algorithm}}{\text{execution time using } p \text{ processors}}. \quad (6.1)$$

The **efficiency** is defined by

$$E(p) = \frac{T(1)}{p \cdot T(p)} = \frac{S(p)}{p} = \frac{\text{speed-up}}{\text{number of processors}}. \quad (6.2)$$

We measure the speed-up and efficiency of our parallized code in a fixed geometry which is then divided among an increasing number of processors. As example, we consider the plane channel flow through a channel of length 10 and height 1 in a domain $\Omega = 10 \times 1 \times 1$. In the third direction, we employ periodic boundary conditions. We set the parabolic steady state solution for the velocity and the steady state solution for the stress components at the inflow boundary (see Section 7.1.1). At the outflow boundary, we set the steady state solution for the velocity and homogeneous Neumann boundary condition for the stress components. We resolve the channel with $400 \times 40 \times 40$ grid cells. We use the semi-implicit projection method to perform the computations for the Oldroyd-B model with $Wi = 0.5$, $Re = 1$ and $\beta = 0.1$. We perform the computations until the time $t = 0.01$, which takes the semi-implicit solver 96 time-steps. We solve the pressure Poisson equation by a Jacobi preconditioned BiCGStab method and the Helmholtz equation for the intermediate velocity by a Jacobi preconditioned CG method.

Table 6.1: Speed-up and efficiency measurements.

p	$T(p)$ in sec.	$S(p)$	$E(p)$ in %
1	5791.00	1.00	100.0
2	3261.49	1.78	88.78
4	1609.42	3.60	89.95
8	815.68	7.10	88.74
16	415.21	13.95	87.17
32	222.05	26.08	81.50
64	125.51	46.14	72.10

The results of the measurements in terms of speed-up and efficiency are shown in Table 6.1. Note that due to the costs for communication, the optimal values $S(p) = p$ and $E(p) = 100\%$ cannot be achieved. Table 6.1 shows that the efficiency decreases with increasing number of processors. This is to be expected since the costs for communication increases. We can observe that the efficiency drops down to 72.10% for 64 processors. This is still a good value since each subdomain consists of only $20 \times 20 \times 25$ grid cells. Therefore, the communication costs are high in comparison to the relatively low computation costs. For refined grids better values of the efficiency for 64 processors are to be expected.

Chapter 7

Numerical Results

This chapter contains our numerical results. We validate our implementations by the investigation of the numerical approximation of the analytical solution for transient plane Poiseuille flow of an Oldroyd-B fluid and by a convergence study of a three-dimensional gravity driven flow through an infinite rectangular channel. Furthermore, we examine the flow through a three-dimensional rectangular channel, the flow over a hole and the Kármán vortex street behind an inclined plate and investigate the results for the different models. Since we want to compare the models in terms of their stress predictions, we need suitable methods to visualize the stress tensor.

Visualization of the Stress Tensor

The interpretation and visualization of the stress state of a fluid is a difficult task. Even though, the plotting of all six components of the stress tensor gives some information about the behaviour of the stress model equations, it is unclear how to relate these values to the total stress state of the fluid at a given point. In solid materials the determination of maximum normal stresses and shear stresses at a point is of considerable interest in the design of structures because failures occur when the magnitudes of stresses exceed allowable (normal or shear) stress values. These maximum stresses are given by the eigenvalues of the Cauchy stress tensor and are called **principal stresses**. However, for a fluid the flow dependent shear and normal stresses are of greater interest than the maximum stresses since the properties of a fluid material like the shear-dependent viscosity, elongational viscosity or normal stress differences, depend on the flow directed shear and normal stresses. We follow the approach of Bollada and Phillips [10] in defining a flow dependent shear and normal stress measure. First, we subtract the mean normal stress

$$\sigma_m = \frac{1}{3} \text{tr } \boldsymbol{\sigma} \quad (7.1)$$

from the Cauchy stress tensor to obtain the traceless **deviatoric** stress tensor

$$\boldsymbol{\sigma}_d = \boldsymbol{\sigma} - \sigma_m \mathbf{I}. \quad (7.2)$$

Note that the mean normal stress σ_m can be interpreted as the pressure. This approach leads for the Oldroyd-B and PTT model to the equation

$$\boldsymbol{\sigma}_d = \boldsymbol{\sigma} - \sigma_m \mathbf{I} = -p \mathbf{I} + 2\beta \mathbf{D} + \boldsymbol{\tau} - \frac{1}{3} (-3p + \text{div } \mathbf{u} + \text{tr } \boldsymbol{\tau}) \mathbf{I} = 2\eta \mathbf{D} + \boldsymbol{\tau} - \frac{1}{3} \text{tr } \boldsymbol{\tau}. \quad (7.3)$$

Furthermore, we consider the direction of the flow field

$$\hat{\mathbf{u}} = \frac{\mathbf{u}}{\|\mathbf{u}\|} \quad (7.4)$$

and choose two arbitrary directions, $\mathbf{u}_\perp^1, \mathbf{u}_\perp^2$ satisfying

$$\mathbf{u}_\perp^1 \cdot \mathbf{u} = \mathbf{u}_\perp^2 \cdot \mathbf{u} = \mathbf{u}_\perp^1 \cdot \mathbf{u}_\perp^2 = 0 \quad (7.5)$$

with $\|\mathbf{u}_\perp^1\| = \|\mathbf{u}_\perp^2\| = 1$ to define a positive flow dependent **shear stress** measure S_1 , independent of the choice of \mathbf{u}_\perp^1 and \mathbf{u}_\perp^2 , as

$$S_1 = \sqrt{(\hat{\mathbf{u}} \cdot \boldsymbol{\sigma}_d \cdot \mathbf{u}_\perp^1)^2 + (\hat{\mathbf{u}} \cdot \boldsymbol{\sigma}_d \cdot \mathbf{u}_\perp^2)^2} \quad (7.6)$$

and a flow dependent **normal stress** measure S_2 in direction of the streamlines as

$$S_2 = \hat{\mathbf{u}} \cdot \boldsymbol{\sigma}_d \cdot \hat{\mathbf{u}}. \quad (7.7)$$

Then, we define the principal stress as

$$pS = \sqrt{S_1^2 + S_2^2}. \quad (7.8)$$

We use these stress measures to visualize the stress tensor with ParaView[32] and Matlab.

7.1 Unsteady Poiseuille Flow of an Oldroyd-B Fluid

The unsteady Poiseuille Flow of an Oldroyd-B Fluid in a plane channel is a benchmark problem for viscoelastic computations since an analytical solution exists for both the steady and the transient problem. In this section, we want to determine the quality of our numerical solution by comparison with the analytical solution for both the steady and the transient problem. Therefore, we first present the analytical solution. Then, we compare the transient development of our numerical solution against the analytical solution at predetermined points in the flow domain. And last, we examine the convergence of the numerical solution to the analytical steady state solution with mesh refinement. We find a very good agreement between the transient analytical solution and the numerical solution and we observe that the numerical solution converges quadratically to the steady state analytical solution.

7.1.1 Analytical Solution

We present the analytical solution of the Poiseuille flow of an Oldroyd-B fluid for both the velocity and stress components. The Poiseuille flow is the flow of a fluid through a channel driven by a constant pressure gradient. For the mathematical description of this problem in two space dimensions, let us consider the constant pressure gradient

$$\frac{\partial p}{\partial x} = \kappa. \quad (7.9)$$

Now, we assume a velocity distribution of the form

$$(u(y, t), 0, 0) \text{ with } 0 < y < L \text{ and } t > 0 \quad (7.10)$$

with boundary conditions

$$u(0, t) = 0 \text{ and } u(L, t) = 0 \quad (7.11)$$

and initial condition

$$u(y, 0) = 0 \text{ with } 0 < y < L. \quad (7.12)$$

Then, the equation of continuity is automatically satisfied, and the flow of the fluid is given by the equation of motion

$$\rho \frac{\partial u}{\partial t} = -\kappa + \nabla \cdot \mathbf{T}, \quad (7.13)$$

where \mathbf{T} is given by the Oldroyd-B equations (3.95). Waters and King [73] derived the solution for this problem and non-dimensionalized the solution in the following manner

$$y^* = \frac{y}{L}, \quad u^* = \frac{u}{U}, \quad U = -\frac{\kappa L^2}{8\eta_0}, \quad t^* = \frac{\eta_0 t}{\rho L^2}. \quad (7.14)$$

This leads to the dimensionless numbers

$$\text{El} = \frac{\lambda \eta_0}{\rho L^2} = \frac{\text{Wi}}{\text{Re}}, \quad \beta = \frac{\eta_S}{\eta_0}, \quad \text{Wi} = \lambda \frac{U}{L}, \quad \text{Re} = \frac{UL\rho}{\eta_0}. \quad (7.15)$$

The solution of Waters and King [73] is given by

$$u^*(y^*, t^*) = 4y^*(1 - y^*) - 32 \sum_{n=1}^{\infty} \frac{\sin(Ny^*)}{N^3} G_N(\text{El}, t^*), \quad (7.16)$$

where

$$G_N(\text{El}, t^*) = \exp\left(-\frac{\alpha_N t^*}{2\text{El}}\right) \left[\cosh\left(\frac{\beta_N t^*}{2\text{El}}\right) + \frac{\gamma_N}{\beta_N} \sinh\left(\frac{\beta_N t^*}{2\text{El}}\right) \right] \quad (7.17)$$

and

$$N = (2n - 1)\pi, \quad \alpha_N = 1 + \text{El}N^2, \quad (7.18)$$

$$\beta_N^2 = \alpha_N^2 - 4N^2\text{El}, \quad \beta_N = \sqrt{\beta_N^2}, \quad (7.19)$$

$$\gamma_N = 1 + N^2\text{El}(\beta - 2). \quad (7.20)$$

If $\beta_N^2 < 0$, then $G_N(\text{El}, t^*)$ changes to

$$G_N(\text{El}, t^*) = \exp\left(-\frac{\alpha_N t^*}{2\text{El}}\right) \left[\cos\left(\frac{\beta_N t^*}{2\text{El}}\right) + \frac{\gamma_N}{\beta_N} \sin\left(\frac{\beta_N t^*}{2\text{El}}\right) \right] \quad (7.21)$$

with

$$\beta_N = \sqrt{-\beta_N^2}. \quad (7.22)$$

The corresponding Newtonian solution is given by

$$u^*(y^*, t^*) = 4y^*(1 - y^*) - 32 \sum_{n=1}^{\infty} \frac{\sin(Ny^*)}{N^3} \exp(-N^2 t^*). \quad (7.23)$$

Note that we have to fit our non-dimensional time scale ($t_{our}^* = (U/L)t$) to the time scale of the analytic solution ($t_{ana}^* = (\eta_0 t)/(\rho L^2)$)

$$t_{ana}^* = \frac{\eta_0 t}{\rho L^2} = \text{El} \frac{t}{\lambda} = \text{El} \frac{tU}{\text{Wi} L} = \frac{t_{our}^*}{\text{Re}}. \quad (7.24)$$

The Newtonian and the Oldroyd-B fluid have the same steady state solution ($t \rightarrow \infty$) for the velocity

$$A(y) = u^*(y^*) = 4y^*(1 - y^*). \quad (7.25)$$

In the following, we will drop the star notation for the sake of simplicity. The steady state solution for the stress components of the Oldroyd-B fluid is given by

$$\tau_{xx} = 2 \text{Wi} \frac{\partial u}{\partial y} \tau_{xy} = 2 \text{Wi} (1 - \beta) \left(\frac{\partial u}{\partial y} \right)^2 = 2 \text{Wi} (1 - \beta) A'(y)^2, \quad (7.26)$$

$$\tau_{xy} = (1 - \beta) \frac{\partial u}{\partial y} = (1 - \beta) A'(y), \quad (7.27)$$

$$\tau_{yy} = 0, \quad (7.28)$$

where

$$A'(y) = \frac{dA(y)}{dy}. \quad (7.29)$$

Carew et al. [13] found the analytical expressions for the stress components using the solution of Waters and King to be

$$\tau_{yy} = 0, \quad (7.30)$$

$$\tau_{xy} = \frac{(1-\beta)}{\text{El}} \left[\text{El} A'(y) - 32 \sum_{n=1}^{\infty} \frac{\cos(Ny)}{N^2} H_N(\text{El}, t) \right] + C_{xy}(\text{El}, y) \exp\left(-\frac{t}{\text{El}}\right), \quad (7.31)$$

$$\begin{aligned} \tau_{xx} = & 2\text{Re} C_{xy}(\text{El}, y) \left[A'(y) \exp\left(-\frac{t}{\text{El}}\right) t - 32 \sum_{n=1}^{\infty} \frac{\cos(Ny)}{N^2} I_N(\text{El}, t) \right] \\ & + 2\text{Re}(1-\beta) A'(y) \left[A'(y) \text{El} - 32 \sum_{n=1}^{\infty} \frac{\cos(Ny)}{N^2} H_N(\text{El}, t) \right] \\ & - \frac{64 \text{Re} A'(y)(1-\beta)}{\text{El}} \sum_{n=1}^{\infty} \frac{\cos(Ny)}{N^2} J_N(\text{El}, t) \\ & + \frac{2 \cdot 32^2 \text{Re}(1-\beta)}{\text{El}} \sum_{n,m=1}^{\infty} \frac{\cos(Ny)}{N^2} \frac{\cos(My)}{M^2} K_{NM}(\text{El}, t) + C_{xx}(\text{El}, y) \exp\left(-\frac{t}{\text{El}}\right), \end{aligned} \quad (7.32)$$

where $M = (2m - 1)\pi$, and C_{xy} and C_{xx} are time-independent functions defined by the requirement that τ_{xy} and τ_{xx} are zero at time $t = 0$, respectively. The coefficients $H_N(\text{El}, t)$, $I_N(\text{El}, t)$, $J_N(\text{El}, t)$ and $K_{NM}(\text{El}, t)$ are given in Appendix B as well as details on their derivation.

7.1.2 Numerical Approximation

In this section, we investigate the quality of the numerical solution. Therefore, we consider a channel of length 8.0 (x -direction) and height 1.0 (y -direction), as illustrated in Figure 7.1. Furthermore, we choose a channel width of 1.0 (z -direction), but we impose periodic boundary conditions in the z -direction, so that we obtain a pseudo-2D simulation. The Reynolds number

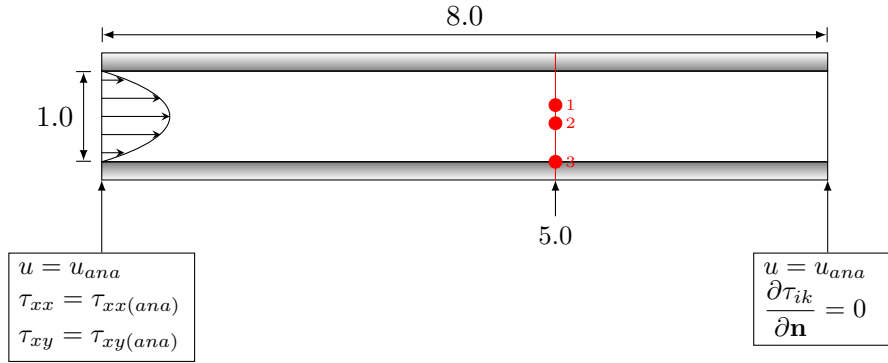


Figure 7.1: Setup of the channel for the Poiseuille flow problem.

is set to 1.0 and β is taken to be 0.1, i.e. the solvent Newtonian contribution to the total viscosity is only 10%. We compute the solution with the semi-implicit scheme and use the VONOS-scheme for the discretization of the convective terms.

Transient Solution

First, we investigate the behaviour of the transient solution. Therefore, we set the velocity to the transient analytical expression (7.16) at inflow and outflow. Similarly, we set the stress components to the transient analytical expression (7.32) at inflow. At outflow, we set homogeneous Neumann boundary conditions for the stresses. At the channel walls, we impose no-slip boundary conditions. We choose a resolution of $160 \times 20 \times 20$, so that we obtain an equidistant grid with a mesh size of 0.05. We examine the flow at three points in the domain: two interior points $P_1 = (5.025, 0.675, 5.025)$, $P_2 = (5.025, 0.425, 5.025)$ and one point at the boundary $P_3 = (5.025, 0.0, 5.025)$. The performance of the scheme is investigated for a Weissenberg number of 0.1 and 1.0.

The results of the computation and the corresponding analytical solution are plotted in Figures 7.2-7.4. The solution displays overshoots and undershoots in the streamwise velocity component and in the stress components until it reaches the steady state. These overshoots and undershoots are not experienced by Newtonian liquids. The overshoots and undershoots increase in amplitude with increasing Weissenberg number. Furthermore, the number of overshoots and undershoots increases as well and it takes the velocity and stress components much longer to attain their steady state values. Thus, for a Weissenberg number of 0.1, we observe one overshoot and a relatively weak undershoot, while for a Weissenberg number of 1.0, we already have three overshoots and two undershoots.

We can now judge the accuracy of the numerical solution from its ability to capture these

Table 7.1: Maximum relative error at each overshoot and undershoot and at steady state in percent.

	$e_{\infty}^t(u)$ in %		$e_{\infty}^t(\tau_{xx})$ in %			$e_{\infty}^t(\tau_{xy})$ in %		
	P_1	P_2	P_1	P_2	P_3	P_1	P_2	P_3
Wi = 0.1								
overshoot ₁	1.58	3.08	7.53	12.21	2.06	5.07	7.49	1.90
undershoot ₁	0.10	0.34	2.23	2.77	0.95	1.30	1.62	0.54
steady state	0.08	0.12	0.75	0.75	0.74	0.37	0.37	0.37
Wi = 1.0								
overshoot ₁	1.32	3.34	7.84	8.20	5.77	4.55	5.62	3.97
undershoot ₁	2.20	5.46	1.33	2.28	1.84	2.74	3.45	2.22
overshoot ₂	0.40	0.81	1.46	1.61	0.23	1.10	1.22	0.34
undershoot ₂	0.04	0.19	1.44	1.25	0.84	0.89	0.66	0.59
overshoot ₃	0.13	0.22	0.45	0.51	0.79	0.47	0.34	0.41
steady state	0.09	0.12	0.44	0.30	0.79	0.37	0.26	0.40

transient overshoots and undershoots. The numerical solution shows overpredictions and underpredictions of the overshoots and undershoots, which we shortly summarize for the two cases. First, for a Weissenberg number of 1.0, we observe an underprediction of the overshoots and an overprediction of the undershoots for the velocity and stress components for the interior points P_1 and P_2 . For the boundary point P_3 , we observe the opposite for the stress components: an overprediction of overshoots and an underprediction of undershoots. After the overshoots and undershoots, the solution attains steady state and stays slightly underpredicted for both velocity and stress components. For a Weissenberg number of 0.1, we observe an underprediction of the overshoot at the interior points P_1 and P_2 for both velocity and stress components and an overprediction of the overshoot at the boundary point P_3 for the stress components. Then, the solution stays slightly underpredicted.

We measure the deviation of the numerical solution from the analytical solution in terms of the maximum relative error occurring at each overshoot and undershoot, and the relative error at the steady state solution. We define the maximum relative error as

$$e_{\infty}^t(u) := \max_{t \in I} \left(\frac{|u_{ana}(t) - u_{num}(t)|}{|u_{ana}(t)|} \right), \quad (7.33)$$

where $u_{ana}(t)$ is the value of the analytical solution at time t , $u_{num}(t)$ is the value of the numerical solution at time t and $\max(\cdot)$ is the maximum over all times t in the time interval I of an overshoot or undershoot, respectively. Table 7.1 shows the relative maximum error in percent at the overshoots and undershoots and the relative error at the steady state solution. The errors for the stress components are slightly greater than for the velocity. For the stress τ_{xx} , the errors are larger than the errors for the other components. However, this result is to be expected, since we use the discretized velocity derivatives to compute the stress components. The error for τ_{xx} is greater than the error for τ_{xy} , because we use τ_{xy} and the discretized velocity derivatives for the computation of τ_{xx} , while for τ_{xy} , we use the discretized velocity derivatives only (see Appendix A). In summary, our scheme approximates the transient solution quite accurately and is able to capture all overshoots and undershoots in phase.

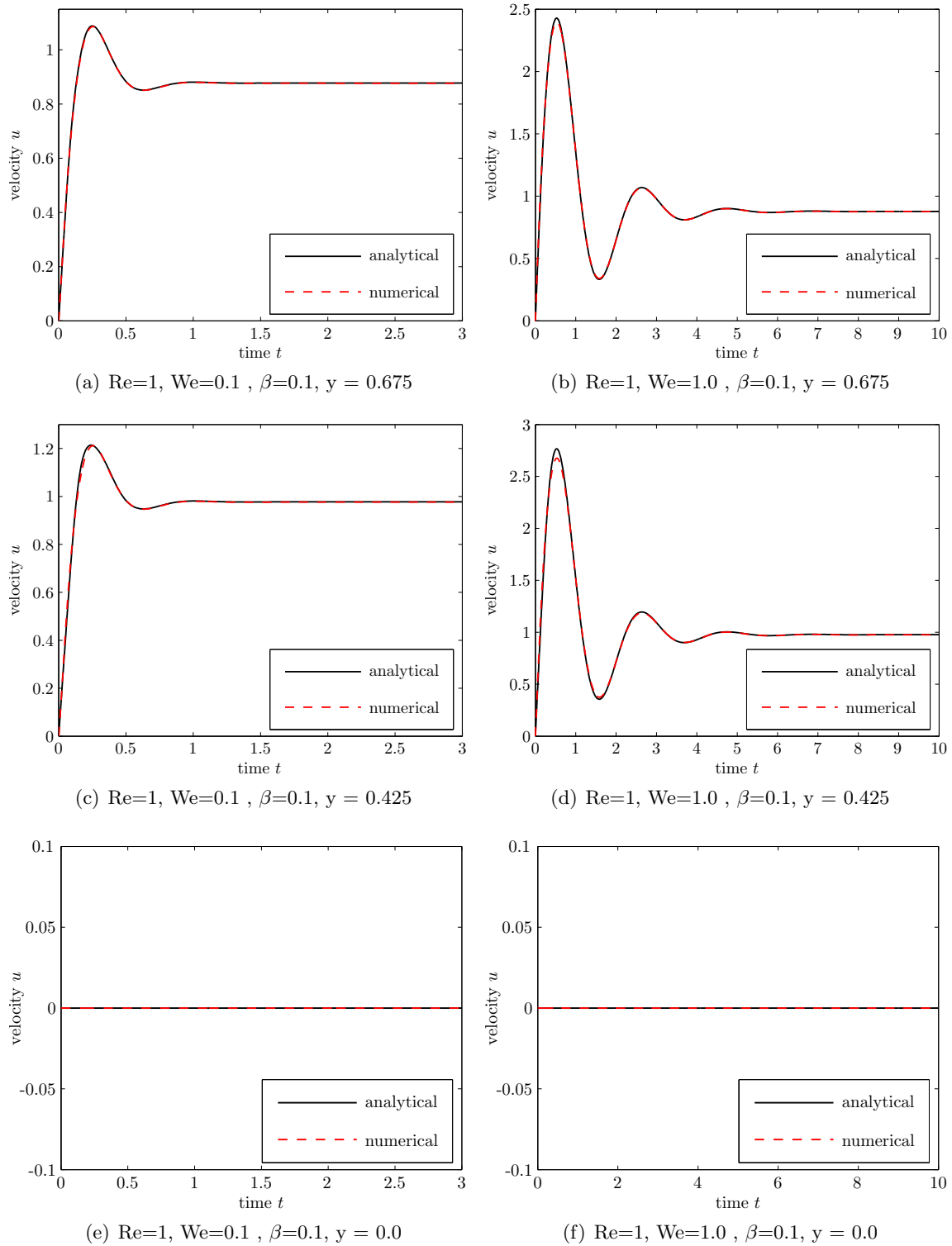


Figure 7.2: Plotted is the velocity u against time t at different points in the cross channel direction y from top to bottom (left: $Wi = 0.1$, right $Wi = 1.0$).

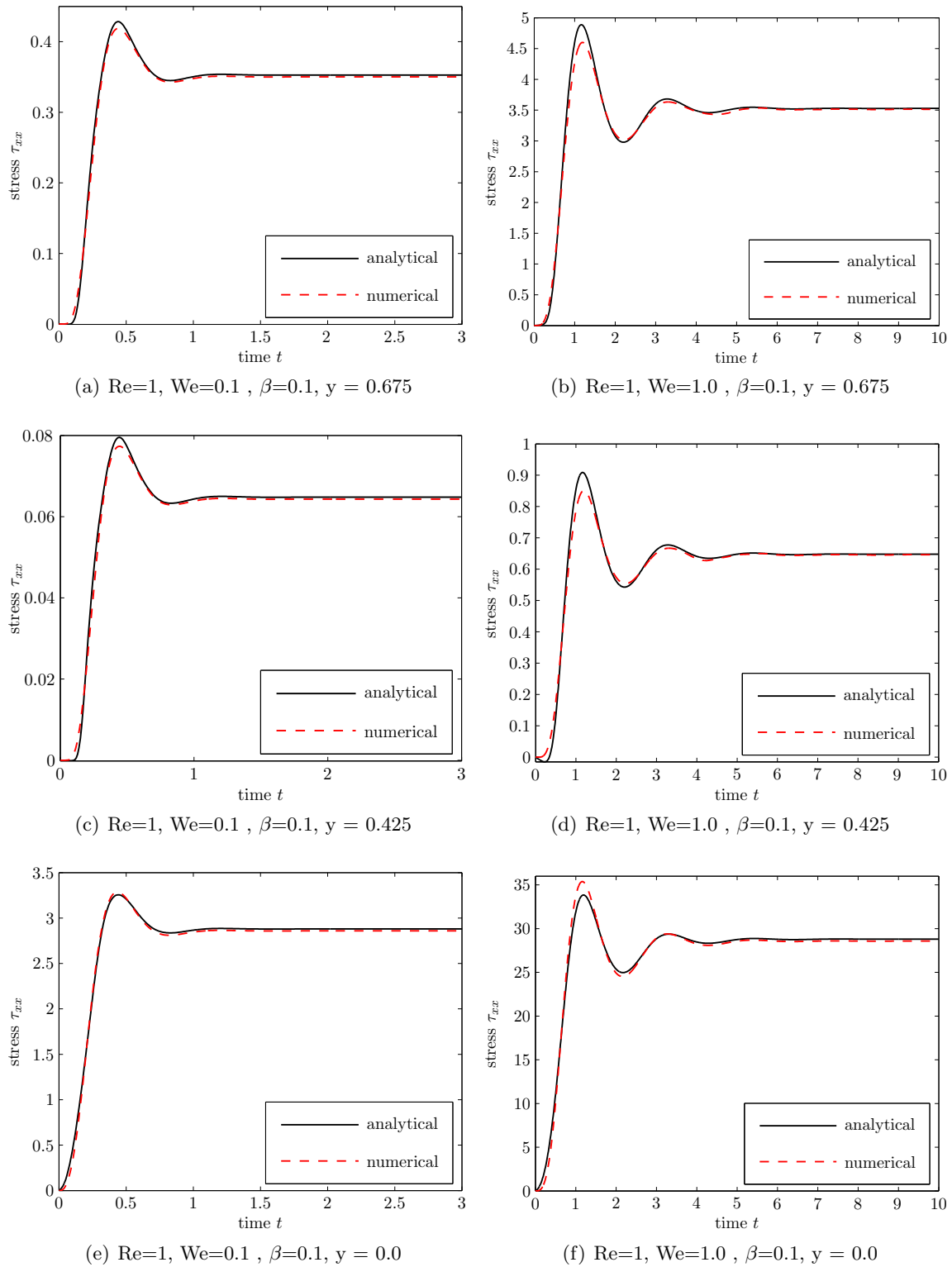


Figure 7.3: Plotted is the stress component τ_{xx} against time t at different points in the cross channel direction y from top to bottom (left: $\text{Wi} = 0.1$, right $\text{Wi} = 1.0$).

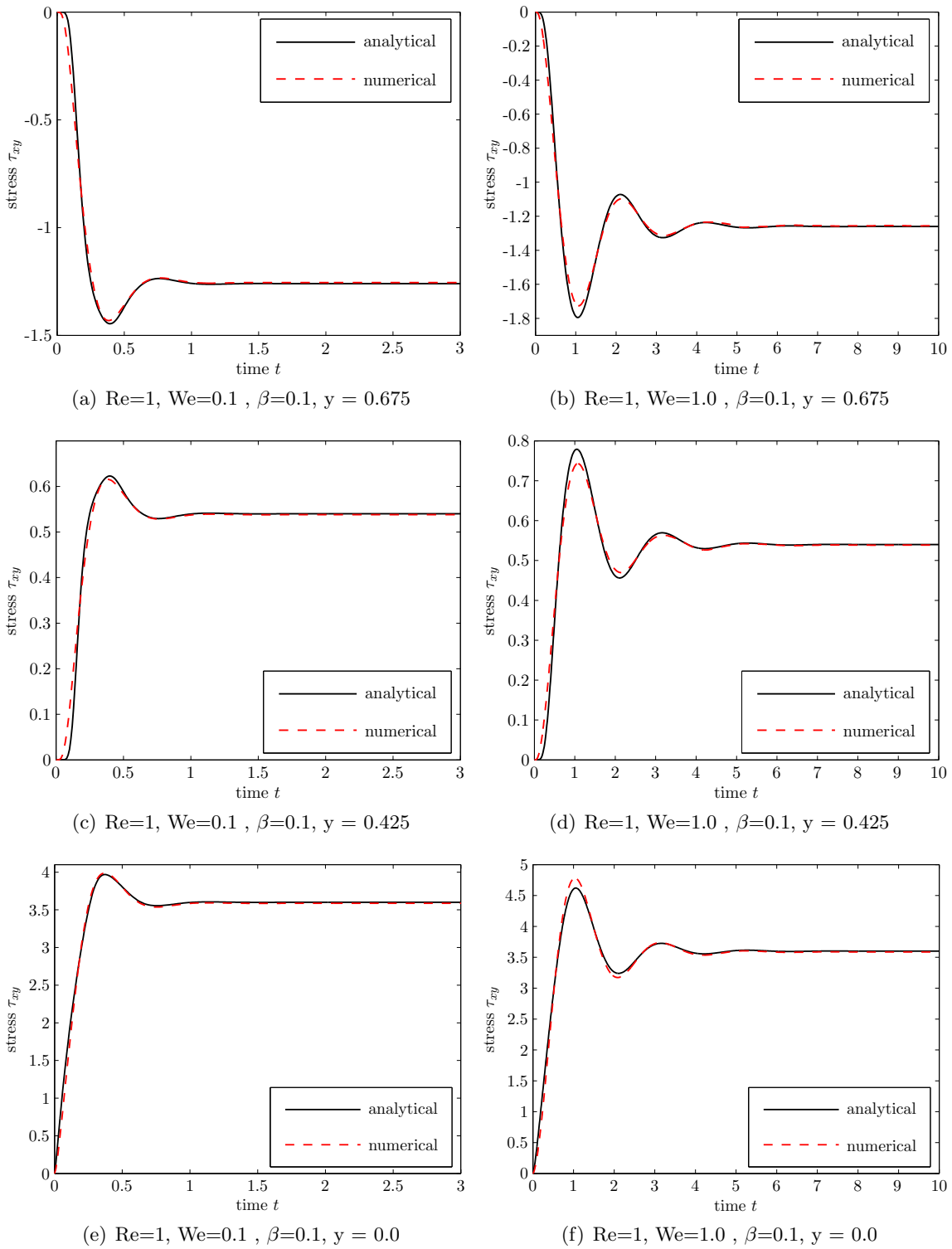


Figure 7.4: Plotted is the stress component τ_{xy} against time t at different points in the cross channel direction y from top to bottom (left: $\text{Wi} = 0.1$, right $\text{Wi} = 1.0$).

Steady State Solution

In this section, we investigate the steady state solution. Here, we set the velocity at inflow and outflow to the steady state analytical expression (7.25). Furthermore, we set the stress components to the steady state analytical expressions (7.28) at inflow and impose homogeneous Neumann boundary conditions at outflow. At the channel walls, we impose no-slip boundary conditions. We observe the flow at a probe line Y over the full height of the channel ($0 \leq y \leq 1.05$) at $(x, z) = (5.0, 0.5)$ (see red line in Figure 7.1).

Figure 7.5 shows the values of the velocity component u , the stress component τ_{xx} and the stress component τ_{xy} together with the respective analytic values for a resolution of the channel of $160 \times 20 \times 20$ and Weissenberg numbers 0.1, 0.5, 1.0, 2.0. We observe excellent agreement between the exact and the numerical solution. To confirm this impression, we examine the quality of the approximation in a convergence study. Therefore, we calculate the steady state solution for a Weissenberg number 0.5 on four successively refined equidistant grids with $40 \times 8 \times 8$, $80 \times 16 \times 16$, $160 \times 32 \times 32$ and $320 \times 64 \times 64$ grid cells, which we denote by level 1, 2, 3 and 4 respectively. Therefore, we have equidistant grids with a mesh size of $h_1 = h = 0.125$, $h_2 = h/2 = 0.0625$, $h_3 = h/4 = 0.03125$ and $h_4 = h/8 = 0.015625$ respectively. We measure the error at the probe line Y in the discrete L_1^l -norm, L_2^l -norm and L_∞^l -norm. That means, we calculate the errors by

$$E_1^l(u) := \|\Delta u_l\|_{L_1^l} = \sum_j |u_{ana}(y_j) - u_l(y_j)| h_l, \quad (7.34)$$

$$E_2^l(u) := \|\Delta u_l\|_{L_2^l} = \sqrt{\sum_j |u_{ana}(y_j) - u_l(y_j)|^2} h_l, \quad (7.35)$$

$$E_\infty^l(u) := \|\Delta u_l\|_{L_\infty^l} = \max_j [|u_{ana}(y_j) - u_l(y_j)|], \quad (7.36)$$

where $u_l(y_j)$ is the value of the discrete numerical solution at mesh level l at position y_j , $u_{ana}(y_j)$ is the value of the analytical solution at position y_j , h_l is the mesh size of mesh level l , the discrete maximum value $\max_j[\cdot]$ and the sum is taken over all grid cells in the y -direction. The results are shown in Table 7.2. With these error values, we can calculate the order of convergence of our scheme, which is given by

$$p_l = \frac{\log(E^l/E^{l+1})}{\log(2)}, \quad (7.37)$$

where E^l and E^{l+1} are the errors at level l and $l+1$ respectively. This definition yields the data gathered in Table 7.3, which shows the result of quadratic convergence for velocity and stress components. To complete the investigation, the behaviour of the errors is displayed as a function of the mesh size in Figure 7.6.

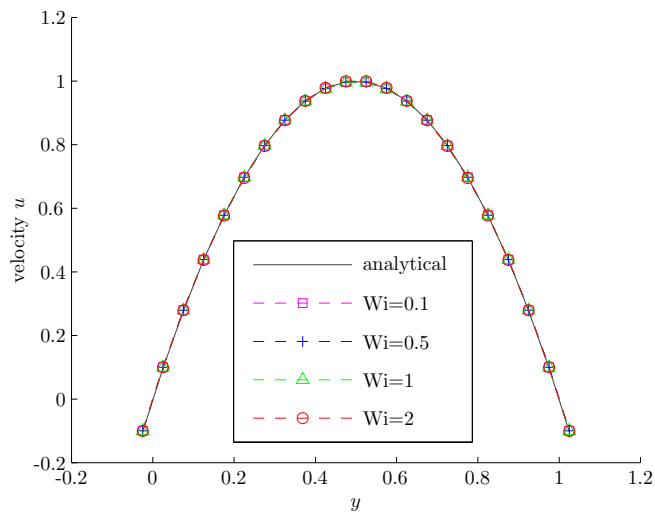
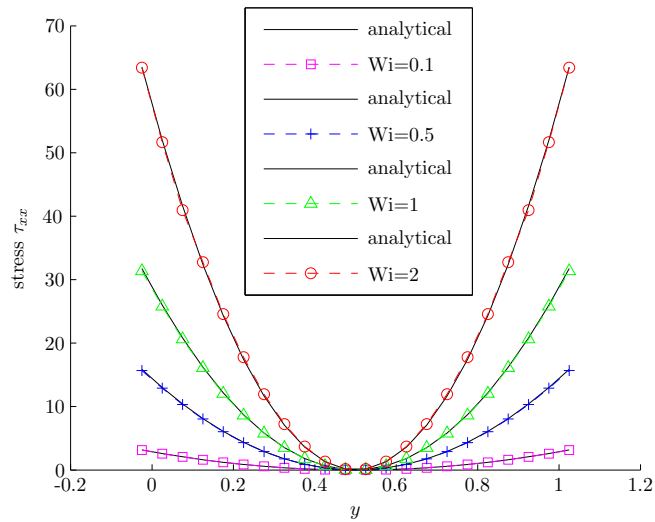
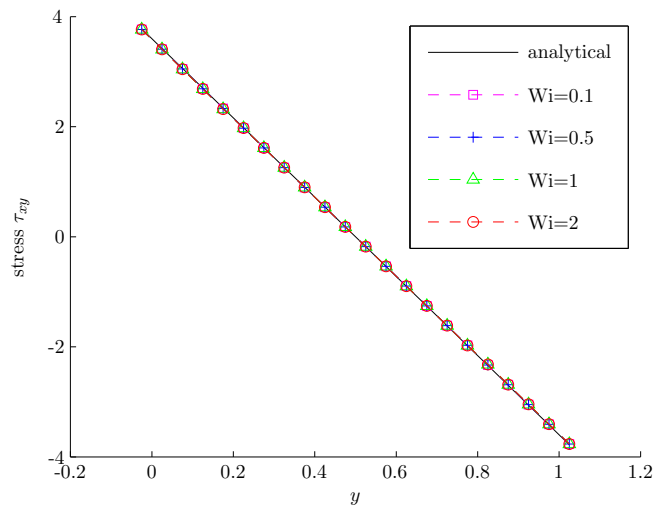
(a) velocity u .(b) stress τ_{xx} .(c) stress τ_{xy} .Figure 7.5: Steady state solution at probe line Y with $(0 \leq y \leq 1.05)$ and $(x, z) = (5.0, 0.5)$.

Table 7.2: Error.

L_1^l -norm			
l	$E_1^l(u)$	$E_1^l(\tau_{xx})$	$E_1^l(\tau_{xy})$
1	1.10 ₋₂	5.25 ₋₁	6.40 ₋₂
2	2.06 ₋₃	9.26 ₋₂	1.32 ₋₂
3	4.44 ₋₄	1.82 ₋₂	2.94 ₋₃
4	1.04 ₋₄	3.82 ₋₃	6.64 ₋₄
L_2^l -norm			
l	$E_2^l(u)$	$E_2^l(\tau_{xx})$	$E_2^l(\tau_{xy})$
1	1.25 ₋₂	6.85 ₋₁	6.58 ₋₂
2	2.37 ₋₃	1.29 ₋₁	1.44 ₋₂
3	5.12 ₋₄	2.59 ₋₂	3.30 ₋₃
4	1.20 ₋₄	5.62 ₋₃	7.96 ₋₄
L_∞^l -norm			
l	$E_\infty^l(u)$	$E_\infty^l(\tau_{xx})$	$E_\infty^l(\tau_{xy})$
1	2.13 ₋₂	1.25 ₀	9.21 ₋₂
2	4.63 ₋₃	2.99 ₋₁	2.22 ₋₂
3	1.07 ₋₃	7.23 ₋₂	5.38 ₋₃
4	2.56 ₋₄	1.80 ₋₂	1.62 ₋₃

Table 7.3: Order of convergence, We=0.5.

order	u			τ_{xx}			τ_{xy}		
	L_1^l	L_2^l	L_∞^l	L_1^l	L_2^l	L_∞^l	L_1^l	L_2^l	L_∞^l
p_1	2.42	2.39	2.20	2.50	2.41	2.06	2.28	2.19	2.05
p_2	2.21	2.21	2.12	2.35	2.32	2.05	2.17	2.12	2.05
p_3	2.10	2.09	2.06	2.25	2.21	2.01	2.15	2.05	1.73

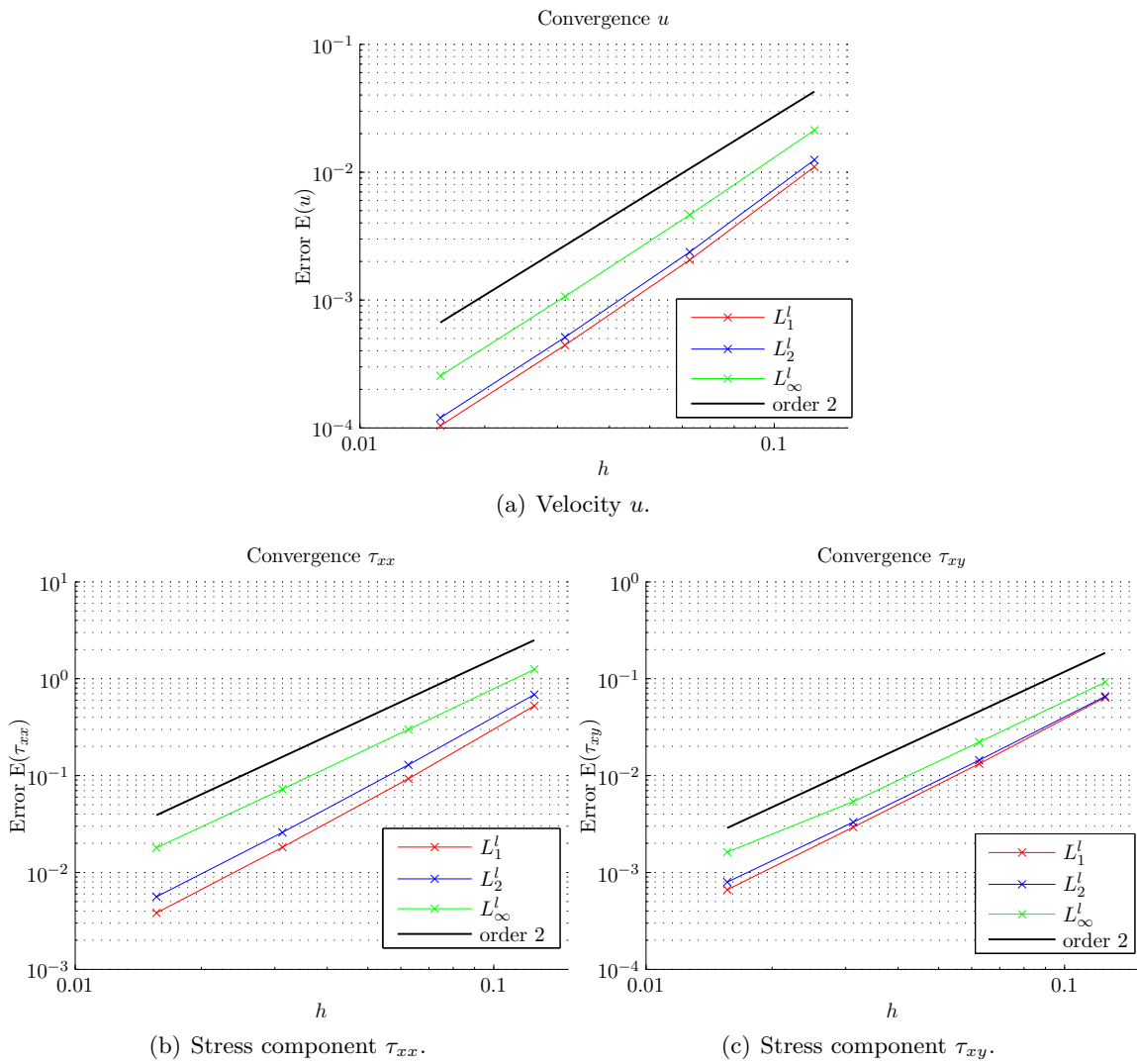


Figure 7.6: Convergence of stresses and velocity.

7.2 Flow through a Rectangular Channel

In the previous section, we examined the steady state solution for the two-dimensional channel flow of an Oldroyd-B fluid. In this section, we want to investigate the three-dimensional channel flow with a rectangular cross section for both an Oldroyd-B and a Phan-Thien Tanner fluid. Therefore, we consider a channel of length 8.0, height 1.0 and width 1.0, which we resolve by $320 \times 64 \times 64$ grid cells. We impose a parabolic velocity profile with a maximum velocity of 1.0 at inflow, which we gain from the channel flow of a Newtonian fluid. This avoids the occurrence of high stress values at the no-slip boundary near the inlet region, which arise if a constant velocity value is prescribed over the whole inflow boundary. The stress tensor components are set to zero at inflow. Furthermore, homogeneous Neumann boundary conditions are set at the outflow boundary for both velocity and stress tensor components. We impose no-slip boundary conditions at the channel walls. A summary of the relevant parameters can be found in Table 7.4. After all components have attained their steady state values, we examine their values at a cut in the cross channel direction at $x = 5.0$. We find that the values for the Phan-Thien Tanner model are equal for the linear form and the exponential form. This is not very surprising, since in the case of the channel flow the shear and elongation rates are not so high and therefore the linear form and the exponential form of the Phan-Thien Tanner equations predict the same behaviour (cf. Figures 3.16-3.18). In Figure 7.7, we see the parabolic velocity profile of u , the constant pressure p , the stress τ_{xx} , τ_{xy} and τ_{xz} for the Oldroyd-B model. The velocity components v, w and the stress components τ_{yy} , τ_{zz} , τ_{yz} have values around 10^{-11} and therefore, they are neglected in our investigation. For the PTT model, we obtain the same values for the velocity component u and the stress components τ_{xy} and τ_{xz} (see Figure 7.8). The parabolic profile of the stress component τ_{xx} of the PTT model is more shallow than the parabolic profile of the stress τ_{xx} of the Oldroyd-B model. Additionally, the PTT model predicts non-zero stress components τ_{yy} and τ_{zz} that cause small velocity values v and w , which induce the stress component τ_{yz} (see Figure 7.9). The pressure reacts to those values and forms a parabolic profile.

Table 7.4: Parameters of three-dimensional channel flow.

Reynolds number	1.0
Weissenberg number	0.1
β	0.1
ξ	0.07
ε	0.25
Projection method	semi-implicit
Convective terms	VONOS

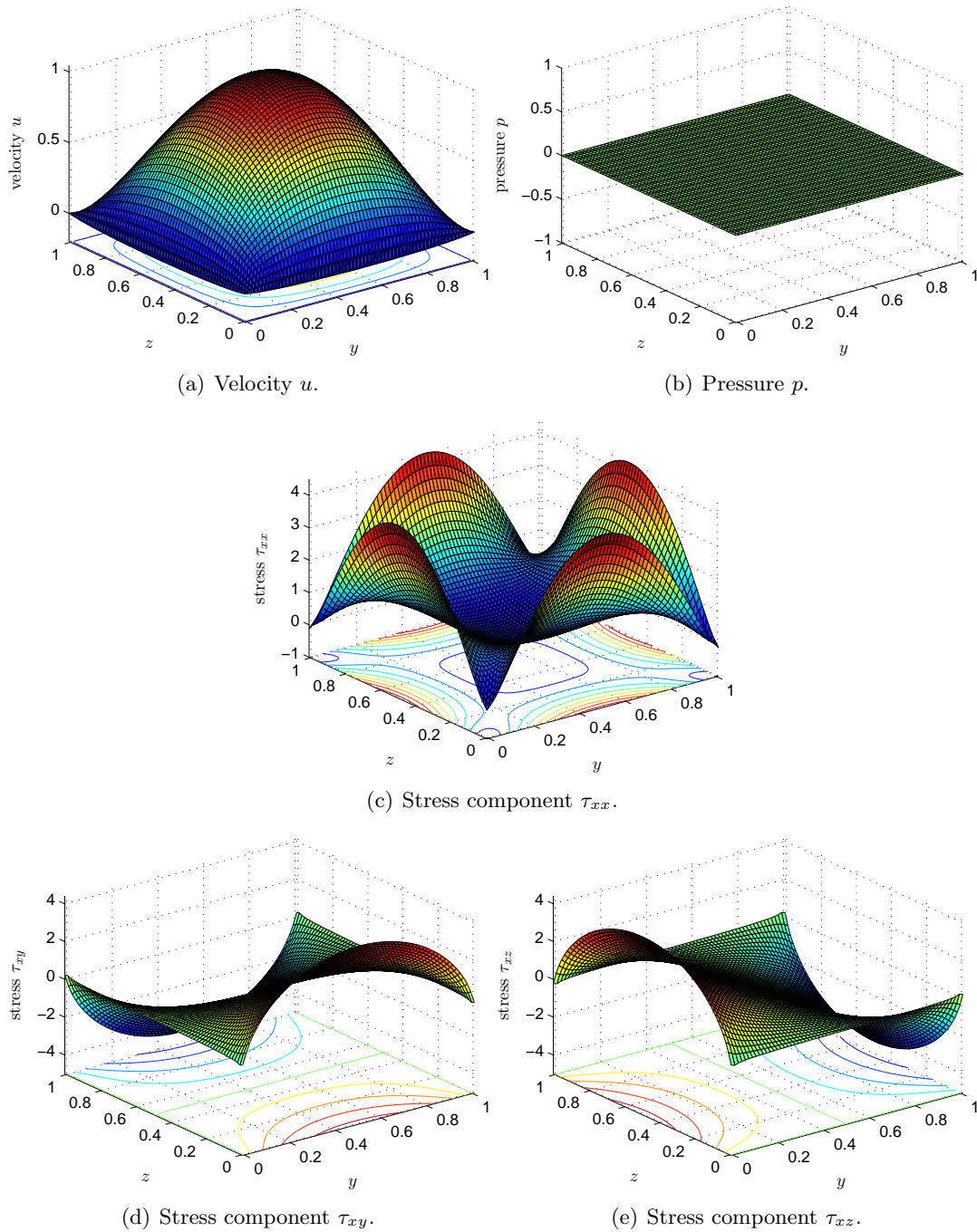


Figure 7.7: Velocity, pressure and stresses for the Oldroyd-B model.

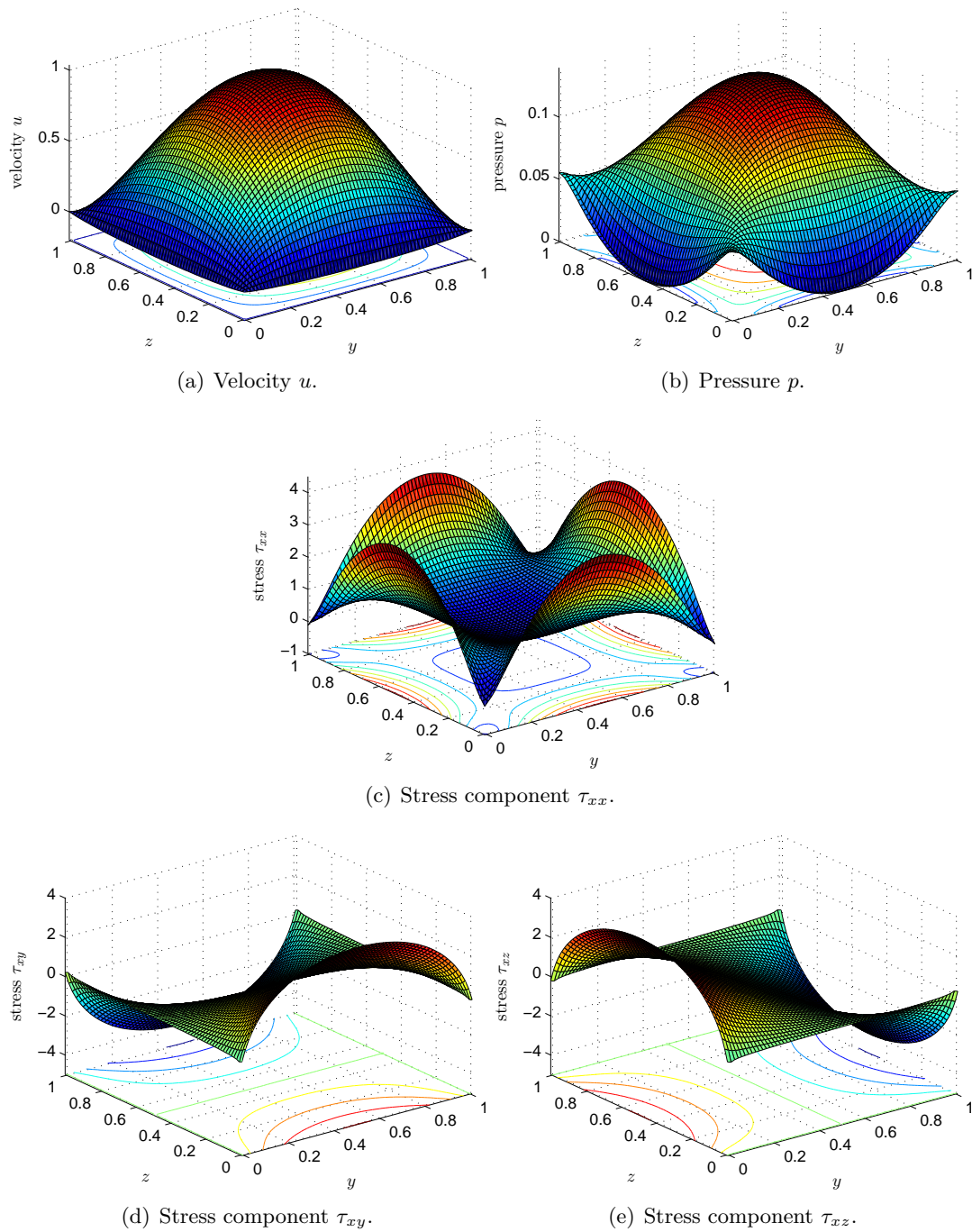


Figure 7.8: Velocity, pressure and stresses for the PTT model.

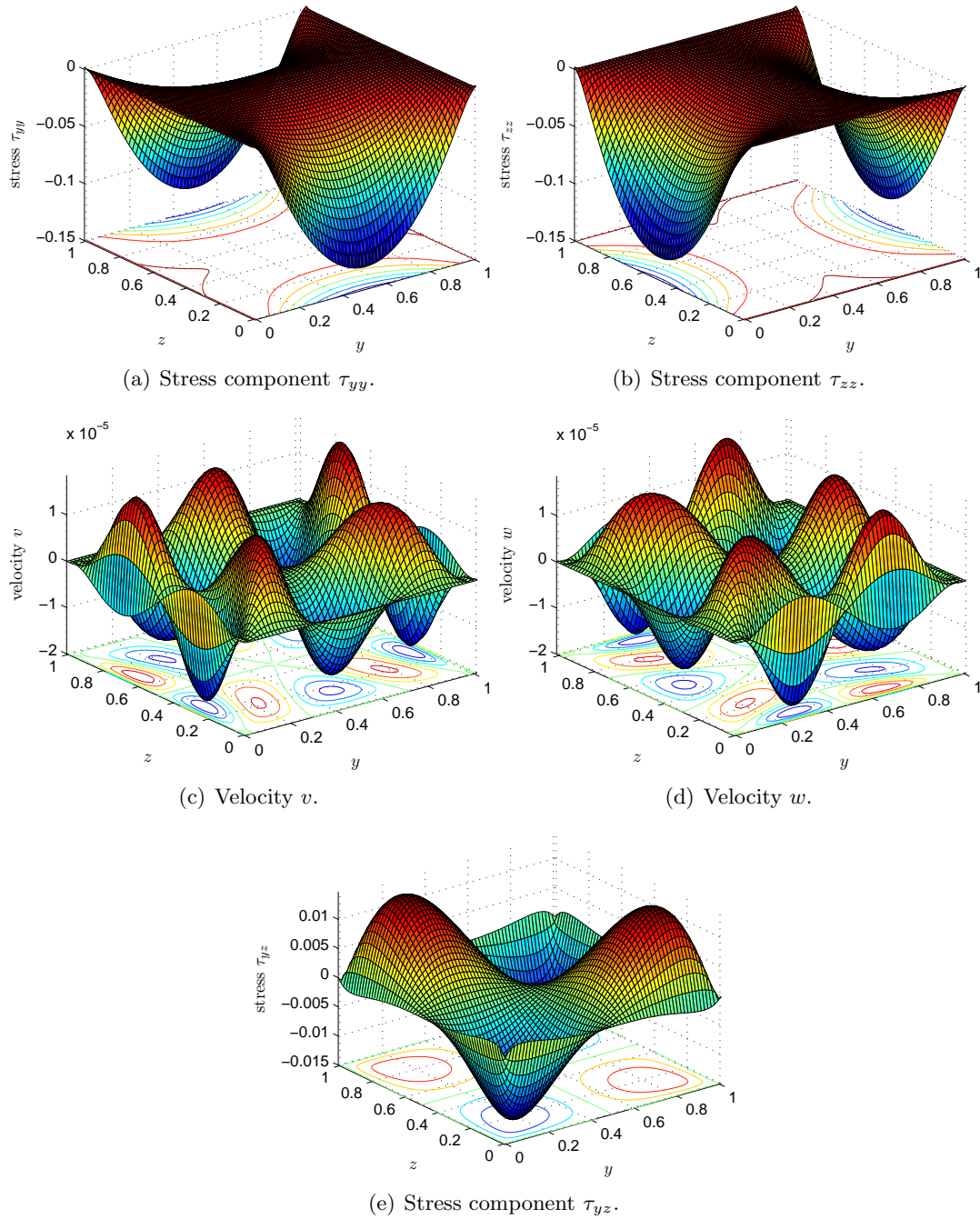


Figure 7.9: Stresses and velocities for the PTT model.

7.3 Convergence Study on a Flow through an Infinite Channel

Since to our knowledge, an analytical solution in three space dimensions for the Oldroyd-B and PTT fluid does not yet exist for both velocity and stress tensor components, we check the convergence of our scheme by a numerical experiment. We investigate a three-dimensional flow through an infinite channel with rectangular cross section.

We choose a rectangular domain $[0, 1]^3$ and impose periodic boundary conditions in the x -direction to build an infinite channel. The flow is driven by a gravity force of $\mathbf{g} = (10, 0, 0)$. At the walls, we impose no-slip boundary conditions. We set a constant time-step of $\Delta t = 0.0002$, which corresponds to the time-step necessary for the computation on the finest grid. The other parameters are chosen as listed in Table 7.5.

Table 7.5: Parameters.

Reynolds number	1.0
Weissenberg number	0.1
β	0.1
ξ	0.07
ε	0.25
Projection method	semi-implicit
Convective terms	VONOS

The discretization error can be estimated from the difference between solutions on refined grids. These errors can then be used to compute the order of convergence. We calculate the steady state solution on five successively refined grids with 8^3 , 16^3 , 32^3 , 64^3 , 128^3 grid cells, which we denote by level 1, 2, 3, 4 and 5 respectively. Therefore, we have equidistant grids with a mesh size of $h_1 = h = 0.125$, $h_2 = h/2 = 0.0625$, $h_3 = h/4 = 0.03125$, $h_4 = h/8 = 0.015625$ and $h_5 = h/16 = 0.0078125$ respectively. We measure the error in the discrete L_1^l -norm, L_2^l -norm and L_∞^l -norm and calculate the errors by

$$E_1^l(u) := \|u_{l+1} - u_l\|_{L_1^l} = \sum_{i,j,k} |u_{l+1}(x_i, y_j, z_k) - u_l(x_i, y_j, z_k)| h_{l+1}^3, \quad (7.38)$$

$$E_2^l(u) := \|u_{l+1} - u_l\|_{L_2^l} = \sqrt{\sum_{i,j,k} |u_{l+1}(x_i, y_j, z_k) - u_l(x_i, y_j, z_k)|^2 h_{l+1}^3}, \quad (7.39)$$

$$E_\infty^l(u) := \|u_{l+1} - u_l\|_{L_\infty^l} = \max_{i,j,k} [|u_{l+1}(x_i, y_j, z_k) - u_l(x_i, y_j, z_k)|], \quad (7.40)$$

where h_{l+1} is the mesh size of mesh level $l + 1$ and $u_{l+1}(x_i, y_j, z_k)$ is the value of the discrete numerical solution of mesh level $l + 1$ at position (x_i, y_j, z_k) . The discrete maximum $\max_{i,j,k}[\cdot]$ and the sum are taken over all grid cells of the finer mesh level $l + 1$. To subtract the discrete numerical solution u_l of the coarse grid level l from the solution $u_{l+1}(x_i, y_j, z_k)$ of the fine grid at position (x_i, y_j, z_k) , we have to interpolate the values of the solution u_l from the coarse grid level l to the fine grid level $l + 1$ for which we use the trilinear interpolation function in

three space dimension of Matlab. Then, we calculate the order of convergence by

$$p_l = \frac{\log(E^l/E^{l+1})}{\log(2)}, \quad (7.41)$$

where E^l and E^{l+1} are the errors at level l and $l + 1$ respectively.

The errors for the Oldroyd-B model are listed in Table 7.6 and the corresponding orders of convergence are gathered in Table 7.7. As for the three dimensional channel flow in the previous section, the velocity components v, w and the stress components $\tau_{yy}, \tau_{zz}, \tau_{yz}$ have values around 10^{-11} . Therefore, we neglect these values in our study. Additionally, the pressure is only around 10^{-8} . Therefore, we neglect the pressure as well, because 10^{-8} is within the scope of the residuum of the Poisson solver. Thus, these values are omitted in the convergence study for the Oldroyd-B model. The components show a similar behaviour for the PTT model and the Oldroyd-B model like in the three-dimensional channel flow introduced in the previous section.

We find very good convergence results for all components: the velocity u converges with an order around two and the stress components converge with an order around two in the L_1^l -norm and L_2^l -norm and with an order of one in the L_∞^l -norm. The linear convergence in the L_∞^l -norm may be explained by the fact, that we calculate the values of the stresses in the corners of the boundary of the rectangular channel by linear extrapolation. Indeed, we can observe that the maximum errors occur always in these corner boundary cells. The linear extrapolation in the boundary corner cells does not have such a drastic influence on the L_1^l -norm and the L_2^l -norm. The stress tensor components show singular behaviour toward the corners while the velocity component has a smooth profile (see Figure 7.7). Therefore, the difference of the stress values is quite large between the coarse and the fine grid. We find that the results match for the components τ_{xy} and τ_{xz} , which are symmetric to each other (see Figure 7.7).

However, the PTT model shows the same results for the linear form and the exponential form. The linear and the exponential form predict the same behaviour for this experiment since the shear and elongation rates are not so high (see Figures 3.16-3.18). For the PTT model, we find approximately the same results for the components $u, \tau_{xx}, \tau_{xy}, \tau_{xz}$. In addition, the PTT model has a non-zero pressure, stress components $\tau_{yy}, \tau_{zz}, \tau_{yz}$ and velocity components v and w . The results for the stress components τ_{yy} and τ_{zz} match as well as the results for the velocity components v and w . The components τ_{yy} and τ_{zz} are symmetric to each other as well as the velocity components v and w (see Figure 7.8-7.9). The components τ_{yy}, τ_{zz} and τ_{yz} converge with an order of two in the L_1^l -norm and L_2^l -norm and an order between 1.14 and 1.88 in the L_∞^l -norm. The velocity components v and w show a convergence rate between 1.86 and 3.03 in the L_1^l -norm and L_2^l -norm and an order between 1.28 and 2.30 in the L_∞^l -norm. Finally, we can observe the convergence of the components in Figure 7.10 for the Oldroyd-B model and in Figure 7.10 for the PTT model.

Table 7.6: Error for the Oldroyd-B model.

L_1^l -norm				
l	$E_1^l(u)$	$E_1^l(\tau_{xx})$	$E_1^l(\tau_{xy})$	$E_1^l(\tau_{xz})$
1	7.06_{-3}	3.09_{-2}	2.38_{-2}	2.38_{-2}
2	1.71_{-3}	6.39_{-3}	4.49_{-3}	4.49_{-3}
3	4.34_{-4}	1.42_{-3}	9.50_{-4}	9.50_{-4}
4	1.10_{-4}	3.31_{-4}	2.15_{-4}	2.15_{-4}
L_2^l -norm				
l	$E_2^l(u)$	$E_2^l(\tau_{xx})$	$E_2^l(\tau_{xy})$	$E_2^l(\tau_{xz})$
1	7.48_{-3}	3.17_{-2}	4.14_{-2}	4.14_{-2}
2	1.89_{-3}	7.57_{-3}	1.01_{-2}	1.01_{-2}
3	4.86_{-4}	1.93_{-3}	2.52_{-3}	2.52_{-3}
4	1.23_{-4}	4.93_{-4}	6.36_{-4}	6.36_{-4}
L_∞^l -norm				
l	$E_\infty^l(u)$	$E_\infty^l(\tau_{xx})$	$E_\infty^l(\tau_{xy})$	$E_\infty^l(\tau_{xz})$
1	2.17_{-2}	5.51_{-2}	1.82_{-1}	1.82_{-1}
2	5.41_{-3}	2.65_{-2}	9.06_{-2}	9.06_{-2}
3	1.35_{-3}	1.10_{-2}	4.52_{-2}	4.52_{-2}
4	3.38_{-4}	4.55_{-3}	2.26_{-2}	2.26_{-2}

Table 7.7: Order of convergence for the Oldroyd-B model.

order	u			τ_{xx}			τ_{xy} / τ_{xz}		
	L_1^l	L_2^l	L_∞^l	L_1^l	L_2^l	L_∞^l	L_1^l	L_2^l	L_∞^l
p_1	2.04	1.98	2.00	2.27	2.07	1.06	2.40	2.04	1.01
p_2	1.98	1.96	2.00	2.17	1.97	1.26	2.24	2.00	1.00
p_3	1.98	1.98	2.00	2.10	1.97	1.28	2.14	1.98	1.00

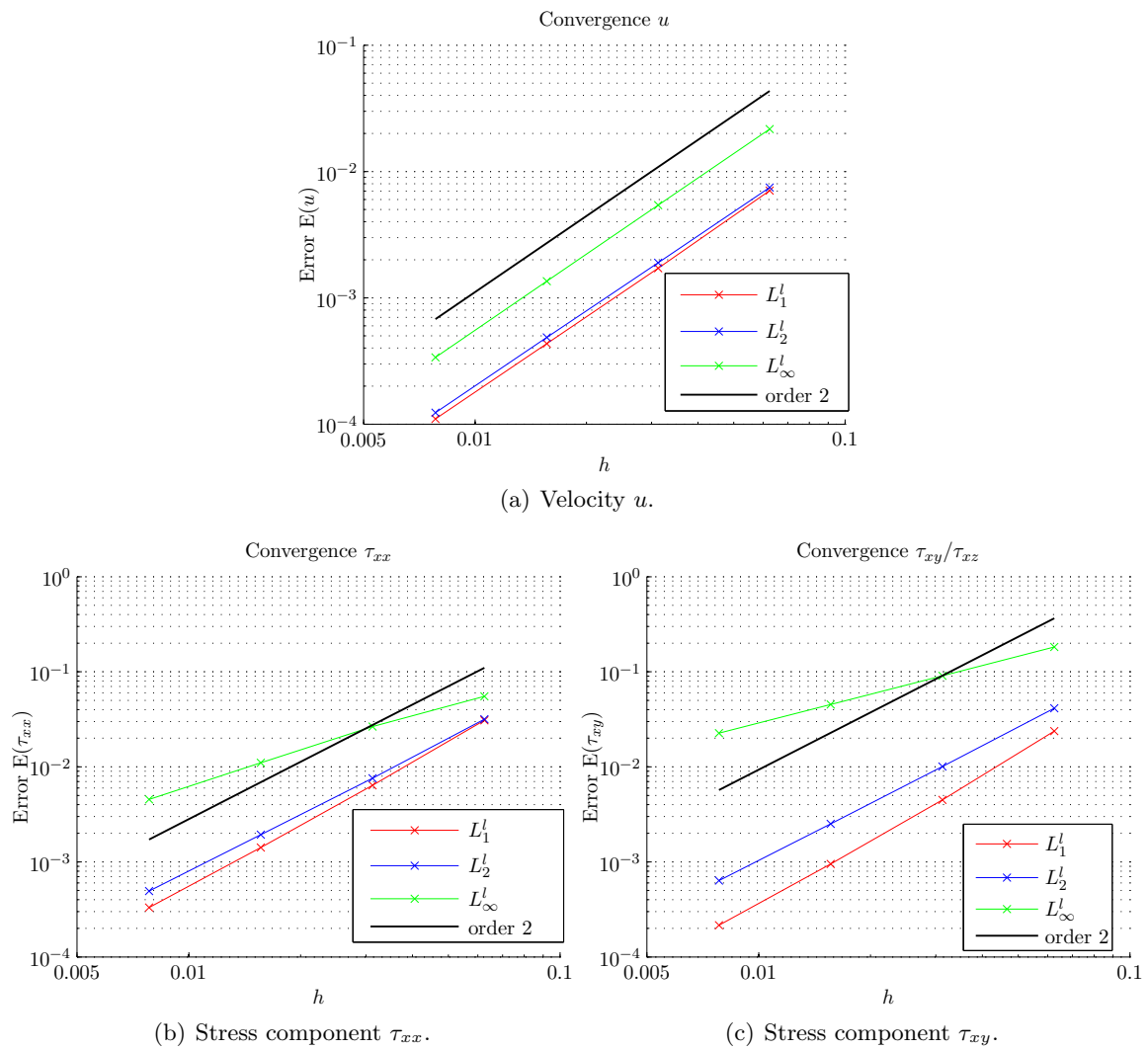


Figure 7.10: Order of convergence for stresses and velocity Oldroyd-B model.

Table 7.8: Errors for the PTT model.

L_1^l -norm										
l	$E_1^l(u)$	$E_1^l(p)$	$E_1^l(\tau_{xx})$	$E_1^l(\tau_{xy})$	$E_1^l(\tau_{xz})$	$E_1^l(\tau_{yy})$	$E_1^l(\tau_{zz})$	$E_1^l(v)$	$E_1^l(w)$	$E_1^l(\tau_{yz})$
1	7.00 ₋₃	2.71 ₋₃	2.97 ₋₂	2.36 ₋₂	2.36 ₋₂	5.65 ₋₄	5.65 ₋₄	1.06 ₋₆	1.06 ₋₆	2.45 ₋₄
2	1.70 ₋₃	7.73 ₋₄	6.15 ₋₃	4.42 ₋₃	4.42 ₋₃	1.14 ₋₄	1.14 ₋₄	2.50 ₋₇	2.50 ₋₇	5.48 ₋₅
3	4.31 ₋₄	2.05 ₋₄	1.37 ₋₃	9.30 ₋₄	9.30 ₋₄	2.52 ₋₅	2.52 ₋₅	3.07 ₋₈	3.07 ₋₈	1.27 ₋₅
4	1.09 ₋₄	5.25 ₋₅	3.20 ₋₄	2.10 ₋₄	2.10 ₋₄	5.85 ₋₆	5.85 ₋₆	3.96 ₋₉	3.96 ₋₉	3.05 ₋₆
L_2^l -norm										
l	$E_2^l(u)$	$E_2^l(p)$	$E_2^l(\tau_{xx})$	$E_2^l(\tau_{xy})$	$E_2^l(\tau_{xz})$	$E_2^l(\tau_{yy})$	$E_2^l(\tau_{zz})$	$E_2^l(v)$	$E_2^l(w)$	$E_2^l(\tau_{yz})$
1	7.41 ₋₃	2.96 ₋₃	3.04 ₋₂	4.16 ₋₂	4.16 ₋₂	6.78 ₋₄	6.78 ₋₄	1.24 ₋₆	1.24 ₋₆	3.24 ₋₄
2	1.88 ₋₃	1.14 ₋₃	7.28 ₋₃	1.01 ₋₂	1.01 ₋₂	1.51 ₋₄	1.51 ₋₄	3.41 ₋₇	3.41 ₋₇	7.47 ₋₅
3	4.82 ₋₄	4.17 ₋₄	1.86 ₋₃	2.52 ₋₃	2.52 ₋₃	3.65 ₋₅	3.65 ₋₅	5.24 ₋₈	5.24 ₋₈	1.75 ₋₅
4	1.23 ₋₄	1.49 ₋₄	4.76 ₋₄	6.34 ₋₄	6.34 ₋₄	9.02 ₋₆	9.02 ₋₆	7.26 ₋₉	7.26 ₋₉	4.24 ₋₆
L_∞^l -norm										
l	$E_\infty^l(u)$	$E_\infty^l(p)$	$E_\infty^l(\tau_{xx})$	$E_\infty^l(\tau_{xy})$	$E_\infty^l(\tau_{xz})$	$E_\infty^l(\tau_{yy})$	$E_\infty^l(\tau_{zz})$	$E_\infty^l(v)$	$E_\infty^l(w)$	$E_\infty^l(\tau_{yz})$
1	2.17 ₋₂	5.22 ₋₃	5.27 ₋₂	1.85 ₋₁	1.85 ₋₁	1.80 ₋₃	1.80 ₋₃	2.63 ₋₆	2.63 ₋₆	1.57 ₋₃
2	5.41 ₋₃	2.83 ₋₃	2.56 ₋₂	9.16 ₋₂	9.16 ₋₂	4.87 ₋₄	4.87 ₋₄	1.09 ₋₆	1.09 ₋₆	5.72 ₋₄
3	1.35 ₋₃	1.46 ₋₃	1.07 ₋₂	4.55 ₋₂	4.55 ₋₂	2.20 ₋₄	2.20 ₋₄	2.84 ₋₇	2.84 ₋₇	1.86 ₋₄
4	3.38 ₋₄	7.46 ₋₄	4.43 ₋₃	2.27 ₋₂	2.27 ₋₂	8.53 ₋₅	8.53 ₋₅	5.78 ₋₈	5.78 ₋₈	5.72 ₋₅

Table 7.9: Order of convergence for the PTT model.

order	u			p			τ_{xx}			τ_{xy} / τ_{xz}			τ_{yy} / τ_{zz}		
	L_1^l	L_2^l	L_∞^l	L_1^l	L_2^l	L_∞^l	L_1^l	L_2^l	L_∞^l	L_1^l	L_2^l	L_∞^l	L_1^l	L_2^l	L_∞^l
p_1	2.04	1.98	2.01	1.81	1.37	0.88	2.27	2.07	1.04	2.41	2.04	1.01	2.32	2.17	1.88
p_2	1.98	1.96	2.00	1.92	1.46	0.95	2.17	1.96	1.26	2.25	2.01	1.01	2.17	2.05	1.14
p_3	1.98	1.98	2.00	1.96	1.48	0.97	2.10	1.97	1.28	2.14	1.99	1.01	2.10	2.02	1.37

order	v			τ_{yz}		
	L_1^l	L_2^l	L_∞^l	L_1^l	L_∞^l	L_∞^l
p_1	2.09	1.86	1.28	2.16	2.12	1.46
p_2	3.03	2.70	1.93	2.11	2.09	1.62
p_3	2.96	2.85	2.30	2.06	2.05	1.70

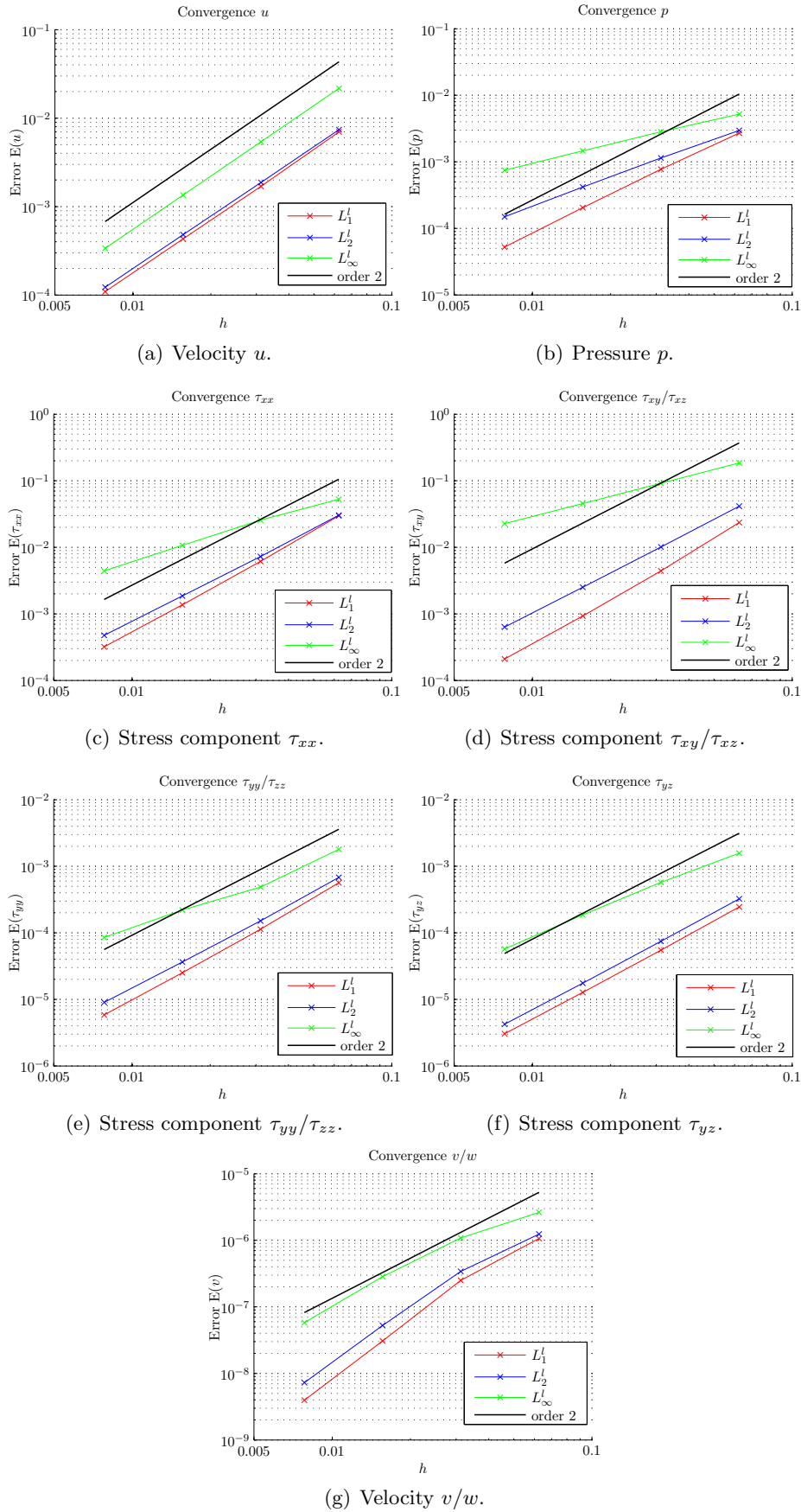


Figure 7.11: Order of convergence for stresses and velocity, PTT model.

7.4 Flow over a Hole

We investigate the flow of viscoelastic fluids and a Newtonian fluid over a square hole. Therefore, we consider a domain $\Omega = 8.0 \times 4.0 \times 2.0$, as illustrated in Figure 7.12. We choose a resolution of $160 \times 80 \times 40$ grid cells resulting in an equidistant grid with mesh space $h = 0.05$. We impose a parabolic velocity profile with a maximum velocity of one at inflow, which we

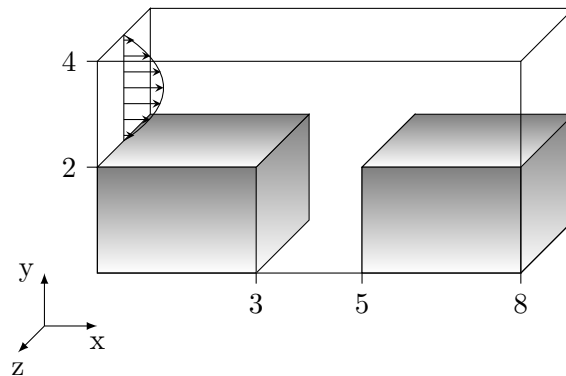


Figure 7.12: Sketch of the flow over a hole.

obtain from the simulation of a flow through a channel of a Newtonian fluid. The stress tensor components are set to zero at inflow. At outflow, we impose homogeneous Neumann boundary conditions for the velocity components and the stress tensor components. Furthermore, we employ no-slip boundary conditions at the walls. We choose the parameters in the simulation as listed in Table 7.10 and analyze the result at time $t = 10$ at a cut normal to the z -axis at $z = 1.0$. Figure 7.13 shows the numerical results for a Newtonian fluid, an Oldroyd-B fluid and different PTT fluids in comparison to experimental results obtained by Boger and Walters [9]. The numerical results are visualized by the Line Integral Convolution (LIC) technique to present vector fields with high accuracy. In the experiment, Boger and Walters investigated a Newtonian and a Boger fluid in the flow over a square hole. They observed that for low Reynolds numbers the recirculating vortex in the hole is essentially symmetric for a Newtonian fluid (see Figure 7.13(c)), but for a viscoelastic Boger fluid the vortex is asymmetric (see Figure 7.13(d)). We were able to reproduce this result in our simulations. While we obtain a symmetric vortex structure for the Newtonian fluid, we attain an asymmetric

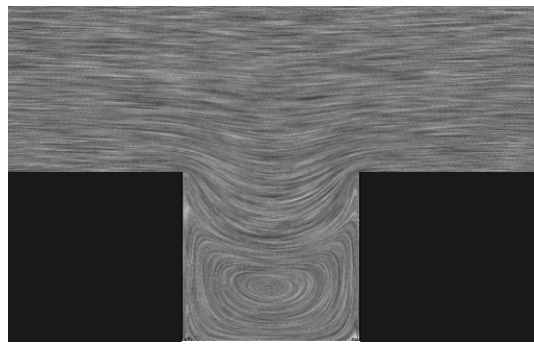
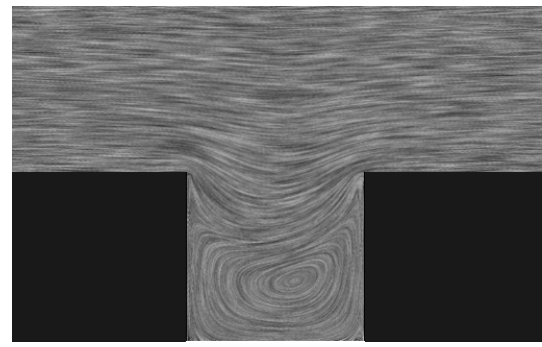
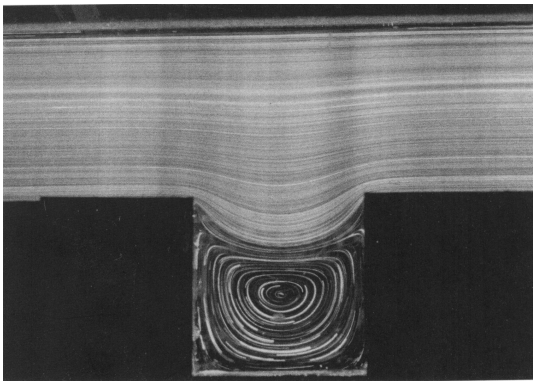
Table 7.10: Parameters of the flow over a hole.

Reynolds number	1.0
Weissenberg number	1.0
β	0.1
ξ	0.07
ε	0.02 and 0.25
Projection method	semi-implicit
Convective terms	WENO

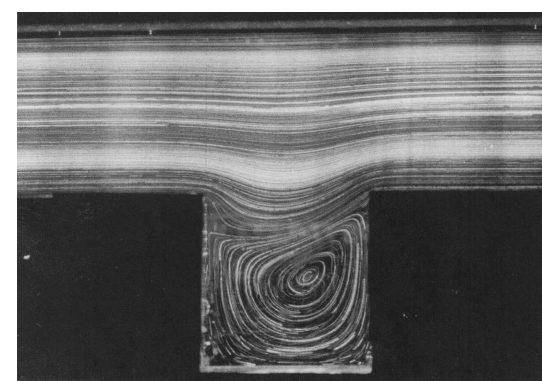
vortex structure for the Oldroyd-B and PTT fluids (see Figure 7.13). The Oldroyd-B fluid shows the highest asymmetry in the vortex structure and fits best to the experimental results of Boger and Walters. This was to be expected since Boger fluids are viscoelastic fluids with a constant shear viscosity and therefore are best represented by the Oldroyd-B fluid, which predicts a constant shear viscosity.

Figure 7.14 shows the contour lines of the vector length of the recirculating vortex in the square hole. Again, we note that the Oldroyd-B model shows the highest asymmetry in the vortex. For the PTT model, we have a slight asymmetry, which increases with decreasing ε . The PTT fluid with $\varepsilon = 0.25$ is stronger extensional thickening and shear thinning than the PTT fluid with $\varepsilon = 0.02$. Furthermore, we obtain a larger vortex core for the PTT model with $\varepsilon = 0.25$ in comparison to the PTT model with $\varepsilon = 0.02$. We achieve similar results for the linear and exponential PTT model. Therefore, we restrict our further investigations to the exponential PTT model.

Furthermore, we examine the stress behaviour in the overall domain. Figure 7.15 shows two cut planes normal to the x -axis through the domain. We situate the first cut near the inflow domain and the second cut at the second corner of the hole. The cuts are shaped by the vector field and coloured by the principal stress pS , which we introduced at the beginning of this chapter. In Figure 7.15, we see that the principal stress values are smaller for the PTT model than for the Oldroyd-B model and that the principal stress has its highest values near the no-slip boundary and its lowest values in the middle of the cuts. We observe the connection between the velocity gradient and principal stress: the higher the velocity gradient, the higher the values of the principal stress. In Figures 7.16-7.18, we colour the cut normal to the z -axis at $z = 1.0$ by velocities and stresses. The Oldroyd-B model has very high values of shear, normal and principal stress at the corner singularities, especially at the second corner of the hole. The shear, normal and principal stresses sharpen much less rapidly for the exponential PTT model. We get the smoothest results with the exponential PTT model with $\varepsilon = 0.25$. This confirms the theoretical findings of Renardy [61] concerning the different thicknesses of boundary layers for different models. The difficulty of resolving the steep stress gradients near the boundary and especially near corner singularities is one reason for the numerical breakdown in simulations of viscoelastic fluids. Figure 7.19 illustrates how steep and dramatic these stress gradients are at the corners. Here, we plot the elastic stress tensor components along a probe line, displayed as the red line in the sketch 7.19(a). The stress gradients are dramatically steep for the Oldroyd-B model. For the PTT model, the stress components show a much smoother behaviour especially with increasing ε .

(a) Newtonian, $Re=1$ (b) Oldroyd-B, $Re=1$, $We=1$, $\beta = 0.1$ 

(c) Newtonian Fluid Experiment



(d) Boger Fluid Experiment

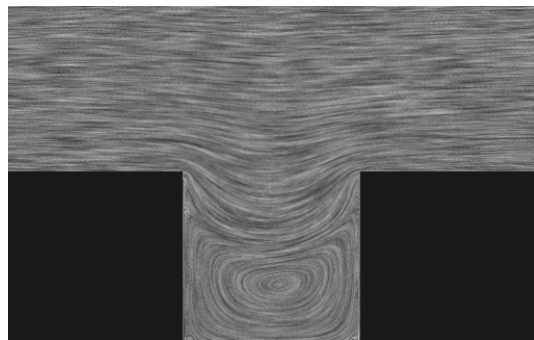
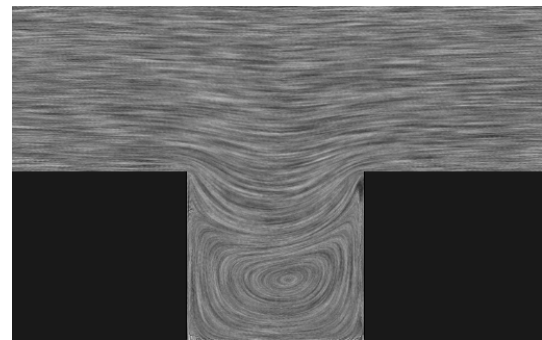
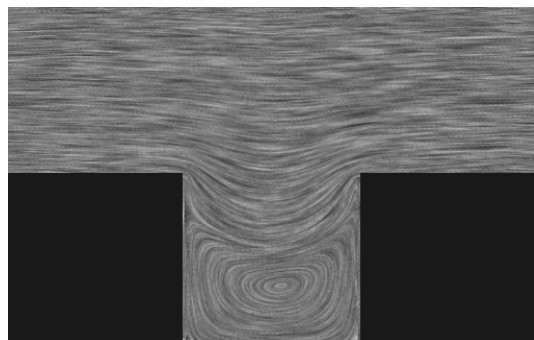
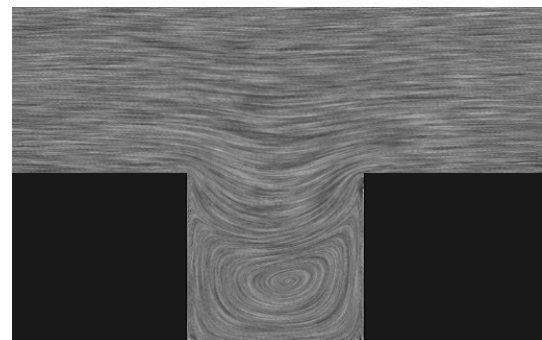
(e) Exponential PTT, $Re=1$, $We=1$, $\beta = 0.1$, $\varepsilon = 0.25$, $\xi = 0.07$ (f) Exponential PTT, $Re=1$, $We=1$, $\beta = 0.1$, $\varepsilon = 0.02$, $\xi = 0.07$ (g) Linear PTT, $Re=1$, $We=1$, $\beta = 0.1$, $\varepsilon = 0.25$, $\xi = 0.07$ (h) Linear PTT, $Re=1$, $We=1$, $\beta = 0.1$, $\varepsilon = 0.02$, $\xi = 0.07$

Figure 7.13: Numerical results in comparison with experimental results for a flow over a hole, ((c), (d) are from D. V. Boger and K. Walters [9]). The numerical results are shown at a cut normal to the z -axis at $z = 1.0$ and they are visualized by the LIC technique.

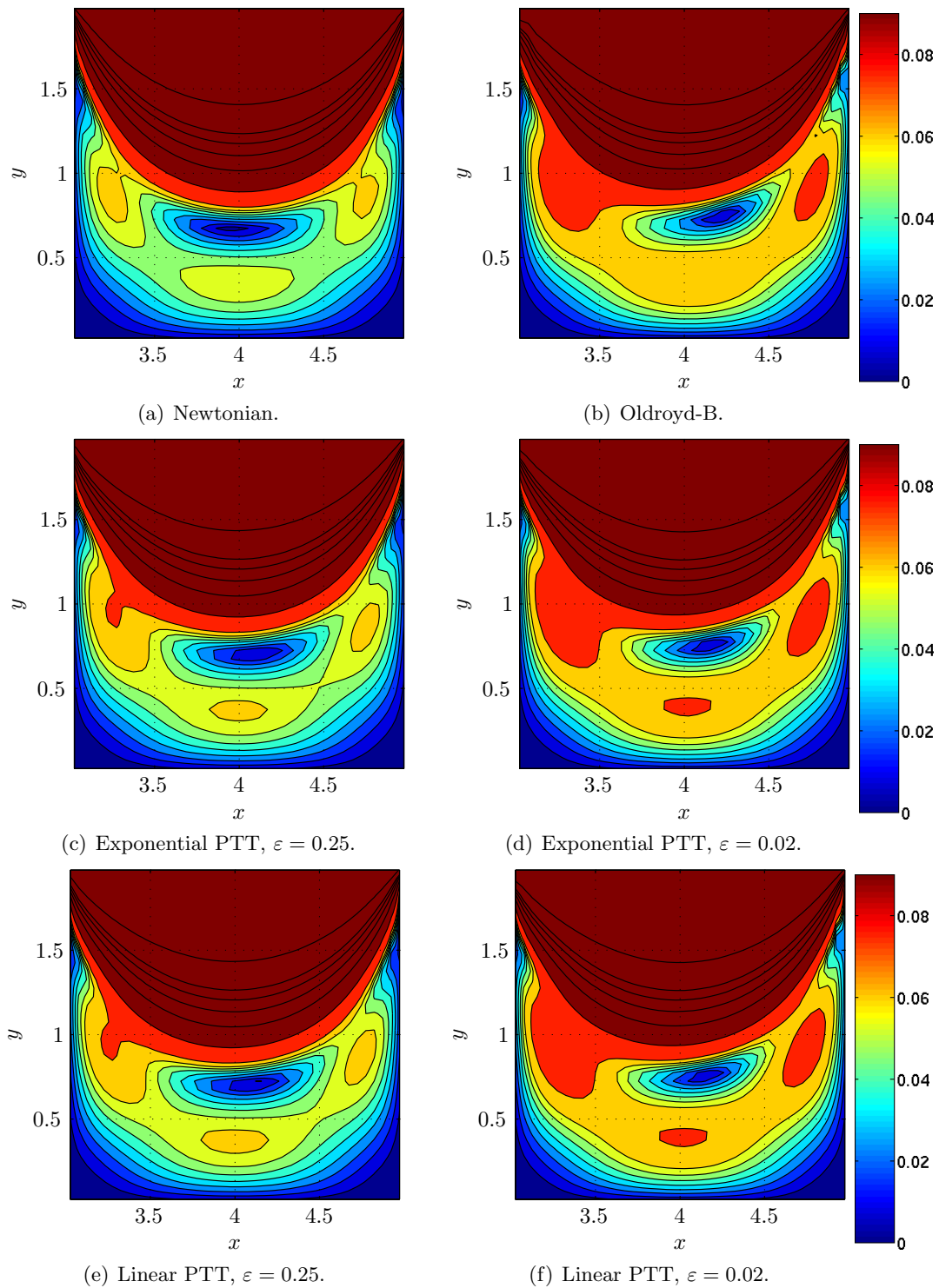
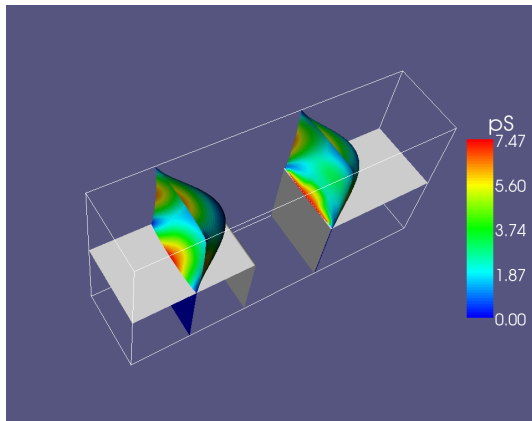
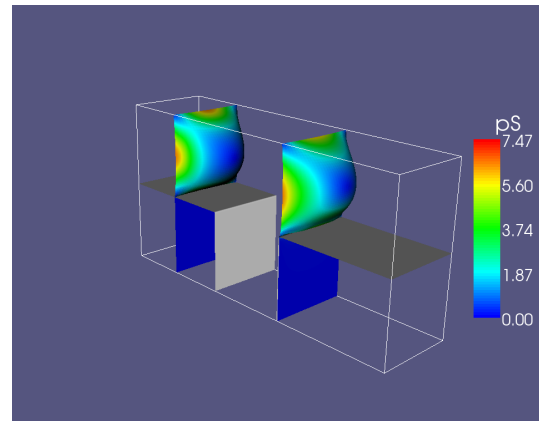


Figure 7.14: Vector length contour lines of the recirculating vortex in the hole at a cut normal to the z -axis at $z = 1.0$ for Newtonian, Oldroyd-B and PTT fluids.



(a) Oldroyd-B, back.



(b) Oldroyd-B, front.

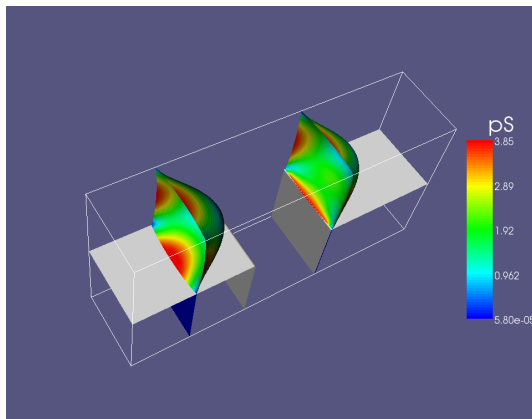
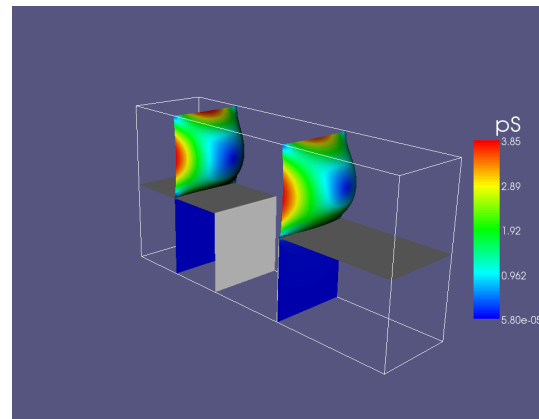
(c) Exponential PTT, $\varepsilon = 0.25$, back.(d) Exponential PTT, $\varepsilon = 0.25$, front.

Figure 7.15: Cut planes in shape of the velocity vector field coloured by the principal stress for the Oldroyd-B and exponential PTT fluid.

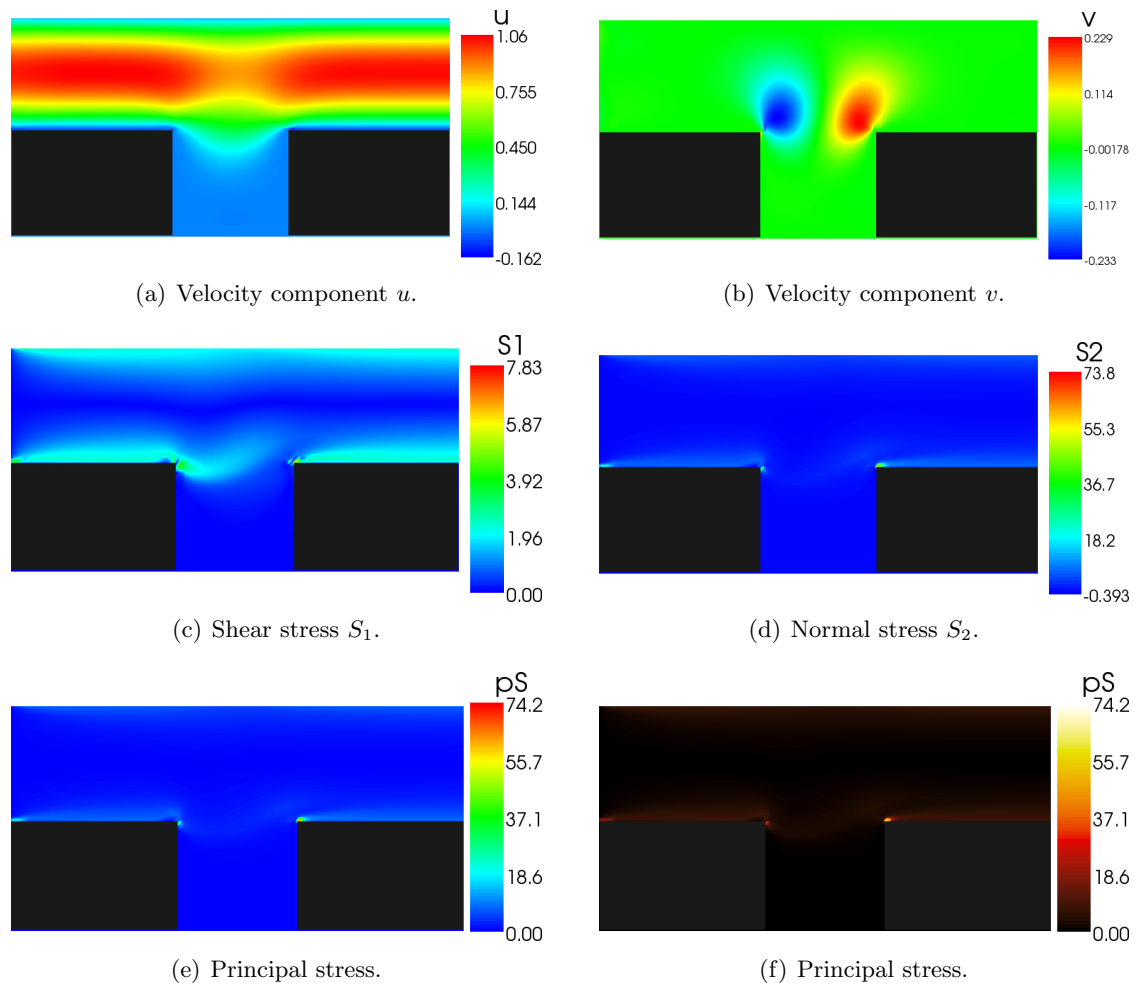


Figure 7.16: Stresses and velocities at a cut normal to the z -axis at $z = 1.0$, Oldroyd-B.

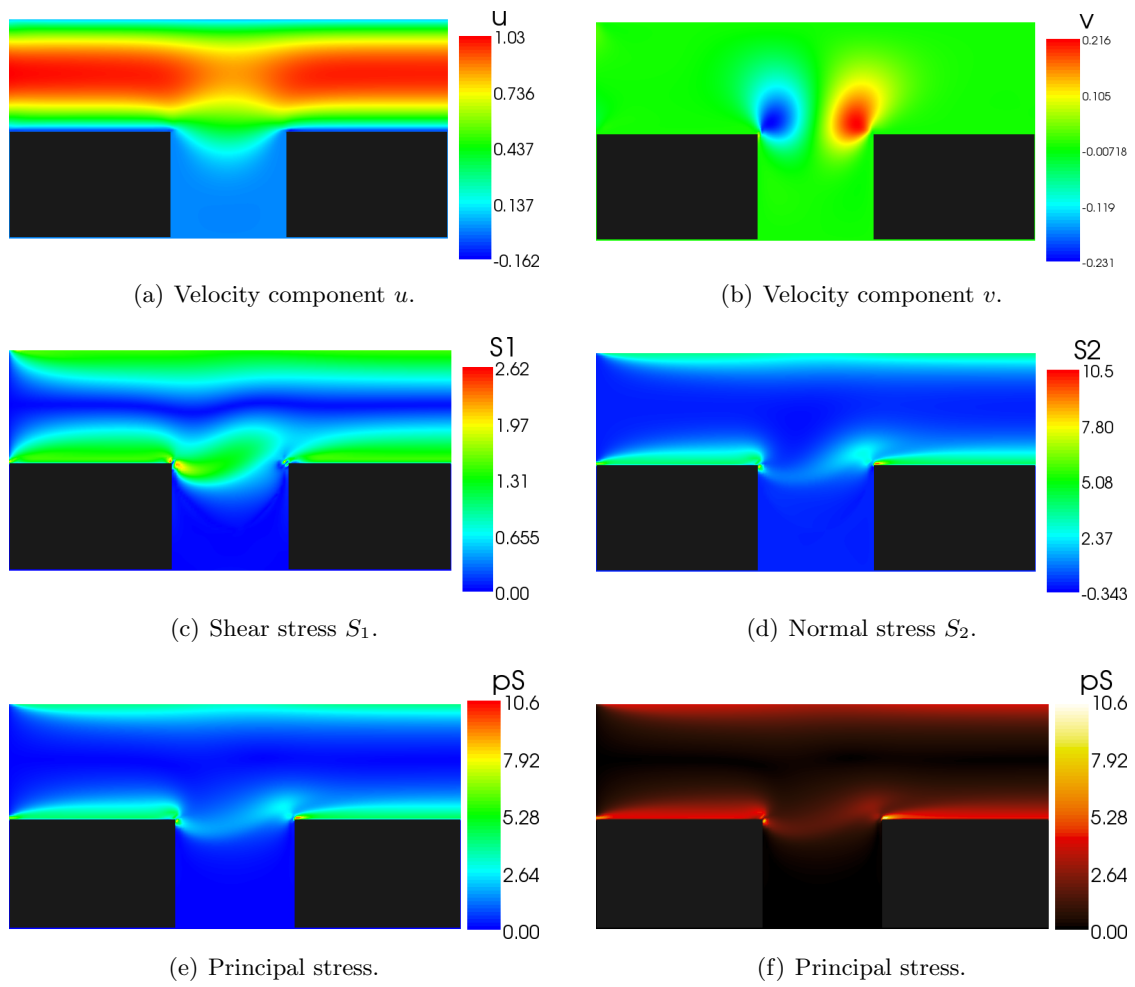


Figure 7.17: Stresses and velocities at a cut normal to the z -axis at $z = 1.0$, exponential PTT $\varepsilon = 0.02$.

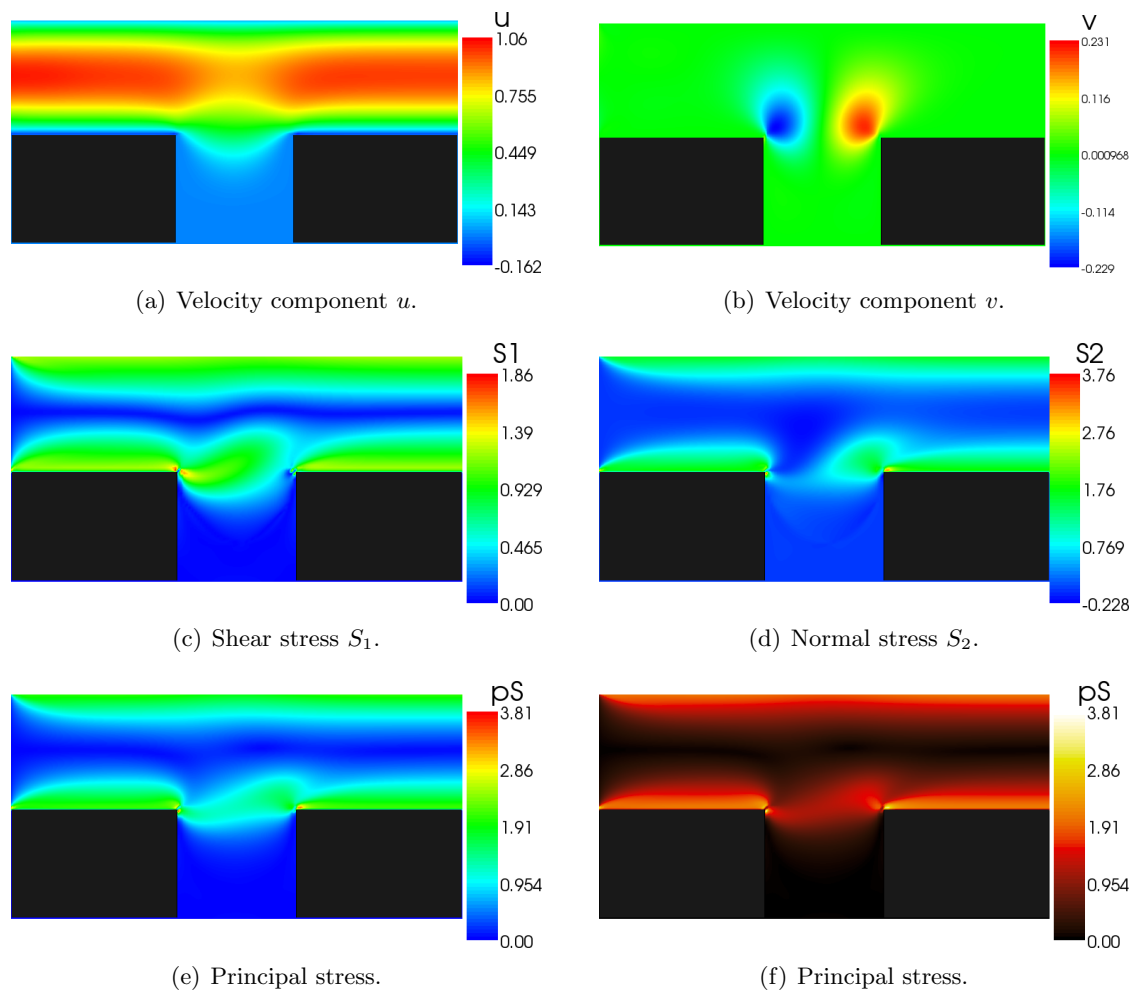


Figure 7.18: Stresses and velocities at a cut normal to the z -axis at $z = 1.0$, exponential PTT $\varepsilon = 0.25$.

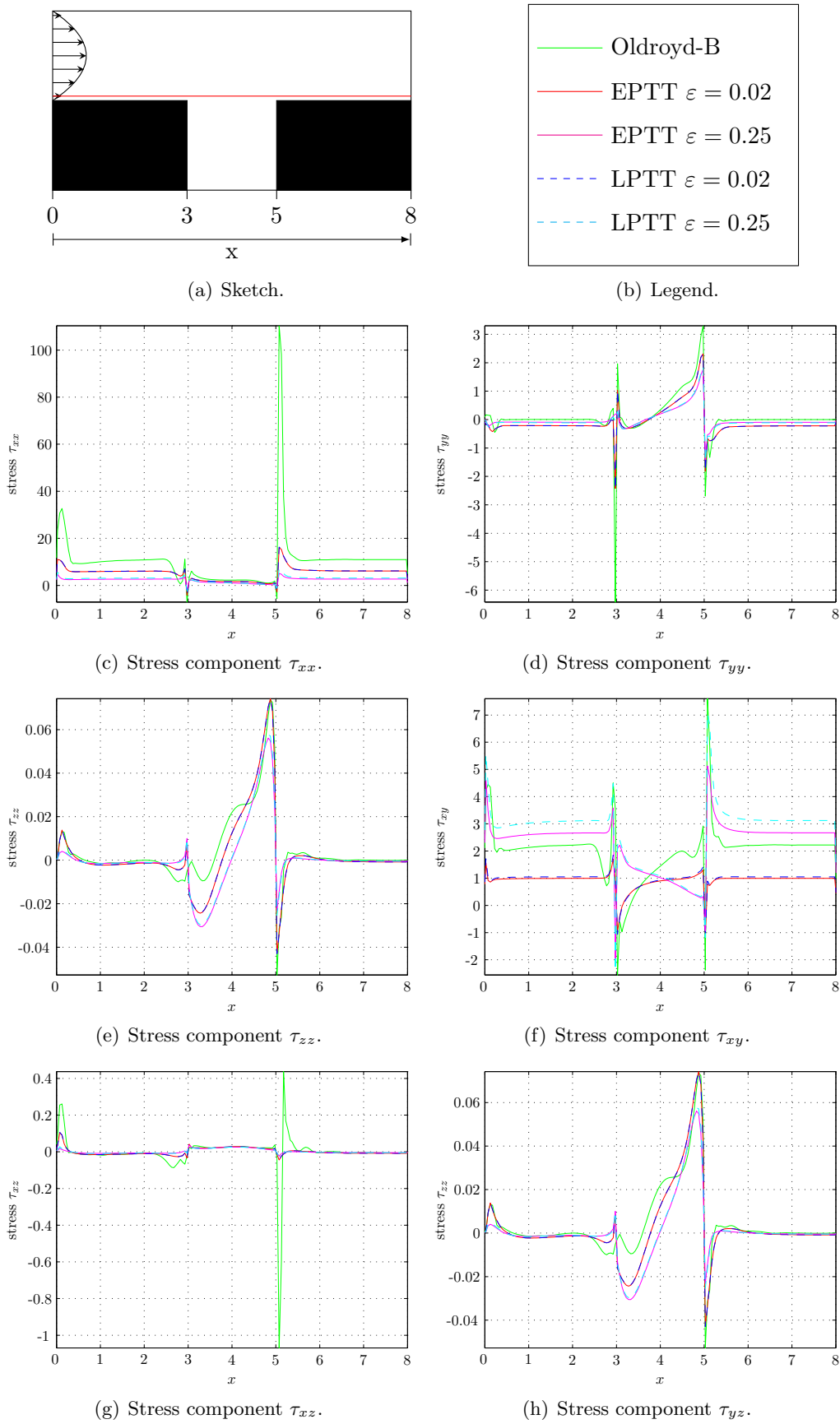


Figure 7.19: Behaviour of the elastic stress tensor components near the corner singularities.

7.5 Kármán Vortex Street

We investigate the flow past an inclined plate, which results in a Kármán Vortex Street. We consider a domain $\Omega = 60.0 \times 12.0 \times 6.0$, which we resolve by $300 \times 60 \times 30$ grid cells resulting in an equidistant grid with a mesh size of 0.2 (see Figure 7.20). We set periodic boundary conditions in the z -direction to simulate an infinite domain in this direction. Therefore, we can set the analytical steady state expressions (7.25) and (7.25) for the velocity and the stress components at inflow. At outflow, we set homogeneous Neumann boundary conditions. The inclined plate is placed in the domain as illustrated in Figure 7.20. The remaining parameters are gathered in Table 7.11. We examine the vortex street at time $t = 160$ and at a cut normal to the z -axis at $z = 3$.

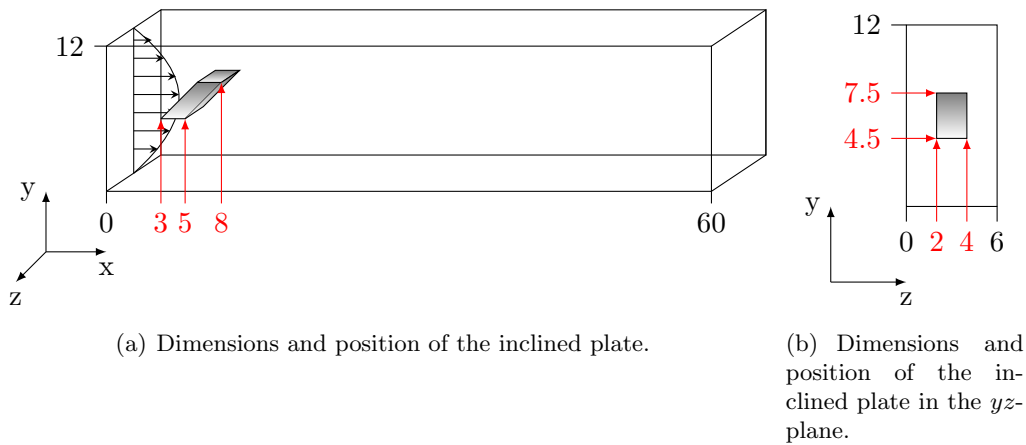
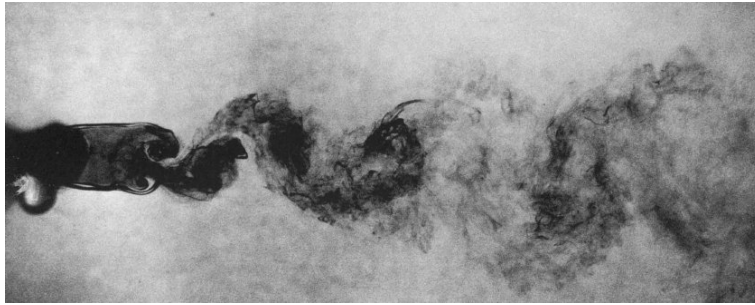


Figure 7.20: Sketch of the Kármán vortex street problem.

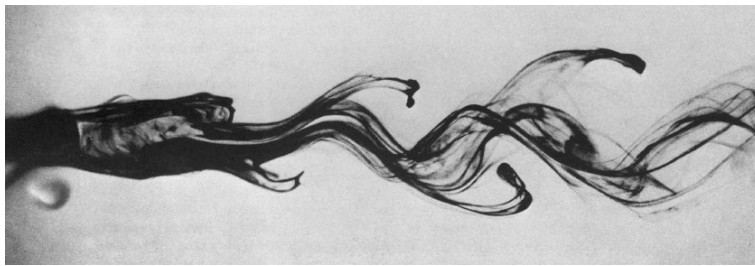
We investigate the Kármán Vortex Street for a Newtonian fluid, an Oldroyd-B fluid and PTT fluids with $\varepsilon = 0.25$ and $\varepsilon = 0.02$ for both the linear form and the exponential form. Figure 7.21 shows pictures from a laboratory experiment of the vortex shedding behind a cylinder for a Newtonian fluid and a dilute polymer solution obtained by Boger and Walters [9]. We observe that adding even small amounts of a dissolved polymer to a Newtonian fluid leads to different vortex shedding behaviour.

Table 7.11: Parameters of Kármán vortex street.

Reynolds number	400
Weissenberg number	0.5
β	0.1
ξ	0.07
ε	0.02 and 0.25
Projection method	explicit
Convective terms	VONOS



(a) Newtonian, water



(b) Viscoelastic, 50 ppm aqueous solution of polyacrylamide (AP 45)

Figure 7.21: Vortex shedding behind a cylinder (from D. V. Boger and K. Walters [9])

Compared to the purely Newtonian solvent, the viscoelastic fluid shows a reduction in frequency of vortex shedding, an increased length of the formation region just behind the cylinder, and an alteration of the form of the relative vorticity patterns. These observations can be explained by the higher elongational viscosity of an elastic liquid and by the suppression of velocity fluctuations by elasticity.

We could observe the same qualitative behaviour in our simulations. Figure 7.22 shows an LIC picture of the Kármán vortex street coloured by the vector length and Figure 7.23 shows the contour lines of the vector length. We observe that the vortices behind the inclined plate have an increased length for all viscoelastic fluids. The Oldroyd-B fluid shows the strongest elongation of the vortices. Additionally, the Oldroyd-B fluid exhibits the strongest suppression of velocity fluctuations. The PTT fluids with $\varepsilon = 0.02$ show also a considerable suppression of velocity fluctuations, while the PTT fluids with $\varepsilon = 0.25$ show only a slight suppression. This could be caused by the stronger shear-thinning of PTT fluids with $\varepsilon = 0.25$.

In Figure 7.24, we observe the principal stress behaviour of the different viscoelastic fluids. The models show a very high stress concentration on the upper left corner of the inclined plate. Especially, the Oldroyd-B model predicts a high stress peak at that corner. Table 7.13 gathers the minimum and the maximum values of the velocity components and the stress components of the different models. We see that the Oldroyd-B model predicts dramatically high values for the stress components τ_{xx} , τ_{yy} and τ_{xy} , while the PTT model predicts moderate stress values and the principal stress values decrease with increasing ε . The biggest contrast is between the Oldroyd-B model and the exponential PTT model with $\varepsilon = 0.25$.

Therefore, we choose these two models for further comparisons. In Figure 7.25 and Figure 7.26, we compare the contour plots of the velocity components and the pressure for the Newtonian fluid, the Oldroyd-B fluid and the exponential PTT fluid. Figure 7.27 shows the normal stress components, Figure 7.28 the shear stress components and Figure 7.29 the normal, shear and

Table 7.12: Maximum values of the velocity and the pressure ($\varepsilon_1 = 0.02$, $\varepsilon_2 = 0.25$).

	u		v		w		p	
	Min	Max	Min	Max	Min	Max	Min	Max
Newton	-1.00	1.72	-1.00	1.09	-0.52	0.44	-1.26	0.77
Old-B	-1.19	1.65	-1.02	0.96	-0.54	0.45	-0.91	1.33
EPTT ε_1	-1.12	1.75	-1.00	0.99	-0.63	0.59	-1.40	1.28
LPTT ε_1	-1.11	1.69	-1.00	1.05	-0.55	0.46	-0.94	0.91
EPTT ε_2	-1.12	1.79	-1.00	1.10	-0.56	0.48	-1.46	1.35
LPTT ε_2	-1.11	1.74	-0.99	1.03	-0.58	0.57	-0.91	0.89

Table 7.13: Maximum values of the stress components ($\varepsilon_1 = 0.02$, $\varepsilon_2 = 0.25$).

	τ_{xx}		τ_{yy}		τ_{zz}		τ_{xy}		τ_{xz}		τ_{yz}		pS	
	Min	Max	Min	Max	Min	Max	Min	Max	Min	Max	Min	Max	Min	Max
Old-B	-262.05	258.85	-149.07	202.75	-3.50	4.81	-114.17	115.91	-17.87	17.80	-10.42	10.21	0.00	300.63
EPTT ε_1	-22.17	37.23	-22.02	24.17	-3.00	6.01	-6.76	3.77	-4.77	5.70	-3.03	2.87	0.00	41.88
LPTT ε_1	-24.40	37.56	-23.26	25.80	-3.02	5.06	-8.72	4.86	-5.24	5.77	-3.02	2.85	0.00	42.24
EPTT ε_2	-1.18	16.23	-5.83	5.98	-2.20	3.96	-1.18	16.23	-4.56	4.54	-2.87	2.81	0.00	19.54
LPTT ε_2	-3.09	20.97	-7.19	7.51	-2.28	3.55	-3.09	20.97	-4.81	4.80	-3.03	2.96	0.00	24.29

principal stress measures. The Figures illustrate the above mentioned differences between the fluids and we see significant differences between them in all components.

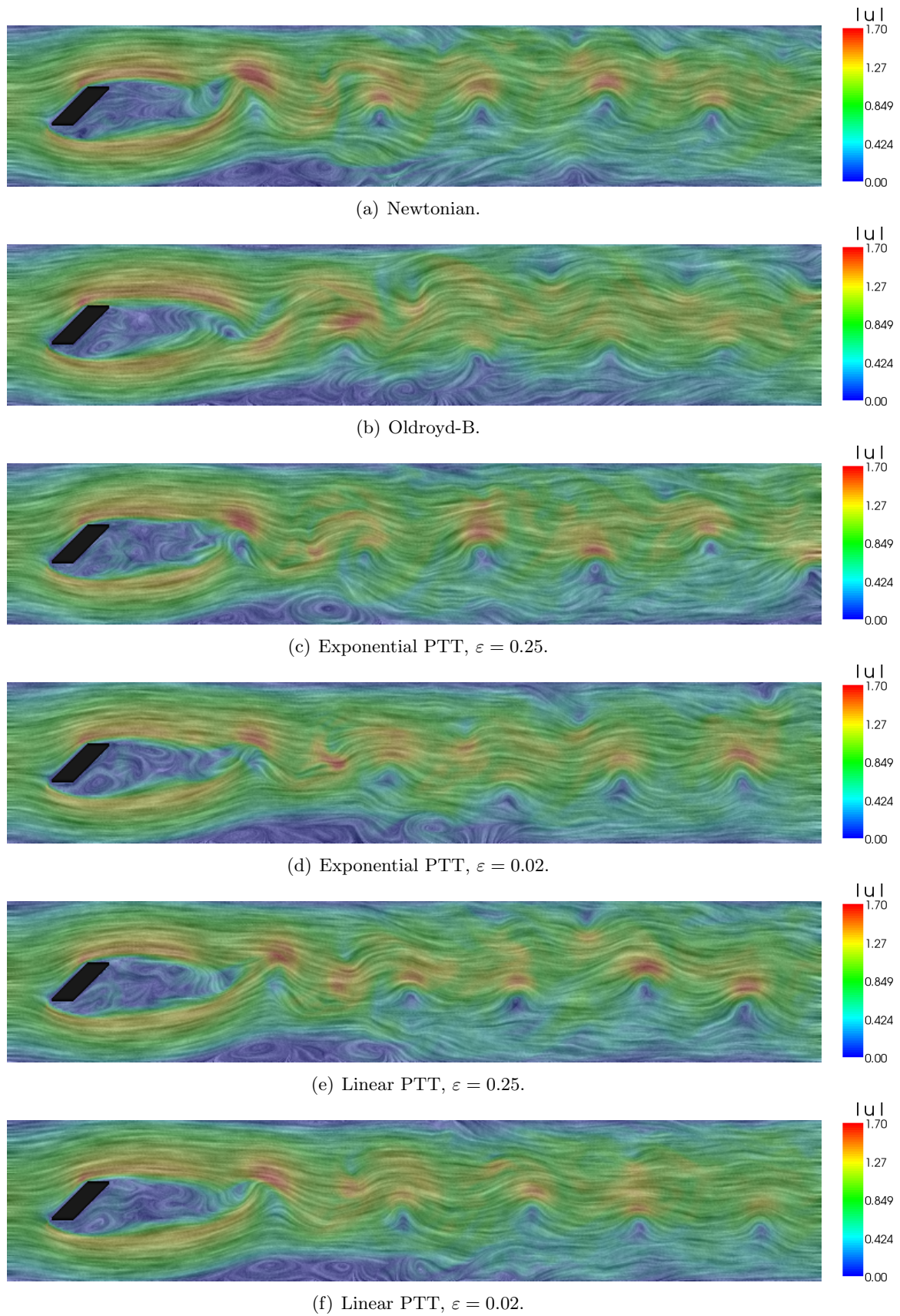
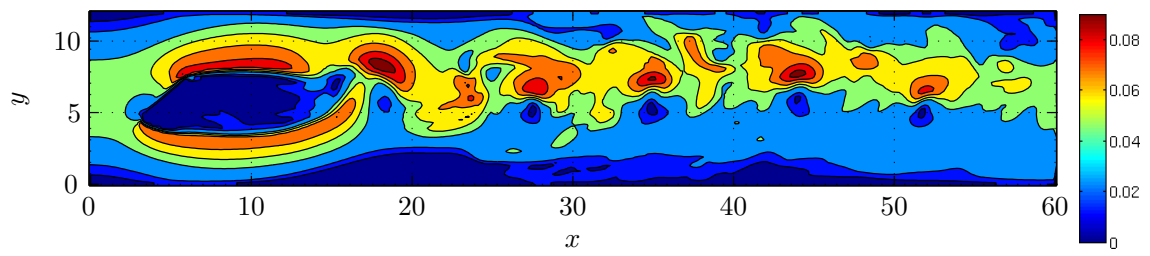
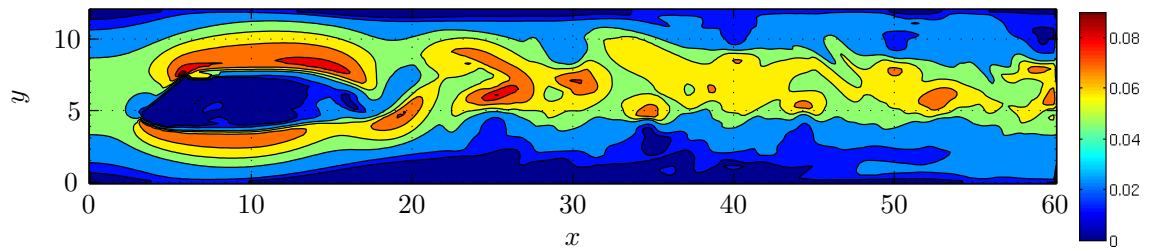


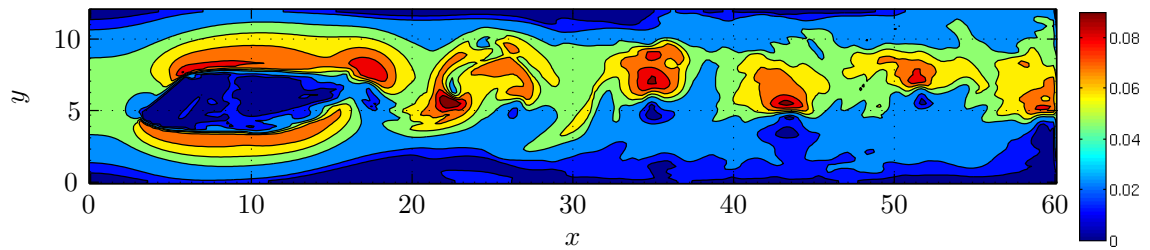
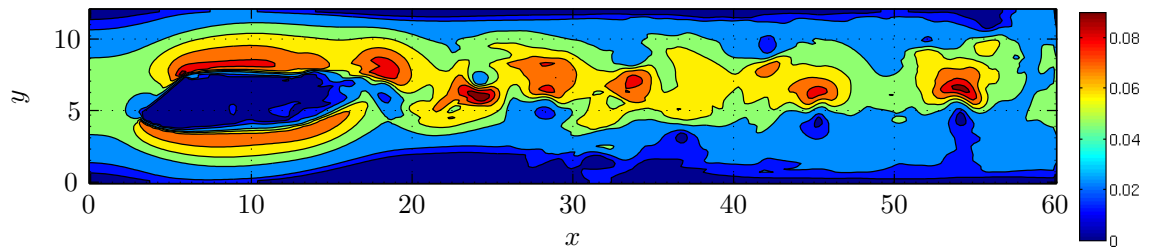
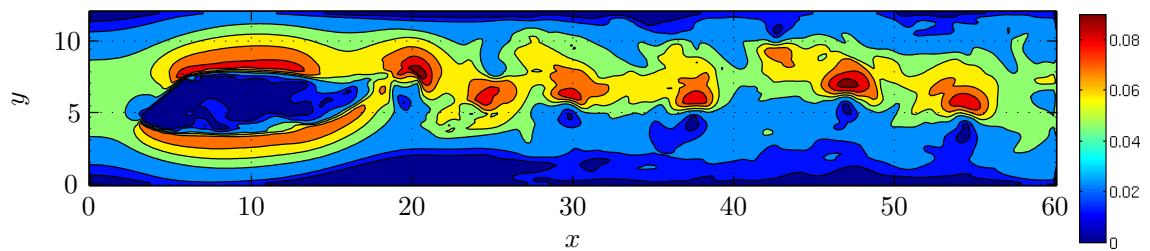
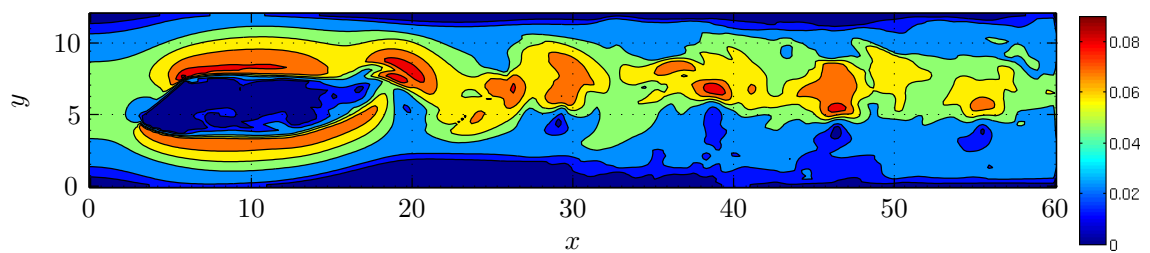
Figure 7.22: LIC picture of the Kármán vortex street coloured by the vector length $\|\mathbf{u}\|$.



(a) Newtonian.



(b) Oldroyd-B.

(c) Exponential PTT, $\varepsilon = 0.25$.(d) Exponential PTT, $\varepsilon = 0.02$.(e) Linear PTT, $\varepsilon = 0.25$.(f) Linear PTT, $\varepsilon = 0.02$.Figure 7.23: Contour lines of the Kármán vortex street of the vector length $\|\mathbf{u}\|$.

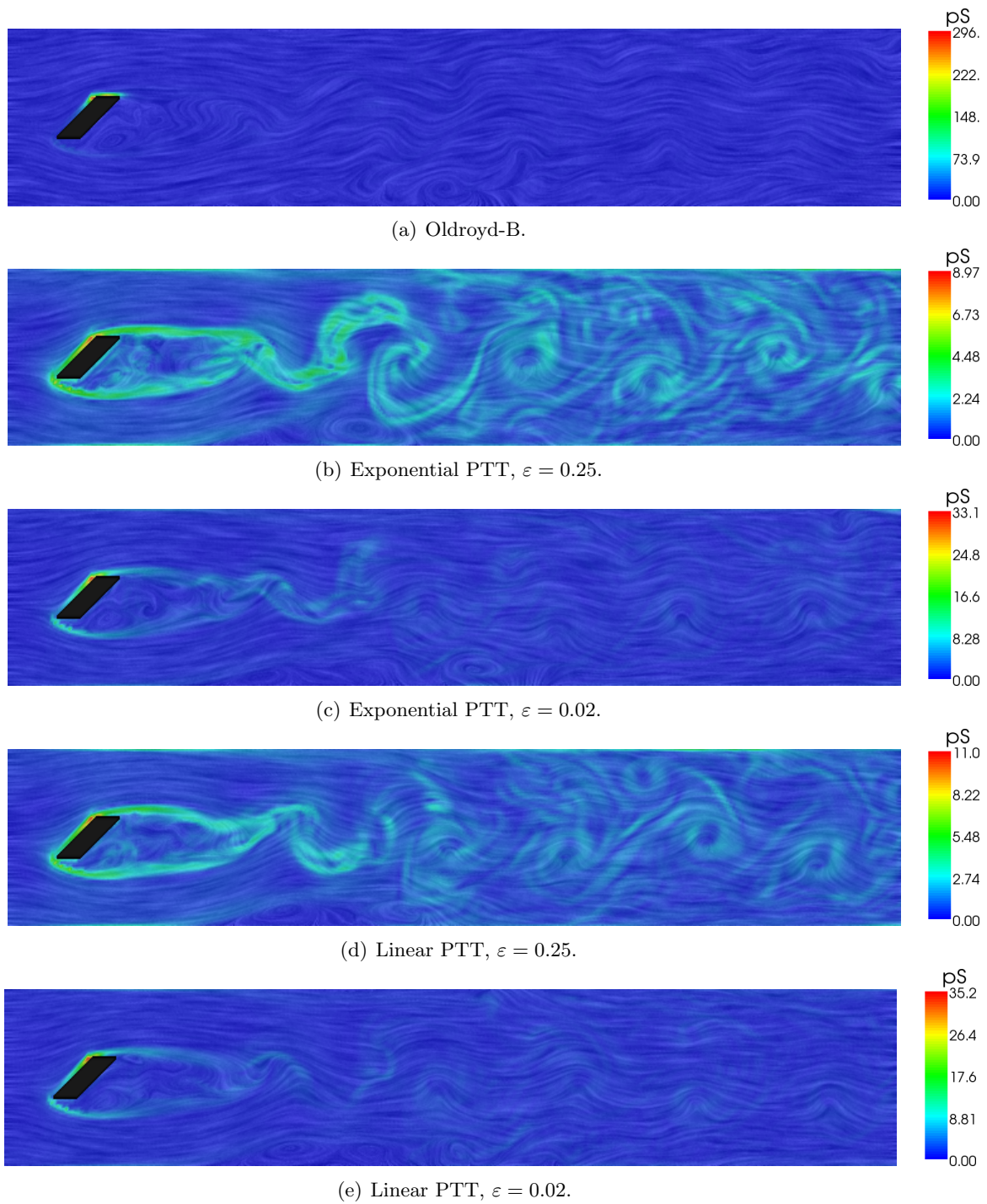
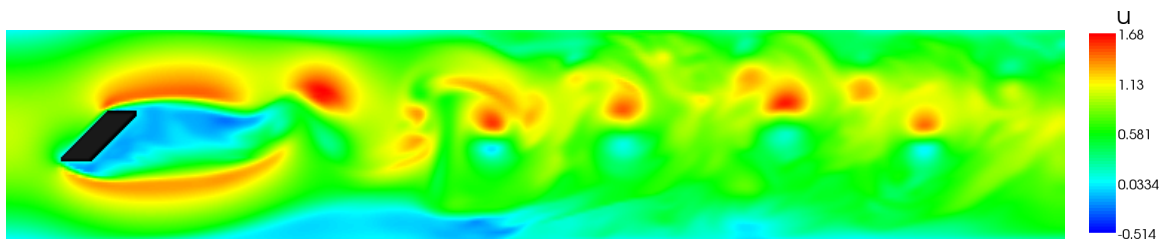
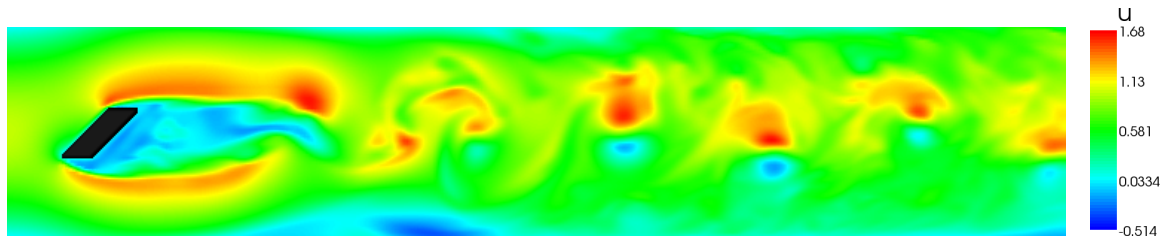
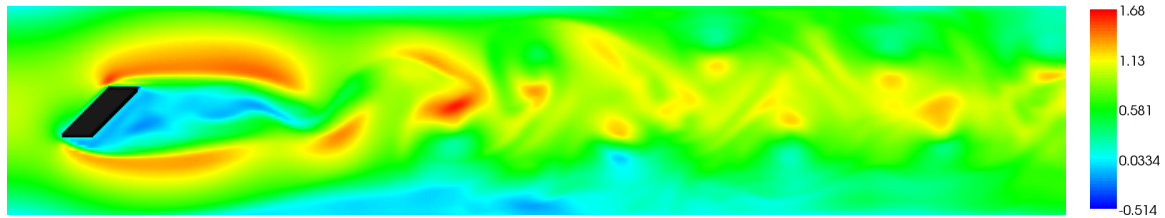
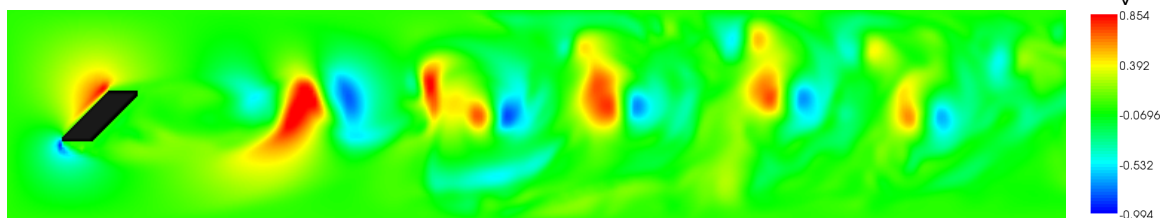
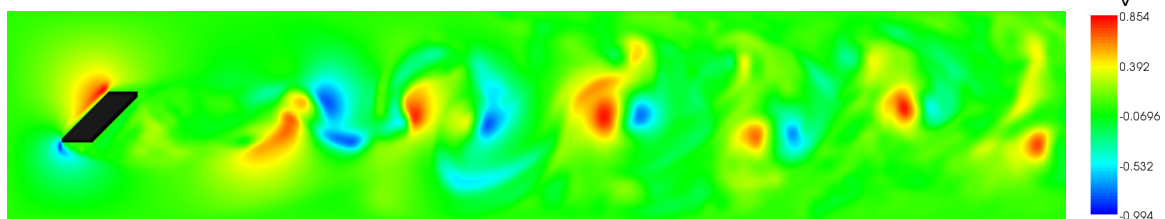
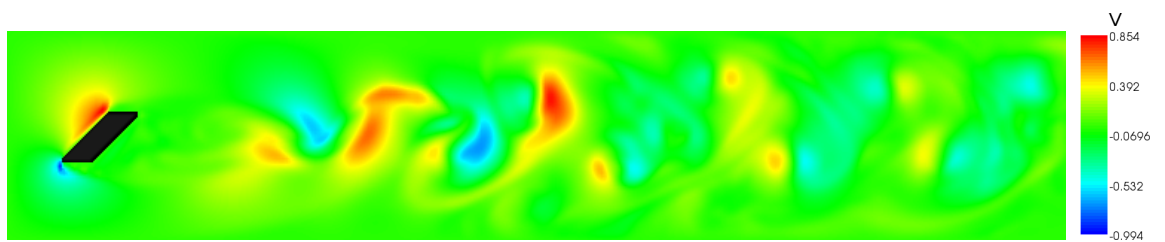
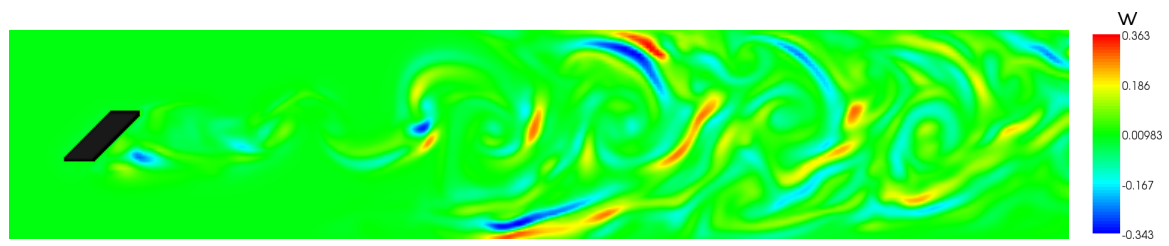
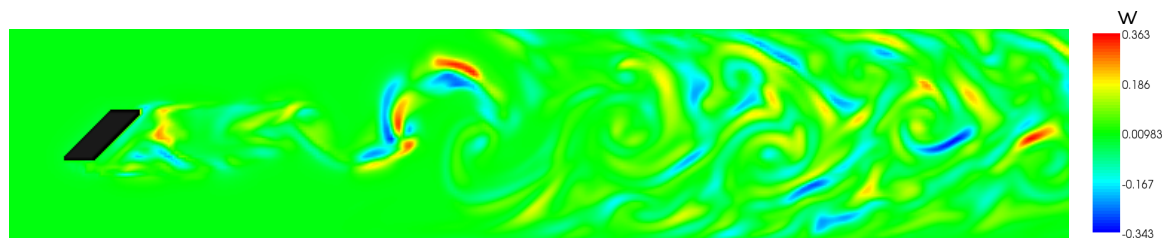
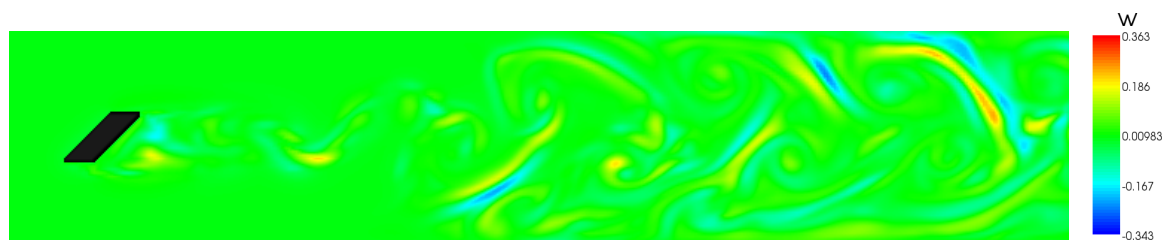
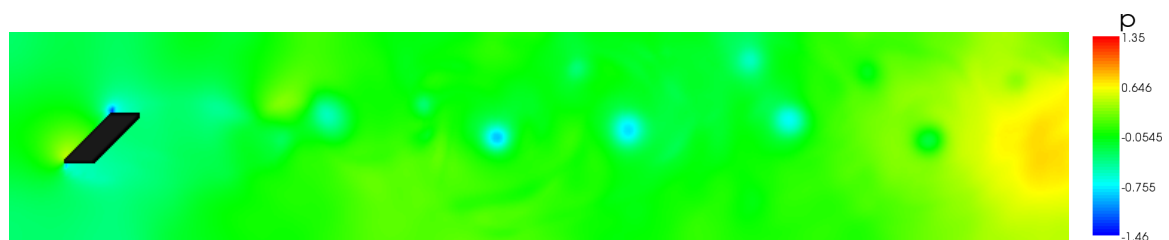
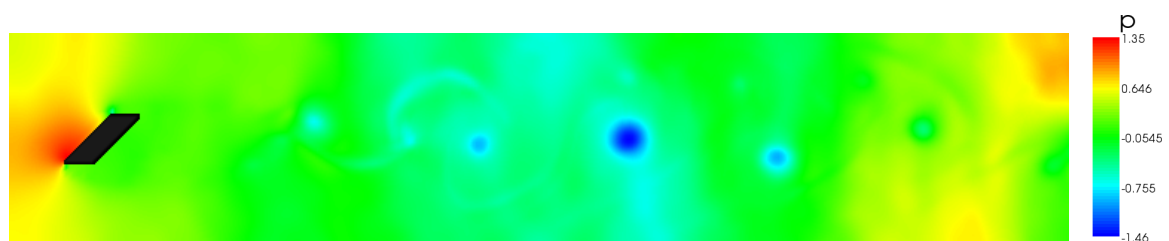
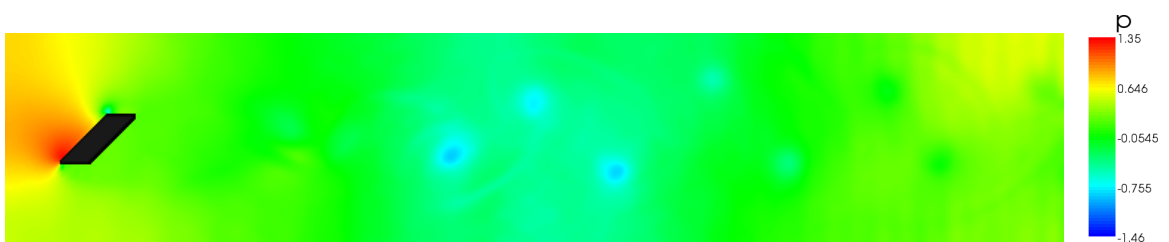


Figure 7.24: LIC picture of the Kármán vortex street coloured by the principle stress pS .

(a) Newtonian, velocity component u .(b) Exponential PTT, $\varepsilon = 0.25$, velocity component u .(c) Oldroyd-B, velocity component u .(d) Newtonian, velocity component v .(e) Exponential PTT, $\varepsilon = 0.25$, velocity component v .(f) Oldroyd-B, velocity component v .Figure 7.25: Velocity components u and v for the Kármán vortex street.

(a) Newtonian, velocity component w .(b) Exponential PTT, $\varepsilon = 0.25$, velocity component w .(c) Oldroyd-B, velocity component w .(d) Newtonian, pressure p .(e) Exponential PTT, $\varepsilon = 0.25$, pressure p .(f) Oldroyd-B, pressure p .Figure 7.26: Velocity component w and pressure p for the Kármán vortex street.

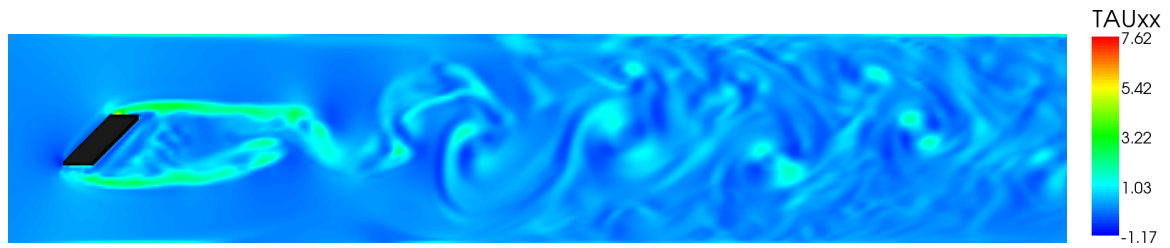
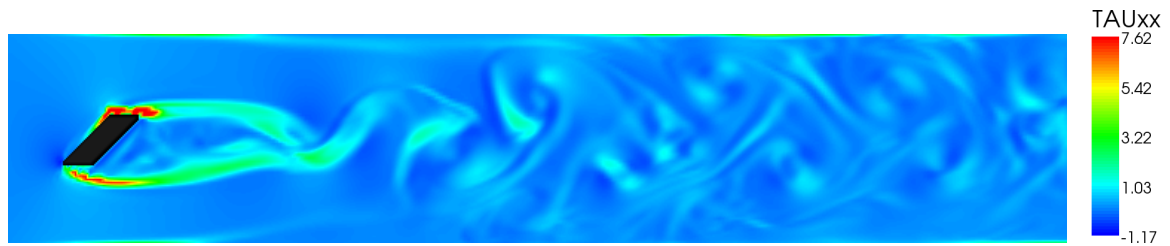
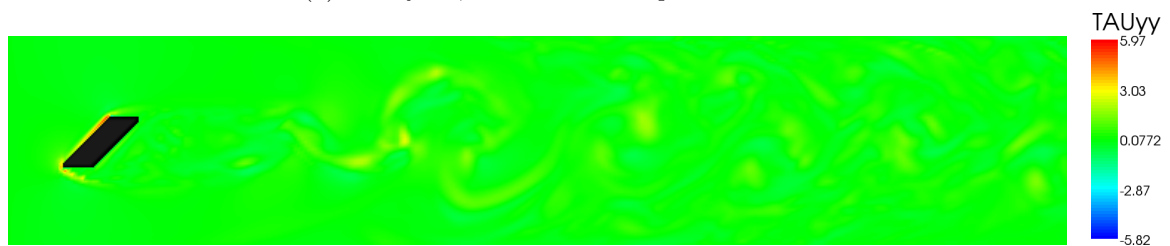
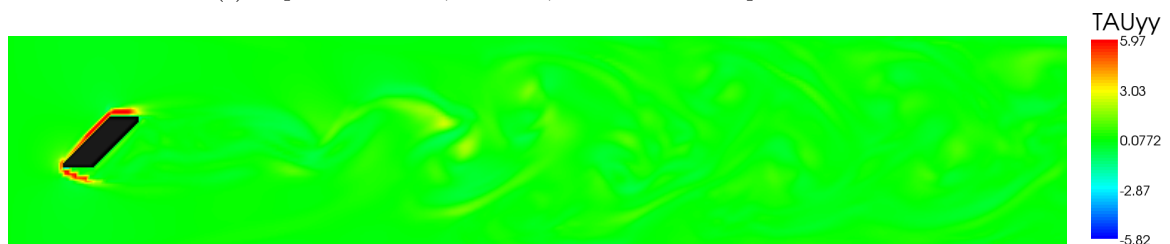
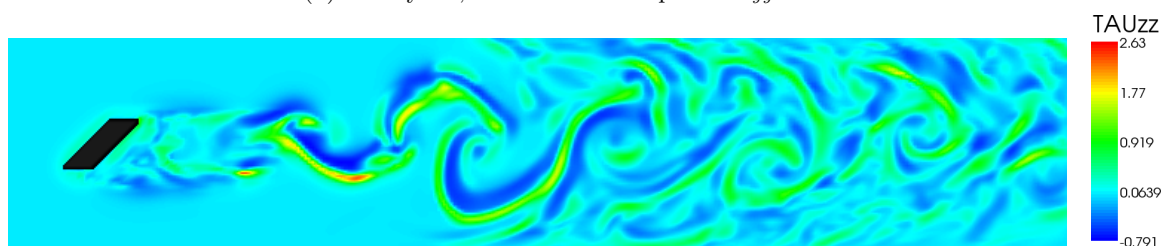
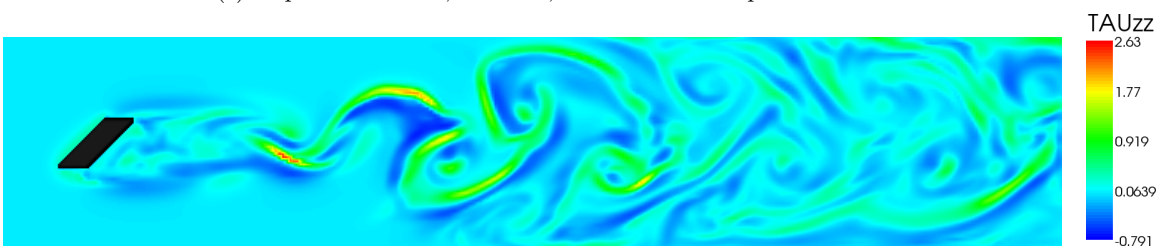
(a) Exponential PTT, $\varepsilon = 0.25$, stress tensor component τ_{xx} .(b) Oldroyd-B, stress tensor component τ_{xx} .(c) Exponential PTT, $\varepsilon = 0.25$, stress tensor component τ_{yy} .(d) Oldroyd-B, stress tensor component τ_{yy} .(e) Exponential PTT, $\varepsilon = 0.25$, stress tensor component τ_{zz} .(f) Oldroyd-B, stress tensor component τ_{zz} .

Figure 7.27: Normal stress components for the Oldroyd-B model and the exponential PTT model for the Kármán vortex street.

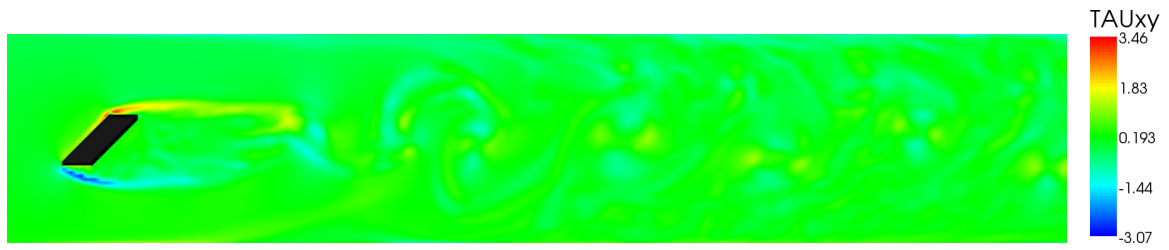
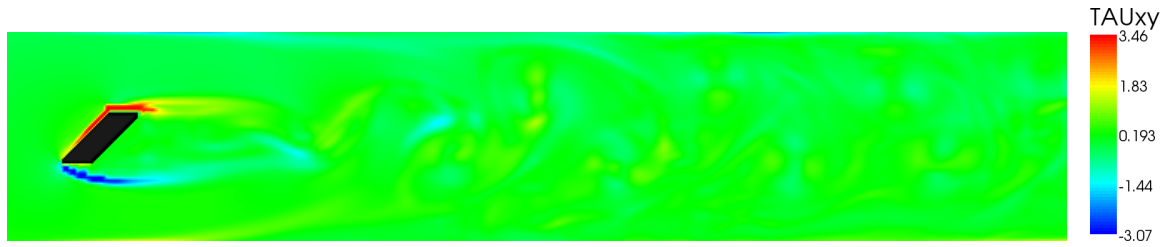
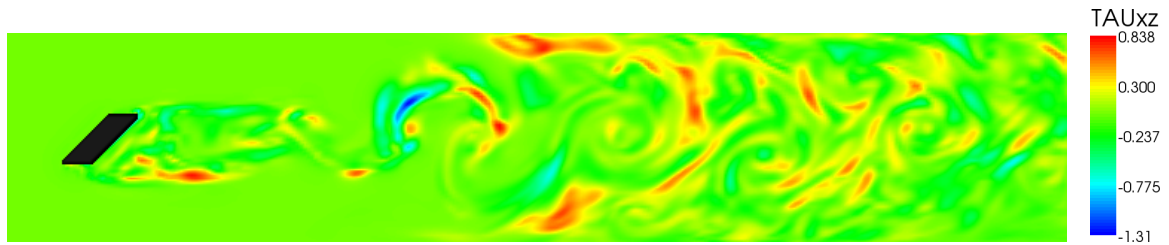
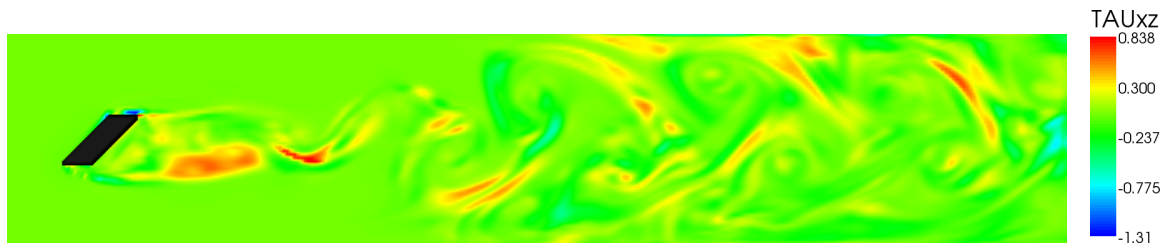
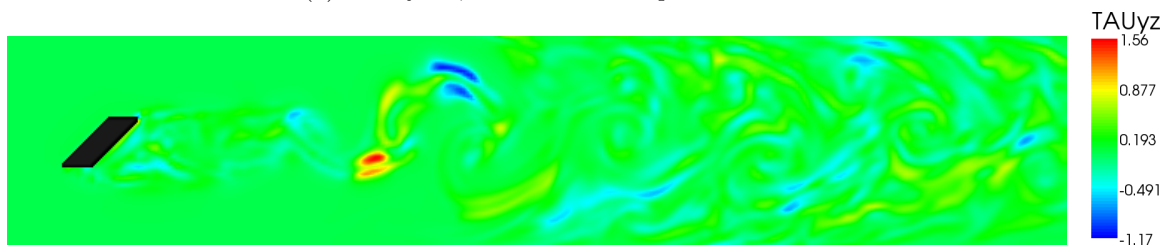
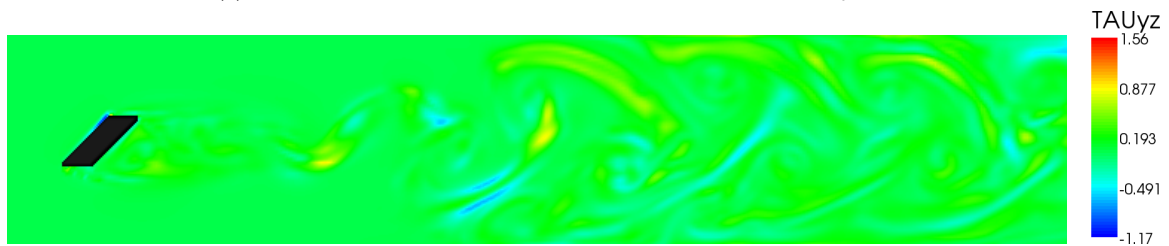
(a) Exponential PTT, $\varepsilon = 0.25$, stress tensor component τ_{xy} .(b) Oldroyd-B, stress tensor component τ_{xy} .(c) Exponential PTT, $\varepsilon = 0.25$, stress tensor component τ_{xz} .(d) Oldroyd-B, stress tensor component τ_{xz} .(e) Exponential PTT, $\varepsilon = 0.25$, stress tensor component τ_{yz} .(f) Oldroyd-B, stress tensor component τ_{yz} .

Figure 7.28: Shear stress components for the Oldroyd-B model and the exponential PTT model for the Kármán vortex street.

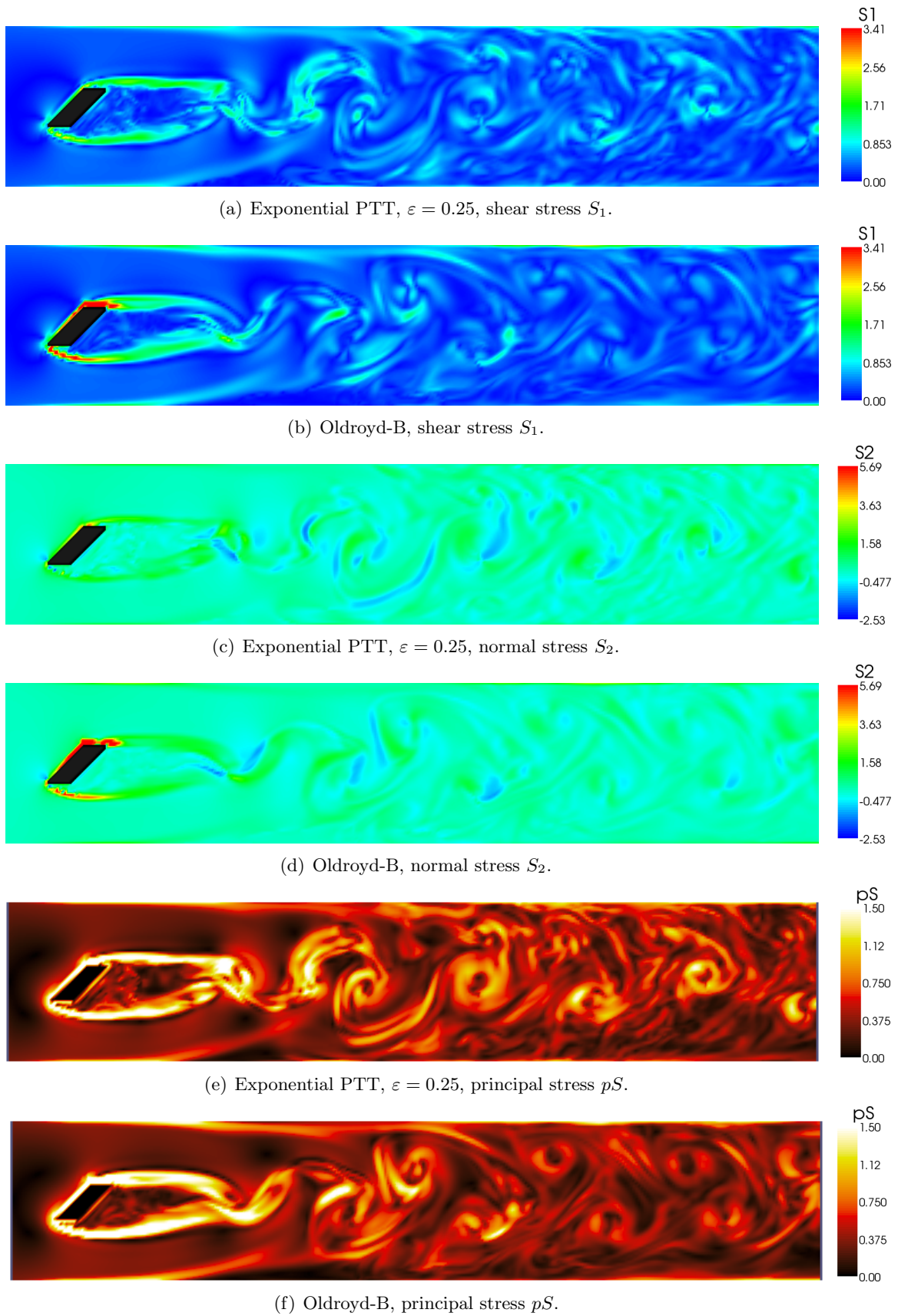


Figure 7.29: Normal and shear stress S_1 and S_2 , and principal stress pS for the Oldroyd-B model and the exponential PTT model for the Kármán vortex street.

Chapter 8

Conclusion

Summary

The main aim of this thesis was to develop a numerical method for solving transient viscoelastic flow problems in three space dimensions. To this end, we chose the Oldroyd-B equations and both the exponential form and the linear form of the Phan-Thien Tanner equations including the prediction of non-affine motion and a Newtonian contribution to the stress tensor to model viscoelasticity. Before, we used these models in our simulations, we investigated their predictions of shear-dependent viscosity, normal stress differences and elongational viscosity and discussed the meaning of their parameters very thoroughly.

To solve the equations, describing the flow of a viscoelastic fluid, we discretized the unknowns on a staggered grid, where the pressure and the stress tensor components were discretized in the centre of the cells, while the velocities were discretized at the cell sides. We discretized the spatial derivatives in the Oldroyd-B and the Phan-Thien Tanner equations by central differences except for the convective terms, for which we employed the VONOS scheme and the WENO scheme. Moreover, we implemented Dirichlet, homogeneous Neumann and no-slip boundary conditions for the stress tensor components. We extended the Navier-Stokes equations by the parameter β in front of the diffusive terms and by the addition of the divergence of the elastic stress tensor, which we discretized by central differences. For the temporal discretization, we employed a Chorin-type projection method and a semi-implicit projection method with implicit treatment of the diffusive terms. Furthermore, we accelerated our computations by parallelization using a domain decomposition method.

In our computations, we could observe significant differences in the flow behaviour of the Oldroyd-B fluid and the Phan-Thien Tanner fluids. To investigate the differences of their stress predictions, we computed a flow directed shear and normal stress to obtain a physically meaningful stress measure in complex flows and used these stress measures to compute a principal stress. In our investigations of the principal stress, we found that the Oldroyd-B fluids show very thin stress boundary layers near the no-slip boundary, while the stress boundary layers occurring in PTT fluids are much wider.

We validated our implementations by the investigation of the numerical approximation of the analytical solution of the transient plane Poiseuille flow of an Oldroyd-B fluid and by a convergence study of a three-dimensional gravity driven flow through an infinite rectangular channel. We found an excellent agreement between the transient analytical solution and the numerical solution for the velocities and the stress tensor components and we observed that the numerical solution converged quadratically to the steady state analytical solution with mesh refinement. We also found quadratic convergence of all components in the convergence study of the three-dimensional gravity driven flow through an infinite rectangular channel

for the Oldroyd-B model and the PTT model.

Furthermore, we examined the flow through a three-dimensional rectangular channel, the flow over a hole and the Kármán vortex street behind an inclined plate and investigated the results for the different models. For the flow through a three-dimensional rectangular channel, we plotted and compared the velocity and stress tensor components for the different models. In the flow over a hole, we could observe an asymmetric vortex structure for the Oldroyd-B fluid and the PTT fluids, as seen in experiments with viscoelastic fluids. In addition, we could observe that the Oldroyd-B model showed extremely steep stress gradients at corner singularities, while the stress gradients for the PTT models were much less dramatic. Moreover, we investigated a Kármán vortex street behind an inclined plate for the different models. We were able to observe different vortex stretching behaviour and suppression of velocity fluctuations as seen in laboratory experiments. We found that the Oldroyd-B model suppresses velocity fluctuations in a very strong manner and leads to the strongest elongation of the vortices behind the inclined plate. To our knowledge, the Kármán vortex street behind an inclined plate, has not yet been numerically investigated for viscoelastic flows.

Outlook

Even though, we were able to simulate three-dimensional transient viscoelastic complex flow situations for different viscoelastic materials, there is still much room for further research and possible extensions.

To aim for numerical simulations of flows with higher Weissenberg numbers, we could employ an adaptive grid refinement scheme, which refines the grid in high deformation regions as to obey the stability criterion on the mesh size $\Delta x \leq |\mathbf{u}| / (2\sqrt{-\det(\nabla\mathbf{u})} - Wi^{-1})$ of Fattal and Kupferman [22, 23]. Additionally, a refinement of the regions near no-slip boundaries and corner singularities in order to resolve the boundary layers and the steep stress gradients could stabilize the calculations.

An extension to two phase flows would give the opportunity to investigate the numerous fascinating free surface phenomena such as die-swell or the Weissenberg effect. Moreover, in order to simulate industrial processes it is inevitable to consider free surface flows. However, the extension to free surface flows is not straightforward since researchers investigate instabilities near the free surface, which have to be prevented by appropriate numerical schemes (see e.g. Khismatullin [41]).

Moreover, it would be interesting to implement other differential constitutive equations like the Giesekus model, the Pom-Pom model and the eXtended Pom-Pom model to be able to simulate a wider variety of viscoelastic liquids.

Appendix A

Components of the Governing Equations

Vectors

$$\mathbf{u} = (u, v, w) \quad (\text{A.1})$$

$$\mathbf{g} = (g_x, g_y, g_z) \quad (\text{A.2})$$

Tensors

$$\mathbf{D} = \begin{pmatrix} \frac{\partial u}{\partial x} & \frac{1}{2}(\frac{\partial u}{\partial y} + \frac{\partial v}{\partial x}) & \frac{1}{2}(\frac{\partial u}{\partial z} + \frac{\partial w}{\partial x}) \\ \frac{1}{2}(\frac{\partial u}{\partial y} + \frac{\partial v}{\partial x}) & \frac{\partial v}{\partial y} & \frac{1}{2}(\frac{\partial v}{\partial z} + \frac{\partial w}{\partial y}) \\ \frac{1}{2}(\frac{\partial u}{\partial z} + \frac{\partial w}{\partial x}) & \frac{1}{2}(\frac{\partial v}{\partial z} + \frac{\partial w}{\partial y}) & \frac{\partial w}{\partial z} \end{pmatrix} \quad (\text{A.3})$$

$$\boldsymbol{\tau} = \begin{pmatrix} \tau_{xx} & \tau_{xy} & \tau_{xz} \\ \tau_{yx} & \tau_{yy} & \tau_{yz} \\ \tau_{zx} & \tau_{zy} & \tau_{zz} \end{pmatrix} \quad (\text{A.4})$$

$$\nabla \mathbf{u} = \begin{pmatrix} \frac{\partial u}{\partial x} & \frac{\partial u}{\partial y} & \frac{\partial u}{\partial z} \\ \frac{\partial v}{\partial x} & \frac{\partial v}{\partial y} & \frac{\partial v}{\partial z} \\ \frac{\partial w}{\partial x} & \frac{\partial w}{\partial y} & \frac{\partial w}{\partial z} \end{pmatrix} \quad (\text{A.5})$$

Momentum Equation

x-component

$$\begin{aligned} \frac{\partial u}{\partial t} + \frac{\partial(u^2)}{\partial x} + \frac{\partial(uv)}{\partial y} + \frac{\partial(uw)}{\partial z} = & -\frac{\partial p}{\partial x} + \frac{1}{\text{Re}}\beta \left[\frac{\partial^2 u}{\partial x^2} + \frac{\partial^2 u}{\partial y^2} + \frac{\partial^2 u}{\partial z^2} \right] \\ & + \frac{1}{\text{Re}} \left[\frac{\partial \tau_{xx}}{\partial x} + \frac{\partial \tau_{xy}}{\partial y} + \frac{\partial \tau_{xz}}{\partial z} \right] + \frac{1}{\text{Fr}^2} g_x \end{aligned} \quad (\text{A.6})$$

y-component

$$\begin{aligned} \frac{\partial v}{\partial t} + \frac{\partial(uv)}{\partial x} + \frac{\partial(v^2)}{\partial y} + \frac{\partial(vw)}{\partial z} = -\frac{\partial p}{\partial y} + \frac{1}{\text{Re}}\beta \left[\frac{\partial^2 v}{\partial x^2} + \frac{\partial^2 v}{\partial y^2} + \frac{\partial^2 v}{\partial z^2} \right] \\ + \frac{1}{\text{Re}} \left[\frac{\partial \tau_{yx}}{\partial x} + \frac{\partial \tau_{yy}}{\partial y} + \frac{\partial \tau_{yz}}{\partial z} \right] + \frac{1}{\text{Fr}^2} g_y \end{aligned} \quad (\text{A.7})$$

z-component

$$\begin{aligned} \frac{\partial w}{\partial t} + \frac{\partial(uw)}{\partial x} + \frac{\partial(vw)}{\partial y} + \frac{\partial(w^2)}{\partial z} = -\frac{\partial p}{\partial z} + \frac{1}{\text{Re}}\beta \left[\frac{\partial^2 w}{\partial x^2} + \frac{\partial^2 w}{\partial y^2} + \frac{\partial^2 w}{\partial z^2} \right] \\ + \frac{1}{\text{Re}} \left[\frac{\partial \tau_{zx}}{\partial x} + \frac{\partial \tau_{zy}}{\partial y} + \frac{\partial \tau_{zz}}{\partial z} \right] + \frac{1}{\text{Fr}^2} g_z \end{aligned} \quad (\text{A.8})$$

Phan-Thien Tanner Equationxx-component

$$\begin{aligned} f(\text{tr } \boldsymbol{\tau})\tau_{xx} + \text{Wi} \left\{ \frac{\partial \tau_{xx}}{\partial t} + u \frac{\partial \tau_{xx}}{\partial x} + v \frac{\partial \tau_{xx}}{\partial y} + w \frac{\partial \tau_{xx}}{\partial z} \right\} \\ + \text{Wi} \left\{ 2(\xi - 1) \frac{\partial u}{\partial x} \tau_{xx} + \left[(\xi - 2) \frac{\partial u}{\partial y} + \xi \frac{\partial v}{\partial x} \right] \tau_{xy} + \left[(\xi - 2) \frac{\partial u}{\partial z} + \xi \frac{\partial w}{\partial x} \right] \tau_{xz} \right\} \\ = 2(1 - \beta) \frac{\partial u}{\partial x} \end{aligned} \quad (\text{A.9})$$

yy-component

$$\begin{aligned} f(\text{tr } \boldsymbol{\tau})\tau_{yy} + \text{Wi} \left\{ \frac{\partial \tau_{yy}}{\partial t} + u \frac{\partial \tau_{yy}}{\partial x} + v \frac{\partial \tau_{yy}}{\partial y} + w \frac{\partial \tau_{yy}}{\partial z} \right\} \\ + \text{Wi} \left\{ \left[(\xi - 2) \frac{\partial v}{\partial x} + \xi \frac{\partial u}{\partial y} \right] \tau_{xy} + 2(\xi - 1) \frac{\partial v}{\partial y} \tau_{yy} + \left[(\xi - 2) \frac{\partial v}{\partial z} + \xi \frac{\partial w}{\partial y} \right] \tau_{yz} \right\} \\ = 2(1 - \beta) \frac{\partial v}{\partial y} \end{aligned} \quad (\text{A.10})$$

zz-component

$$\begin{aligned} f(\text{tr } \boldsymbol{\tau})\tau_{zz} + \text{Wi} \left\{ \frac{\partial \tau_{zz}}{\partial t} + u \frac{\partial \tau_{zz}}{\partial x} + v \frac{\partial \tau_{zz}}{\partial y} + w \frac{\partial \tau_{zz}}{\partial z} \right\} \\ + \text{Wi} \left\{ \left[(\xi - 2) \frac{\partial w}{\partial x} + \xi \frac{\partial u}{\partial z} \right] \tau_{xz} + \left[(\xi - 2) \frac{\partial w}{\partial y} + \xi \frac{\partial v}{\partial z} \right] \tau_{yz} + 2(\xi - 1) \frac{\partial w}{\partial z} \tau_{zz} \right\} \\ = 2(1 - \beta) \frac{\partial w}{\partial z} \end{aligned} \quad (\text{A.11})$$

xy-component/yz-component

$$\begin{aligned}
& f(\text{tr } \boldsymbol{\tau})\tau_{xy} + \text{Wi} \left\{ \frac{\partial \tau_{xy}}{\partial t} + u \frac{\partial \tau_{xy}}{\partial x} + v \frac{\partial \tau_{xy}}{\partial y} + w \frac{\partial \tau_{xy}}{\partial z} \right\} \\
& + \text{Wi} \left\{ (\xi - 1) \left[\frac{\partial u}{\partial x} + \frac{\partial v}{\partial y} \right] \tau_{xy} + \frac{1}{2} \left[(\xi - 2) \frac{\partial u}{\partial y} + \xi \frac{\partial v}{\partial x} \right] \tau_{yy} \right\} \\
& + \text{Wi} \left\{ \frac{1}{2} \left[(\xi - 2) \frac{\partial u}{\partial z} + \xi \frac{\partial w}{\partial x} \right] \tau_{yz} + \frac{1}{2} \left[(\xi - 2) \frac{\partial v}{\partial x} + \xi \frac{\partial u}{\partial y} \right] \tau_{xx} + \frac{1}{2} \left[(\xi - 2) \frac{\partial v}{\partial z} + \xi \frac{\partial w}{\partial y} \right] \tau_{xz} \right\} \\
& = (1 - \beta) \left(\frac{\partial u}{\partial y} + \frac{\partial v}{\partial x} \right)
\end{aligned} \tag{A.12}$$

xz-component/yz-component

$$\begin{aligned}
& f(\text{tr } \boldsymbol{\tau})\tau_{xz} + \text{Wi} \left\{ \frac{\partial \tau_{xz}}{\partial t} + u \frac{\partial \tau_{xz}}{\partial x} + v \frac{\partial \tau_{xz}}{\partial y} + w \frac{\partial \tau_{xz}}{\partial z} \right\} \\
& + \text{Wi} \left\{ (\xi - 1) \left[\frac{\partial u}{\partial x} + \frac{\partial w}{\partial z} \right] \tau_{xz} + \frac{1}{2} \left[(\xi - 2) \frac{\partial u}{\partial y} + \xi \frac{\partial v}{\partial x} \right] \tau_{yz} \right\} \\
& + \text{Wi} \left\{ \frac{1}{2} \left[(\xi - 2) \frac{\partial u}{\partial z} + \xi \frac{\partial w}{\partial x} \right] \tau_{zz} + \frac{1}{2} \left[(\xi - 2) \frac{\partial w}{\partial x} + \xi \frac{\partial u}{\partial z} \right] \tau_{xx} + \frac{1}{2} \left[(\xi - 2) \frac{\partial w}{\partial y} + \xi \frac{\partial v}{\partial z} \right] \tau_{xy} \right\} \\
& = (1 - \beta) \left(\frac{\partial u}{\partial z} + \frac{\partial w}{\partial x} \right)
\end{aligned} \tag{A.13}$$

yz-component/yz-component

$$\begin{aligned}
& f(\text{tr } \boldsymbol{\tau})\tau_{yz} + \text{Wi} \left\{ \frac{\partial \tau_{yz}}{\partial t} + u \frac{\partial \tau_{yz}}{\partial x} + v \frac{\partial \tau_{yz}}{\partial y} + w \frac{\partial \tau_{yz}}{\partial z} \right\} \\
& + \text{Wi} \left\{ \frac{1}{2} \left[(\xi - 2) \frac{\partial v}{\partial x} + \xi \frac{\partial u}{\partial y} \right] \tau_{xz} + (\xi - 1) \left[\frac{\partial v}{\partial y} + \frac{\partial w}{\partial z} \right] \tau_{yz} \right\} \\
& + \text{Wi} \left\{ \frac{1}{2} \left[(\xi - 2) \frac{\partial v}{\partial z} + \xi \frac{\partial w}{\partial y} \right] \tau_{zz} + \frac{1}{2} \left[(\xi - 2) \frac{\partial w}{\partial x} + \xi \frac{\partial u}{\partial z} \right] \tau_{xy} + \frac{1}{2} \left[(\xi - 2) \frac{\partial w}{\partial y} + \xi \frac{\partial v}{\partial z} \right] \tau_{yy} \right\} \\
& = (1 - \beta) \left(\frac{\partial v}{\partial z} + \frac{\partial w}{\partial y} \right)
\end{aligned} \tag{A.14}$$

linear form

$$f(\text{tr } \boldsymbol{\tau}) = 1 + \frac{\text{Wi} \varepsilon}{(1 - \beta)} (\tau_{xx} + \tau_{yy} + \tau_{zz}) \tag{A.15}$$

exponential form

$$f(\text{tr } \boldsymbol{\tau}) = \exp \left(\frac{\text{Wi} \varepsilon}{(1 - \beta)} (\tau_{xx} + \tau_{yy} + \tau_{zz}) \right) \tag{A.16}$$

Continuity Equation

$$\frac{\partial u}{\partial x} + \frac{\partial v}{\partial y} + \frac{\partial w}{\partial z} = 0 \quad (\text{A.17})$$

Appendix B

Analytical Solution of the Poiseuille Flow of an Oldroyd-B Fluid

In this section, we will describe the derivation of the expressions for the stress tensor components using the analytical solution of Waters and King [73]. The analytical solution of Waters and King can be written as

$$u(y, t) = 4y(1 - y) - 32 \sum_{n=1}^{\infty} \frac{\sin(Ny)}{N^3} G_N(\text{El}, t), \quad (\text{B.1})$$

where

$$N = (2n - 1)\pi, \quad A(y) = 4y(1 - y), \quad (\text{B.2})$$

$$\alpha_N = 1 + \text{El}N^2 \quad \beta_N^2 = \alpha_N^2 - 4N^2\text{El}, \quad \beta_N = \sqrt{\beta_N^2}, \quad (\text{B.3})$$

$$\gamma_N = 1 + N^2\text{El}(\beta - 2), \quad \alpha_N^* = \frac{\alpha_N}{2\text{El}}, \quad \beta_N^* = \frac{\beta_N}{2\text{El}} \quad (\text{B.4})$$

$$a_N = 1 + \frac{\gamma_N}{\beta_N}, \quad b_N = 1 - \frac{\gamma_N}{\beta_N}, \quad p_N = -\alpha_N^* + \beta_N^*, \quad q_N = -\alpha_N^* - \beta_N^*, \quad (\text{B.5})$$

and

$$G_N(\text{El}, t^*) = \begin{cases} \frac{1}{2} [a_N \exp(p_N t) + b_N \exp(q_N t)] & \text{if } \beta_N^2 \geq 0, \\ \exp(-\alpha_N^* t) \left[\cos(\beta_N^* t) + \frac{\gamma_N}{\beta_N} \sin(\beta_N^* t) \right] & \text{if } \beta_N^2 < 0. \end{cases} \quad (\text{B.6})$$

For the Poiseuille Flow all derivatives in the channel direction (x) are zero and $v = 0$. Therefore, the equations for the elastic stress tensor components reduce to

$$\tau_{xx} + \text{El} \frac{\partial \tau_{xx}}{\partial t} = 2\text{Wi} \frac{\partial u}{\partial y} \tau_{xy}, \quad (\text{B.7})$$

$$\tau_{xy} + \text{El} \frac{\partial \tau_{xy}}{\partial t} = (1 - \beta) \frac{\partial u}{\partial y} + \text{Wi} \frac{\partial u}{\partial y} \tau_{yy}, \quad (\text{B.8})$$

$$\tau_{yy} + \text{El} \frac{\partial \tau_{yy}}{\partial t} = 0, \quad (\text{B.9})$$

when the non-dimensionalization of Waters and King (7.14) is used. To solve these equations, let us introduce the change of variables

$$\tau = \exp\left(-\frac{t}{\text{El}}\right) \tilde{\tau}. \quad (\text{B.10})$$

By introducing (B.10) into (B.7) - (B.9), we obtain

$$\frac{\partial \tilde{\tau}_{xx}}{\partial t} = 2\text{Re} \frac{\partial u \sim}{\partial y} \tilde{\tau}_{xy}, \quad (\text{B.11})$$

$$\frac{\partial \tilde{\tau}_{xy}}{\partial t} = \frac{(1-\beta)}{\text{El}} \frac{\partial u}{\partial y} \exp\left(\frac{t}{\text{El}}\right) + \text{Re} \frac{\partial u \sim}{\partial y} \tilde{\tau}_{yy}, \quad (\text{B.12})$$

$$\frac{\partial \tilde{\tau}_{yy}}{\partial t} = 0. \quad (\text{B.13})$$

With the initial condition

$$\boldsymbol{\tau} = 0 \quad \text{at } t = 0, \quad (\text{B.14})$$

we obtain

$$\tau_{yy} = 0. \quad (\text{B.15})$$

Therefore, equation (B.12) reduces to

$$\frac{\partial \tilde{\tau}_{xy}}{\partial t} = \frac{(1-\beta)}{\text{El}} \frac{\partial u}{\partial y} \exp\left(\frac{t}{\text{El}}\right), \quad (\text{B.16})$$

which gives on integration over $[0, t]$

$$\tilde{\tau}_{xy}(t) - \tilde{\tau}_{xy}(0) = \frac{(1-\beta)}{\text{El}} \int_0^t \frac{\partial u}{\partial y} \exp\left(\frac{t}{\text{El}}\right) dt. \quad (\text{B.17})$$

The derivative of the velocity component is given by

$$\frac{\partial u}{\partial y} = A'(y) - 32 \sum_{n=1}^{\infty} \frac{\cos(Ny)}{N^2} G_N(\text{El}, t), \quad (\text{B.18})$$

where

$$A'(y) = \frac{dA(y)}{dy} = 4(1-2y). \quad (\text{B.19})$$

After integration, and with $\tilde{\tau}_{xy}(0) = 0$, we obtain

$$\tilde{\tau}_{xy}(t) = \frac{(1-\beta)}{\text{El}} \exp\left(\frac{t}{\text{El}}\right) \left[\text{El} A'(y) - 32 \sum_{n=1}^{\infty} \frac{\cos(Ny)}{N^2} H_N(\text{El}, t) \right] + C_{xy}(\text{El}, y), \quad (\text{B.20})$$

where $C_{xy}(\text{El}, y)$ is the sum of the results of the integrals for $t = 0$ and

$$H_N(\text{El}, t^*) = \begin{cases} \frac{1}{2} \left[\frac{a_N}{p_N + 1/\text{El}} \exp(p_N t) + \frac{b_N}{q_N + 1/\text{El}} \exp(q_N t) \right] & \text{if } \beta_N^2 \geq 0, \\ \frac{\exp(-\alpha_N^* t)}{c_N} \left[\left(\beta_N^* + h_N \frac{\gamma_N}{\beta_N} \right) \sin(\beta_N^* t) + \left(h_N - \beta_N^* \frac{\gamma_N}{\beta_N} \right) \cos(\beta_N^* t) \right] & \text{if } \beta_N^2 < 0 \end{cases} \quad (\text{B.21})$$

with

$$h_N = -\alpha_N^* + \frac{1}{\text{El}}, \quad c_N = h_N^2 + (\beta_N^*)^2. \quad (\text{B.22})$$

Finally, by multiplying equation (B.20) with $\exp(-t/\text{El})$, we obtain

$$\tau_{xy}(t) = \frac{(1-\beta)}{\text{El}} \left[\text{El} A'(y) - 32 \sum_{n=1}^{\infty} \frac{\cos(Ny)}{N^2} H_N(\text{El}, t) \right] + C_{xy}(\text{El}, y) \exp\left(-\frac{t}{\text{El}}\right). \quad (\text{B.23})$$

Now, we can calculate the expression for τ_{xx} with

$$\tilde{\tau}_{xx}(t) = 2\text{Re} \int_0^t \frac{\partial u_{\sim}}{\partial y} \tau_{xy} dt. \quad (\text{B.24})$$

With (B.20) and (B.20) this yields

$$\begin{aligned} \tilde{\tau}_{xx}(t) = & 2\text{Re} C_{xy}(\text{El}, y) \left[A'(y) \int_0^t dt - 32 \sum_{n=1}^{\infty} \frac{\cos(Ny)}{N^2} \int_0^t G_N(\text{El}, t) dt \right] \\ & + 2\text{Re} (1-\beta) A'(y) \left[A'(y) \text{El} \exp\left(\frac{t}{\text{El}}\right) - 32 \sum_{n=1}^{\infty} \frac{\cos(Ny)}{N^2} \int_0^t G_N(\text{El}, t) \exp\left(\frac{t}{\text{El}}\right) dt \right] \\ & - \frac{64 \text{Re} A'(y)(1-\beta)}{\text{El}} \sum_{n=1}^{\infty} \frac{\cos(Ny)}{N^2} \int_0^t H_N(\text{El}, t) \exp\left(\frac{t}{\text{El}}\right) dt \\ & + \frac{2 \cdot 32^2 \text{Re} (1-\beta)}{\text{El}} \sum_{n,m=1}^{\infty} \frac{\cos(Ny)}{N^2} \frac{\cos(My)}{M^2} \int_0^t H_N(\text{El}, t) G_M(\text{El}, t) \exp\left(\frac{t}{\text{El}}\right) dt. \end{aligned} \quad (\text{B.25})$$

Integrating and multiplying by $\exp(-t/\text{El})$ results in

$$\begin{aligned} \tau_{xx}(t) = & 2\text{Re} C_{xy}(\text{El}, y) \left[A'(y) \exp\left(-\frac{t}{\text{El}}\right) t - 32 \sum_{n=1}^{\infty} \frac{\cos(Ny)}{N^2} I_N(\text{El}, t) \right] \\ & + 2\text{Re} (1-\beta) A'(y) \left[A'(y) \text{El} - 32 \sum_{n=1}^{\infty} \frac{\cos(Ny)}{N^2} H_N(\text{El}, t) \right] \\ & - \frac{64 \text{Re} A'(y)(1-\beta)}{\text{El}} \sum_{n=1}^{\infty} \frac{\cos(Ny)}{N^2} J_N(\text{El}, t) \\ & + \frac{2 \cdot 32^2 \text{Re} (1-\beta)}{\text{El}} \sum_{n,m=1}^{\infty} \frac{\cos(Ny)}{N^2} \frac{\cos(My)}{M^2} K_{NM}(\text{El}, t) + C_{xx}(\text{El}, y) \exp\left(-\frac{t}{\text{El}}\right), \end{aligned} \quad (\text{B.26})$$

where

$$I_N(\text{El}, t^*) = \frac{1}{2} \left[\frac{a_N}{p_N} \exp((p_N - 1/\text{El})t) + \frac{b_N}{q_N} \exp((q_N - 1/\text{El})t) \right], \text{ if } \beta_N^2 \geq 0, \quad (\text{B.27})$$

$$I_N(\text{El}, t^*) = \frac{\exp((- \alpha_N^* - 1/\text{El})t)}{(\alpha_N^*)^2 + (\beta_N^*)^2} \left[\left(\beta_N^* - \alpha_N^* \frac{\gamma_N}{\beta_N} \right) \sin(\beta_N^* t) + \left(-\alpha_N^* - \beta_N^* \frac{\gamma_N}{\beta_N} \right) \cos(\beta_N^* t) \right], \text{ if } \beta_N^2 < 0, \quad (\text{B.28})$$

$$J_N(\text{El}, t^*) = \frac{1}{2} \left[\frac{a_N}{(p_N + 1/\text{El})^2} \exp(p_N t) + \frac{b_N}{(q_N + 1/\text{El})^2} \exp(q_N t) \right], \text{ if } \beta_N^2 \geq 0, \quad (\text{B.29})$$

$$J_N(\text{El}, t^*) = \frac{\exp(-\alpha_N^* t)}{c_N^2} \times \left[\left\{ h_N \left(\beta_N^* + h_N \frac{\gamma_N}{\beta_N} \right) + \beta_N^* \left(h_N - \beta_N^* \frac{\gamma_N}{\beta_N} \right) \right\} \sin(\beta_N^* t) + \left\{ h_N \left(h_N - \beta_N^* \frac{\gamma_N}{\beta_N} \right) - \beta_N^* \left(\beta_N^* + h_N \frac{\gamma_N}{\beta_N} \right) \right\} \cos(\beta_N^* t) \right], \text{ if } \beta_N^2 < 0, \quad (\text{B.30})$$

and

$$K_{NM}(\text{El}, t^*) = \frac{1}{2} \left[\frac{a_N a_M}{(p_M + 1/\text{El})(p_N + p_M + 1/\text{El})} \exp((p_N + p_M)t) + \frac{a_N b_M}{(q_M + 1/\text{El})(p_N + q_M + 1/\text{El})} \exp((p_N + q_M)t) + \frac{b_N a_M}{(p_M + 1/\text{El})(q_N + p_M + 1/\text{El})} \exp((q_N + p_M)t) + \frac{b_N b_M}{(q_M + 1/\text{El})(q_N + q_M + 1/\text{El})} \exp((q_N + q_M)t) \right], \text{ if } \beta_N^2 \geq 0, \beta_M^2 \geq 0, \quad (\text{B.31})$$

$$K_{NM}(\text{El}, t^*) = \frac{\exp(-(\alpha_N^* + \alpha_M^*)t)}{c_M} \times \left[\frac{A_{NM} h_{NM} + D_{NM} \beta_{NM+}}{c_{NM+}} \sin(\beta_{NM+} t) + \frac{D_{NM} h_{NM} - A_{NM} \beta_{NM+}}{c_{NM+}} \cos(\beta_{NM+} t) + \frac{B_{NM} h_{NM} + E_{NM} \beta_{NM-}}{c_{NM-}} \sin(\beta_{NM-} t) + \frac{E_{NM} h_{NM} - B_{NM} \beta_{NM-}}{c_{NM-}} \cos(\beta_{NM-} t) \right], \text{ if } \beta_N^2 < 0, \beta_M^2 < 0 \quad (\text{B.32})$$

with

$$h_{NM} = -\alpha_N^* - \alpha_M^* + \frac{1}{\mathbf{E}l}, \quad \beta_{NM+} = \beta_N^* + \beta_M^*, \quad \beta_{NM-} = \beta_N^* - \beta_M^*, \quad (\text{B.33})$$

$$c_{NM+} = h_{NM}^2 + \beta_{NM+}^2, \quad c_{NM-} = h_{NM}^2 + \beta_{NM-}^2, \quad (\text{B.34})$$

$$A_{NM} = \frac{\beta_M^* + h_M \frac{\gamma_M}{\beta_M} + h_M \frac{\gamma_N}{\beta_N} - \beta_M^* \left(\frac{\gamma_N}{\beta_N} \right) \left(\frac{\gamma_M}{\beta_M} \right)}{2}, \quad (\text{B.35})$$

$$B_{NM} = \frac{-\beta_M^* - h_M \frac{\gamma_M}{\beta_M} + h_M \frac{\gamma_N}{\beta_N} - \beta_M^* \left(\frac{\gamma_N}{\beta_N} \right) \left(\frac{\gamma_M}{\beta_M} \right)}{2}, \quad (\text{B.36})$$

$$D_{NM} = \frac{h_M - \beta_M^* \frac{\gamma_M}{\beta_M} - \beta_M^* \frac{\gamma_N}{\beta_N} - h_M \left(\frac{\gamma_N}{\beta_N} \right) \left(\frac{\gamma_M}{\beta_M} \right)}{2}, \quad (\text{B.37})$$

$$E_{NM} = \frac{h_M - \beta_M^* \frac{\gamma_M}{\beta_M} + \beta_M^* \frac{\gamma_N}{\beta_N} + h_M \left(\frac{\gamma_N}{\beta_N} \right) \left(\frac{\gamma_M}{\beta_M} \right)}{2}. \quad (\text{B.38})$$

Bibliography

- [1] <http://wissrech.ins.uni-bonn.de/research/projects/NaSt3DGP/index.htm>.
- [2] <http://www-unix.mcs.anl.gov/mpi/mpich1/>.
- [3] ALVES, M.A., P.J. OLIVEIRA and F.T. PINHO: *Benchmark solutions for the flow of Oldroyd-B and PTT fluids in planar contractions*. J. Non-Newtonian Fluid Mech., 110:45–75, 2003.
- [4] BELL, J.B. and P. COLELLA: *A Second-Order Projection Method for the Incompressible Navier-Stokes Equations*. J. Comput. Phys., 85:257–283, 1989.
- [5] BERNSTEIN, B., E.A. KEARSLEY and L.J. ZAPAS: *A study of stress relaxation with finite strain*. Trans. Soc. Rheol., 7:391–410, 1963.
- [6] BIRD, R.B., C.F. CURTISS, R.C. ARMSTRONG and O. HASSAGER: *Dynamics of Polymeric Liquids*, volume 2. John Wiley and Sons, New York, 1987.
- [7] BIRD, R.B., C.F. CURTISS, R.C. ARMSTRONG and O. HASSAGER: *Dynamics of Polymeric Liquids*, volume 1. John Wiley and Sons, New York, 1987.
- [8] BIRD, R.B., P.J. DOTSON and N.L. JOHNSON: *Polymer solution rheology based on a finitely extensible bead-spring chain model*. J. Non-Newtonian Fluid Mech., 7:213–235, 1980.
- [9] BOGER, D.V. and K. WALTERS: *Rheological Phenomena in Focus*. Elsevier, Amsterdam, 1993.
- [10] BOLLADA, P.C. and T.N. PHILLIPS: *A physical decomposition of the stress tensor for complex flows*. Rheologica Acta, 2008. (available at <http://www.springerlink.com/content/y645558036677463>).
- [11] BROWN, D.L., R. CORTEZ and M.L. MINION: *Accurate Projection Methods for the Incompressible Navier–Stokes Equations*. J. Comput. Phys., 168:464–499, 2001.
- [12] BÖHME, G.: *Strömungsmechanik nichtnewtonscher Fluide*. Teubner, Stuttgart, Leipzig, Wiesbaden, 2000.
- [13] CAREW, E.O., P. TOWNSEND and M.F. WEBSTER: *Taylor-Galerkin Algorithms for Viscoelastic Flow: Application to a Model Problem*. Numer. Meth. Partial Differential Equations, 10:171–190, 1994.
- [14] CHILCOTT, M.D. and J.M. RALLISON: *Creeping flow of dilute polymer solutions past cylinders and spheres*. J. Non-Newtonian Fluid Mech., 29:381–432, 1988.
- [15] CHORIN, A.J.: *Numerical solution of the Navier-Stokes equations*. Math. Comp., 22:745–762, 1968.
- [16] CHORIN, A.J. and J.E. MARSDEN: *Mathematical Analysis of Viscoelastic Flows*. SIAM, Philadelphia, 2000.

- [17] CROCE, R.: *Ein paralleler, dreidimensionaler Navier-Stokes-Löser für inkompressible Zweiphasenströmungen mit Oberflächenspannung, Hindernissen und dynamischen Kontaktflächen*. Diplomarbeit, Institut für Angewandte Mathematik, Universität Bonn, Bonn, Germany, 2002.
- [18] DOI, M. and S.F. EDWARDS: *Dynamics of concentrated polymer systems: Brownian motion in the equilibrium state*. J. Chem. Soc. Faraday Trans., 74:1789–1801, 1978.
- [19] DOI, M. and S.F. EDWARDS: *Dynamics of concentrated polymer systems: Molecular motion under flow*. J. Chem. Soc. Faraday Trans., 74:1802–1817, 1978.
- [20] DOI, M. and S.F. EDWARDS: *Dynamics of concentrated polymer systems: The constitutive equation*. J. Chem. Soc. Faraday Trans., 74:1818–1832, 1978.
- [21] DUPRET, F., J.M. MARCHAL and M.J. CROCHET: *On the consequence of discretization errors in the numerical calculation of viscoelastic flow*. J. Non-Newtonian Fluid Mech., 18:173–186, 1985.
- [22] FATTAL, R. and R. KUPFERMAN: *Constitutive laws for the matrix-logarithm of the conformation tensor*. J. Non-Newtonian Fluid Mech., 123:281–285, 2004.
- [23] FATTAL, R. and R. KUPFERMAN: *Time-dependent simulation of viscoelastic flows at high Weissenberg number using the log-conformation representation*. J. Non-Newtonian Fluid Mech., 126:23–37, 2005.
- [24] FONTELOS, M.A. and A. FRIEDMAN: *The flow of a class of Oldroyd fluids around a re-entrant corner*. J. Non-Newtonian Fluid Mech., 95:185–198, 2000.
- [25] GERRITSMAN, M.I.: *Time dependent numerical simulations of a viscoelastic fluid on a staggered grid*. Proefschrift Rijksuniversiteit Groningen, Cip-Gegevens koninklijke bibliotheek, den Haag, 1996.
- [26] GIESEKUS, H.: *Die Elastizität von Flüssigkeiten*. Rheol. Acta, 5:29–35, 1966.
- [27] GIESEKUS, H.: *A simple constitutive equation for polymer fluids based on the concept deformation-dependent tensorial mobility*. J. Non-Newtonian Fluid Mech., 11:69–109, 1982.
- [28] GREEN, M.S. and A.V. TOBOLSKY: *A New Approach to the Theory of Relaxing Polymeric Media*. J. Chem. Phys., 14:80–92, 1946.
- [29] GRIEBEL, M., T. DORNSEIFER and T. NEUNHOEFFER: *Numerical Simulation in Fluid Dynamics: A Practical Introduction*. SIAM, Philadelphia, 1998.
- [30] HUILGOL, R.R. and N. PHAN-THIEN: *Fluid Mechanics of Viscoelasticity*. Elsevier, Amsterdam, 1997.
- [31] HULSEN, M.A.: *A sufficient condition for a positive definite configuration tensor in differential models*. J. Non-Newtonian Fluid Mech., 38:93–100, 1990.
- [32] INC., KITWARE: *ParaView 3.3.0*. <http://www.paraview.org/New/index.html>, July 10, 2008.
- [33] JOHNSON, M.W. and D. SEGALMAN: *A model for viscoelastic fluid behavior which allows non-affine deformation*. J. Non-Newtonian Fluid Mech., 2:255–270, 1977.
- [34] JOSEPH, D.D.: *Fluid Dynamics of Viscoelastic Liquids*. Springer-Verlag, New York, 1990.

- [35] JOSEPH, D.D., M. RENARDY and J.C. SAUT: *Hyperbolicity and change of type in the flow of viscoelastic fluids*. Arch. Rat. Mech. Anal., 87:213–251, 1985.
- [36] JOSEPH, D.D. and J.C. SAUT: *Change of type and loss of evolution in the flow of viscoelastic fluids*. J. Non-Newtonian Fluid Mech., 20:117–141, 1986.
- [37] KAYE, A.: *Non-Newtonian flow in incompressible fluids*. Technical Report 134, College of Aeronautics, Cranfield, U.K., 1962.
- [38] KEILLER, R.A.: *Numerical instability of time-dependent flows*. J. Non-Newtonian Fluid Mech., 43:229–246, 1992.
- [39] KEUNINGS, R.: *On the high Weissenberg number problem*. J. Non-Newtonian Fluid Mech., 20:209–226, 1986.
- [40] KEUNINGS, R.: *Simulation of Viscoelastic Fluid Flow, in Fundamentals of Computer Modeling for Polymer Processing*, pages 402–470. Carl Hanser Verlag, 1989.
- [41] KHISMATULLIN, D., Y. RENARDY and M. RENARDY: *Development and implementation of VOF-PROST for 3D viscoelastic liquid–liquid simulations*. J. Non-Newtonian Fluid Mech., 140:120–131, 2006.
- [42] KLITZ, M.: *Homogenised Fluid Flow Equations in Porous Media with Application to Permeability Computations in Textiles*. Diplomarbeit, Institut für Numerische Simulation, Universität Bonn, Bonn, Germany, 2006.
- [43] KRAMERS, H.A.: *The behavior of macromolecules in inhomogeneous flow*. J. Chem. Phys., 14:415–424, 1946.
- [44] LARSON, R.G.: *Constitutive equations for polymer melts and solutions*. Butterworths, Boston, 1988.
- [45] LODGE, A.S.: *A network theory of flow birefringence and stress in concentrated polymer solutions*. Trans. Faraday Soc., 52:120–130, 1956.
- [46] LODGE, A.S.: *Elastic Liquids*. Academic Press, New York, 1964.
- [47] MACOSKO, C.W.: *Rheology: Principles, Measurements, and Applications*. Wiley-VCH, New York, 1994.
- [48] MCKINLEY, G.H.: *Non-Newtonian Fluid Dynamics Research Group, Massachusetts Institute of Technology*. <http://web.mit.edu/nmf/>, April 2, 2008.
- [49] MCLEISH, T.C.B. and R.G. LARSON: *Molecular constitutive equations for a class of branched polymers: The pom-pom polymer*. J. Rheol., 42:81–110, 1998.
- [50] OWENS, R.G. and T.N. PHILLIPS: *Computational Rheology*. Imperial College Press, Singapore, 2005.
- [51] PERERA, M.G.N. and K. WALTERS: *Long-range memory effects in flows involving abrupt changes in geometry. Part I: Flows associated with L-shaped and T-shaped geometries*. J. Non-Newtonian Fluid Mech., 2:49–81, 1977.
- [52] PETERLIN, A.: *Hydrodynamics of macromolecules in a velocity field with longitudinal gradient*. J. Polym. Sci. B, 4:287–291, 1966.
- [53] PHAN-THIEN, N.: *A nonlinear network viscoelastic model*. Trans. Soc. Rheol., 22:259–283, 1978.

- [54] PHAN-THIEN, N.: *Understanding Viscoelasticity: Basics of Rheology*. Springer-Verlag, New York, 2002.
- [55] PHAN-THIEN, N. and R.I. TANNER: *A new constitutive equation derived from network theory*. J. Non-Newtonian Fluid Mech., 2:353–365, 1977.
- [56] PSIDOT: *The Barus Effect*. <http://www.youtube.com/watch?v=KcNWLlIv8gc>, July 14, 2007.
- [57] PSIDOT: *Fano Flow*. <http://www.youtube.com/watch?v=aY7xiGQ-7iw>, July 19, 2007.
- [58] RENARDY, M.: *Inflow boundary conditions for steady flows of viscoelastic fluids with differential constitutive laws*. Rocky Mt. J. Math., 18:445–453, 1988.
- [59] RENARDY, M.: *An alternative approach to inflow boundary conditions for Maxwell fluids in three space dimensions*. J. Non-Newtonian Fluid Mech., 36:419–425, 1990.
- [60] RENARDY, M.: *Re-entrant corner behavior of the PTT fluid*. J. Non-Newtonian Fluid Mech., 69:99–104, 1997.
- [61] RENARDY, M.: *Mathematical Analysis of Viscoelastic Flows*. SIAM, Philadelphia, 2000.
- [62] RIVLIN, R.S. and K.N. SAWYERS: *Nonlinear continuum mechanics of viscoelastic fluids*. Ann. Rev. Fluid Mech., 3:117–146, 1971.
- [63] SCHIEBER, J.D. and H.C. ÖTTINGER: *The effects of the bead inertia on the Rouse model*. J. Chem. Phys., 89:6972–6981, 1988.
- [64] SMITH, M.D., R.C. ARMSTRONG, R.A. BROWN and R. SURESHKUMAR: *Finite-element analysis of stability of two-dimensional viscoelastic flows to three-dimensional perturbations*. J. Non-Newtonian Fluid Mech., 93:203–244, 2000.
- [65] SUN, J., N. PHAN-THIEN and R.I. TANNER: *An adaptive viscoelastic stress splitting scheme and its applications: AVSS/SI and AVSS/SUPG*. J. Non-Newtonian Fluid Mech., 65:75–91, 1996.
- [66] SURESHKUMAR, R., M.D. SMITH, R.C. ARMSTRONG and R.A. BROWN: *Linear stability and dynamics of viscoelastic flows using time-dependent numerical simulation*. J. Non-Newtonian Fluid Mech., 82:57–104, 1999.
- [67] TANNER, R.I.: *Engineering Rheology*. Oxford University Press, New York, 2002.
- [68] TEMAM, R.: *Sur l'approximation de la solution des équations de Navier-Stokes par la méthode des pas fractionnaires*. Arch. Rational Mech. Anal., 32:135–153, 1969.
- [69] TREBOTICH, D., P. COLELLA and G.H. MILLER: *A stable and convergent scheme for viscoelastic flow in contraction channels*. J. Comput. Phys., 205:315–342, 2005.
- [70] VERBEETEN, W.M.H., G.W.M. PETERS and F.P.T. BAAIJENS: *Differential constitutive equations for polymer melts: The extended Pom–Pom model*. J. Rheol., 45:823–843, 2001.
- [71] VERBEETEN, W.M.H., G.W.M. PETERS and F.P.T. BAAIJENS: *Numerical simulations of the planar contraction flow for a polyethylene melt using the XPP model*. J. Non-Newtonian Fluid Mech., 117:73–84, 2004.
- [72] WARNER, H.R.: *Kinetic Theory and Rheology of Dilute Suspensions of Finitely Extensible Dumbbells*. Ind. Eng. Chem. Fund., 11:379–387, 1972.

-
- [73] WATERS, N.D. and M.J. KING: *Unsteady flow of an elastico-viscous liquid*. Rheol. Acta, 9:345–355, 1970.
- [74] WESSELING, P.: *Principles of Computational Fluid Dynamics*. Springer-Verlag, New York, 2001.
- [75] YAMAMOTO, M.: *The Visco-elastic Properties of Network Structure I. General Formalism*. J. Phys. Soc. Japan, 11:413–421, 1956.
- [76] YAMAMOTO, M.: *The Visco-elastic Properties of Network Structure II. Structural Viscosity*. J. Phys. Soc. Japan, 12:1148–1158, 1957.
- [77] YAMAMOTO, M.: *The Visco-elastic Properties of Network Structure III. Normal Stress Effect (Weissenberg Effect)*. J. Phys. Soc. Japan, 13:1200–1211, 1958.
- [78] ÖTTINGER, H.C.: *Stochastic Processes in Polymeric Fluids: Tools and Examples for Developing Simulation Algorithms*. Springer-Verlag, New York, 1996.